THÈSE

Pour obtenir le grade de

**DOCTEUR DE L'UNIVERSITÉ GRENOBLE ALPES**

École doctorale : I-MEP² - Ingénierie - Matériaux, Mécanique, Environnement, Energétique, Procédés, Production
Spécialité : 2MGE - Matériaux, Mécanique, Génie civil, Electrochimie
Unité de recherche : CEA/LITEN - Laboratoire d'Innovation pour les Technologies des Energies Nouvelles et les Nanomatériaux

# Cellules silicium pour l'environnement spatial : compréhension des mécanismes de dégradation et optimisation des performances

# Silicon solar cells for space environments: understanding degradation mechanisms and optimizing performance


Présentée par :

**Océane GUILLOT**


Direction de thèse :

| | |
|---|---|
| **Sébastien DUBOIS**<br>DIRECTEUR DE RECHERCHE, CEA - Centre de Grenoble | Directeur de thèse |
| **Romain CARIOU**<br>INGENIEUR CHERCHEUR, CEA | Co-encadrant de thèse |
| **Jordi VEIRMAN**<br>INGENIEUR CHERCHEUR, EURAC | Co-encadrant de thèse |

Rapporteurs :

**Jean-Paul KLEIDER**
DIRECTEUR DE RECHERCHE, CNRS délégation Ile-de-France sud
**Jef (Jozef) POORTMANS**
FULL PROFESSOR, Katholieke Universiteit Leuven

Thèse soutenue publiquement le **27 novembre 2025**, devant le jury composé de :

| | |
|---|---|
| **Erwann FOURMOND,**<br>PROFESSEUR DES UNIVERSITES, INSA Lyon | Président |
| **Sébastien DUBOIS,**<br>DIRECTEUR DE RECHERCHE, CEA centre de Grenoble | Directeur de thèse |
| **Jean-Paul KLEIDER,**<br>DIRECTEUR DE RECHERCHE, CNRS délégation Ile-de-France sud | Rapporteur |
| **Jef (Jozef) POORTMANS,**<br>FULL PROFESSOR, Katholieke Universiteit Leuven | Rapporteur |
| **Sophie DUZELLIER,**<br>DOCTEURE EN SCIENCES, Centre ONERA Toulouse | Examinatrice |
| **Stephen TAYLOR,**<br>DOCTEUR EN SCIENCES, European Space Agency | Examinateur |

Invités :

**Romain Cariou**
DOCTEUR EN SCIENCES, CEA
**Julien Mekki**
DOCTEUR EN SCIENCES, CNES

*But look on the bright side,*
*you say.*
*Has there ever been such brightness?*

— *Margaret Atwood*

# Acknowledgments

J'aimerais tout d'abord remercier Jean-Paul Kleider et Jef Poortmans, rapporteurs, ainsi que Stephen Taylor, Sophie Duzellier et Erwann Fourmond, examinateurs, d'avoir accepté de faire partie de mon jury de thèse, vos commentaires et questions lors de la soutenance ont été précieux.

Je remercie le CEA et le CNES de m'avoir donné l'opportunité de réaliser cette thèse. En particulier, j'ai pu participer au cours de cette thèse à de nombreuses conférences internationales et formations qui ont largement contribué à enrichir mon parcours.

Ma thèse n'aurait pas été la même sans mes encadrants. Mes remerciements vont bien entendu tout droit à mon directeur de thèse Sébastien Dubois. Merci pour ton implication durant ces trois années, je retiendrai particulièrement ton engouement pour chaque nouveau résultat qui apportait son lot de questionnements. Merci à mes encadrants, Romain Cariou pendant ces 3 années, et Jordi Veirman la première année. Ce fut un réel plaisir de travailler avec vous au quotidien, tant pour votre bonne humeur à chaque réunion que pour le partage de vos expertises respectives... sans oublier votre patience face aux inévitables rushs de dernière minute.

Côté CNES, j'ai pu travailler avec Corinne Aicardi, dans un premier temps, puis Julien Mekki et Matthieu Fongral. J'ai beaucoup apprécié nos échanges, apportant bien souvent un regard précieux sur ces résultats.

Les cellules solaires ont été irradiées par électrons à la plateforme d'irradiation Sirius à Saclay. J'ai pu assister à certaines de ces irradiations, mais aussi réaliser des mesures de durée de vie sur place. A ce titre, j'aimerais remercier Antonino et Olivier pour leur accueil. J'aimerais également remercier Gaëlle pour son accueil à la plateforme d'irradiation protons JANNuS à Saclay.

Les cellules solaires utilisées durant cette thèse ont été fabriquées sur la ligne pilote de l'INES. La finesse de ces cellules ainsi que la multitude de variations auront parfois été un challenge pour les équipes, encore merci à vous. Merci Adrien pour ton aide précieuse dans la supervision de ces lots, ainsi que pour tes nombreux partages de connaissances : impossible de repartir d'Écureuil sans avoir appris quelque chose ! Je remercie particulièrement Nico avec qui j'ai eu la chance de beaucoup travailler. Merci pour ta positivité, les nombreuses formations d'équipements, les réparations d'LBIC, mais surtout pour ton soutien lors des campagnes d'irradiation qui sont toujours arrivées bien trop vite. Merci à toutes les personnes m'ayant donné un coup de main de près ou de loin, que ce soit pour du process, de la caractérisation

ou de la simulation: merci Christine, Philippe, Tristan, Jordi, Charles, Raph, Renaud, et Pierre !

Je remercie plus largement les équipes cellules et modules que j'ai pu côtoyer durant cette thèse en salle blanche (ou en salle café) pour des discussions scientifiques (ou non). C'est certainement avec tous les locataires du fameux bureau des doctorants que j'ai le plus échangé, pour des astuces EQE, Origin,... mais encore plus souvent pour des moments de décompression bienvenus. Merci donc à Benjamin, Nicolas, Victor et Carla (la team de l'espace), Dylan, Julien, Vincent, Antoine, Lucie, Nathalie, Felicia, Shyrna, Hugo, Rosa et Zeinab, mais aussi Jules et Noémie bien que non thésards. Il y a eu aussi beaucoup de visiteurs dans ce bureau qui ont contribué à cette synergie, Jean-Baptiste (mais après 19h), ou plus régulièrement le temps du midi avec Louis, Corentin, Mathieu, Guillaume, Marc et les nombreux stagiaires du Lynx 4. Merci aussi à Julci, Amanda et Antoine pour votre bonne humeur lors des trajets en bus !

Faire sa thèse à l'INES est aussi synonyme de nombreux moments partagés dans le sport *outdoor*. Cela a commencé par des cours de skating avec Rémi, Timéa, Lucie, puis Rosa. Je finis cette thèse loin de maitriser cette discipline mais avec le souvenir d'avoir passé de très bons moments ! Merci Lucie de m'avoir fait rejoindre le désormais fameux groupe de vélo des Nikoolos, indispensable pour un regain d'énergie au détour d'un chat ou lors de weekends cyclosportifs. Impossible de ne pas nous remarquer avec nos couleurs chat-toyantes, la liste est longue, Nico (évidemment), Charles, Baptiste, Jeff et Hugo (les compétiteurs de l'extrême), Lucie, Léa et Thibaut (les enduranciers de l'extrême), mais aussi Hugo, Clarisse, Raphaël, Seb,... Merci particulièrement à Baptiste d'avoir été d'un grand soutien durant cette dernière année de thèse.

Enfin, je voudrais remercier tout mon entourage présent depuis des années, à commencer par ma famille. Un grand merci pour votre présence et pour m'avoir donné les moyens d'accomplir mes projets. Je n'oublie bien évidemment pas mes amis, un merci particulier à Pierrot, Thomas, Gauthier, Barbara, Marius et Amaury pour votre soutien indéfectible.

# Contents

**Abstract** **vi**

**Résumé** **vii**

**Glossary** **viii**

**Introduction** **1**
0.1 Early developments in the space domain ..... 1
0.2 Developments in the silicon photovoltaic industry ..... 2
0.3 Current trends in space solar cell technology ..... 3

**1 Theoretical Background** **7**
1.1 Basics and current trends of silicon solar cells ..... 7
1.1.1 Fundamentals of photovoltaic conversion ..... 7
1.1.1.1 Generation ..... 7
1.1.1.2 Current flow ..... 10
1.1.1.3 pn junction and charge collection ..... 10
1.1.2 Recombination activity ..... 12
1.1.2.1 Bulk recombination mechanisms ..... 12
1.1.2.2 Surface recombination ..... 14
1.1.2.3 Resulting carrier lifetime ..... 14
1.1.3 Solar cells operation ..... 15
1.1.3.1 I-V curves ..... 15
1.1.3.2 Spectral response ..... 18
1.1.4 Crystalline silicon ..... 19
1.1.4.1 Czochralski pulling ..... 19
1.1.4.2 Defects in as-grown Si ..... 21
1.1.5 Solar cell architectures ..... 23
1.1.5.1 Towards passivated contacts ..... 23
1.1.5.2 SHJ development ..... 24
1.2 Influence of electron/proton irradiations on silicon solar cells ..... 26
1.2.1 Space Environment ..... 26
1.2.2 From radiation environment to atomic displacement ..... 28
1.2.3 Displacement damage ..... 31
1.2.3.1 Carrier lifetime degradation ..... 33
1.2.3.2 Carrier removal effect ..... 34
1.2.3.3 Modeling radiation-induced degradation ..... 35
1.2.3.4 Irradiation-induced defect levels in c-Si ..... 38

1.2.4 Irradiation resilient c-Si solar cells: materials and designs ..... 40
1.2.4.1 Effect of material composition ..... 40
1.2.4.2 Si solar cells design ..... 42
1.2.4.3 Effect of annealing ..... 45
Conclusion and research objectives ..... 46

**2 Materials and methods** **49**
2.1 Solar cells production ..... 49
2.1.1 Wet chemistry ..... 51
2.1.2 a-Si:H deposition ..... 51
2.1.3 TCO deposition ..... 52
2.1.4 Screen-printing and curing ..... 52
2.1.5 $SiN_x$:H deposition ..... 52
2.1.6 Laser cut ..... 52
2.2 Irradiation facilities ..... 53
2.2.1 Electron irradiation ..... 53
2.2.2 Proton irradiation ..... 54
2.3 Characterization of the samples ..... 55
2.3.1 Majority carrier concentration and mobility ..... 55
2.3.2 Sheet resistance ..... 56
2.3.3 Composition properties with OxyMap ..... 56
2.3.4 Carrier lifetime ..... 57
2.3.5 Suns-$V_{OC}$ ..... 58
2.3.6 I-V measurements ..... 58
2.3.7 External quantum efficiency ..... 59
2.3.8 Light Beam Induced Current ..... 61
2.4 Simulation softwares used ..... 62
2.4.1 Effects of proton irradiation ..... 62
2.4.2 Solar cell modeling program ..... 62

**3 Electron irradiation of SHJ cells: effects of the material composition and wafer thickness** **65**
3.1 Design of experiments ..... 66
3.2 Initial properties ..... 69
3.3 Equilibrium hole concentration and mobility ..... 74
3.4 Recombination ..... 75
3.4.1 Carrier lifetime ..... 75
3.4.2 SRH modeling ..... 76
3.4.3 Influence of dopant atom on carrier lifetime ..... 79
3.5 Performance of the Ga-doped solar cells ..... 81
3.5.1 $J_{SC}$ and electron diffusion length ..... 82
3.5.2 In-plane electron diffusion length variations ..... 85
3.5.3 $V_{OC}$ ..... 89
3.5.4 Fill factor ..... 90
3.5.5 Resulting efficiency ..... 92
Conclusion ..... 93

**4 Proton irradiation of high resistivity SHJ cells** **95**
4.1 Experimental methods ..... 97

4.2 1 Sun I-V results ..... 100
4.3 Spectral response analyses ..... 103
4.3.1 Influence of bias light ..... 103
4.3.2 PC1D modeling of the proton irradiated cells ..... 107
4.3.3 In-plane parameters variations ..... 114
4.4 Bulk resistivity variations with increasing proton fluence ..... 121
Conclusion ..... 124

**Conclusion & perspectives** **127**

**Appendix. Optical properties adaptation for improved EOL performances** **133**

**Bibliography** **137**

**Résumé détaillé** **155**
Introduction ..... 155
Irradiation par électrons de cellules SHJ : effets de la composition du matériau et de l'épaisseur du wafer ..... 156
Irradiation par protons de cellules SHJ de haute résistivité ..... 160
Conclusion ..... 163
Références ..... 164

**List of publications** **167**

# Abstract

Historically, crystalline silicon solar technologies have supported the development of space activities. p-type silicon cells were the mainstream space solar devices until the 2000s. However, since then, all the solar photovoltaic generators of satellites have been manufactured with multi-junction cells based on III-V materials, with higher efficiency and radiation hardness. silicon-based cells and modules are once again becoming an attractive solution for space applications, driven by the increasing focus on cost reduction in the space sector and the exponential demand for satellites. Over the past 20 years, silicon cell efficiencies have significantly improved thanks to material innovations and the development of new cell architectures. However, the specific constraints of the space environment (essentially electron and proton irradiations) are responsible for significant aging of silicon solar cells. Then, building on the latest advances in terrestrial photovoltaic to invent the space silicon photovoltaic technologies of tomorrow requires innovations in materials, cells and modules along with advanced understanding regarding the various degradation mechanisms occurring in space. In this context, this PhD thesis focuses on the radiation hardness of silicon heterojunction cells (amorphous silicon / crystalline silicon), studying the degradation mechanisms of their electronic properties and their relationship with photovoltaic performance. Several irradiation conditions are evaluated, including electrons (1 $MeV$) and protons (1 $MeV$ and 3 $MeV$). For electron irradiation, the influences of the substrate composition and thickness are investigated. The main degradation mechanisms are identified (primarily related to carrier lifetime reductions), and guidelines are provided for improving radiation hardness. For the low proton irradiation conditions tested, significant decreases in the majority charge carrier density are highlighted (carrier removal effect), accentuating in-plane electronic inhomogeneities and creating heterogeneous properties through the cell depth. The experimental results obatined are well reproduced and explained through numerical simulations.

# Résumé

Historiquement, les technologies photovoltaïques en silicium cristallin ont accompagné le développement de la conquête spatiale. Jusqu'aux années 2000, les cellules en silicium de type p étaient les dispositifs solaires spatiaux les plus utilisés. À partir des années 2000, les générateurs solaires photovoltaïques ont progressivement adopté les cellules multi-jonctions III-V, plus performantes et plus résilientes aux irradiations. Cependant, la tendance actuelle à la réduction des coûts dans le secteur spatial, portée par la demande exponentielle en satellites, couplée aux progrès considérables réalisés par l'industrie photovoltaïque du silicium (matériaux, procédés, dispositifs, capacités de production et coûts) incitent à reconsidérer le potentiel du silicium pour certaines missions spatiales. Néanmoins, les contraintes spécifiques de l'environnement spatial entraînent un vieillissement marqué des cellules en silicium cristallin. Il est donc essentiel de comprendre les mécanismes de dégradation liés à cet environnement pour les technologies silicium les plus récentes du photovoltaïque terrestre (matériaux, cellules), afin de les adapter à cet environnement. Dans ce contexte, ce travail de thèse se concentre sur la résilience aux irradiations des cellules à hétérojonction silicium (silicium amorphe / silicium cristallin), à travers l'étude des mécanismes de dégradation des propriétés électroniques et de leur lien sur les performances photovoltaïques. Plusieurs conditions d'irradiation sont évaluées, notamment sous faisceaux d'électrons (1 $MeV$) et faisceaux de protons (1 $MeV$ et 3 $MeV$). Pour les irradiations électrons, l'impact de la composition du matériau et l'impact de l'épaisseur des cellules sont analysés. Cette étude permet de comprendre les principaux mécanismes de dégradation (essentiellement associés à des réductions de la durée de vie des porteurs). Des lignes directrices sont proposées pour optimiser la tenue aux radiations. Pour des cellules irradiées par des protons de basse énergie, des diminutions importantes de la concentration en porteurs de charge majoritaires sont mises en évidence, accentuant les inhomogénéités des propriétés électroniques dans le plan, en plus de créer des zones hétérogènes dans l'épaisseur de la cellule. Le comportement de ces cellules irradiées a pu être reproduit et expliqué par des simulations numériques.

# Glossary

## List of symbols

| | |
|---|---|
| B | Boron |
| Cz | Czochralski |
| c-Si | Crystalline silicon |
| $\Delta n$ | Carrier injection level |
| $E_c$ | Conduction band energy |
| $E_g$ | Energy bandgap |
| $E_i$ | Intrinsic energy level |
| $E_t$ | Defect energy level |
| $E_v$ | Valence band energy |
| $FF$ | Fill Factor |
| Ga | Gallium |
| $h$ | Planck constant |
| $J_{SC}$ | Short-circuit current density |
| $K_L$ | Minority carrier damage coefficient |
| $K_\tau$ | Carrier lifetime damage coefficient |
| $k$ | Symmetry factor |
| $k_B$ | Boltzmann constant |
| $L_n$ | Electron diffusion length |
| $\lambda$ | Wavelength |
| $\mu_n$ | Equilibrium electron mobility |
| $\mu_p$ | Equilibrium hole mobility |
| $n$ | Electron concentration |
| $n_i$ | Intrinsic carrier density |
| $n_0$ | Equilibrium electron concentration |
| n-type | Electron as majority carrier |
| $p$ | Hole concentration |
| $p_0$ | Equilibrium hole concentration |
| p-type | Hole as majority carrier |
| $pFF$ | Pseudo fill factor |
| QSS-PC | Quasi-steady state photoconductance |
| $R$ | Reflectance |
| $R_c$ | Carrier removal rate |
| $R_{sh}$ | Shunt resistance |
| $R_s$ | Series resistance |
| $r_H$ | Hall factor |
| $\rho$ | Resistivity |
| $R_{sheet}$ | Sheet resistivity |
| Si | Silicon |

| | |
|---|---|
| $\sigma$ | Conductivity |
| $\tau$ | Carrier lifetime |
| $\tau_{bulk}$ | Bulk carrier lifetime |
| $\tau_{p0/n0}$ | SRH capture time-constants for holes/electrons |
| TD | Thermal donor |
| $T$ | Temperature |

## List of acronyms

| | |
|---|---|
| BOL | Beginning-Of-Life |
| DDD | Displacement Damage Dose |
| DLTS | Deep-Level Transient Spectroscopy |
| EOL | End-Of-Life |
| EQE | External Quantum Efficiency |
| LBIC | Light Beam Induced Current |
| LeTID | Light-and elevated-Temperature-Induced Degradation |
| LID | Light-Induced Degradation |
| MJSC | Multi-Junction Solar Cells |
| NIEL | Non-Ionizing Energy Loss |
| PV | Photovoltaic |
| PVA | Photovoltaic Assemblies |
| QSS-PC | Quasi-steady state photoconductance |
| RF | Remaining Factor |
| SCR | Space Charge Region |
| SHJ | Silicon Heterojunction |
| SRH | Shockley-Read-Hall |
| SRV | Surface Recombination Velocity |
| T-IDLS | Temperature-Injection Dependence Level Spectroscopy |

# Introduction

Despite having been widely studied and used in the past century, we will see in the following pages how the crystalline silicon (c-Si) solar cells are once again at the center of research on space solar cells. This introduction provides a historical overview of photovoltaic (PV) technologies, including their early development for space applications and the development of c-Si PV for terrestrial applications. Then, the current interest in readily available and cost-effective solar cells for space applications is emphasized. As a result, this manuscript focuses on the topic of c-Si solar cells radiation hardness. More specifically, it aims at understanding the degradation mechanisms and optimizing the performance of Si heterojunction solar cells (SHJ) in space environments.

## 0.1 Early developments in the space domain

The story of Si solar cells begins in the 1950s, driven by the need for reliable power sources for space exploration. The first solar cell was developed by Bell Labs in 1954, with an efficiency of about 6% [1]. This initial breakthrough paved the way for further advancements in solar cell technology. One of the earliest and most significant milestones in space solar cell technology was the launch of the Vanguard 1 satellite in 1958, which was the first satellite powered by $\approx 10\%$ efficiency c-Si solar cells [2]. This mission demonstrated the feasibility of using solar power in space and marked the beginning of a new era in space exploration. Solar generators, such as those on Vanguard 1, enabled several years of autonomy for long-duration missions to the inner planets of the solar system, where sunlight is sufficient to power the solar panels. Significant advancements were then progressively made in solar cell efficiency and reliability, driven by the demands of space missions.

Research into high-efficiency devices led to the use of gallium arsenide (GaAs)-based solar cells in 1970, which sparked the beginning of III-V materials usage [3]. The first satellite equipped with GaAs-based solar cells followed with a launch in 1977 [4]. In parallel, multi-junction solar cells (MJSC) were developed, which consist of several subcells grown on top of each other, primarily composed of germanium (Ge) (used as substrate and bottom cell) and III-V materials. This subcells stack optimizes the photogeneration, thereby increasing efficiency.

MJSCs soon surpassed c-Si-based solar cells for space applications due to their higher efficiency and higher resilience to high energy particles, which are constantly bombarding solar arrays in space. For instance, nowadays, the quadruple junction solar cells commercialized by Azur Space feature 32% AM0 efficiency at beginning-of-life (BOL) and 28.7% AM0 efficiency at end-of-life (EOL) for $1 \times 10^{15}$ $cm^{-2}$ 1 $MeV$ electron fluence. In comparison, the same

company offers Si-based solar cells designed for space with a 16.9% AM0 BOL efficiency and 12.5% AM0 EOL efficiency for the same irradiation parameters [5]. The AM1.5G BOL evolution of best research PV conversion efficiency values for the main solar cells technologies are shown in Figure 0.1, and highlight the high efficiency of MJSCs.

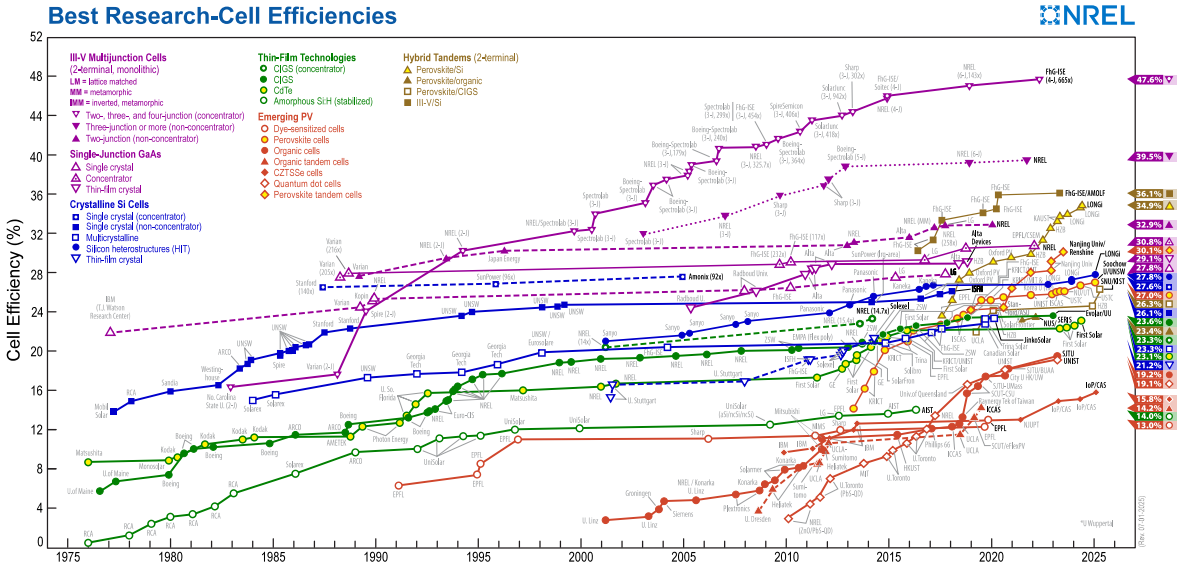


Figure 0.1: Best research-cell efficiency chart from NREL institute. The solar spectra used are AM1.5G for flat-plate devices and AM1.5D for concentrator devices [6].

## 0.2 Developments in the silicon photovoltaic industry

While the initial focus was on space applications, the benefits of solar energy were soon recognized for terrestrial use. The oil crisis of the 1970s further accelerated the development of solar cell technologies for terrestrial applications, as there was a growing need for alternative and renewable energy sources. This transition brought about significant improvements in manufacturing processes, materials, and cell designs, making progressively solar power an economically viable source of renewable energy.

As shown in Figure 0.1, there has been a steady increase in c-Si solar cell efficiency over the past few decades, with recent advances getting closer to their 32.2% Shockley–Queisser limit efficiency [7], [8]. Currently, the highest efficiency record of 27.8% was obtained with a c-Si-based hybrid-interdigitated-back-contact (HIBC) solar cell designed by LONGi [9], [10]. This structure combines SHJ, TOPCon and back contact designs.

Several key improvements have contributed to this progress. Carrier recombination losses were reduced through improved surface passivation at the interface between metal contacts and the c-Si substrate, and by lowering defect concentrations in the c-Si material. The latter

could be achieved by the improvements led on Czochralski (Cz) c-Si pulling, offering reduced oxygen (O) and metal impurities concentrations [11]. The Cz pulling now enables to use larger wafer dimensions and at reduced cost, through recent innovations such as melt recharging [12]. The doping of c-Si wafers also constituted a strong advancement. Gallium (Ga) replaced boron (B) as acceptor element for p-type doping, avoiding light-induced degradation (LID) effects due to the formation of recombination-active B-O complexes [13]. A switch is occurring from p-type to n-type doped c-Si with phosphorus (P) atoms allowing the industrial deployment of advanced cell architectures featuring stronger efficiency values [14]. The light trapping was enhanced through wafer texturing and anti reflection coating (ARC) layers. The metalization grids were also optimized, e.g. by reducing the shadowing [15]. The wafer thickness could also be reduced from 300 $\mu m$ to under 150 $\mu m$ with the improvement of slicing methods, with potential for further thinning during solar cell manufacturing [16].

SHJ solar cell design [17], [18], [19], [20] combines these advances and is among the c-Si cell designs resulting in the highest efficiencies [10].

## 0.3 Current trends in space solar cell technology

Until recently, the space solar cell market was dominated by MJSCs due to the advantages mentioned above. Other technologies are also gaining interest [21], such as copper indium gallium diselenide (CIGS) thin-film solar cells, which offer flexibility and high resilience to irradiation but with lower BOL efficiency compared to c-Si-based solar cells (under 24% for lab-scale devices, under 1 sun AM1.5G conditions [6]) [22], [23]. Another promising technology is the family of perovskite-based solar cells, which also exhibit high resilience to particle irradiation and low-cost potential [24]. However, the technology still faces stability and manufacturing issues, and is therefore not yet a ready-to-use solution.

In recent years, there has been a resurgence of interest in c-Si solar cells for space applications. The demand for cost-effective and reliable power sources continues to grow with the arrival of numerous private actors launching large telecommunication satellite constellations [21]. c-Si solar cells offer a promising solution due to their well-established manufacturing processes. The production capacity—the biggest obstacle to the use of MJSCs—is thus very large with $\approx 600\ GW$ installed at the end of 2024 [16]. Moreover, the cost per watt produced by c-Si-based modules (0.08 $\$/W$) is a few hundreds times cheaper compared to MJSCs. However, this low price is slightly counterbalanced by the EOL efficiency of the c-Si-based solar cells, which is roughly half that of MJSCs, leading to additional costs related to the extra weight needed to increase the solar cell surface area. Figure 0.2 shows the improvements made over the past 70 years on c-Si-based solar cells efficiency for terrestrial use in comparison with those related to space use [25]. It highlights the lack of research on this last topic these past 20 years and the need for further developments to improve EOL efficiency to match the advances made in terrestrial applications.

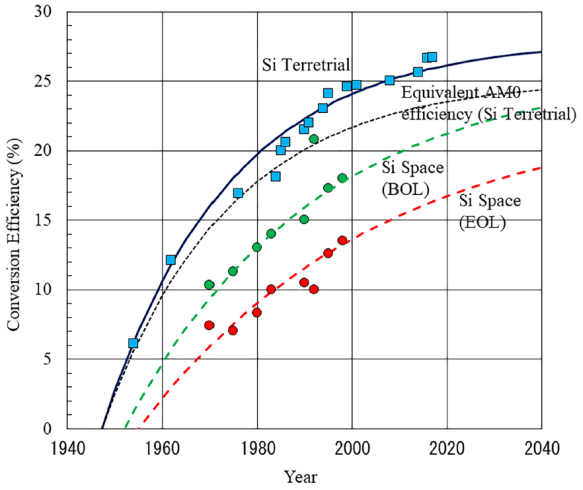


Figure 0.2: Chronological improvements and future trends in AM0 beginning-of-life (BOL) and end-of-life (EOL) efficiencies of c-Si space solar cells in comparison with AM1.5G efficiencies of c-Si solar cells for terrestrial use [25].

Given the high demand of solar cells suitable for space applications, and the need for cost-effective solutions, both driven by the launches of large telecommunications satellite constellations, c-Si solar cells are well-positioned to meet these needs. Among the various c-Si technologies, SHJ solar cells stand out as particularly promising for space missions. These cells can be manufactured to achieve high BOL efficiency, and they are compatible with front emitters and p-type substrates, as well as thin wafers. Such features make them highly attractive for improving EOL performance. Recent studies have highlighted the growing interest in the application of SHJ solar cells for space missions [26], [27], [28], [29].

The radiation hardness of c-Si solar cells is closely linked to both the material properties and the cell architecture. Since much of the existing research on this topic dates back over 20 years, it thus appears relevant to analyse the radiation hardness of state-of-the-art cell technologies, which have benefited from significant advancements in both materials and designs. Understanding the degradation mechanisms in these enhanced materials and cell structures is thus crucial for developing solar cells that will maintain reliable performance over extended periods in space.

To address this, the following studies investigate the radiation hardness of SHJ solar cells with two axes. First, a detailed analysis of the properties of Ga-doped c-Si wafers focuses on the impact of resistivity, Ga concentration, oxygen content, and oxygen-related defects on the resilience of the material to electron irradiation. Then, the limitations of c-Si solar cells are explored by simulating a harsh space environment using high fluences of low-energy protons, which induce heterogeneous defect creation throughout the cell's depth.

The manuscript is organized as follows:

- **Chapter 1** provides a theoretical overview of the main parameters influencing solar cell operation, as well as the challenges posed by charged particle irradiation. Additionaly,

more details about the research objectives of the thesis are provided.

- **Chapter 2** introduces the materials and methods used in the subsequent studies.
- **Chapter 3** evaluates the impact of electron irradiation on Ga-doped SHJ cells, using wafers with three distinct material compositions.
- **Chapter 4** explores the limits of high-resistivity SHJ cells under low-energy proton irradiation.

CHAPTER 1

# Theoretical Background

## 1.1 Basics and current trends of silicon solar cells

### 1.1.1 Fundamentals of photovoltaic conversion

The solar cells produce energy through the photovoltaic effect, by which semiconductors generate charge carriers from the absorption of sun light photons. In solar cells, these carriers are then extracted and collected, usually thanks to a p-n junction which combines a semiconductor material with holes as majority carriers (p-type) and a semiconductor material with electrons as majority carriers (n-type).

The performance of the solar cell is the result of different mechanisms driving the photogeneration, the flow, the collection, and the recombination of charge carriers. These mechanisms are presented briefly below; more details can be found in [30], [31], [32].

#### 1.1.1.1 Generation

A semiconductor material is a material whose electrical conductivity lies between that of an insulator and a metal. If sufficient energy is provided, specifically higher than the bandgap energy $E_g$ (eV), valence electrons in the semiconductor gain enough energy to move from the valence band $VB$ to the conduction band $CB$, making the material conductive. $E_g$ is an intrinsic property of a material, and is equal to 1.12 eV for crystalline-silicon (c-Si) at room temperature.

Thermal generation $G_{th}$ ($electron - hole\ pairs/cm^3.s$) occurs when thermal vibrations, or phonons, transfer energy to electrons, exciting them from $VB$ to $CB$ and creating electron-hole pairs *ehp*. This process is influenced by temperature and the material's bandgap: thermal generation increases with higher temperatures and in semiconductors with smaller bandgaps. In equilibrium condition, in the dark and without voltage bias, the generated carriers recombine. This results in a thermal equilibrium state between $G_{th}$ and thermal recombination $R_{th}$, which can be expressed as: $G_{th} = R_{th}$.

The intrinsic carrier density $n_i$ ($cm^{-3}$) is given by the law of mass action $np = {n_i}^2$ where $n$ and $p$ are the electron and hole concentrations, respectively, with $n = p$ for undoped c-Si. Under thermal equilibrium conditions, $n$ and $p$ refer to the following equilibrium electron and

hole concentrations $n_0$ and $p_0$, respectively:

$$n_0 = N_c exp\left(\frac{E_F - E_C}{k_B T}\right),\ p_0 = N_v exp\left(\frac{E_v - E_F}{k_B T}\right) \tag{1.1}$$

where $N_V$ and $N_C$ are the density of states ($cm^{-3}$) in the valence band and in the conduction band, respectively. $E_v$ ($eV$) is the valence band energy level and $E_c$ ($eV$) is the conduction band energy level. $E_F$ is the Fermi level ($eV$), which indicates the energy level that separates the filled electron states from the empty states in a semiconductor, thus determining the distribution of electrons in the conduction band and holes in the valence band. $T$ is the temperature ($K$) and $k_B$ is the Boltzmann constant ($1.38 \times 10^{-23}\ J.K^{-1}$).

Thus:

$$n_i = \sqrt{N_c N_v exp\left(\frac{-E_g}{k_B T}\right)} \tag{1.2}$$

The dominant generation process that occurs for solar cells under illumination is the photo-generation (several orders of magnitude higher than thermal generation). An *ehp* is generated if $E = \frac{hc}{\lambda} > E_g$, where $E$ is the energy of the incoming photon, $h$ the Planck constant ($6.63 \times 10^{-34}\ m^2 kg/s$), $c$ the light velocity ($299,792,458\ m/s$), and $\lambda$ its wavelength ($m$). The absorption of a photon in the material follows the Beer–Lambert law, which describes an exponential attenuation of light intensity $I$ ($W/cm^2$) with the material depth x ($cm$):

$$I(\lambda, x) = I_0(\lambda) e^{-\alpha(\lambda)x} \tag{1.3}$$

where $I_0$ refers to the incident light intensity ($W/cm^2$) and $\alpha$ is the absorption coefficient ($cm^{-1}$), which is a function of the wavelength of the photon and is defined as:

$$\alpha(\lambda) = \frac{4\pi\kappa(\lambda)}{\lambda} \tag{1.4}$$

where $\lambda$ is expressed in $cm$, and $\kappa$ is the extinction coefficient of the material (unitless). The resulting absorption depth ($\alpha^{-1}$) versus the wavelength for c-Si is shown in Figure 1.1. It highlights that short-wavelength (high-energy) photons are absorbed near the surface, while long-wavelength photons penetrate deeper.

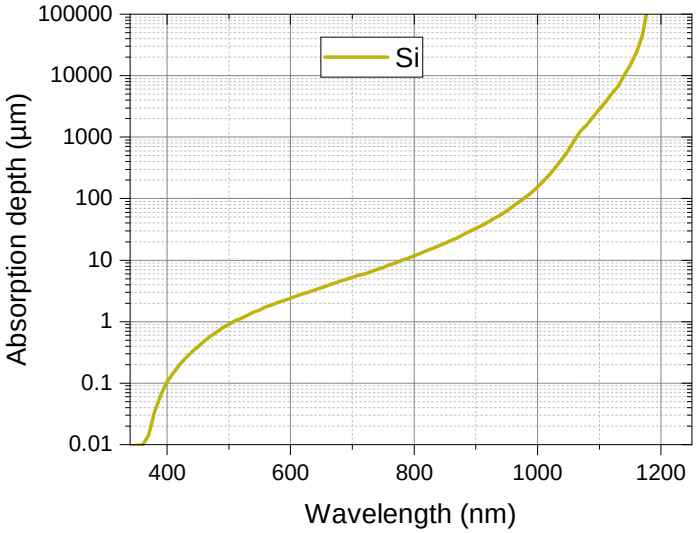


Figure 1.1: c-Si absorption depth.

The total charge carrier photogeneration rate $G$ $(ehp.cm^{-3}.s)$, for a given material thickness $x$, by taking into account front side reflectance losses $R(E)$ (unitless), is expressed as:

$$G(x) = \int_{E_g}^{\infty} [1 - R(E)]\alpha(E)\Gamma_0(E)e^{-\alpha(E)x} \tag{1.5}$$

where $\Gamma_0$ is the incident photon flux $(photons/cm^2/s)$.

As c-Si is an indirect semiconductor (the conduction band minimum and the valence band maximum occur for different crystal wave vectors), the absorption of a photon needs to be assisted by a phonon to effectively lead to photogeneration. Consequently, the c-Si $\alpha$ is lower in comparison with direct bandgap semiconductors such as most III-V materials. For instance, the quasi-full absorption of the sun spectrum photons beyond $E_g$ requires only few microns of monocrystalline GaAs, while $\approx 100\ \mu m$ of c-Si are required to achieve similar absorption levels.

Under illumination or bias voltage, the carrier injection levels $\Delta n = \Delta p$ $(cm^{-3})$ are generated, and we have:

$$\Delta n = \Delta p = G\tau \tag{1.6}$$

where $\tau$ is the carrier lifetime $(s)$. $n$ and $p$ are modified by $\Delta n$:

$$n = n_0 + \Delta n = N_c exp\left(\frac{E_{F,n} - E_c}{k_B T}\right),\ p = p_0 + \Delta p = N_v exp\left(\frac{E_v - E_{F,p}}{k_B T}\right) \tag{1.7}$$

where $E_{F,n}$ and $E_{F,p}$ are the electron and hole quasi Fermi levels $(eV)$, respectively, which give indications on the degree of excess electrons and holes under non thermal equilibrium conditions.

#### 1.1.1.2 Current flow

Once the free charges are photogenerated, they displace through the semiconductor with a current flow combining drift and diffusion effects. Considering a semi-infinite semiconductor, the current flow can be determined through:

- **the drift current density $\mathbf{J_{(n/p),drift}}$** $(mA/cm^2)$ which is the result of the carrier motion in an electric field **E**. It is expressed as:

$$\mathbf{J_{n,drift}} = nq\mu_n\mathbf{E}\,,\ \mathbf{J_{p,drift}} = pq\mu_p\mathbf{E} \tag{1.8}$$

  where $q$ is the elementary charge $(1.602 \times 10^{-19}\ C)$, and $\mu_n$ & $\mu_p$ are respectively the electron and hole **mobility** $(cm^2/V.s)$ and quantify the ability of a charge to move through a semiconductor when an electric field is applied. It is defined as $\mu_{n/p} = \frac{q\tau_c}{m^*_{e/h}}$ where $m^*_{e/h}$ is respectively the effective mass of an electron and a hole $(g)$ and $\tau_c$ is the scattering time $(s)$. $\tau_c$ refers to the average time between two collisions, either between charge carriers themselves or between a carrier and impurities or phonons. It is typically a function of temperature, semiconductor doping, bulk impurities and interface defects. The total drift current is expressed as $\mathbf{J_{drift}} = \sigma\mathbf{E}$ where $\sigma$ is the **conductivity** $(S/cm)$ and the inverse of the **resistivity** $\rho$ $(\Omega.cm)$. $\sigma$ is thus defined as:

$$\sigma = \frac{1}{\rho} = nq\mu_n + pq\mu_p \tag{1.9}$$

  The resistivity of a material is thus a function of not only the carrier concentrations but also of the electron and hole mobilities.
- **the diffusion current $\mathbf{J_{(n/p),diff}}$** $(mA/cm^2)$ which acknowledges the gradient of free carriers in a semiconductor and the flow from a high carrier concentration region to a low carrier concentration region. It is expressed as:

$$\mathbf{J_{n,diff}} = qD_n\nabla\mathbf{n}\,,\ \mathbf{J_{p,diff}} = -qD_p\nabla\mathbf{p} \tag{1.10}$$

  where $D_n$ and $D_p$, respectively the electron and hole **diffusivities** $(cm^2/s)$, are defined by the Einstein law as:

$$D_n = \frac{k_BT}{q}\mu_n\,,\ D_p = \frac{k_BT}{q}\mu_p \tag{1.11}$$

As a result, the transport equation is:

$$\mathbf{J_{total}} = \mathbf{J_{n,drift}} + \mathbf{J_{n,diff}} + \mathbf{J_{p,drift}} + \mathbf{J_{p,diff}} \tag{1.12}$$

#### 1.1.1.3 pn junction and charge collection

The extraction and collection of photogenerated carriers in a solar cell rely on two essential phenomena: the presence of an internal electric field **E** and a spatial gradient of minority carrier concentration established under illumination. These mechanisms enable the drift and diffusion of charge carriers toward their respective contacts.

In conventional c-Si solar cells, the electric field usually originates from a pn junction (illustrated for a p-type cell in Figure 1.2), formed by contacting p-type and n-type semiconductor regions. In the case of a p-type solar cell, a typical architecture includes:

- a lightly doped p-type c-Si substrate (the absorber),
- a highly doped $n^+$ emitter layer on the front side, forming the pn junction,
- and often a highly doped $p^+$ layer on the rear side, which can help to reduce recombination and improve the contact quality.

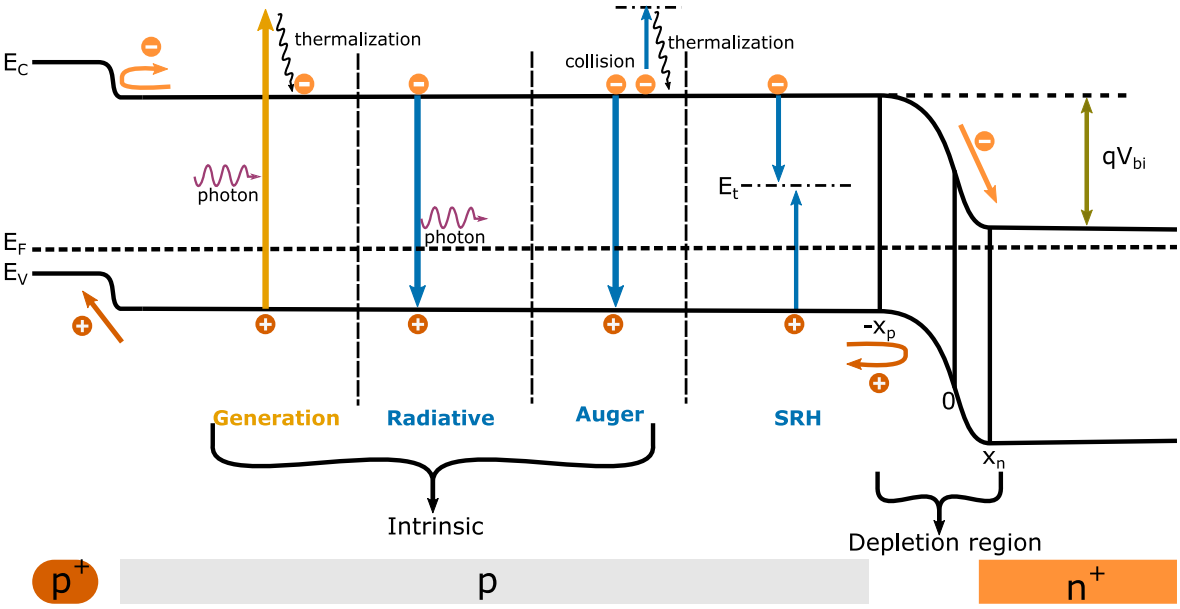


Figure 1.2: Schematic of c-Si homojunction band diagram with illustrations of carriers flow and generation/recombination mechanisms.

When the $n^+$ and p-type regions are brought into contact, electrons from the $n^+$ region diffuse into the p-type region and recombine with holes, while holes diffuse in the opposite direction. This mutual diffusion leaves behind fixed ionized dopants and results in a space charge region (SCR) or depletion region. In this region, an internal electric field $\mathbf{E}_{bi}$ is established. This field gives rise to the built-in voltage $V_{bi}$, which can be expressed for a homojunction (e.g., crystalline silicon with diffused dopants) as:

$$V_{bi} = \frac{k_B T}{q} \ln\left(\frac{p_0 n_0}{n_i^2}\right) \tag{1.13}$$

where $p_0$ and $n_0$ are the equilibrium hole and electron concentrations in the p-type and n-type regions, respectively.

The combination of drift in the SCR and diffusion in the neutral zones enables efficient charge collection.

### 1.1.2 Recombination activity

PV power production requires to collect the photogenerated free carriers before they recombine through various mechanisms. The average time between carrier photogeneration and recombination is called the effective carrier lifetime $\tau$, or $\tau_{eff}$ $(s)$, and results from intrinsic recombination mechanisms, impurities, defects in the bulk and non-ideal surface passivation.

#### 1.1.2.1 Bulk recombination mechanisms

The bulk carrier lifetime $\tau_{bulk}$ is governed by 3 types of recombination mechanisms: radiative, Auger (both intrinsic) and Shockley-Read-Hall (SRH). Their associated recombination lifetime is linked to $\Delta n$ in p-type c-Si via the volume recombination rate $U$ $(cm^{-3}.s^{-1})$ by:

$$U = \frac{\Delta n}{\tau_{bulk}} \tag{1.14}$$

- the **radiative recombination rate** $U_{rad}$ is a spontaneous flux dependant of the photon flux and the absorption from the material and is given by:

$$U_{rad} = B_r(np - n_i^2) \tag{1.15}$$

where $B_r$ $(cm^3/s)$ is the radiative recombination coefficient [33]. The resulting recombination lifetime for a p-type material is given by:

$$\tau_{rad} \approx \frac{1}{B_r(p_0 + \Delta n)} \approx \begin{cases} \frac{1}{B_r p_0}, & \text{if } \Delta n \ll p_0 \text{ (low injection)} \\ \frac{1}{B_r \Delta n}, & \text{if } \Delta n \gg p_0 \text{ (high injection)} \end{cases} \tag{1.16}$$

- the **Auger-Meitner recombination rate** $U_{Auger}$ [34], [35], [36] is a three-particle process in which an electron from the conduction band recombines with a hole in the valence band, dissipating its energy by increasing the kinetic energy of a second electron in the conduction band. This third carrier can for instance dissipate its excess energy through thermalization. Under non-equilibrium condition, it is given by:

$$U_{Auger} = B_{Auger,p}(p^2 n - p_0^2 n_0) + B_{Auger,n}(n^2 p - n_0^2 p_0) \tag{1.17}$$

where $B_{Auger,p}$ and $B_{Auger,n}$ are the Auger recombination coefficients [37]. From this, we have an approximation of the Auger-limited carrier lifetime in a p-type material:

$$\tau_{Auger} \approx \begin{cases} \frac{1}{(B_{Auger,p}) p_0^2}, & \text{if } \Delta n \ll p_0 \text{ (low injection)} \\ \frac{1}{(B_{Auger,p} + B_{Auger,n}) \Delta n^2}, & \text{if } \Delta n \gg p_0 \text{ (high injection)} \end{cases} \tag{1.18}$$

Subsequent studies have further refined the description of this effect, including [38], [39], [40].

- the **SRH recombination rate** $U_{SRH}$ [41] is most often the main recombination mechanism in c-Si-based solar cells. It originates from defect levels which have the

ability to spatially capture and emit free carriers but can also act as recombination centers, especially when located near the middle of the bandgap. It is given by:

$$U_{SRH} = \frac{np - n_i^2}{\tau_{p0}(n + \hat{n}) + \tau_{n0}(p + \hat{p})} \tag{1.19}$$

where $\tau_{n0/p0}$ are the SRH capture time-constants for electrons/holes and are defined as:

$$\tau_{n0} = \frac{1}{\sigma_n N_t \nu_{th}}\ ,\ \tau_{p0} = \frac{1}{\sigma_p N_t \nu_{th}} \tag{1.20}$$

where $v_{th}$ is the thermal velocity (assumed equal for electrons and holes), $\sigma_{n/p}$ is the electron/hole capture cross section of the recombination center and $N_t$ is the recombination center density. We also define the electron and hole densities when $E_F$ is located at $E_t$ (the defect energy level), using the intrinsic energy level $E_i$, by:

$$\hat{n} = n_i exp\left(\frac{E_t - E_i}{k_B T}\right)\ ,\ \hat{p} = n_i exp\left(\frac{E_i - E_t}{k_B T}\right) \tag{1.21}$$

As a result, the SRH recombination lifetime is given by:

$$\tau_{SRH} = \frac{\tau_{n_0}(p_0 + \hat{p} + \Delta n) + \tau_{p_0}(n_0 + \hat{n} + \Delta n)}{p_0 + n_0 + \Delta n} \tag{1.22}$$

We can also define the capture-cross section ratio or symmetry factor $k$ of the recombination center, which is sometimes used in the parametrization of defects, as:

$$k = \frac{\sigma_n}{\sigma_p} \tag{1.23}$$

**Point defects** SRH recombination can originate from point defects present in the c-Si lattice (illustrated in Figure 1.3). Contaminants can result in atoms present in nonlattice positions (interstitial atoms noted $A_i$) or in replacement of an original atom (substitutional atoms noted $A_s$). A Frenkel pair is formed when a Si atom leaves its classic position to reach a nonlattice position, thus creating a vacancy and a self-intertitial atom. Two adjacent vacancies form a divacancy.

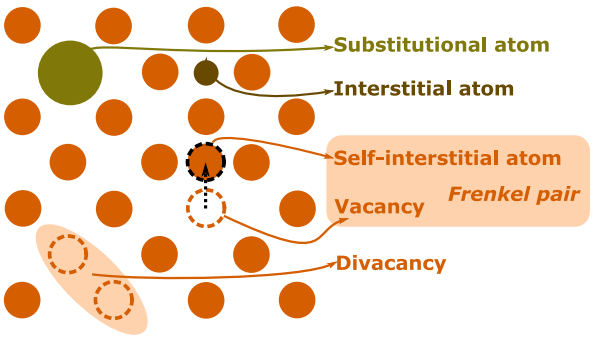


Figure 1.3: Point defects in crystalline lattice.

#### 1.1.2.2 Surface recombination

The carrier lifetime is also strongly dependent on the surface recombination, which originates mostly from unpassivated dangling bonds and absorbed impurity atoms and molecules. This leads to a high density of trap states at the surface. The surface recombination rate ($U_{surf}$) can be expressed in SRH formalism if one considers that the surface recombination occurs via a single-level interface state with an energy $E_t$, thus giving:

$$U_{surf} = \frac{n_n p_s - n_i^2}{\frac{n_s+\hat{n}}{S_{p0}} + \frac{p_s+\hat{p}}{S_{n0}}} \tag{1.24}$$

where $n_s$ and $p_s$ ($cm^{-3}$) are the electron and hole concentrations at the surface, which are a function of the electron and hole bulk concentrations, respectively, along with the surface band bending. $S_{n0}$ and $S_{p0}$ ($cm/s$) parameters are defined as:

$$S_{n0} \equiv \sigma_n \nu_{th} N_{st} \, , \; S_{p0} \equiv \sigma_p \nu_{th} N_{st} \tag{1.25}$$

where $N_{st}$ ($cm^{-2}$) is the number of interface states per unit area.

In the case of symmetrically passivated surfaces, the surface carrier lifetime $\tau_{surf}$ is defined as:

$$\tau_{surf} = \frac{W}{2S_{eff}} + \frac{1}{D_n}\left(\frac{W}{\pi}\right)^2 \tag{1.26}$$

where $S_{eff}$ is the surface recombination velocity (SRV) at the distance from the surface where the bands remain flat and $\Delta n = \Delta p$, and $W$ is the sample thickness. This expression can be approximated in the case of a sufficiently well passivated surface, i.e.: $\frac{S_{eff}W}{D_n} < \frac{1}{4}$, then:

$$\tau_{surf} \approx \frac{W}{2S_{eff}} \tag{1.27}$$

A good surface passivation is thus required to reach high $\tau$ levels. It can be enhanced via:

- chemical passivation: by the reduction of defect states with the saturation of dangling bonds (e.g. with hydrogen (H) SiH bonding)
- field-effect passivation: by the repulsion of minority or majority carriers from the interface by fixed charges (e.g. with fixed charges in dielectric, highly doped silicon layers, or dopant diffused layers).

#### 1.1.2.3 Resulting carrier lifetime

The above-mentioned recombination channels contribute to $\tau$ according to the following formula:

$$\frac{1}{\tau} = \frac{1}{\tau_{Auger}} + \frac{1}{\tau_{Radiative}} + \frac{1}{\tau_{SRH}} + \frac{1}{\tau_{surf}} \tag{1.28}$$

As the $\tau$ can only be measured with samples without metalization (the so-called precursor solar cells), the minority carrier diffusion length ($L_n$ for p-type c-Si) is commonly used to evaluate the recombination in finished devices. It is linked with the $\tau$ through the minority

carrier diffusivity ($D_n$ for electrons) by Fick law:

$$L_n = \sqrt{D_n \tau} \tag{1.29}$$

### 1.1.3 Solar cells operation

#### 1.1.3.1 I-V curves

The solar cell performances are usually obtained through the so-called I-V curves (or J-V curves considering the current density). The behavior of the solar cell under illumination can be approximated by the following one-diode model:

$$J = J_L - J_0 exp\left(\frac{qV}{nk_BT}\right) + J_0 \tag{1.30}$$

where $J$ is the current density ($mA/cm^2$), $V$ is the voltage ($mV$), $J_0$ is the saturation current density, $J_L$ the light generated current density and n is the ideality factor (unitless). Under illumination, the $J_0$ term can be neglected. $J_0$ strongly depends on the recombination in solar cells and on the temperature (through $n_i$ parameter, see Equation 1.2). It is defined for p-type solar cells as:

$$J_0 = q\frac{D_n n_i^2}{L_n p_0} \tag{1.31}$$

This one-diode model can be improved by taking into account the effects of the series resistance $R_s$ ($\Omega$) and the shunt resistance $R_{sh}$ ($\Omega$) (see Figure 1.4), thus:

$$J = J_L - J_0 exp\left(\frac{q(V + JR_s)}{nk_BT}\right) - \frac{V + JR_s}{R_{sh}} \tag{1.32}$$

The second term represents the voltage-dependent current density lost due to recombination and is denoted by $J_D$. The third term represents the current lost due to $R_{sh}$ and is denoted by $J_{sh}$. Therefore, we have:

$$J = J_L - J_D - J_{sh} \tag{1.33}$$

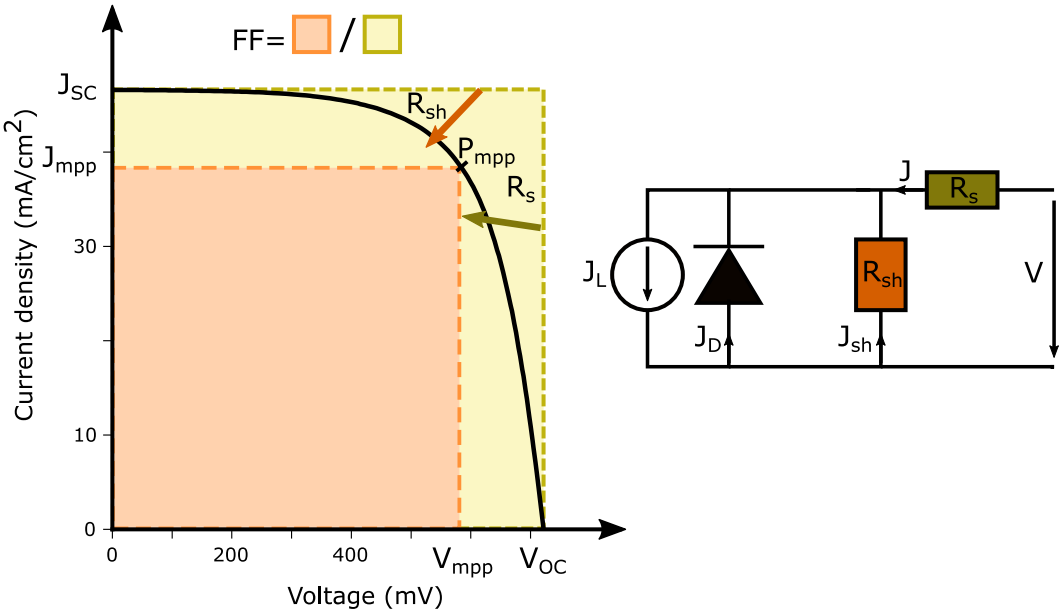


Figure 1.4: Example of an I-V curve and the associated one-diode circuit diagram. The expected losses due to series and shunt resistances are indicated.

The I-V curve under illumination is characterized by the following parameters:

- the **short-circuit current density** $J_{SC}$ $(mA/cm^2)$ is the maximum current density measured, and occurs when the voltage across the solar cell is null. This parameter reflects the generation and collection of the free carriers. It is a function of the number of incident photons, the spectrum of the incident light, the optical properties of the solar cells, and $\tau$. The $J_{SC}$ can also be obtained from external quantum efficiency (EQE) measurements (see hereafter), which provide a more representative view of this parameter.
- the **open-circuit voltage** $V_{OC}$ $(mV)$ is the maximum voltage measured, and occurs when the net current through the solar cell is null. It can be expressed as:

$$V_{OC} = \frac{nk_BT}{q} \ln\left(\frac{J_{SC}}{J_0} + 1\right) \tag{1.34}$$

  $V_{OC}$ is therefore mainly driven by the carrier recombination in the solar cell and the temperature, represented by the $J_0$ term. It is also possible to express it in function of $\Delta n$ (in p-type solar cells) with:

$$V_{OC} = \frac{k_BT}{q} \ln\left(\frac{\Delta n(p_0 + \Delta n)}{{n_i}^2} + 1\right) \tag{1.35}$$

  In this expression, $\Delta n$ refers to the average $\Delta n$ (on the sample thickness), provided that the surfaces are well passivated, and that $L_n$ is greater than the wafer thickness. If not, $\Delta n$ refers to the local excess carrier density and other approximations can be found in [42].
- the **maximum power density** $P_{mpp}$ $(mW/cm^2)$ denotes the maximum of the power

curve (given by $I \times V$) that occurs at voltage $V_{mpp}$ and current density $J_{mpp}$ ($P_{mpp} = V_{mpp} \times J_{mpp}$).

- the **series resistance** $R_s$ ($\Omega$) affects mostly the slope of the I-V curve near the $V_{OC}$, but not the $V_{OC}$ itself. A high $R_s$ will reduce the $J_{SC}$. Its value depends on the movement of current through the emitter and the base of the solar cell, the contact resistance between metal contacts and c-Si, and the resistance of the top and rear metal contacts.
- the **shunt resistance** $R_{sh}$ ($\Omega$) affects mostly the slope of the I-V curve near the $J_{SC}$, but not the $J_{SC}$ itself. A high $R_{sh}$ will reduce the $V_{OC}$. Its value is decreased mostly due to manufacturing defects and is heightened by low illumination conditions [43].
- the **fill factor** $FF$ (%) represents the percentage of ideality of the I-V curve, which should be a square under perfect conditions. In practice, the $FF$ strongly depends on the resistances—$R_s$ should be null and $R_{sh}$ infinite—as they distort the I-V curve, but it is also influenced by other physical factors such as recombination in the space charge region. It is quantified by the ratio of *orange square/yellow square* (see Figure 1.4), or more formally:

$$FF = \frac{P_{mpp}}{J_{SC}V_{OC}} = \frac{J_{mpp}V_{mpp}}{J_{SC}V_{OC}} \tag{1.36}$$

The power conversion efficiency—$\eta$ or PCE—(%) of the solar cell results from these parameters and is given by:

$$\eta = \frac{V_{OC}J_{SC}FF}{P_{inc}} = \frac{P_{mpp}}{P_{inc}} \tag{1.37}$$

where $P_{inc}$ is the incident light power per unit area. Two solar spectra are of interest in our study: AM0 and AM1.5G, where AM refers to Air Mass and quantifies the reduction in the power of light as it passes through the atmosphere and is absorbed by air molecules and dust. AM0 corresponds to the solar spectrum before it passes through the atmosphere; thus it is the reference for space missions. AM1.5G is the standard spectrum at the Earth's surface and includes both direct and diffuse irradiances. Absorption bands of atmospheric molecules such as ozone, carbon dioxide and water vapor can be seen by comparing an extract of AM0 and AM1.5G spectra in Figure 1.5. Their corresponding integrated spectral irradiance are 1366 $W/m^2$ for AM0 and 1000 $W/m^2$ for AM1.5G. The AM1.5G spectrum shows additional absorption bands—mainly in the near-infrared region—these bands correspond to wavelengths above the silicon band gap and therefore do not significantly contribute to electrical power generation. However, they are still included in $P_{inc}$. As a result, the efficiency calculated under AM0 conditions is actually lower than under AM1.5G conditions, because a larger portion of the AM0 incident power lies outside the energy-conversion-relevant spectral range.

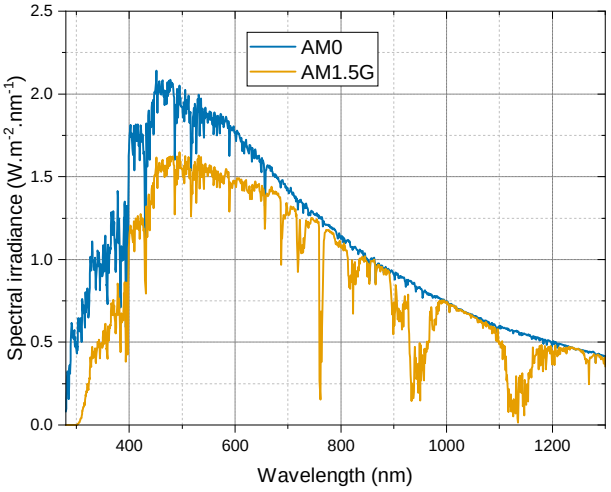


Figure 1.5: AM0 and AM1.5G spectra [44]. The wavelength range was defined to fit our set-up measurement range.

#### 1.1.3.2 Spectral response

The EQE is a dimensionless quantity derived from spectral response measurement and is defined as the ratio of collected charge carriers to the number of incident photons, this as a function of the incident wavelength. It then gives insights on the PV conversion as function of the cell depth (see Figure 1.6). The main factors impacting the EQE are:

- optical losses,
- front and rear recombination resulting from high SRV,
- bulk recombination.

In current state-of-the-art, optical losses include shading of the metal contacts (3–4%), surface reflection (3%), parasitic absorption in dielectric layers and contacts (<1%), free-carrier absorption (<1%), or imperfect light management (<1%) [45].

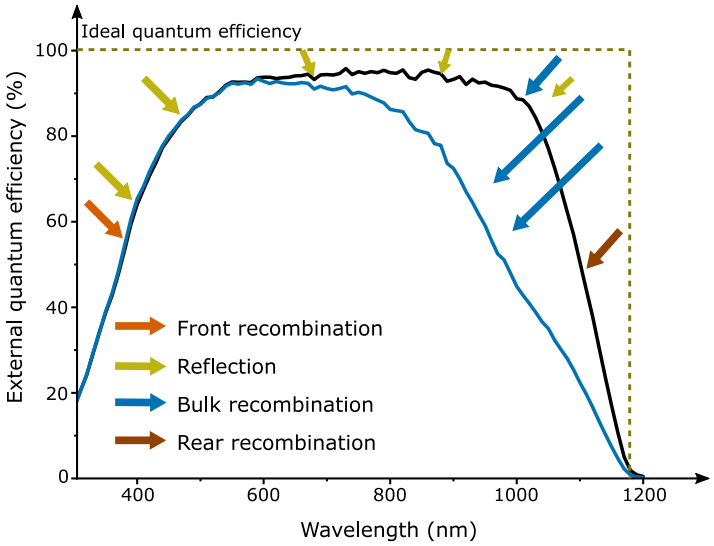


Figure 1.6: Example of two EQE curves with typical losses expected, with high—BOL—(black curve) and low—EOL—(blue curve) $L_n$. The two curves are extracted from Chapter 3.

From this measurement, it is possible to retrieve the $L_n$ parameter in the case of a front emitter, when the degradation is homogeneous in the bulk, and when $L_n$ is significantly lower than the cell thickness [46]. It is also possible to determine the $J_{SC}$ parameter from EQE with:

$$J_{SC} = \frac{q}{hc} \int_0^{\lambda_g} \lambda I(\lambda) EQE(\lambda) d\lambda \tag{1.38}$$

where $I(\lambda)$ is the spectral irradiance ($W.m^{-2}.nm^{-1}$) as a function of the wavelength $\lambda$ and $\lambda_g$ is the cutoff wavelength corresponding to the bandgap energy $E_g$ of the absorber material, defined as $\lambda_g = \frac{hc}{E_g}$.

### 1.1.4 Crystalline silicon

While monocrystalline Si accounted for less than 40% of the Si PV wafer market share in 2016 —with the remaining 60% being multicrystalline Si—it reached 100% in 2024 due to improved material quality and significant price reductions [16]. Therefore, this work focused only on monocrystalline-Si made through Czochralski (Cz) process. Float-zone (FZ) crystallization was sometimes used in space-relative c-Si solar cells studies as it was at this time a good way to reach high quality c-Si with low [O]. This FZ process produces high-purity monocrystalline Si ingots by moving a molten zone along a Si rod using induction heating, which segregates impurities toward one end and enables in-situ doping through gas-phase injection. However, this is a high cost process with limited wafer diameters, making it unsuitable for large-scale PV applications.

#### 1.1.4.1 Czochralski pulling

Cz process allows the formation of large-diameter monocrystalline-Si crystals with relatively low defect densities and controlled doping. During this process, a Si feedstock is placed in

a rotating cylindrical quartz crucible and is entirely melted. This molten c-Si (1412 $°C$) is doped with e.g. either B, Ga (to produce p-type c-Si) or phosphorus (P), antimony (Sb) (for n-type c-Si). A monocrystalline Si seed, which rotates in the opposite direction to the quartz crucible, is then brought into contact with the surface of the molten Si. The seed is slowly withdrawn vertically while continuing to rotate in the opposite direction, causing the Si to solidify on the seed crystal and grow into a single-crystal ingot (see Figure 1.7). The process parameters, such as the pulling rate, the rotation rate of the crystal and the thermal gradients, are precisely controlled to ensure uniform diameter and crystal quality. The pulling process includes several key stages. During the necking process, the seed is pulled quickly creating a few mm wide rod to eliminate dislocations. During the crowning phase, the pulling rate is gradually reduced while the diameter increases until the desired ingot diameter is reached. The pulling and rotation parameters are then stabilized during the crystal growth of the ingot body to maintain a constant ingot diameter. Finally, in the tailing phase, the pulling rate is increased again to taper the ingot and avoid the formation of thermal stress and dislocations near the end of growth [47].

This process can take several tens of hours to produce ingots up to a few meters long with diameter reaching now 300 mm.

The Si PV industry currently relies on the Cz process with melt-recharging. This process consists of periodically adding Si feedstock to the melt between ingot growths, which allows multiple crystals to be pulled from a single crucible. This strategy improves feedstock utilization and throughput, ultimately lowering the cost of ingot manufacturing. Additionally, this method facilitates doping control, especially when using dopants with low segregation coefficients, such as Ga [48], [49].

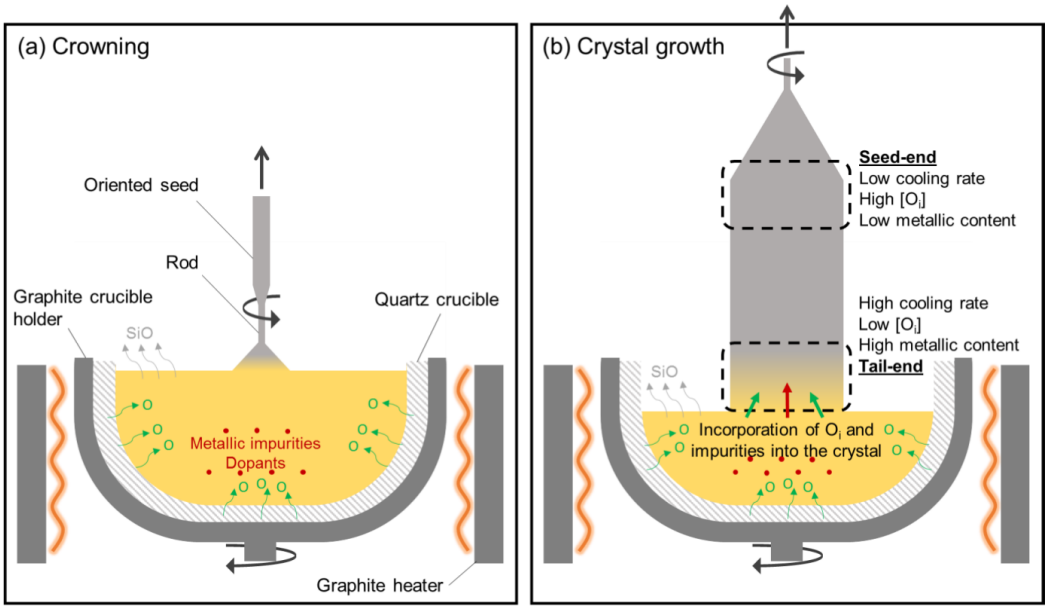


Figure 1.7: Schematic representation of Cz pulling for monocrystalline Si crystallization [50].

The main impurities in Cz ingots are oxygen (O), and to a lesser extent, carbon and metallic impurities. Their concentrations or related defects can be reduced by improving the

puller design [47], [51] or by impurity engineering (e.g. external gettering steps) [52], [45]. Oxygen primarily comes from the dissolution of the quartz crucible in contact with the molten Si. A significant fraction of the oxygen is lost through the formation and evaporation of silicon monoxide (SiO) gas, but part of it remains dissolved in the melt and is incorporated into the crystal as interstitial oxygen ($O_i$). Due to convective flow in the melt, oxygen tends to accumulate along the central axis of the ingot, while the SiO evaporation near the edges leads to lower oxygen concentrations at the periphery. As a result, the $O_i$ concentration shows a characteristic radial distribution, with a maximum near the center, often forming so-called ring-like structures.

The axial distribution of $O_i$ also varies along the height of the ingot. Typically, $[O_i]$ is higher near the seed-end. This is mainly due to the ratio of the melt-crucible contact area to the free surface, which decreases during ingot growth. In contrast, metallic impurities tend to accumulate near the tail-end of the ingot due to segregation effects (see Figure 1.7(b)). One can also note the specificity of Ga-doped ingots, which present a wider [Ga] distribution within the same ingot than its B-doped counterparts. This is due to the smaller segregation coefficient of Ga in Si [53].

#### 1.1.4.2 Defects in as-grown Si

Cz c-Si contains a relatively high concentration of $O_i$, originating from the quartz crucible, that can reach concentrations as high as $1 \times 10^{18}$ cm$^{-3}$. This oxygen plays a dual role: while it can help to strengthen the c-Si lattice and improve mechanical properties, it also leads to the formation of O-related electrically active defects during processing and operation.

Indeed, the initial presence of O in the material can lead to the creation of Si oxide precipitates ($SiO_x$), which form during the thermal processes (ingot growth and solar cell fabrication under high temperature ($\approx 1000$ °$C$) and whom recombination activity increases with their size. Their presence can reduce the solar cell efficiency by 4% (absolute) [54]. A high [O] also leads to the creation of O-related thermal donors (TD) at $350 - 500$ °$C$ that consist of an electrically active "core" surrounded by aggregating O atoms [55], [56]. They deactivate at temperatures above 650 °$C$. TD have two configurations: H, which has no recombination activity, and X, which has a recombination activity. As their names indicate, these TD have the property to behave as donors, and more specifically double donors since TD are usually doubly ionized at room temperature [57]. Thus, they influence the resulting majority carrier concentration. In the case of Ga-doped c-Si, we thus have:

$$p_0 = [Ga] - 2[TD] \tag{1.39}$$

Similarly to $[O_i]$, [TD] is usually higher at the seed-end of the ingot, resulting in lower $p_0$ (higher $\rho$) than at the tail end, even with similar doping (i.e. Ga) concentration [58]. As [TD] strongly depends on $[O_i]$ (which is not homogeneously distributed in the wafer plane), the resulting $p_0$ can be heterogeneous in the wafer plane, usually following ring-like structures. The effect of TD on $p_0$ can be intensified in compensated c-Si, which is defined by similar concentrations of acceptor and donor species, i.e $2[TD]/[Ga] \approx 1$ in Ga-doped c-Si [59].

These O-related ring-like structures can also have impacts on the τ of the charge carriers, and thus on the minority carrier diffusion length as depicted in Figure 1.8(a). It can be the result of the formation of TD, but also of oxide precipitates [60]. For instance, in [61], the higher $[O_i]$ present at the middle of the wafers resulted in lower photoluminescence (PL) response, related with lower τ. In n-type c-Si, a lower [TD] was shown to result in higher τ as shown in Figure 1.8(b) in which the sample resulting in the highest τ (B) was the one with the lowest [TD] [62].

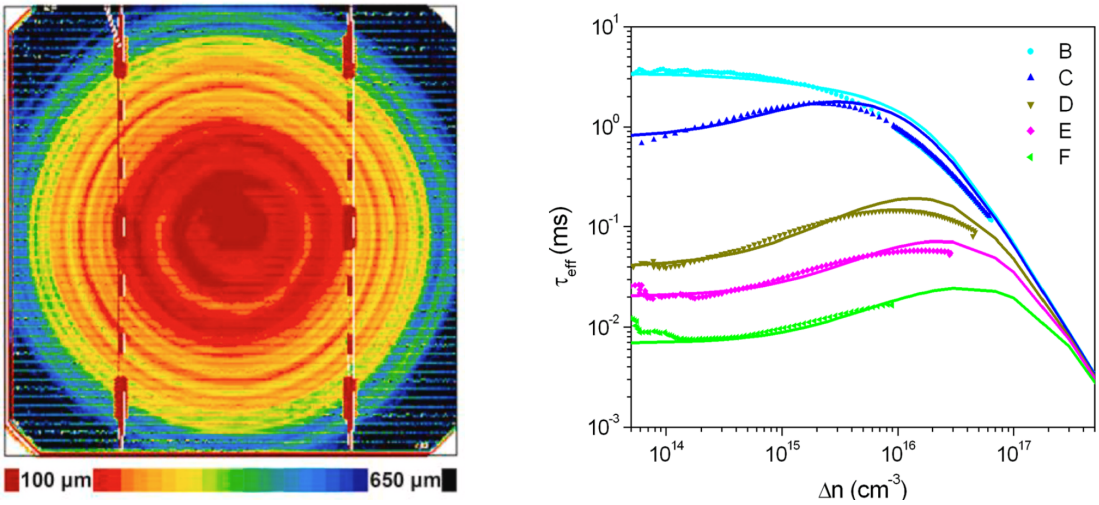


(a) (b)

Figure 1.8: (a) Light-beam induced current mapping showing the radial distribution of $L_n$ in an aluminum back-surface field (Al-BSF) p-type Cz-Si solar cell [60] (b) Effective carrier lifetime measurements for various n-type samples (data points) and related best fits obtained with the SRH recombination parameters (lines). B sample refers to the lowest $[TD] = 1.9 \times 10^{14}\ cm^{-3}$ and F sample to the highest $[TD] = 6.9 \times 10^{15}\ cm^{-3}$ [62].

Beside these defects, B-doped Si is affected by light-induced degradations (LID), which occur in the presence of excess charge carriers when the material has a high concentration of O and B. The τ is reduced within a few hours of carrier injection and exhibits a near-linear dependence on B concentration and an approximately quadratic relationship with $[O_i]$ [11]. LID can be mitigated either via hydrogenation or via the use of Ga dopant [13]. In addition to $B-O$ complexes, Cu complexes or precipitates can also induce specific LID effects in p-type c-Si [63], [50].

Another degradation mechanism known as light-and elevated-temperature-induced degradation (LeTID), implies notably the degradation of B- and Ga-doped c-Si, possibly linked to hydrogen [64]. No correlation was made between LeTID levels and [B] or $[O_i]$. As to date, the exact origin of this defect is still unclear but Ga-doped c-Si is less prone to LeTID degradation than B-doped c-Si [65], [66].

LID and LeTID degradation mechanisms are at the origin of the recent switch from B-doping to Ga-doping for p-type c-Si in the PV industry, resulting in higher τ that compensate largely the wider [Ga] distribution. Additional effects relative to Ga-doping can be mentioned

such as the τ improvement thanks to the hydrogenation of the material. However, this latter process requires caution as if H is present in too high concentration, it can increase the susceptibility to LeTID effect [67].

### 1.1.5 Solar cell architectures

#### 1.1.5.1 Towards passivated contacts

In addition to improved $\tau_{bulk}$, the solar cells technologies have moved from aluminum-back-surface-field (Al-BSF) towards passivated contacts architectures, thereby enhancing $\tau_{surf}$ among other benefits [45], [68] (see Figure 1.9). Indeed, Al-BSF suffered from strong recombination losses due to the entire c-Si surface being in direct contact with metalization, resulting in high SRV. The passivated-emitter-and-rear-cell (PERC) solar cells marked the first widespread adoption of passivated rear contacts, by reducing the highly recombinant contact surface, thereby significantly improving the efficiency. This was followed by the development of silicon heterojunction (SHJ) and tunnel-oxide-passivated-contact (TOPCon) cells that both offer superior surface passivation on the entire cell surface. These two technologies also marked the switch from p-type bulk Si to n-type bulk Si in the PV industry, offering better $\tau_{bulk}$ and better tolerance to oxygen and metallic impurities [69]. In the long term, a shift in solar cell production from p-type to n-type wafers is expected, as P-doped c-Si exhibits greater tolerance to O and common metallic impurities compared to B-doped c-Si. Please note that the solar cells efficiencies mentioned hereinafter refer to measurements under the global AM1.5 spectrum (1000 $W.m^{-2}$) at 25 $°C$ (IEC 60904-3:2008 or ASTM G-173-03 global).

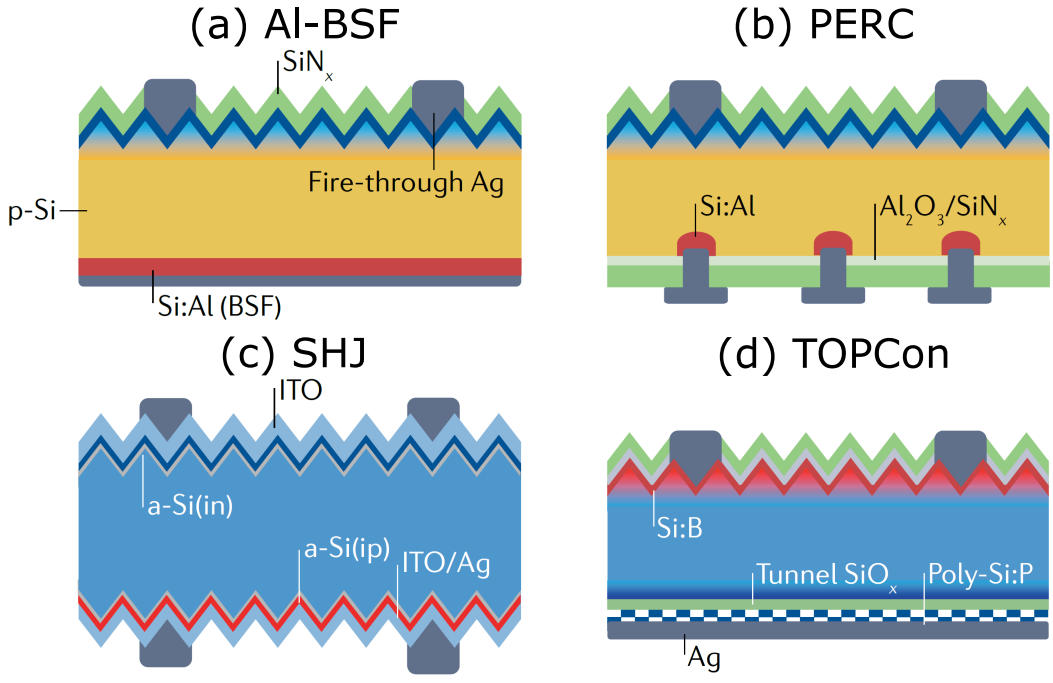


Figure 1.9: Schematics of 4 main industrial c-Si cells architectures over the past 25 years: (a) Al-BSF, (b) PERC, (c) SHJ, (d) TOPCon [45].

The **Al-BSF** design features a rear surface of the c-Si wafer that is covered with an aluminum layer. This stack is usually called back-surface-field (BSF) and serves a dual function: it reflects minority charge carriers back into the absorber and provides a high-quality contact for the rear metalization. This BSF reduces recombination at the rear surface and helps to maintain an acceptable $V_{OC}$. However, the interface between metal and c-Si is highly recombinant, this issue was thus the starting point of the following improvements.

The **PERC** architecture is an enhancement of the standard Al-BSF solar cell architecture. In PERC, the rear side of the c-Si wafer is modified to include a dielectric passivation layer, typically a stack $AlO_x/SiN$—which serves to reduce surface recombination and to improve rear reflectivity. A localized opening is then created through this passivation layer to form point contacts with an aluminum metalization layer, allowing for charge carrier collection while minimizing recombination losses. This architecture significantly improves $V_{OC}$ and $J_{SC}$ compared to conventional Al-BSF cells. As a result, PERC cells efficiency can achieve 25% in laboratory conditions [10].

The **SHJ** architecture uses a combination of c-Si and thin layers of amorphous silicon (a-Si) on both the front and rear sides of the wafer. These amorphous layers are used to extract the charges (doped layers) but also to passivate the surfaces (intrinsic layers), greatly reducing recombination and improving the cell overall performances. SHJ also offers low recombination on the entire surface, thereby leading to high $V_{OC}$ of over 740 $mV$. This results in efficiencies above 26% in laboratory conditions [10]. Additionally, SHJ cells are well-suited for low thickness and bifacial designs, where both sides of the cell can contribute to energy generation.

The **TOPCon** architecture represents a high-efficiency c-Si solar cell design characterized by advanced carrier-selective contacts. The key feature of TOPCon is the use of a thin ($\approx 1.5\ nm$) silicon oxide ($SiO_x$) tunnel layer, grown thermally or chemically, which is overlaid by a doped polycrystalline silicon (poly-Si) layer. This stack is typically applied to the rear side of n-type c-Si wafers, forming a passivated contact that permits efficient tunneling of majority carriers while suppressing carrier recombination. TOPCon offers excellent surface passivation on the entire surface and reduced contact resistivity, enabling high $V_{OC}$ (typically $> 730\ mV$) and high $FF$. These benefits contribute to cell efficiencies also above 26% in laboratory conditions [10]. Furthermore, the structure is compatible with bifacial designs and benefits from a more favourable temperature-coefficient compared to PERC.

#### 1.1.5.2 SHJ development

The SHJ concept ([17], [18], [19], [20]) consists in combining different Si materials, with different bandgaps, to form carrier collecting structures. The SHJ structure is made of a c-Si bulk with $E_{g,1} = 1.1eV$ and hydrogenated amorphous Si (a-Si:H) layers with a wider bandgap $E_{g,2} = 1.7\ eV$ (see Figure 1.10(a)). This difference of bandgap results in band offsets and discontinuities, notably a spike and a notch in the conduction band (see Figure 1.10(b)) parameterized by $\Delta E_c$. The spike then acts as a barrier to electron transport from the n-type (n) a-Si:H emitter to the p-type (p) c-Si bulk. The electron movement can be made via tunneling, and trap assisted tunneling of thermionic emission. Intrinsic (i) a-Si:H layers are

commonly inserted between the doped (n) or (p) a-Si:H layers and the c-Si bulk (at the front and the rear sides). This (i)a-Si:H layer included at the a-Si:H/c-Si interfaces is used to passivate the dangling bonds on the c-Si surface, thus reducing the high defect density at the interfaces. As a result, an excellent surface passivation of c-Si is reached at the front and rear a-Si:H/c-Si interfaces, and high levels of $V_{OC}$ and $FF$ are obtained.

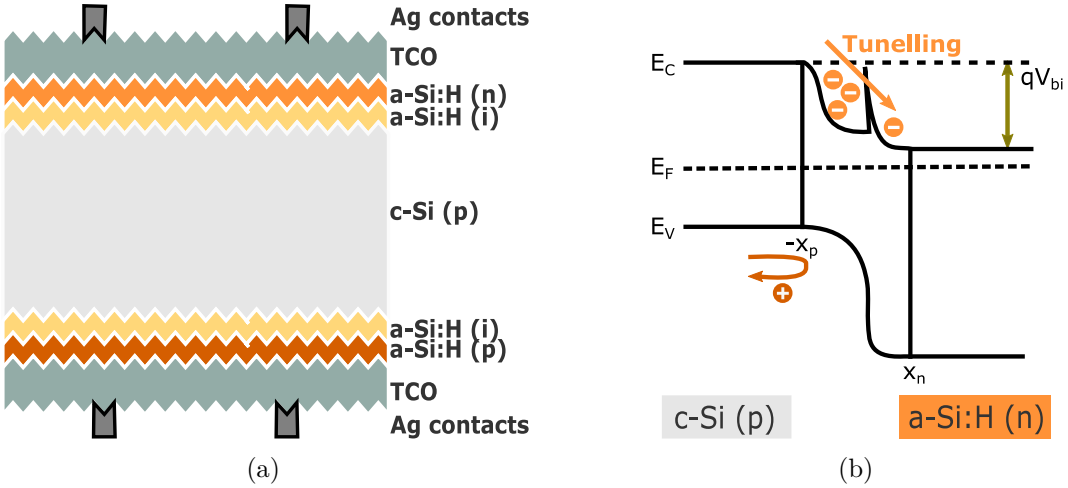


(a) (b)

Figure 1.10: (a) SHJ structure with p-type bulk (b) Energy band of a hetero-interface, here between a p-type c-Si bulk and a n-type a-Si:H layer.

A transparent-conductive-oxide (TCO) layer is usually used to facilitate the lateral carrier transport to the metalic contacts as the a-Si:H is highly resistive. This layer is often made of indium tin oxide (ITO). As In is considered as a critical material, researches are conducted in order to reduce this layer thickness or find alternative solutions [70], [71].

SHJ structure is characterized by high $V_{OC}$ in comparison with other technologies. This high $V_{OC}$ is due to good surface passivation provided in particular by an excellent chemical passivation. Thanks to the higher $V_{OC}$ achieved compared to the other cell designs presented, the solar cell efficiency is less affected by temperature increases [72]. However, it suffers from a loss in $J_{SC}$ due to the relatively high absorption of ITO and a-Si:H layers. Therefore, nanocrystalline Si (nc-Si) layers are beginning to replace the a-Si:H layers, thereby achieving similar passivation but with higher transparency [73].

Another advantage of this technology is the low temperature process (below 250 $°C$) in comparison to the $\geq$ 800 $°C$ temperatures required to form the pn junction by thermal diffusion for homojunction structures. It then decreases the thermal budget, thereby also limiting the thermal degradation of the c-Si wafer quality. Furthermore, it enables the use of thinner wafers (below 100 $\mu m$) as, for instance, wrapping issues related to high temperature processes can be avoided. This latter aspect is a strong advantage for our purpose as will be detailed in Chapter 3.

## 1.2 Influence of electron/proton irradiations on silicon solar cells

### 1.2.1 Space Environment

The space environment around Earth presents significant challenges for the design of space equipment, depending on the mission's orbit. The orbits can be divided into three main categories. The first is the low-Earth-orbit (LEO) for satellite altitudes $< 2000\ km$ with short transmission delays ($\approx ms$). However, a high satellite density is required to cover the whole Earth surface, leading to the satellite constellations that are now numerous, especially for telecommunication purposes. The second is the middle-Earth-orbit (MEO) whose altitude is comprised between the two other orbit types. The third is the geostationary-Earth-orbit (GEO) at $35,786\ km$ from Earth, which is synchronized with the Earth rotation, thus enabling the satellites to always point above a specific location. The satellites placed on this orbit offer a wide coverage of the Earth surface due to their high altitude [74] (see Figure 1.11(a)).

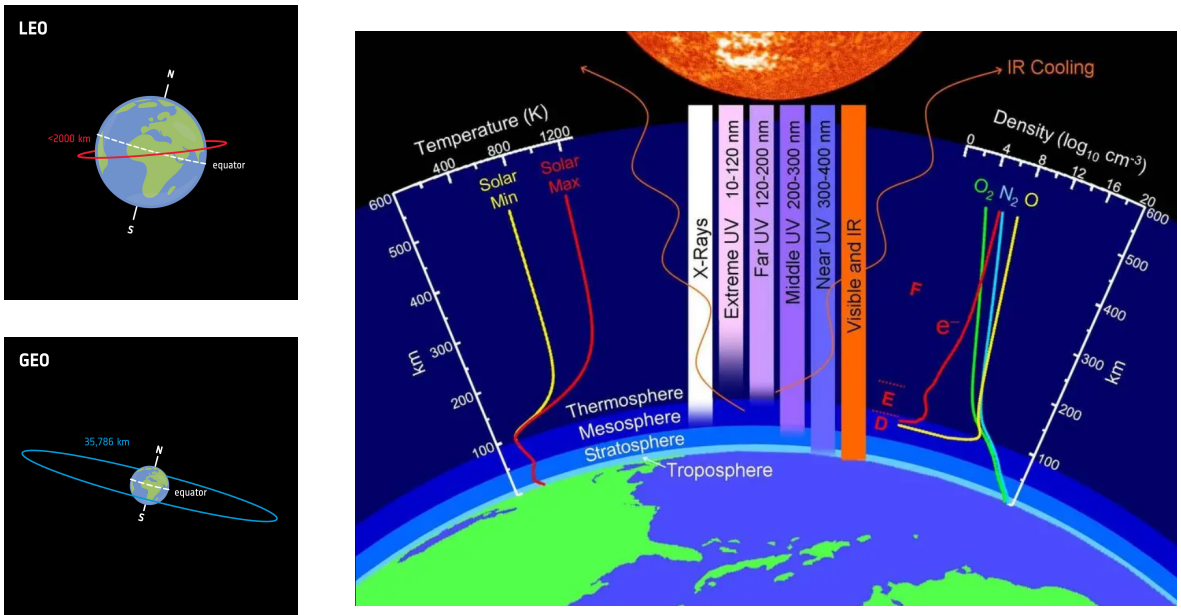


(a) (b)

Figure 1.11: (a) Representation of LEO (up) and GEO (down) Earth orbits [74]. (b) Properties of Earth's upper atmosphere [75].

Different orbits have distinct properties, with varying temperatures, chemical environments, and vacuum levels depending on both the altitude and atmospheric layers (for altitudes up to 350–800 km, this range depends on solar activity) (see Figure 1.11(b)). For altitudes outside of the atmosphere, AM0 is the typical spectrum received by the solar panels on the satellite (see Figure 1.5). It is worth noting that already at an altitude of 30 km, the solar spectrum nearly matches the AM0 standard for wavelengths above 200 nm, since atmospheric absorption becomes minimal. The ultra-high vacuum (typically $10^{-8}\ Pa$ at $800\ km$ from Earth) provokes an absence of convection and gaseous conduction. Materials also outgas when

exposed to space vacuum, progressively emitting gaseous species—a behavior that intensifies with rising temperature.

The space environment gathers the following harsh constraints, against which solar arrays are particularly exposed given their wing geometry [76], [77]:

- the **radiative environment**. It includes the Sun photon radiation, the albedo effect (defined as the fraction of solar radiation reflected by the Earth surface), and the Earth radiation.
  A part of these energy sources results in strong temperature variations on the satellites. The temperatures encountered around Earth orbits typically range between $-100\ °C$ and $100\ °C$ with over $\approx 5000$ thermal cycles per year for LEO satellites and between $-180\ °C$ and $150\ °C$ with up to $\approx 1000$ thermal cycles per year for GEO satellites. The nominal operating temperatures when the sun is facing the photovoltaic assemblies (PVA) in LEO are $60 - 70\ °C$.
  $\rightarrow$ The temperature ranges found in space environment alter strongly the performances of the solar cells, in addition to mechanical issues. This comes mainly from the strong dependency of the $n_i$ parameter with temperature (see Equation 1.2), resulting in a small increase of $J_{SC}$ with increasing temperature and a strong decrease of $V_{OC}$ with increasing temperature.
  Additionally, the photons from the ultraviolet (UV) part of the AM0 spectrum can induce strong damages on materials as their energy is sufficient to break some chemical bonds (e.g. $C - C$, $C - O$, $Si - O$,...) or to create excited electronic states leading to the coloration of transparent materials.
  $\rightarrow$ Encapsulation materials in PVA are commonly made of polymers. Thus, they must be chosen carefully to avoid UV sensitivity.

- the **chemical environment**. This includes atomic oxygen (ATOX)—particularly in LEO orbits—that originates from molecular oxygen dissociation occurring from 100 km up to 800 km from Earth Surface. Though ATOX in space is far from dense, the average impact energy collided with spacecraft operating at a speed of $7 - 8\ km/s$ can go up to $4 - 5\ eV$, which is sufficient for breaking the chemical bonds of many materials. ATOX provokes oxidation with especially strong degradation of organic polymers, leading to contamination and erosion on exposed faces of the satellites. Beyond ATOX, the contamination issues, resulting among others from outgasing or oxidation, can have numerous effects which alter the proprieties of optical components and provoke electric discharge phenomena, leading to equipment failure.
  $\rightarrow$ The chemical environment, and especially the atomic oxygen, affects only the encapsulation part of the solar panels which is made of insulating materials.

- **meteorites and debris**. Meteorites and debris are being ever more numerous and their numbers are still expected to grow [78], [79], [80].
  $\rightarrow$ The possible impacts made by meteorites and debris can produce breakdown of the PVA [81].

- the **charged particle radiation**. Charged particles originate from the interaction between the Earth magnetic field and solar events, but also galactic cosmic rays, and have several effects, depending on the particle/ion radiation energy and the technology. Charged particles trigger cumulative effects (**ionization** and **atomic displacement**), which will be detailed hereafter. They also lead to **single event effects**, which result from high energy particles producing potentially destructive effects (e.g latch up, burn-out) on technologies like metal-oxide-semiconductor-field-effect-transistors (MOSFETs). → Charged particles (and especially electrons and protons) damage dramatically the solar cells performances and are the main issue for solar PVA in space environment. For instance, the solar panels that equipped ATS-1 and Intelsat II-4 satellites were only partially covered with coverglass. As a result, they experienced strong degradations and even the failure of the solar cells in non-covered areas due to low-energy ($< 2\ MeV$) protons [82].

### 1.2.2 From radiation environment to atomic displacement

The Van Allen radiation belts were discovered by James Van Allen in 1959 [83] and consist of two distinct regions in the Earth's magnetosphere, filled with highly energetic particles ($\geq 0.1\ MeV$), primarily electrons and protons that are trapped by the Earth's magnetic field, spiraling along field lines between the poles (see Figure 1.12(a)). Most of these energetic particles originate from the solar wind. The inner radiation belt, located at altitudes of approximately 1–2 Earth radii ($RE = 6378\ km$), is mainly composed of high-energy protons. A fraction of these protons is produced indirectly by galactic cosmic rays. The outer belt, found at altitudes of roughly 4–7 $RE$, primarily contains energetic electrons originating from the solar wind, which are injected and accelerated during geomagnetic storms. A temporary third belt, between the inner and outer belts, was observed in 2013 by NASA's Van Allen Probes and was attributed to the coronal mass ejection from the Sun [84].

The altitude of the inner belt varies with geographic location and actually dips closer to Earth's surface over the South Atlantic Ocean (south Atlantic anomaly). Additionally, radiation levels within the Van Allen belts are dynamic and fluctuate with the solar activity. During periods of a high solar activity, such as solar storms or coronal mass ejections, the radiation intensity can increase significantly, expanding the size and strength of the belts [85] (see Figure 1.12(b)).

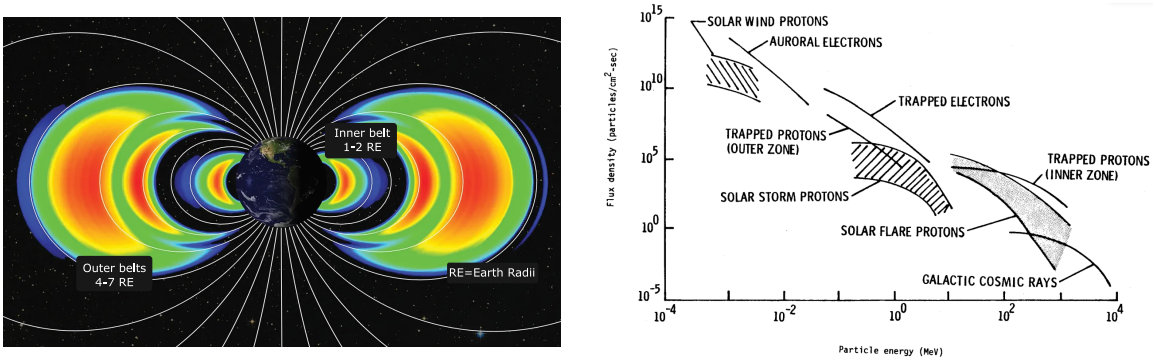


(a) (b)

Figure 1.12: (a) Representation of the Van Allen radiation belts. Adapted from NASA's Goddard Space Flight Center/Johns Hopkins University, Applied Physics Laboratory [84]. (b) Space Radiation environment, from NASA-STD-3000 154 [86].

The high-energy particles in these belts can damage electronic components, degrade materials, and affect the performance of the solar cells. The particle fluence expected to be received on a satellite and on a specific orbit can be computed through several calculation tools (e.g. OMERE, SPENVIS, etc). An example is shown in Figure 1.13 for both electron and proton particles for different orbits [87].

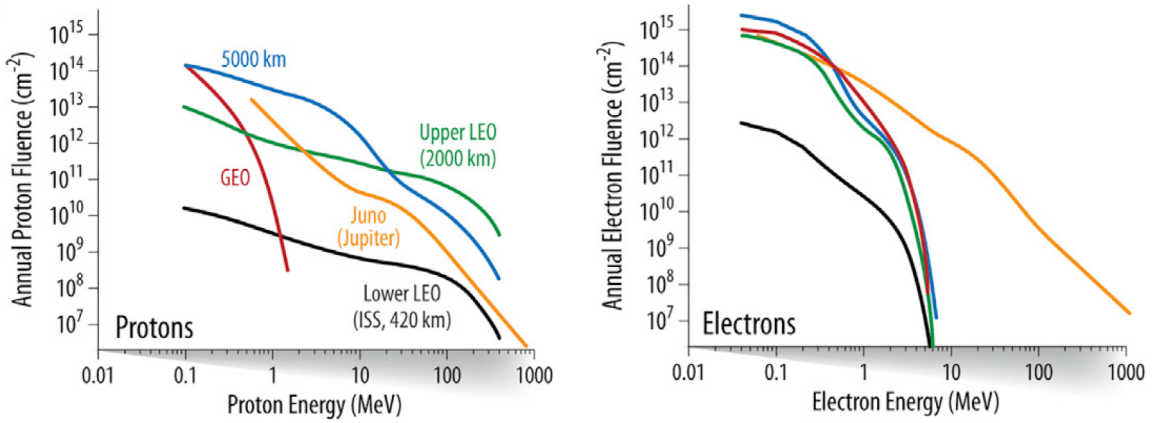


(a) (b)

Figure 1.13: Simulated annual fluences from SPENVIS software for protons (a) and electrons (b) as a function of energies for ISS (black), upper-LEO (green), GEO (red), 5,000 km (blue), and Juno (yellow) orbits, taken from Kirmani *et al.* [87].

Materials in space environment are thus exposed to energetic charged particles, i.e. protons and electrons. These particles loose a part of their energy when going through a solid via ionizing and non-ionizing processes, the latter being also referred to as atomic displacement. The fraction of energy lost by a particle between these two processes is displayed in Figure 1.14(a). As one can see, the non-ionizing energy loss (NIEL) rate is much lower, about 0.1% of total energy at 1 $MeV$ proton for instance. The atomic displacement phenomena induces strong damages in c-Si, which are widely detailed in [88], [89], [90].

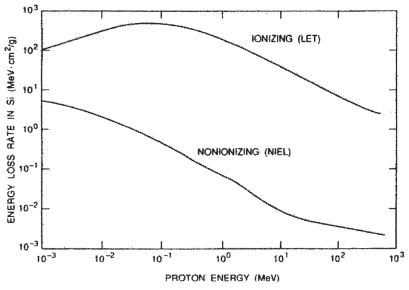


(a)

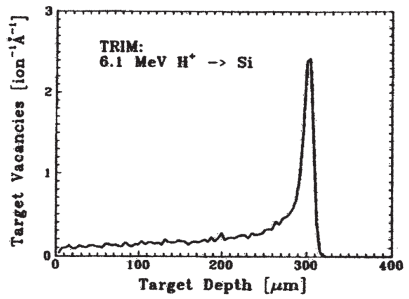


(b)

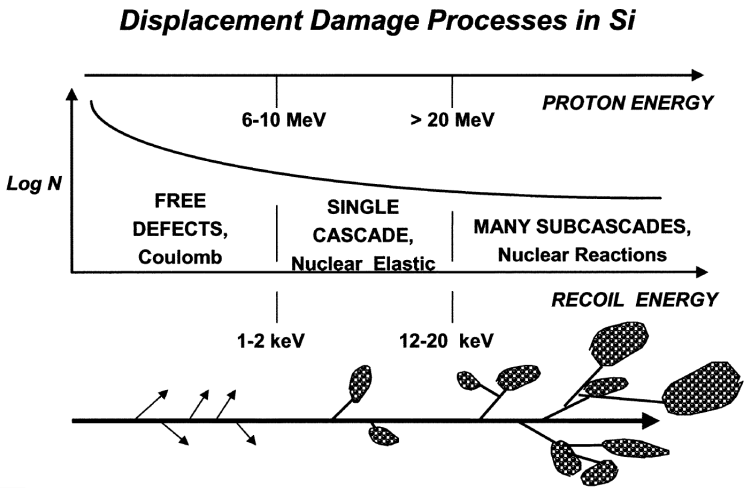


(c)

Figure 1.14: (a) Energy loss rate in Si through LET and NIEL [88], [91]. (b) Monte Carlo simulation (TRIM) of the vacancy production profile by 6.1 MeV protons in Si [88], [92]. (c) Schematic representation of defect and subcascade formation as a function of PKA energy [89], [93].

**Ionization** in c-Si excites the electrons of the $VB$ to the $CB$, creating electron-hole pairs and thus free charge carriers in a similar way that they are generated by photon absorption. The ionization process differentiates from the latter as an energy three times higher than the photon energy threshold is required to produce those free carriers. Ionization is quantified by the total ionizing dose TID ($MeV/g$), which refers to the cumulative dose of ionizing radiation absorbed by a material over time by the product of particle fluence and the linear energy transfer LET [88]. LET is generally defined as the energy loss per unit length ($MeV/cm$), primarily due to electronic stopping power. Ionization will not be further detailed here as it impacts mostly oxide and polymer materials and its effects on c-Si materials (for solar cells) are negligible.

**Atomic displacement** occurs when sufficiently high energetic particles collide with an atom of the crystal lattice, ejecting it from its equilibrium position. This creates a vacancy and an interstitial atom (see Figure 1.3). Vacancies lead to the creation of complex defects at room temperature e.g. by being trapped with impurity atoms. As vacancies are highly mobile, most of the Frenkel pairs recombine and only a fraction of the vacancies created eventually leads to a stable defect creation.

Atomic displacement cascades occur for two reasons:

- Firstly, the energy required to produce a Frenkel pair is $< 100\ eV$, meaning that a MeV particle will not lose all its energy with one displacement and will thereby provoke a collision cascade, i.e. a series of displacements along its track in the material. The creation of defects along the tail of this track is mostly uniform, but most of the defects are produced near its end, where the particle stops. This depth is called the projected range ($R_p$), and this parameter increases with increasing incident particle energy. The material thickness beyond $R_p$ is left undamaged. 1 $MeV$ electrons induce an uniform distribution of defects throughout c-Si solar cell depth ($R_p \approx 1\ mm$ vs cell thickness $< 200\ \mu m$). Because of their mass, protons have a lower projected range than for electrons for a same particle energy. The number of displacements (vacancies) along the particle track can be simulated with the use of numerical codes based on Monte Carlo simulations, stopping and range of ions in matter (SRIM) or transport of radiation in matter (TRIM) codes for instance [94]. An example of vacancies produced in c-Si after the bombardment by 6.1 $MeV$ protons is displayed in Figure 1.14(b).
- Secondly, under high energetic particles, this first atom displaced—primary knock-on atom (PKA)—can itself collide with another atom, and so on so forth, eventually creating defect clusters. This scenario is displayed in Figure 1.14(c) in cases of protons with various energies.

Heavy particles as protons, on top of being abundant in the inner Van Allen radiation belt, are particularly effective in causing atomic displacement as the atomic displacement probability increases with growing particle energy and mass.

The displacement damage is quantified by the displacement damage dose DDD ($MeV/g$), which is the total accumulated displacement damage in a material. It combines the particle fluence and the non-ionizing energy loss NIEL ($MeV.cm^2/g$), which refers to the part of the energy that goes into lattice damage. This NIEL results from elastic (e) and inelastic (i) contributions as [89]:

$$NIEL = \frac{N_A}{A}(\sigma_e T_e + \sigma_i T_i) \tag{1.40}$$

where $\sigma_e$ and $\sigma_i$ refer to the elastic and inelastic capture cross sections respectively, $T_e$ and $T_i$ refer to the elastic and inelastic effective recoil energies corrected for ionization loss, respectively, $N_A$ is the Avogadro's number ($6.022 \times 10^{23}\ mol^{-1}$), and A the gram atomic weight of the irradiated material (28 $g/mol$ in Si case). An example is found in Figure 1.14(a) for Si material.

As displayed in Figure 1.14(a), the NIEL only represents a fraction of 1% of the total energy loss. However, this is the strongest damaging effect for c-Si solar cells, and is thus the focus of this work.

### 1.2.3 Displacement damage

The performance of semiconductor devices deteriorates under irradiation due to atomic displacements in the crystal lattice. These displacement-induced defects can be point defects,

complexes, or defect clusters. They can act as recombination centers, trapping centers, or compensating centers. Following the classification proposed by Srour and McGarrity [95], five primary electrical degradation mechanisms caused by radiation-induced displacement defects can be distinguished (see Figure 1.15):

- the **thermal generation.** The introduction of mid-gap energy levels leads to an increased generation of electron-hole pairs, contributing to dark current and leakage in reverse-biased junctions, and reduction of $V_{OC}$. Only these mid-gap energy levels can significantly enhance the thermal generation of electron-hole pairs, even in the absence of external stimuli. This process dominates over charge capture when the concentration of free carriers is significantly lower than their equilibrium values i.e. in depletion regions.
- the **recombination.** Defects can also act as recombination centers by capturing an electron and a hole. This process refers to the SRH recombination introduced earlier (Section 1.1.2.1). The recombination reduces the lifetime of charge carriers, thereby lowering the charge collection efficiency of the solar cells. The recombination rate depends on the defect center density, the free carrier concentration, the hole and electron capture cross sections and the energy level position.
- the **carrier trapping.** Shallow defect energy levels can temporarily capture a free carrier that will be emitted later to its band, without recombination.
- the **compensation.** Radiation-induced defects can neutralize dopants by forming electrically inactive complexes or defects counteracting the doping type. Indeed, particle irradiation can deactivate or displace dopant atoms from their substitutional (active) sites into interstitial (inactive) positions, or cause them to form electrically neutral defect complexes. These effects reduce the effective doping concentration. Furthermore, some radiation-induced defects may act as dopants of opposite polarity (e.g., donors in p-type material), leading to compensation or even to a conductivity type inversion of the material. As a result, the free carrier concentration changes and the Fermi level shifts accordingly, modifying the solar cells' electrical characteristics.
- the **tunneling.** Due to the irradiation-induced defects, carriers can tunnel through potential barriers or between defect states within the bandgap. This mechanism can contribute to leakage current and noise, particularly at low temperatures or in thin depletion regions.

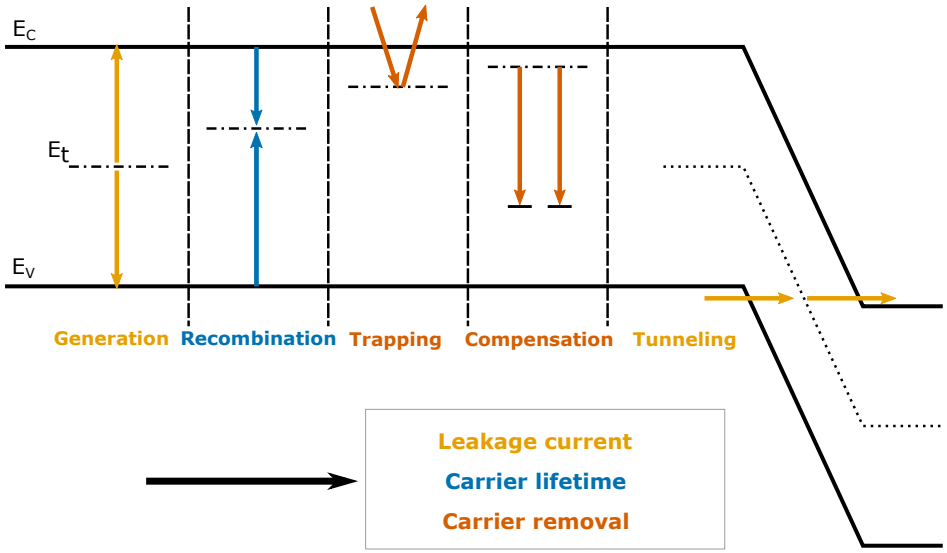


Figure 1.15: Degradation mechanisms caused by radiation-induced displacement defects [95], [96].

Another process with far less impact on the solar cells performance is the radiation-induced defects acting as scattering centers, which affect mostly the majority carrier mobility [89], [88], [97].

As a result, the PV performance of the solar cells will decrease after exposure to a certain level of irradiation. Two bulk parameters drive this degradation, the main one for low DDD is the carrier lifetime degradation, the second one is the carrier removal which occurs for high DDD, as detailed hereafter. p-Type c-Si was recognized from a long time to be more resilient to degradation than n-type c-Si, the latter showing more pronounced impact on leakage current and $\tau$ [98]. This would be due to differences of introduction rates of recombination centers and of capture cross-sections [25]. Therefore p-type c-Si was widely used for satellites from the early space PV developments [99] and **the following of the chapter focuses on the use of p-type solar cells, with front emitters, unless otherwise stated**. However, n-type c-Si has recently sparked interest [100]. One can note in particular that the advantage of p-type c-Si could be reduced by a good irradiation defect recovery capability of n-type Si.

#### 1.2.3.1 Carrier lifetime degradation

The impact of irradiation on carrier recombination is commonly modeled with the minority carrier diffusion length damage coefficient $K_L$ (unitless) [101], [102] based on Loferski *et al.* [103]. $K_L$ is expressed for p-type c-Si as:

$$K_L\phi = \frac{1}{L_n(\phi)^2} - \frac{1}{L_n(0)^2} = \sum I_{r_i}\sigma_i v_{th}\phi/D_n \tag{1.41}$$

where $L_n(0)$ and $L_n(\phi)$ denote the electron diffusion length $L_n$ before and after irradiation, respectively. $I_{r_i}$ refers to the introduction rate ($cm^{-1}$) of the $i^{th}$ recombination center, and $\phi$

the fluence ($cm^{-2}$).

Naturally, a translation of $K_L$ can be made towards the carrier lifetime damage coefficient $K_\tau$ ($cm^2.s^{-1}$) with Equation 1.29. $K_L$ and $K_\tau$ are both relevant metrics to quantify the recombination losses. A parameter is chosen over the other depending on the sample features (precursor or finished device), $K_L$ thus being widely used for metalized solar cells.

#### 1.2.3.2 Carrier removal effect

A characteristic effect observed in irradiated c-Si is the increase in resistivity (or decrease of $p_0$ for p-type c-Si) due to compensation and trapping effects. The effect is called the carrier removal.

This carrier removal effect depends on the carrier removal rate $R_C$ ($cm^{-1}$) via the equation (expressed for p-type c-Si) [104]:

$$R_c\phi \approx p_0(0) - p_0(\phi) \tag{1.42}$$

where $p_0(0)$ and $p_0(\phi)$ are the equilibrium hole concentrations before and after irradiation, respectively.

Naturally, the resistivity of the base layer is increased after a reduction of majority carrier concentration. An example of this resistivity increase within the sample depth with increasing 3.2 $MeV$ proton fluence on n-type c-Si is displayed in Figure 1.16.

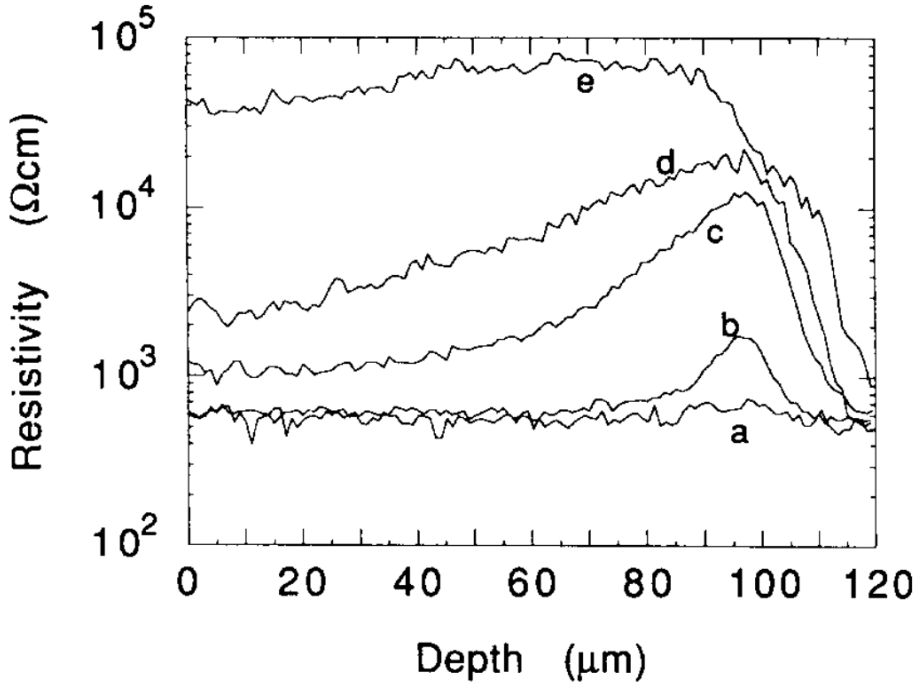


Figure 1.16: Measured resistivity profiles in n-type c-Si (FZ 650 $\Omega.cm$ wafers) irradiated with 3.2 $MeV$ protons. Fluences for the different profiles are (a) $1 \times 10^{10}$, (b) $5 \times 10^{10}$, (c) $2 \times 10^{11}$, (d) $5 \times 10^{11}$, and (e) $2 \times 10^{12}$ $cm^{-2}$ [105].

This carrier removal effect has consequences on all the electrical parameters, the more spectacular being the drop of $J_{SC}$ reported at high proton and electron fluences, as shown hereafter [106], [107]. Figure 1.17 shows three different behaviors of p-type solar cells under irradiation with increasing 1 $MeV$ electron fluence [106]. A similar behavior is also obtained when the cells are irradiated under 10 $MeV$ protons [107]. For fluences $< 10^{16}$ $cm^{-2}$ (i), a slow and monotonic decrease of $J_{SC}$ and $V_{OC}$ is observed. For fluences $(2-5) \times 10^{16}$ $cm^{-2}$ (ii), $J_{SC}$ increases in an unexpected way while $V_{OC}$ decreases more sharply. For high fluences $> 5 \times 10^{16}$ $cm^{-2}$ (iii), an abrupt failure of the solar cell occurs.

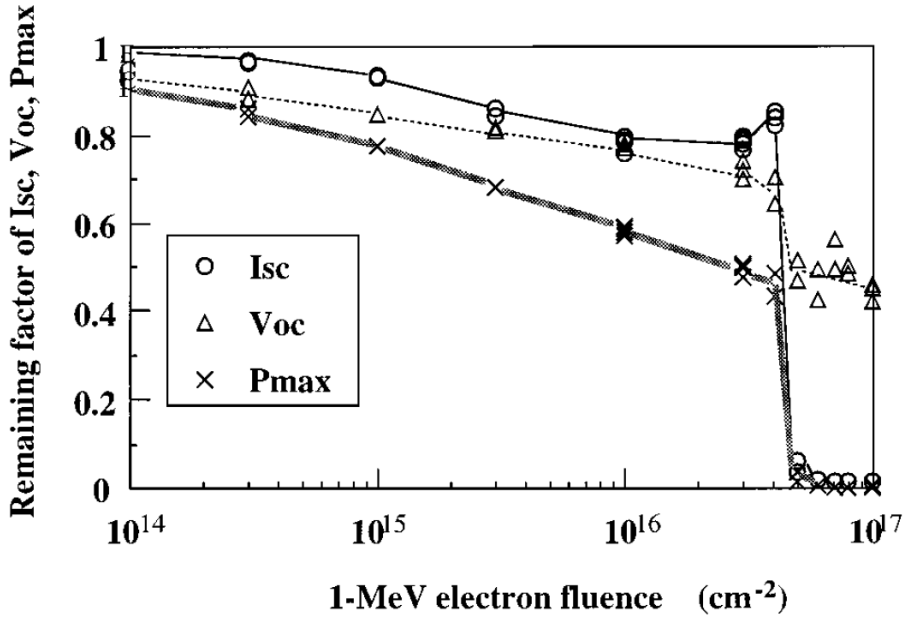


Figure 1.17: Evolution of I-V parameters ($I_{SC}$, $V_{OC}$ and $P_{max}$) of p-type Si solar cells as a function of 1 $MeV$ electron fluence [106].

The evolution of the $J_{SC}$ curve was modeled by varying three parameters: $\tau$, the SCR width and $p_0$. For each fluence region, the behavior of the cell is driven by one of these parameters: (i) decreasing of $\tau$, (ii) broadening of the depletion layer, and (iii) strong reduction of $p_0$. For behavior (iii), $p_0(\phi)$ depends on $R_c$ via the following equation: $p_0(\phi) = p_0(0)e^{-R_c\phi/p_0(0)}$.

For high fluences ($> 5 \times 10^{16}$ $cm^{-2}$ in the study mentioned above), carrier concentration becomes so low that an inversion of the conductivity type (i.e. switch from p to n) mentioned previously occurs, explaining the abrupt failure of the cell performance. An electron beam induced current (EBIC) line scan combined with capacitance-voltage (C-V) measurements were later performed on p-type diodes and showed a conversion of the type of the base, turning the $n^+ - p - p^+$ structure into a $n^+ - n - p^+$ one [108]. This type inversion was also observed in [109] and [110] for instance.

#### 1.2.3.3 Modeling radiation-induced degradation

A good correlation between $K_L$ and NIEL when plotted with the particle energy is found [91]. Additionally, $\tau$, $p_0$ and solar cells PV parameters mostly experience linear degradations

with increasing fluence in a restricted fluence range and for a broad range of energies. Therefore, it is possible to predict the I-V parameters degradation without microscopic knowledge of the radiation-induced defects through two main models, either from JPL (Jet Propulsion Lab), which uses the equivalent fluence frame work, or from NRL (Naval Research Lab), which uses DDD. The former is derived from experimental data and results in relative damage coefficients (RDCs), while the latter is mainly based on the semiconductor material properties used is the solar cells and results in NIEL. The two methods were detailed and compared by Messenger *et al.* [111] and Baur [112], with a good correlation found between the two methods. The NRL model is more commonly used as it requires fewer experimental data.

The **JPL method** uses the critical fluence $\Phi_c$, which is the particle fluence for which the I-V parameter of interest is reduced to 75% of its initial value. In the proton case, the RDC is determined for each particle energy in the desired range by normalizing the $\Phi_c$ for the proton energy range with the $\Phi_c$ obtained for 10 $MeV$ protons. In the electron case, the normalization is done using the $\Phi_c$ obtained for 1 $MeV$ electrons. This normalization yields a RDC curve, which is plotted as a function of the particle energy. A step further is to calculate the 1 $MeV$ electron equivalent fluence that would reproduce the damage encountered in a specific mission. More information can be found in [111]. An example of fluences required to produce a 25% loss in $J_{SC}$ for 1 $\Omega.cm$ p-type c-Si cells is shown in Table 1.1.

| Particle | Fluence required to produce a 25% loss in $J_{SC}$ ($cm^{-2}$) |
|---|---|
| 1 $MeV$ electron | $5 \times 10^{14}$ |
| 1 $MeV$ proton | $2 \times 10^{10}$ |
| 10 $MeV$ proton | $6 \times 10^{10}$ |

Table 1.1: Damage equivalence in n-p 1 $\Omega.cm$ solar cells [90].

The **NRL method** is based on the use of NIEL (expressed in Equation 1.40), which can be calculated from the material and the particle energy. Once a solar cell is tested within one particle energy irradiation condition (for several fluences) and I-V characterized, it is possible to predict the I-V damage for other particle energies by translating the particle fluence $\phi$ to DDD, expressed as:

$$DDD(n) = NIEL(n, E_n)\phi(n, E_n) \tag{1.43}$$

where $n$ is the particle type and $E_n$ its energy. By using the DDD, all the damage curves for different particle energies plotted versus the fluence collapse into one single curve, this time plotted versus the DDD, as displayed in Figure 1.18. It is thus possible to predict the end-of-life (EOL) performances of a solar cell when knowing the radiation environment due to electrons and protons (e.g. with SPENVIS software).

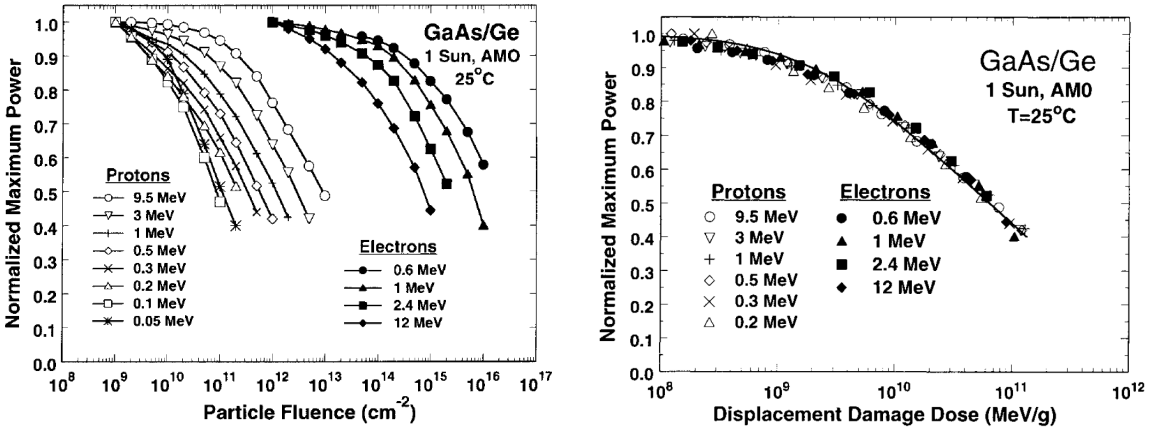


(a) (b)

Figure 1.18: GaAs/Ge based solar cell normalized maximum power plotted versus particle fluence (a) and DDD (b) [111].

This method was developed for III-V materials-based solar cells, which feature thin absorber materials (a few microns-thick). The c-Si solar cells have an indirect bandgap and therefore require a thick absorber material (typically $50 - 150$ $\mu m$-thick, depending on the light management optimization). This thickness can be larger than the projected ranges of low energy protons (usually $< 10$ $MeV$), as displayed in Figure 1.19(a). Therefore, the total amount of NIEL generated in the total thickness is not representative of the damage provoked on the I-V parameters of the solar cell. In this case, the NRL method is thus not sufficient. However, a way was found to adapt the method to c-Si solar cells by integrating SRIM data, thus taking into account the non-uniform damage produced across the thickness of the c-Si cell, using RDCs as detailed in [113] and shown in Figure 1.19.

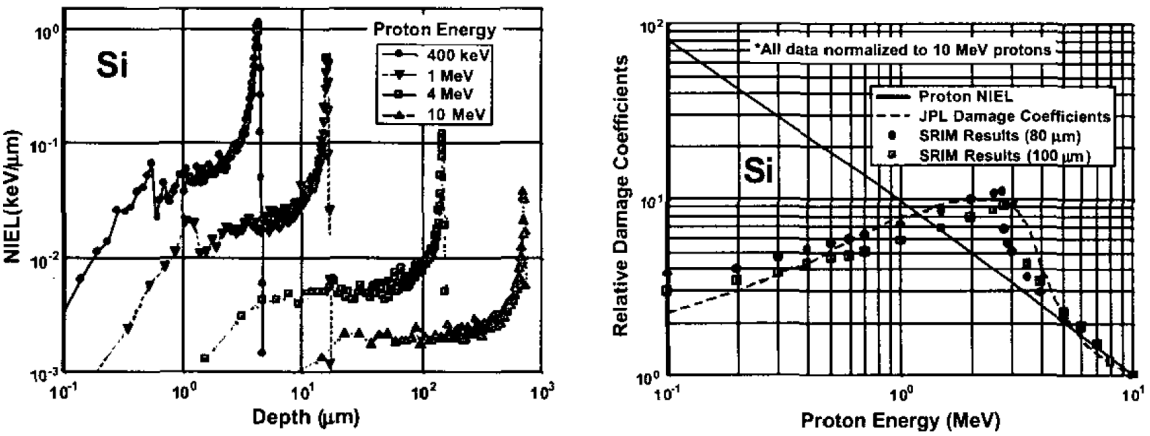


(a) (b)

Figure 1.19: For c-Si solar cells: NIEL as a function of material depth (a), and RDC as a function of proton energy (b) [113].

The RDCs specific to each I-V parameter for p-type c-Si solar cells are displayed in Figure 1.20 [114]. One can note that the proton energy for which the maximum damage

occurs differs between $J_{SC}$ and $V_{OC}$.

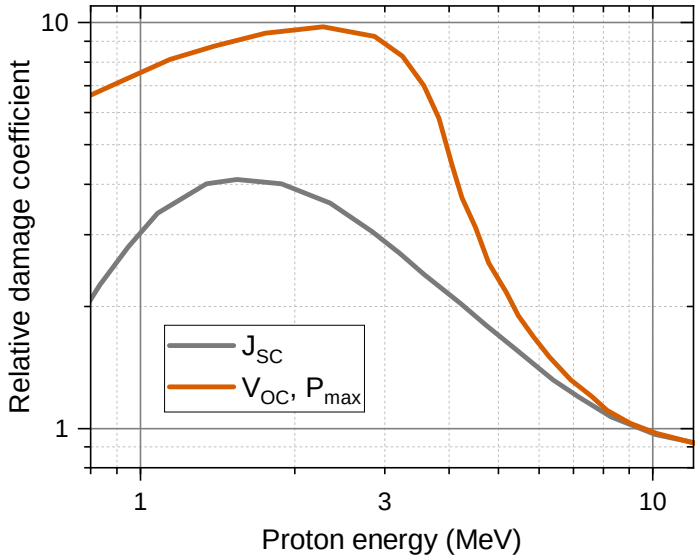


Figure 1.20: RDCs obtained for p-type c-Si solar cells and normalized to 10 $MeV$ protons for $J_{SC}$ parameter (grey curve) and $V_{OC}$, $P_{max}$ parameters (orange line). Adapted from [114].

#### 1.2.3.4 Irradiation-induced defect levels in c-Si

As mentioned earlier, a macroscopic approach is usually sufficient to model the radiation-induced degradation. However, a wide range of studies detail the possible defects responsible for the degradation and provide valuable information on the behavior of particle-irradiated solar cells.

To study these radiation-induced defects, three key techniques are commonly employed: deep-level transient spectroscopy (DLTS), electron paramagnetic resonance (EPR), and temperature-injection dependence level spectroscopy (T-IDLS). DLTS is a powerful method for characterizing deep-level traps in semiconductors, providing detailed information about the energy levels, capture cross-sections, and concentrations of these traps. In DLTS, the transient response of capacitance or current of the material is measured after applying a voltage pulse, allowing the identification of defect levels in the bandgap. An important consideration in studies linking device performance to specific defect centers is the temperature range at which DLTS measurements are made. These measurements are often conducted at temperatures that may differ from the operating conditions of a device. EPR, on the other hand, measures the magnetic properties of paramagnetic centers (such as vacancies or interstitials) in the irradiated silicon. EPR is sensitive to the unpaired electron spins of defects, and gives structural and chemical information of defects. However, both techniques do not give direct information about the recombination activity of the defects, which requires both $\sigma_n$ and $\sigma_p$, in addition to $E_t$ and $N_t$. For instance, DLTS usually gives only the majority capture cross-section. T-IDLS is a lifetime spectroscopy technique in which defect parameters are extracted from charge carrier lifetime measurements. Specifically, the carrier lifetime measurements are made for a range of carrier injection levels and for several temperatures. T-IDLS thus gives information on the

recombination activity of one (or two) main defect(s) that dominates the overall charge carrier recombination. However, two possible combinations for each defect result from the analysis [32].

An overview of the defects observed in irradiated c-Si materials can be found in [115], [88]. Resulting from these studies, divacancy complexes $V-V$ and vacancy related defects were shown to have a strong role in the EOL properties of c-Si [116], [117], [118]. A non-exhaustive list of defects observed in c-Si can be found in Table 1.2, and includes the results of the following studies: [119], [120], [88], [121], [122], [123], [124].

| **Energy level (eV)** | **Possible identity** | **Remarks** | **Anneal stage** |
|---|---|---|---|
| $E_v + (0.18 - 0.23)$ | $V^+ - V$<br>$Ga_i - O_i$?<br>$C_i - C_s$? | (B, Ga) [119], [120], [88], [121], [122]<br>(Ga) [122]<br>(Ga) [122] | $200 - 300\ °C$<br>-<br>- |
| $E_v + (0.35 - 0.38)$ | $C_i^+ - O_i$<br>(+B-related defect?)<br>$V - O - C$ | recombination center<br>& majority carrier trap center (B,Ga) [120], [122] [123],[119] | $200\ °C$,<br>stable up to $\geq 300\ °C$ |
| $E_c - 0.42$ | $V - V^-$ | dominant recombination center at low $\Delta n$ [120], [88] & generation center | $200 - 300\ °C$ |
| $E_c - (0.26 - 0.27)$ | $B_i - O_i$ | - [119], [124], [88] | $\approx 200\ °C$ |
| $E_c - 0.23$ | $V^- - V^{--}$ | recombination & generation center [120], [88] | $200 - 300\ °C$ |
| $E_c - (0.18 - 0.20)$ | $B_i - O_i$ | donor center (B) [122] | - |
| $E_c - 0.17$ | $V - O$ | dominant recombination center at high $\Delta n$ [120], [88] | stable up to $\geq 300\ °C$ |
| $E_c - 0.11$ | $Ga_i - O_i$? | (Ga) [122] | - |

Table 1.2: Summary of radiation-induced defects in B- and Ga-doped silicon. In [122] study, defects are categorized whether they were found in Ga-doped c-Si or B-doped c-Si. This is reproduced in this table in (Ga), for a defect only observed in Ga-doped Si, (B) for a defect only observed in B-doped c-Si, and (B,Ga) for a defect observed in both.

Hallen *et al.* achieved to obtain both $\sigma_n$ and $\sigma_p$ parameters from DLTS for the radiation-induced defects displayed in Table 1.2 [120]. From this, the EOL $\tau_{bulk}$ was evaluated in n- and p-type c-Si, with a good correlation with the experimental measurements. The $E_c - 0.42\ eV$ defect energy level, related with $V - V^-$ complex, turned out to be the dominant recombination centre in proton or electron irradiated n- and p-type c-Si for low $\Delta n$. At high $\Delta n$, the $E_c - 0.16\ eV$ level associated with the $V - O$ complex (also known as A-center [125]) became the dominant recombination centre. On the other hand, $E_v + 0.23\ eV$ associated to a divacancy complex was found to drive the EOL $\tau$ in another study [121].

Detailed studies were conducted on B-doped c-Si solar cells, e.g. [119], [126]. From the latter, several key defects were identified through DLTS. The $E_v + 0.36\ eV$ defect, related to a majority carrier trap, acts as a recombination center and is associated with a degradation in carrier lifetime. This defect is correlated with the $C_i - O_i$ complex. The $E_c - 0.18\ eV$ defect, a deep donor center caused by the $O_i - B_i$ complex, plays an important role in carrier removal and could be responsible for type conversion in the material. The concentration of this defect increases with higher boron and oxygen concentrations. Additionally, a majority carrier trap, $E_v + 0.18\ eV$, linked to a divancy complex, appears at low concentrations. A high-fluence-induced trap at $E_c - 0.71\ eV$ appears when there is a conversion from p-type to n-type c-Si. The resilience of hydrogenated B-doped c-Si towards electron irradiation was also investigated. Two possible defect levels resulted from T-IDLS measurements: $E_v + 0.22\ eV$

and $E_c - 0.26\ eV$ possibly linked to vacancy-related defect complexes [127].

For Ga-doped c-Si, further DLTS analyses showed some differences in the radiation-induced defects compared to B-doped c-Si [122]. Notably, the $E_c - 0.18\ eV$ defect, associated with the $B_i - O_i$ complex, was absent in Ga-doped c-Si. Additionally, Ga doping reduced the $E_v + 0.36\ eV$ recombination center concentration, potentially improving the EOL $\tau$. However, the $C_i - O_i$ complex is expected to be present at similar concentrations as in B-doped c-Si. A new trap level at $E_c - 0.11\ eV$ was observed, likely related to the $Ga_i - O_i$ complex. In B-doped c-Si, $E_v + 0.36\ eV$ was found to be the main recombination center, while $E_v + 0.36\ eV$ and $E_c - 0.18\ eV$ were found to be at the origin of the carrier removal effect [126]. As the concentration of these two defects was found to be reduced in Ga-doped c-Si [122], this suggests better $K_L$ and $R_c$ with Ga dopant.

### 1.2.4 Irradiation resilient c-Si solar cells: materials and designs

The c-Si material is therefore subject to displacement damage induced by particle irradiation. From the time c-Si solar cells were first used in satellites, research has focused on radiation-hardened cell designs. This has included the optimization of the material, the cell structure, and annealing processes, i.e., the recovery of the initial performance after degradation. This section focuses on the key results; further information can be found in [90], [99], [25].

#### 1.2.4.1 Effect of material composition

**Oxygen concentration**

The oxygen concentration is commonly studied by comparing Cz-Si with FZ-Si as $[O_i]$ is several orders of magnitude higher in Cz-Si than in FZ-Si.

The advantage of each is still a matter of debate. In some studies, FZ-Si solar cells resulted in better irradiation resilience than Cz-Si solar cells [90]. In other studies, FZ-Si resulted in higher beginning-of-life (BOL) efficiency than Cz-Si but displayed similar $K_L$ after irradiation [128], [129]. Nevertheless, the use of FZ-Si with significantly smaller $[O_i]$ than Cz-Si appears to result in harder substrates considering the carrier removal effect [130]. However, FZ-Si based solar cells were shown to likely suffer from photon degradation (i.e. degradation of the I-V curve of particle irradiated solar cells after consequent photon exposure) when operating in space [131], [90]. Cz-Si was thus preferred over FZ-Si.

**Dopant nature**

Regarding p-type Cz-Si, B was the usual dopant atom studied. However, several studies investigated the influence of alternative dopants, particularly Ga: [130], [132], [99], [133], [27].

Overall, the use of Ga dopant rather than B dopant enabled less degradation after irradiation, whether for $\tau$, $p_0$ [133], or efficiency [27] reductions. However, higher segregation coefficient is found for Ga-doped Si during Cz ingot growth. This can result in higher resistivity variations that can lower the efficiency of the solar cells [99]. On the other hand, Matsuura *et al.* found no impact of the dopant nature (whether B, Al or Ga) on the $p_0$ evolution with

increasing 1 $MeV$ electron fluence [130]. This also suggests that the donor center may not be related to $B_i - O_i$ complex as stated elsewhere [122].

Therefore, the possible advantage of Ga-doping over B-doping for space c-Si solar cells is still controversial.

**Base equilibrium carrier concentration**

The base equilibrium carrier concentration ($p_0$ for p-type) dependence of solar cells resilience to particle irradiation was underlined long ago [90], [114]. In these studies, the resistivity of the c-Si bulk went from 1 $\Omega.cm$ to 15 $\Omega.cm$. Most of these studies were led before 2000s, and were conducted on homojunction solar cells. It is therefore important to mention that at this time, the BOL performance gap between low and high $p_0$ c-Si based solar cells was high, favoring high $p_0$. This usually explained the better efficiency obtained for high $p_0$ at lower fluence in most of the studies.

However, studies focusing on the c-Si electronic properties usually converge on the higher resilience of lower initial $p_0$ substrates in tested ranges (usually corresponding to a resistivity of 10 $\Omega.cm$), particularly showing higher EOL $\tau$. Indeed, the main degradation mechanism occurring at low fluence (for which carrier removal effect is not yet significant) is the decrease of $\tau$. This advantage for lower $p_0$ appears to be stronger at low $\Delta n$ [117].

This effect was mainly counterbalanced as lower $p_0$ resulted in lower efficiency at BOL and low fluence. It was therefore upper a certain fluence threshold (thickness dependent) [134] that the advantage of the higher resistivity arised. From this, a c-Si wafer resistivity of 10 $\Omega.cm$ was usually chosen due to its higher EOL efficiency compared to those obtained with 2 $\Omega.cm$ resistivity wafers [90].

It is also noteworthy that the carrier removal effect is leading the degradation at high fluence (typically for $> 3 \times 10^{15}$ $cm^{-2}$ 1 $MeV$ electron fluences). Therefore, this could favor the solar cells with initially high $p_0$ in these conditions. This is nuanced in [130] in which the authors found a smaller rate of carrier removal effect for 10 $\Omega.cm$ c-Si than for 1 $\Omega.cm$ c-Si.

Thus, it is important to evaluate the total irradiated dose that the solar cells should receive to optimize the $p_0$ leading to the best efficiency during a specific mission. With PC1D simulation, the phenomenon was quantified [129] (see Figure 1.21). According to their model, Yamaguchi *et al.* computed the influence of the carrier concentration on AM0 efficiency for 50 $\mu m$-thick p-type back-surface-field-and-reflector (BSFR) solar cells. For 1 $MeV$ electron fluences lower than $(1 - 3) \times 10^{15}$ $cm^{-2}$ fluences, they showed that the EOL efficiency is improved by lowering the $p_0$ (until $5 \times 10^{14}$ $cm^{-3}$) compared to the optimal $p_0$ value at BOL. For higher fluences, the optimal efficiency is found by increasing again the $p_0$.

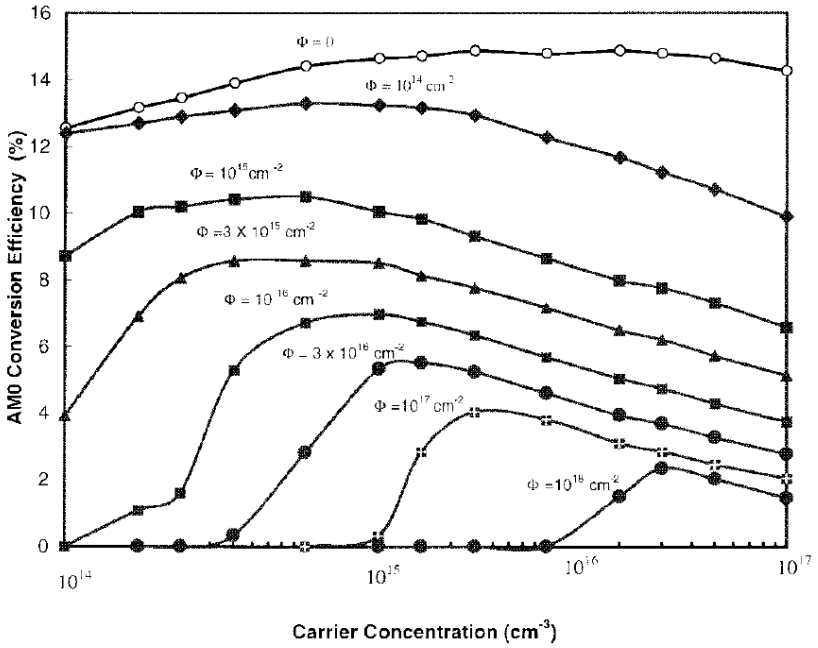


Figure 1.21: Base carrier concentration dependence of AM0 performance of conventionally available 50 $\mu m$ thick Cz-grown p-type c-Si BSFR space solar cells as a function of 1 $MeV$ electron fluence [129].

For their part, Mihailetchi *et al.* recently suggested an optimal resistivity range of $1-5\ \Omega.cm$ based on simulation studies with different cell concepts investigated (e.g. PERC, Al-BSF and TOPCon) [135]. However, no corresponding fluence is mentioned.

In a recent study [25], Yamaguchi *et al.* used data from Tada *et al.* [114], Suzuki *et al.* [136] and Washio *et al.* [137] to compare the effect of resistivity (2 and 10 $\Omega.cm$ tested) on the output power of conventional and BSFR solar cells. It appears that the advantage towards higher resistivity starts from $3 \times 10^{15}\ cm^{-2}$ 1 $MeV$ electron fluence for conventional solar cells, and even from $3 \times 10^{14}\ cm^{-2}$ 1 $MeV$ electron fluence for BSFR solar cells. This difference is mainly due to the lower BOL output power of 10 $\Omega.cm$ in comparison to 2 $\Omega.cm$ in the case of conventional solar cells.

#### 1.2.4.2 Si solar cells design

**Thinning the solar cells**

Thinning the c-Si solar cells absorber was at the center of mitigation strategies; with laboratory homojunction p-type c-Si cells as thin as 50 $\mu m$ produced in the 1990s [107]. At this time, the main advantage of the thinning was the higher power-to-weight ratio, which led to overall cost reductions [134]. The thinner cells resulted in lower BOL $J_{SC}$ due to long wavelengths less collected, as depicted in the EQE spectral variations in Figure 1.22. Nevertheless, all the thicknesses tested resulted in the same EOL spectral response, making the thin solar cells suitable for space applications [105].

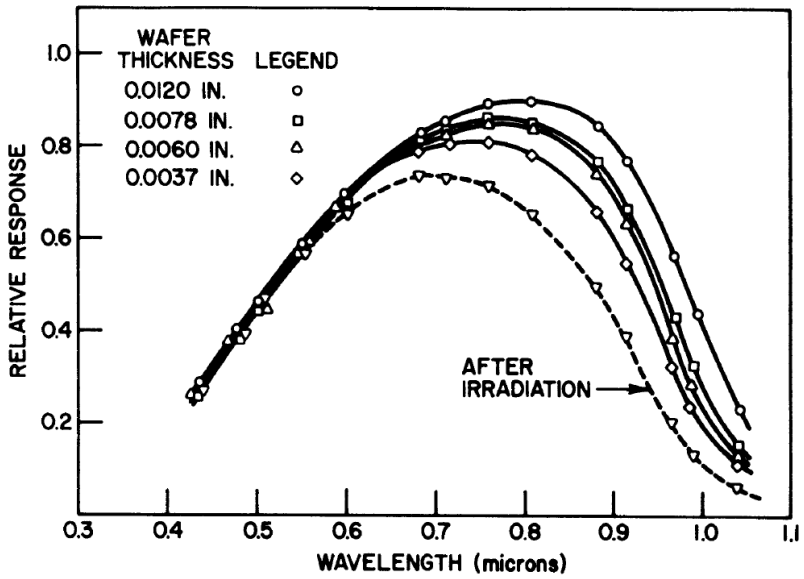


Figure 1.22: BOL Spectral response of c-Si solar cells of various thicknesses. After irradiation at a $5 \times 10^{15}$ $cm^{-2}$ 1 $MeV$ electron fluence, all the cells have the same spectral response (down triangles).

However, since then, the light management and the rear passivation were optimized. For instance, rear side reflectors were implemented. On the one hand, it allowed improved BOL efficiency for thin solar cells [138], [139], with long-wavelengths that could be better collected. On the other hand, the thinner cells could even minimize irradiation-related losses considering the low $\tau$ obtained after irradiation. Yamaguchi *et al.* found $\approx 10$ $mW$ higher output power for thinner cells, respectively $\approx 70$ $mW$ and $\approx 60$ $mW$ for 50 $\mu m$ and 300 $\mu m$ solar cells with 10 $\Omega.cm$ resistivity and irradiated at a $1 \times 10^{14}$ $cm^{-2}$ 1 $MeV$ electron fluence. However, this effect disappeared for higher electron fluence ($1 \times 10^{16}$ $cm^{-2}$ in the study) [25]. Cappelletti *et al.* found the same effect [140].

**Cell architectures**

Unless otherwise specified, all of the following solar cells feature p-type base doping with a front emitter, as these configurations are known to yield higher EOL efficiency values, as aforementioned. As the space industry stopped using c-Si PV technologies in the end of the 90s, the research has been driven by terrestrial applications since then, for which using n-type c-Si over p-type c-Si is beneficial.

Yamaguchi *et al.* [25] compared the irradiation hardness of the conventional homojunction c-Si cell structures with the following design improvements (schematic structures can be found in [21]):

- BSF: reduces the carrier recombination losses at the interface with the back contact metal,
- back-side-reflection (BSR): thin layer (often metallic) on the back surface to reduce transmittance loss,

- BSFR: combination of BSF and BSR,
- passivated-emitter-and-rear-locally-diffused (PERL): composed of an inverted pyramid light trapping structure, a double ARC layer, a localized BSF region, and a BSR.

The highest output power after irradiation at a $1 \times 10^{15}$ $cm^{-2}$ 1 $MeV$ fluence is observed in the BSFR cell structure ($\approx 40$ $mW$), yielding approximately $\approx 10$ $mW$ more output power than the conventional structure, with the BSF and BSR structures showing intermediate performances. This demonstrates the potential for significant improvements in EOL efficiency through optimized design. c-Si structures were particularly improved with the reduction of bulk and surface recombination. This is for example the case of PERL cells, PERC cells, IBC or SHJ cells. It was thus suggested that these cells should be considered for space applications [25]. Considering the $\tau$ obtained after irradiation and the rear-side junction of IBC cells, they are not appropriate for space use. Indeed, in these IBC cells, the charges need to move vertically and laterally to reach the contacts. This is also stated in [135]. PERL solar cells showed better BOL efficiency than BSF cells, but BSF cells were shown to be more resilient to irradiations, and have thus a better efficiency than PERL structures for 1 $MeV$ electron fluences higher than $1 \times 10^{14}$ $cm^{-2}$ [25]. This is due to stronger $V_{OC}$ losses for the PERL cells [141]. This degradation is explained by a high SRV resulting from the ionization of the oxide coating used, as introduced in [114], [142]. This could also come from the high carrier lifetime degradation in the thick n-type emitter layer. With a simulation based on BOL experimental data, Ma *et al.* compared the irradiation hardness of PERC and TOPCon designs [143]. They only found a slight advantage for the TOPCon design in case of low $p_0$ ($1 \times 10^{14}$ $cm^{-3}$) for $V_{OC}$ and $FF$ parameters. Specifically, the TOPCon design was shown to feature less impact of $R_s$ on $FF$ than PERC design. This is attributed to its full contact area for both minority and majority carriers.

SHJ structures could be a good alternative as the surface passivation is not made thanks to an oxide layer and as the emitter layer is nanometric. SHJ solar cells are also compatible with thin wafers, as aforementioned. However, they should be used with p-type base layers (and thus front emitters) to fit space purposes [25]. Neitzert *et al.* compared results under irradiation with or without front intrinsic amorphous layer. Overall, the use of intrinsic amorphous layer was found to have no effect on $L_n$ [144]. Therefore, they concluded that the dominant degradation was due to the degradation of the c-Si base layer recombination properties, and not to the solar cell architecture. Indeed, the homojunction and SHJ cells displayed comparable values for $K_L$ [145].

Since the beginning of this thesis, the interest on the impact of particle irradiation on SHJ stuctures has been rising [26], [27], [29], [28]. Gurimskaya *et al.* studied the effect of annealing on 20 $\mu m$-thick SHJ cells (introduced hereafter) [26]. Kalinovskii *et al.* found higher EOL efficiency ($1 \times 10^{15}$ $cm^{-2}$ 1 $MeV$ electron fluence) for Ga-doped SHJ solar cells in comparison with B-doped (>1% difference of absolute efficiency value), or with P-doped (near 0% efficiency) SHJ cells, and no significant influence on the use of microcrystalline front layers instead of amorphous layers. In [29], Cariou *et al.* showed the relevance of using wafers as thin as 60 $\mu m$ with a gain of almost 2% absolute of efficiency in comparison to 160 $\mu m$-thick solar cells. Lately, Duarte-Cano *et al* showed a strong degradation of n-type SHJ cells irradiated to

protons, mainly driven by $FF$ reductions.

**Original designs**

Original c-Si solar cells designed for space applications were previously developed. We can cite Presting *et al.* who made trenched p-type solar cells in order to decrease partially the collection length. Compared to a reference c-Si cell, the EOL efficiency (1 $MeV$ electron fluence of $3 \times 10^{15}$ $cm^{-2}$) increased from 9.7% to 10.1% for $100 - 50$ $\mu m$ deep holes for a 200 $\mu m$ cell thickness in comparison with the reference cell [146]. Concepts such as nanowires are promising with low collection length [147]. Suzuki *et al.* [148] emphasized the advantage of using 100 $\mu m$ non-reflective surface (NRS)/BSF cells, with a 20% higher $P_{max}$ compared to 100 $\mu m$ BSFR cells (1 $MeV$ electron fluence of $1 \times 10^{15}$ $cm^{-2}$). Based on these cells, Tonomura *et al.* made a 70 $\mu m$ both-side junction c-Si solar cell (3-terminal configuration). They reached a maximum EOL (1 $MeV$ electron irradiated up to $1 \times 10^{15}$ $cm^{-2}$) efficiency of 13.4%. This structure is nonetheless more difficult to produce and was obtained on a $2 \times 2$ $cm^2$ surface area [149].

#### 1.2.4.3 Effect of annealing

Above a certain temperature threshold, defects in c-Si can be annealed. A detailed list of annealing reactions for interstitial related defects in c-Si can be found in [115]. In particular, annealing studies demonstrated that B-doped c-Si that underwent type inversion due to high irradiation levels could return to p-type after annealing above 200 $°C$. They classified defects based on their annealing behavior: defects such as the $B_i - O_i$ complexes were associated with lower annealing temperatures ($150 - 200$ $°C$), while the annealing of the $C_i - O_i$ complex was associated to higher annealing temperatures ($200 - 300$ $°C$ and above). In the case of the conductivity type inversion of the base layer, this base layer could retrieve its initial conductivity type after annealing, possibly after the annihilation of the $C_i - O_i$ complex [122], [150].

These annealing temperatures are higher than the ones encountered in LEO orbits. Therefore, annealing does not occur naturally in space environment. Thus, studies have been conducted on decreasing the temperature at which a recovery of performance is obtained.

Earlier in the 60s-70s, lithium (Li) was reported to enhance the annealing of radiation-induced damage [90]. Indeed, Brucker [151] and Wysocky *et al.* [152] found out that thanks to its high mobility, Li was able to form complexes with defect centers, especially the one known as A-center occurring at $E_c - 0.18$ $eV$. This was observed in both n-type and p-type solar cells [153].

A Patent by mPower claims the use of intentional annealing steps during the mission [154]. This patent consists in applying a reverse current in the solar cell to heat it and thus improve annealing. The power used corresponds to 1/10 of the power that will be saved thanks to this process but even with the annealing, there is an accumulation of damages that continues to degrade the power output from the cells.

Khan *et al.* (2019) demonstrated that hydrogenation of 1.8 $\Omega.cm$ B-doped symmetric samples prior to electron irradiation significantly improved the efficiency of a 150 $°C$ dark

annealing treatment, enhancing the $\tau$ recovery after irradiation (see Figure 1.23) [127]. After irradiation at a $1 \times 10^{13}$ $cm^{-2}$ 1 $MeV$ fluence, $\tau$ recovered to 80% of its initial value for a sample with bulk hydrogenation following a 400 min dark annealing at 150 °$C$. In contrast, no enhancement in $\tau$ was observed for a sample without bulk hydrogenation under the same conditions. The positive effect of bulk hydrogenation was also reported on electron-irradiated Ga-doped PERC precursor solar cells [155].

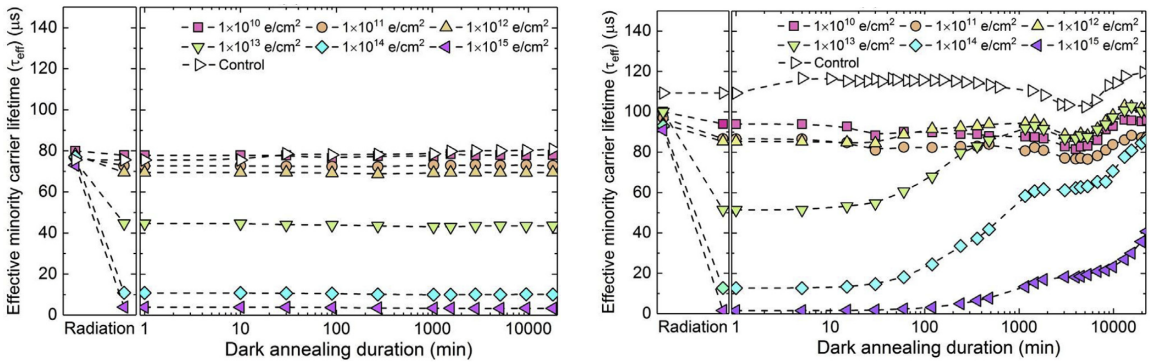


(a) (b)

Figure 1.23: Effective carrier lifetime as a function of dark annealing time at a temperature of 150 °$C$ for 1.8 $\Omega.cm$ B-doped c-Si symmetric structure samples (a) without bulk hydrogenation and (b) with bulk introduction of hydrogen prior to electron irradiation.

Recently, annealing temperatures below 100 °$C$ were obtained on c-Si SHJ solar cells irradiated at a $1 \times 10^{15}$ $cm^{-2}$ 1 $MeV$ electron fluence [26]. For $V_{OC}$, a 80 °$C$ annealing rate of 120 $mV/hr$ was obtained on 20 $\mu m$ ultra-thin cells.

Annealing is thus a promising alternative to enhance the radiation hardness of the solar cells, but was however beyond the scope of this work.

## Conclusion

As presented in introduction, c-Si based solar PVAs are currently essential to fulfill the LEO satellite needs. This PhD work focuses on the solar cell component of the PVAs, since charged particle irradiation in the space environment is the dominant cause of performance degradation in PVAs. In particular, we chose to focus on understanding the degradation mechanisms and optimizing the performances of state-of-the-art SHJ cells.

Several topics have been explored in the literature and will be further investigated in this manuscript:

- **influence of** $[O_i]$. The influence of $[O_i]$ in c-Si substrates reveals apparent contradictions. While FZ-Si, with its low $[O_i]$, generally exhibits higher resiliance to irradiation, Cz-Si, typically containing higher $[O_i]$, has been favored, notably for its greater availability. However, these observations are not always consistent in the literature. Therefore, Chapter 3 aims at providing new insights by systematically determining both the oxygen and the O-related thermal donor concentrations in the materials investigated.

- **c-Si dopant used**. While B-doped c-Si has traditionally been used, there is growing evidence suggesting that Ga-doped c-Si may offer better EOL cell performance, with generally better radiation hardness of carrier lifetime and less carrier removal effect. This shift from B to Ga has already been adopted in the terrestrial cells photovoltaic industry. Chapter 3 aims at comparing Ga-doped c-Si and B-doped c-Si carrier lifetime resilience, while Chapter 4 intends to assess the impact of high displacement damage on the carrier removal effect of 60 $\Omega.cm$ Ga-doped c-Si cells.
- **resistivity/$\mathbf{p_0}$**. A consensus was previously reached on using 10 $\Omega.cm$ resistivity for optimum B-doped c-Si cell EOL performances. However, this assumption is being challenged, as the limitations associated with high-resistivity wafers (such as low BOL efficiency) are becoming less relevant. Therefore, Chapter 3 aims to explore modern Ga-doped c-Si across a wide range of resistivity values, from 0.9 $\Omega.cm$ to 60 $\Omega.cm$, and Chapter 4 explores the limitations of using wafers with high resistivity values.
- **wafer thickness**. Owing to numerous advancements in the cell design, the wafer thickness no longer significantly impacts the solar cell performance. Progress can yet still be made, particularly in overcoming the manufacturing challenges associated with processing thin wafers. This is crucial, as thinning the wafers not only reduces the PVA weight but can also improve the EOL efficiency of the solar cells. Chapter 3 quantifies the efficiency gains associated with wafer thickness reductions from 160 $\mu m$ to 80 $\mu m$.
- **relevant design**. A front emitter structure should be used along with a p-type base layer to optimize the performance of c-Si-based solar cells. SHJ solar cells offer numerous advantages for space applications. Particularly, they can include a front emitter with p-type wafers, and their fabrication process is rather well compliant with thin wafers, making them ideal for lightweight, high-efficiency systems. Additionally, their compatibility with European industrial production lines positions them as a highly promising solution for upcoming European space missions. Despite these clear advantages, the radiation hardness of SHJ cells is still an under-explored topic. With this respect, Chapter 3 and Chapter 4 aim at investigating the effects of electron and proton irradiations on the SHJ cell performance.

In this context:

- **Chapter 2** introduces the materials and methods, covering the solar cell fabrication processes, irradiation facilities, characterization techniques, and modeling softwares.
- **Chapter 3** evaluates the impact of electron irradiation on Ga-doped SHJ cells. The core of this chapter focuses on the influence of the wafer composition properties and of the cell thickness on the radiation hardness.
- **Chapter 4** investigates the performance limits of Ga-doped SHJ cells with high resistivity subjected to proton irradiation. The study simulates a harsh environment by exposing the cells to high fluences of low-energy protons, resulting in a non-uniform defect distribution throughout the cell depth.

CHAPTER 2

# Materials and methods

This chapter presents first the process flow used in this PhD thesis work for the fabrication of silicon heterojunction (SHJ) solar cells. It then describes the irradiation facilities employed for electron and proton irradiations. The main characterization techniques used throughout this work are subsequently introduced, followed by a brief overview of the simulation tools used in the course of this thesis.

## 2.1 Solar cells production

Two types of SHJ samples – solar cells and non-metalized solar cells – were produced from wafers of the same batch in order to assess both the electronic and photovoltaic (PV) properties associated to each wafer type. The SHJ fabrication was made on CEA/INES pilot line (see Figure 2.1).

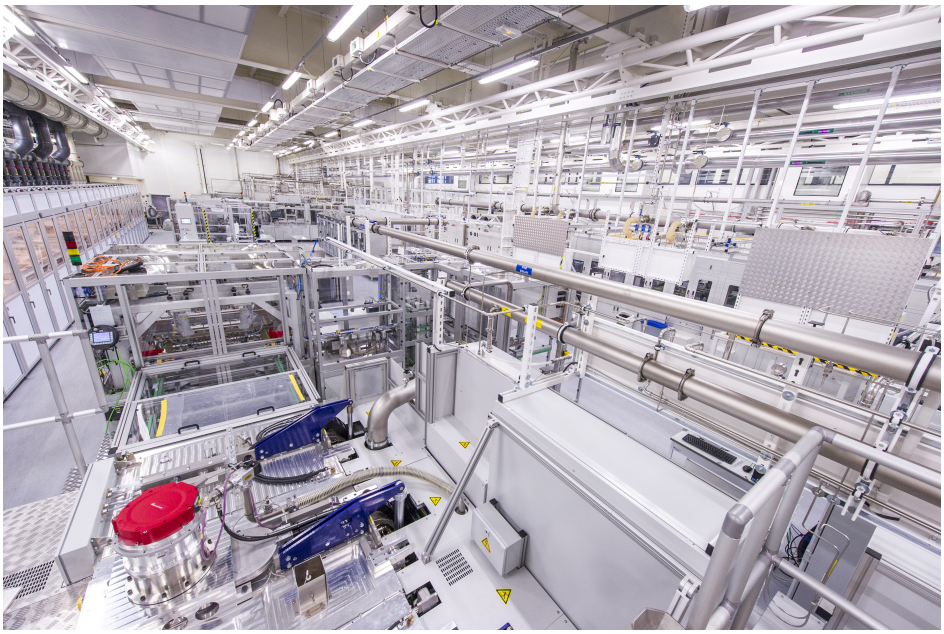

Figure 2.1: Picture of the CEA/INES SHJ pilot line.

The process flow used in this PhD work is illustrated in Figure 2.2. The main steps include wafer thickness reduction, cleaning and texturing, hydrogenated amorphous silicon (a-Si:H) deposition, transparent-conductive-oxide (TCO) deposition, screen printing and curing, and optionally $SiN_x$:H deposition. A specificity of the SHJ fabrication process is the low-temperature (usually below 230 $°C$) at which the intrinsic and doped a-Si:H layers are deposited. The temperature of all the remaining steps needs to be kept below $200 - 250$ $°C$ to avoid passivation degradation, for instance due to hydrogen effusion [45]. The role of the different layers was previously discussed in Section 1.1.5.2.

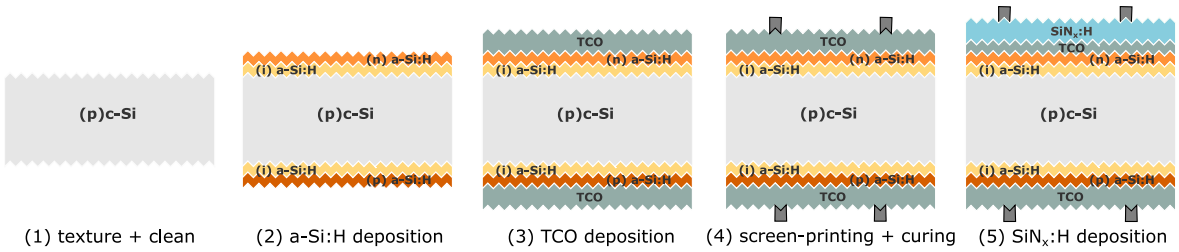


Figure 2.2: SHJ fabrication process steps used in this PhD thesis work. Please note that the $SiN_x$:H deposition (not systematically used) is performed on top of the metalization (not represented here for clarity).

All the crystalline silicon (c-Si) wafers used in these studies were obtained via a Czochralski (Cz) pulling process, which was introduced in Section 1.1.4.1. The format used is M2 with 156.75 $mm$ side length. The c-Si wafers used in these studies were either B- or Ga-doped and displayed various resistivity levels, depending on the targeted designs of experiments. Table 2.1 presents a summary of the wafer resistivity values and thin layers properties for each solar cell group studied in this PhD thesis. The composition properties of the different wafer groups is analyzed thoroughly in Chapter 3. It is worth noting that each wafer of a resistivity group comes from the same ingot. The initial thickness of the wafers varied from one material to another, e.g. 130 $\mu m$, 160 $\mu m$ or 170 $\mu m$.

| Group label | Ga0.9 | Ga15 | Ga60 | B1 | Ga2 |
|---|---|---|---|---|---|
| **Front** | | | | | |
| $SiN_x$:H (nm) | 0 | | | | 100 |
| TCO (nm) | 100 | | | | 15 |
| a-Si:H (n) (nm) | 5 | | | | |
| a-Si:H (i) (nm) | 3 | | | | |
| **Bulk** | | | | | |
| Dopant | Ga | | | B | Ga |
| Resistivity ($\Omega.cm$) | 0.9 | 15 | 60 | 1 | 2 |
| Thickness ($\mu m$) | 80 & 110 & 160 | | | 95 | 110 |
| **Rear** | | | | | |
| a-Si:H (i) (nm) | 3 | | | | |
| a-Si:H (nm) | (p) 5 | | | (n) 5 | (p) 5 |
| TCO (nm) | 100 | | | | 40 |
| used in Chapter(s) | 3 | | 3 & 4 | 3 | 3 |

Table 2.1: Summary of wafer resistivity values and thin layers properties of the fabricated SHJ precursors and solar cells.

### 2.1.1 Wet chemistry

When required for the different studies, thickness reduction to values as low as 80 $\mu m$ was achieved using a potassium hydroxide (KOH) 20% concentrated solution. Texturing was then performed using KOH 3.5% concentrated solution, creating pyramidal structures that reduce external optical reflection and improve internal light trapping [156]. Finally, a last HF bath was conducted to prepare the wafers for the a-Si:H deposition steps, ensuring a clean and well-prepared surface. These processes were carried out using a GAMA wet bench from *Akrion Technologies*.

### 2.1.2 a-Si:H deposition

The intrinsic a-Si:H(i) and doped a-Si:H(n)/a-Si:H(p) layers (see Figure 2.2 (2)) were deposited by plasma enhanced chemical vapor deposition (PECVD) with a HELiA equipment from *Meyer Burger*. The PECVD process is detailed in [157]. This process operates by introducing gaseous precursor molecules into a low-pressure chamber where a high-frequency plasma is generated. The precursors used were $SiH_4, H_2$ for a-Si:H(i), $SiH_4, H_2, PH_3$ for a-Si:H(n), and $SiH_4, H_2, B_2H_6$ for a-Si:H(p). The plasma energy breaks down the precursor gases into reactive radicals and ions, which then chemically react and deposit as thin layers on the c-Si wafer. This plasma-assisted process allows deposition at relatively low substrate temperatures (200 $°C$). The typical deposition time was around 5 min, with a capacity to process 56 wafers (loaded on horizontal trays) per PECVD run. The vacuum level was maintained at approximately $10^{-4}$ mbar during the process.

### 2.1.3 TCO deposition

TCO—and more specifically indium-tin-oxide (ITO)—layers (see Figure 2.2 (3)) were deposited by physical-vapor-deposition (PVD), using the HELiA-PVD sputtering tool from *Meyer Burger*. This process is detailed in [158]. It is a vacuum-based technique, from which the deposition is made from a solid target material (e.g. 3% $SnO_2$, 97% $In_2O_3$ used for ITO) physically vaporized and then condensed onto the substrate to form a thin film. The cell placement on the locally-opened horizontal trays (allowing the double-side TCO deposition) causes the rear perimeter of each cell to be masked by approximately 1 $mm$ of edge exclusion. This prevents TCO deposition on the cell edges, preserving the electrical isolation between the front and rear sides of the cells, thereby minimizing shunting. The process temperature was typically 200 $°C$, with a capacity to process 24 M2 wafers per run. The process duration was around $2-3$ $min$.

### 2.1.4 Screen-printing and curing

The solar cell metal contact grid (see Figure 2.2 (4)) was deposited by screen printing [15]. A mask with openings corresponding to the targeted metal pattern is placed on one side of the cell. A squeegee drags along the mask a silver (Ag) metal paste (mixed with solvents) that is deposited locally on the substrate through the designed openings in the mask. These masks result in metalization grids, made of busbars (120 $\mu m$-thick lines) and fingers (45 $\mu m$-thin lines perpendicular to busbars). The standard grid pattern used in this PhD work consisted in 6 busbars per face. However, a specific mask was used for preparing smaller cells with one busbar—significantly wider—per cell (see Figure 2.3). A curing was made during about 20 $min$ at 210 $°C$ to evaporate the solvents, and to achieve a low contact resistance between Ag and TCO. Both screen printing and curing steps were performed on an equipment from *Applied-Baccini*.

### 2.1.5 $SiN_x$:H deposition

For some solar cells, SiNx:H layers (see Figure 2.2 (5)) were deposited on top of the ITO layers and metalization. A PECVD process was used with $SiH_4$ and $NH_3$ precursors, but this time with a TWYN RD-2T equipment from *Semco Technologies*. In this study, the deposition duration was $4-5$ $min$, with a temperature comprised in the $150-200$ $°C$ range.

### 2.1.6 Laser cut

To comply with the irradiation facilities specifications and to optimize beam time, the initial M2-size cells and precursors were reduced to smaller dimensions using laser cutting (see Figure 2.3). A laser scribing is performed along the perimeter of the surface to be cut, after which the individual parts are separated by bending. This scribing was carried out on the side opposite the emitter (the rear side in our p-type cells) to prevent the formation of parasitic shunts that could degrade device performance.

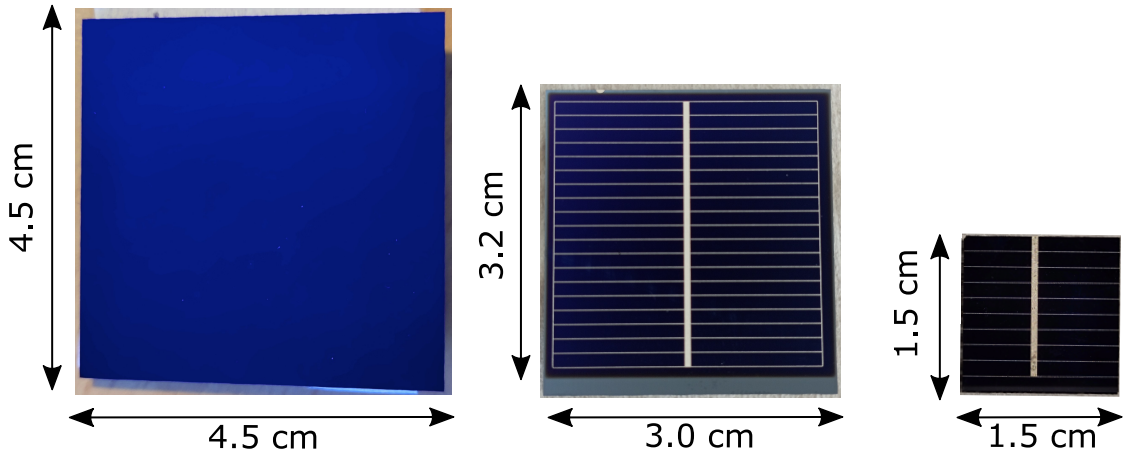


Figure 2.3: Pictures of cut precursor/finished cells used in the following studies.

## 2.2 Irradiation facilities

Sending the solar cells in orbit to test their resilience to charged particle irradiation would be extremely costly and time consuming. An alternative is to perform accelerated particle irradiation tests on Earth, using few monoenergetic particles beam conditions. Two methods can be used to link these tests with the cells degradation in orbit: JPL and NRL [111], as detailed in Chapter 1. In the NRL approach for instance, the damage expected during a specific mission is represented by a calculated equivalent DDD ($MeV/g$). Experimental degradation curves measured for 2 electron and 1 proton mono-energetic beams are sufficient to calculate a single degradation curve, specific to a cell technology, as a function of DDD. The remaining power for a specific mission at EOL—for which its corresponding DDD is known—can then be easily deduced from this single degradation curve.

The irradiation test conditions performed in the course of this thesis were chosen for investigation purposes. If new cells are to be brought to space market, a complete set of irradiation tests will need to be done, in compliance with ECSS-E-ST-20-08C standard for instance [159]. Nevertheless, this standard was mainly designed for III-V cells, and the test conditions will probably need some adaptations to take into account the specific features of modern c-Si cells (e.g. self-curing effects, etc.).

### 2.2.1 Electron irradiation

In Chapter 3, the solar cells were irradiated by 1 $MeV$ electrons with fluences ranging from $1.5 \times 10^{14}$ $cm^{-2}$ to $1.5 \times 10^{15}$ $cm^{-2}$ at room temperature at Sirius-Saclay facility [160]. A pelletron accelerator—an electrostatic accelerator—was used, more details on this type of accelerator can be found in [161].

A large copper sample holder with a surface area of ($180 \times 130$ $mm^2$) was used, with the samples maintained by Kapton tape. The backscattered electrons from the copper holder below the samples were not counted properly to calculate the total fluence. This resulted in an additional fluence on the samples of about 50% for our c-Si solar cells. A correction factor of

1.5 was thus applied on target values to get the effective fluence on the samples. The fluences reported in this manuscript refer to the effective fluences. The samples are irradiated by scanning the sample holder using servomotors in front of the approximately 2.5 $cm$ wide fixed electron beam (see Figure 2.4). The displacement velocity of the sample holder is synchronized with a digital charge integrator to ensure uniform electron fluence across the entire surface to be irradiated. The samples are thus scanned line by line until the desired fluence is reached on their whole surface. The applied flux was $5 \times 10^{11}$ $e/cm^2/s$, which was the standard flux used in this irradiation facility. This flux value corresponds to the maximum flux accepted to fit the ECSS standard, for target electron fluences up to $1 \times 10^{15}$ $cm^{-2}$ [159].

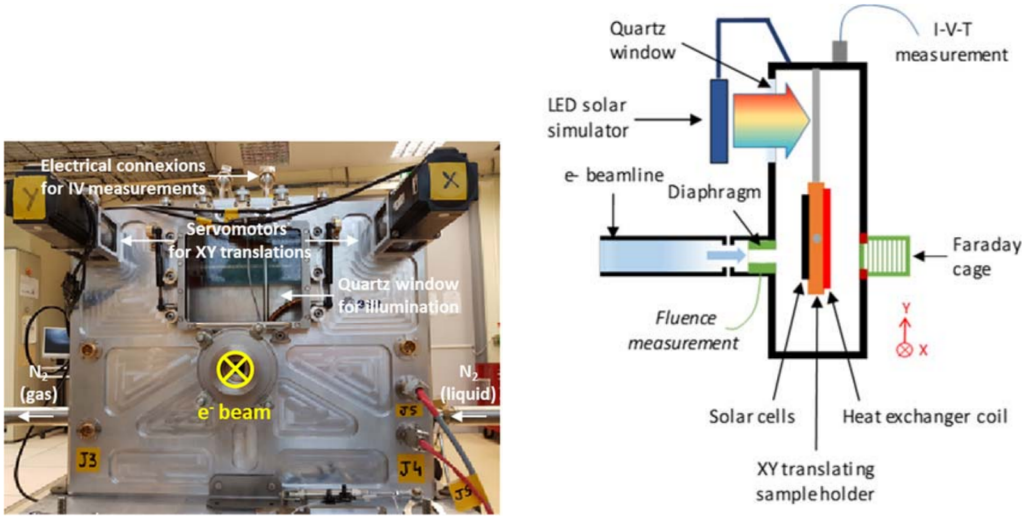


(a) (b)

Figure 2.4: (a) Picture and (b) schematic longitudinal section of the large area irradiation setup connected to the electron beam line at Sirius-Saclay facility [160].

The scanning mode combined with an electron beam shape, which presents tails towards the edges, results in uncertainties on the fluence seen by the sample, especially at edges and at scanning lines overlap regions. At samples edges, the fluence is lower ($\approx 30\%$) due to beam tail, and at scanning line overlap regions, the fluence uncertainty is included in an interval of $[-40\%; +30\%]$. This effect can be seen in the following electron diffusion length $L_n$ mappings: Figure 3.21 and Figure 3.23 of Chapter 3. Based on these $L_n$ mappings, the width of this overlap region was estimated to range from 5 $mm$ to 9 $mm$. In the case presented in Figure 3.23, a relative difference of 6.5% was found for the average $L_n$ of a region with a width of 7.6 $mm$, corresponding to the gap between scan lines, compared to a region that received the targeted fluence.

### 2.2.2 Proton irradiation

In Chapter 4, the solar cells were irradiated by 1 $MeV$ and 3 $MeV$ protons with fluences ranging from $1 \times 10^{12}$ $cm^{-2}$ to $1 \times 10^{14}$ $cm^{-2}$ at room temperature at JANNuS-Saclay facility. This is a triple-beam facility as illustrated in Figure 2.5(a). In the study, only the Japet

beam (see Figure 2.5(b)) was used, which is a 2 MV Tandem Pelletron (6SDH-2, National Electrostatics Corp.) equipped with an external SNICS-II ion source (negative ions by cesium sputtering [162]. This system is capable to produce energies of 0.5 $MeV$ to 4.0 $MeV$ for single-charged ions (e.g $H^+$ ions). The flux used was $1 \times 10^{11}$ $cm^{-2}s^{-1}$—the minimum flux available in this irradiation facility—for 1 $MeV$ and 3 $MeV$ protons. It is worth noting that this used flux is higher than the one recommended in ECSS standard—between $1 \times 10^9$ $cm^{-2}.s^{-1}$ and $6 \times 10^{10}$ $cm^{-2}.s^{-1}$—[159], this limit being set to avoid solar cells heating during irradiation, and thus possible defect annealing. Due to this relatively high flux, the created mechanisms and dynamics may therefore differ from standard conditions. Additionally, the uncertainty on the lowest targeted fluence ($1 \times 10^{12}$ $cm^{-2}$) was in the range of 20%.

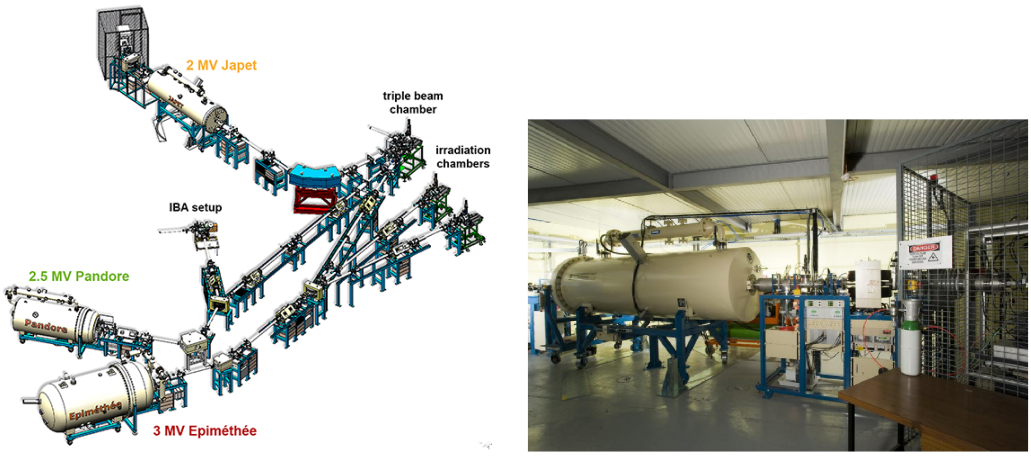


(a) (b)

Figure 2.5: (a) Overview of the JANNuS-Saclay platform [163]. (b) 2 MV tandem Pelletron JAPET [162].

The available irradiation surface was small, consequently $1.5 \times 1.5$ $cm^2$ cells were irradiated. However, no scanning mode was required, allowing better homogeneity on the surface. The solar cells were maintained on the substrate holder with carbon tape at the back of the cells. Thus, only 160 $\mu m$-thick solar cells were irradiated to reduce the risk of breakage when removing the tape.

## 2.3 Characterization of the samples

During this PhD work, all characterization measurements were carried out at room temperature.

### 2.3.1 Majority carrier concentration and mobility

The equilibrium hole mobility $\mu_p$ and concentration $p_0$ were measured on $1.5 \times 1.5$ $cm^2$ c-Si p-type square wafers using Hall effect measurements combined with resistivity $\rho$ measurements (using the Van der Pauw method [164]), with an equipment from *Ecopia*. Hall effect measurements provide the Hall majority carrier concentration $p_H$, which differs from

the actual concentration $p_0$ by the Hall factor $r_H$ (unitless), such that $p_0 = p_H \times r_H$. $r_H$ depends on the type and concentration of the charge carriers, the dominant mobility-limiting scattering mechanism, the temperature, and the magnetic field [165]. In this work, $r_H$ was set to 0.75, following [166]. In order to electrically contact the wafers, four silver-based contacts were deposited at the corners of each sample. The sample size and contact placement are critical, as they can introduce non-negligible uncertainties, as discussed in [167].

$\mu_p$ is then calculated by combining Hall effect and resistivity measurements, using Equation 1.9: $\mu_p = \frac{1}{p_0 q \rho}$.

### 2.3.2 Sheet resistance

The sheet resistance $R_{sheet}$ ($\Omega/sq$) was measured using the 4-point probe technique [168], using a *Napson* equipment. This method involves injecting a current $I$ through the two outer probes, while the resulting voltage $V$ is measured between the two inner probes. The measured $V$ is a function of $I$, $R_{sheet}$, and a geometric correction factor that depends on the probe configuration and sample dimensions. Usually, $\rho$ can then be calculated as:

$$\rho = R_{sheet} \times d \tag{2.1}$$

where $d$ is the thickness of the layer. This layer differs from the sample thickness in case of the presence of an insulating layer, formed by a pn junction for instance. In this PhD work, all 4-point probe measurements were made at wafer center.

### 2.3.3 Composition properties with OxyMap

The composition properties of the Ga-doped c-Si wafers (i.e. $[O_i]$, [TD], [Ga]) were obtained using the OxyMap technique. This technique is fully described in [169], and is based on [170]. $\rho$ is measured at room temperature by non-contact eddy current measurements on the wafer at several stages of the characterization procedure. The first $\rho = \rho_1$ measurement is made before any process. Then, a 450 $°C$ annealing is performed and a $\rho = \rho_2$ measurement follows. At 450 $°C$, TDs are generated effectively with a kinetic strongly dependent on $[O_i]$. Afterwards, another annealing stage at 700 $°C$ is performed and a $\rho = \rho_3$ measurement follows. The 700 $°C$ annealing step allows to annihilate the TDs. Therefore, $[TD] \approx 0\ cm^{-3}$ and Equation 1.39 gives $p_0 \approx [Ga]$ in the case of Ga-doped c-Si, and thus $\rho_3$ gives [Ga]. Knowing [Ga], it is therefore possible to get the initial [TD] from $\rho_1$ by taking into account the double donor activity. Knowing [Ga] and [TD], $[O_i]$ is subsequently determined from $\rho_2$ using an internally developed empirical expression for the TD generation kinetics at 450 $°C$.

$\rho$ measurements are made at 19 points equally spaced on one diagonal of the M2 wafer. The values displayed in the manuscript refer to the average values of these 19 measurement points.

### 2.3.4 Carrier lifetime

The effective carrier lifetime $\tau$ was measured on cell precursors (i.e., non-metalized samples) using both transient and quasi-steady-state (QSS) photoconductance techniques with a *Sinton* equipment [171]. These methods rely on the principle that a light pulse induces a carrier injection level $\Delta n$, which in turn increases the conductivity of the sample. The change in conductivity is detected inductively via an RF coil positioned beneath the wafer. $\tau$ is then derived from the general relationship:

$$\tau(\Delta n) = \frac{\Delta n(t)}{G(t) - \frac{d\Delta n(t)}{dt}} \tag{2.2}$$

where $G(t)$ represents the generation rate of excess carriers, which is determined by measuring the incident photon flux using a calibrated reference solar cell placed adjacent to the sample. To accurately evaluate $G(t)$, both the reflectivity and the absorption coefficient of c-Si must be accounted for. An optical constant of 1.1 was used in the different studies of this manuscript.

**Transient**

In the transient mode, a short, high-intensity light pulse is used to abruptly generate a large carrier injection level. The subsequent decay of the excess carrier density—inferred from the photoconductance signal—is monitored. $\tau$ is then extracted from the initial slope of the decay curve, using the simplified expression [172]:

$$\tau(\Delta n) = -\frac{\Delta n(t)}{\frac{d\Delta n(t)}{dt}} \tag{2.3}$$

This technique is particularly suited for high-quality c-Si wafers exhibiting long $\tau$ (typically $\tau > 200\ \mu s$) [42]. To evaluate the reproducibility of transient $\tau$ measurements, ten measurements were performed on the same BOL Ga60 160 $\mu m$ cell precursors, reinserted into the setup before each acquisition. The resulting average $\tau$ was 1931 $\mu s$, with a standard deviation of 172 $\mu s$.

**QSS**

For short $\tau$ (typically $\tau < 200\ \mu s$), the QSS method was employed [171]. In this approach, the sample is exposed to a slowly varying illumination, allowing the carrier populations to remain in quasi-equilibrium during the measurement. The condition for QSS is fulfilled when $\tau$ is much shorter than the characteristic decay time of the light pulse. Under this assumption, $\tau$ is determined using the following simplified relation:

$$\tau = \frac{\Delta n(t)}{G(t)} \tag{2.4}$$

To evaluate the reproducibility of QSS-PC $\tau$ measurements, ten measurements were performed on the same EOL ($1.5 \times 10^{14}\ cm^{-2}$ 1 $MeV$ electron fluence) Ga0.9 110 $\mu m$ cell precursor, reinserted into the setup before each acquisition. The resulting average $\tau$ was

1.40 $\mu s$, with a standard deviation of 0.02 $\mu s$.

### 2.3.5 Suns-$V_{OC}$

The Suns-$V_{OC}$ measurements, conducted using a *Sinton* equipment, provide access to the I-V curve of the diode without the effects of series resistances $R_s$ [173]. The principle of this technique consists in illuminating the solar cell with a rapidly varying light intensity while measuring the open-circuit voltage $V_{OC}$ corresponding to each illumination level. Since the measurements are performed under open-circuit conditions, no current flows through the device, and the $R_s$ influence is eliminated. This approach enables the determination of the so-called pseudo-I-V curve, which represents the I-V curve in the absence of $R_s$. In this work, the Suns-$V_{OC}$ technique was employed primarily to determine the pseudo fill factor ($pFF$) of the samples. The $pFF$ corresponds to the fill factor ($FF$) that the device would exhibit if $R_s$ were negligible.

To evaluate the reproducibility of pFF measurements, ten measurements were performed on the same BOL Ga60 160 $\mu m$ cell, reinserted into the setup before each acquisition. The resulting average $pFF$ is 78.15%, with a standard deviation of 0.05%.

### 2.3.6 I-V measurements

I-V curves under illumination enable to assess the performances of the solar cells in standardized conditions. With the current being normalized by the cell surface, the J-V curves offer suitable comparison metrics for any cell sizes. An example is shown in Figure 1.4. The main parameters extracted from such J-V curves are the short-circuit density $J_{SC}$, the $V_{OC}$, the $FF$ and the resulting efficiency, as calculated from Equation 1.37.

The BOL I-V of the solar cells of Chapter 3 were measured with a *Neonsee* system, which illuminates the samples with an AM1.5G spectrum generated by a Xe lamp. However, there was a high breakage rate with our thin SHJ cells due to the contact probe system of this set-up. Therefore, we switched to another sun simulator from *Wavelabs* for all the other I-V measurements, with more suitable contacting probes for our samples. This second solar simulator is a LED-based system offering customized spectra—including AM1.5G and AM0—at various intensities. The included AM1.5G spectrum is of class A++ (spectral match within 5%, according to IEC 6090-9 ED.2). The AM0 spectrum intensity was derived to match the certified AM0 $J_{SC}$ of a reference cell. The comparison of this AM0 solar simulator spectrum with the reference AM0 spectrum [44] is displayed in Figure 2.6. As one can see, the LED spectrum fails to deliver proper irradiance at short wavelenghts ($< 350\ nm$), and also presents significant irradiance oscillations above and below the reference, up to the c-Si bandgap wavelength. This is inherent to LED sun simulators, which are based on a limited number of LED light sources across the desired wavelength range. Both sun simulators are designed to work in 4-wire measurement configurations.

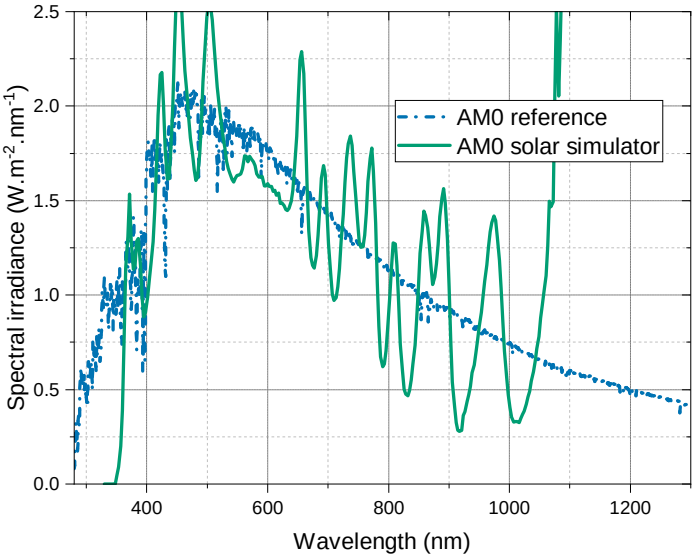


Figure 2.6: Comparison of LED solar simulator AM0 spectrum (green) with the reference AM0 spectrum (blue) [44].

For both sun simulators, busbars with multiple contacting probes are mounted on a frame for the front contacts. In the case of our small solar cells (a few square centimeters), the *Wavelabs* system uses only two front contacting probes at the extremities of a single busbar, which helps to reduce shading. All contacts are spring-loaded, applying a moderate pressure to the solar cells during measurements. For the *Wavelabs* system, two voltage contacts are embedded in the chuck below the sample, whereas the *Neonsee* system uses rear probe contact points, which also press the cells from rear side, contributing to the high breakage rate.

### 2.3.7 External quantum efficiency

External quantum efficiency (EQE) measurements (introduced in Chapter 1) enable to identify the main regions of poor collection (i.e. front surface vs c-Si bulk/rear surface) of the irradiated cells.

The equipment used in Chapter 3 and Chapter 4 was from *Newport*. The light source is a 100 W Xe white lamp, whose spectrum is shown in Figure 2.7. It is spectrally filtered using a monochromator to transmit a narrow band of wavelengths of light. The slit width is set to achieve a spectral resolution between 9 and 10 $nm$ in the $340 - 1200$ $nm$ range (for our measurements).

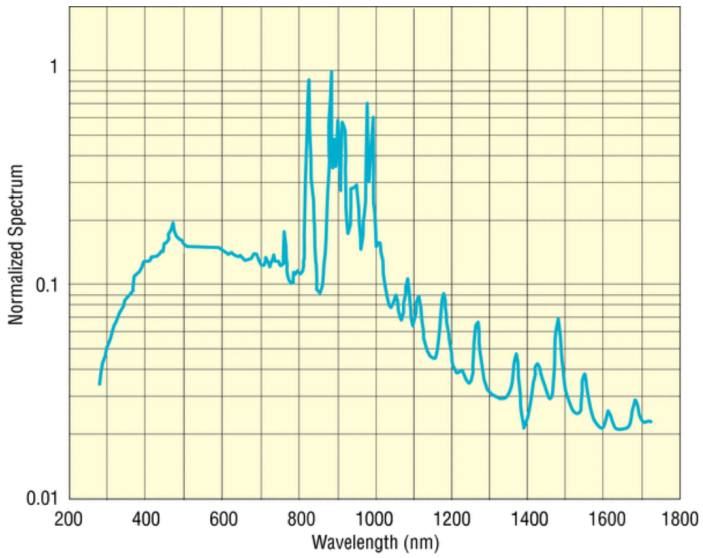


Figure 2.7: Spectrum of a Xenon lamp used in EQE measurements in Chapters 3 and 4 [174].

This equipment was upgraded between Chapter 3 and Chapter 4 studies. The change in the setup compared to the original configuration resulted in a relative deviation of 3.8% in AM0 $J_{SC}$ calculated from EQE. In the upgraded version, the spot size ($1.1\ mm \times 1.2\ mm \pm 0.1\ mm$) was small enough to fit between two fingers, whereas the spot in the original setup was more elongated, partially overlapping the metal fingers at certain wavelengths. Additionally, a part of this deviation might arise from in-plane variations in the bulk electronic properties of the Ga60 solar cells used for this comparison, as discussed in Chapter 4.

A white bias light, included in the EQE setup, was used without any filter in Chapter 4 (see Figure 4.6) study on proton-irradiated solar cells. This was a 50 $W$ quartz tungsten halogen lamp with a color temperature of 3200 $K$, more details can be found in [175]. A potentiometer was employed to adjust the intensity of the lamp, with a scale ranging from 0 to 6, where 0 represents no light and 6 denotes the maximum intensity. The influence of bias light on EQE of a non-irradiated Ga60 160 $\mu m$ cell is shown in Figure 2.8. The bias light induces weak perturbations in the measurement (i.e., slightly noisy data), but does not influence the values themselves.

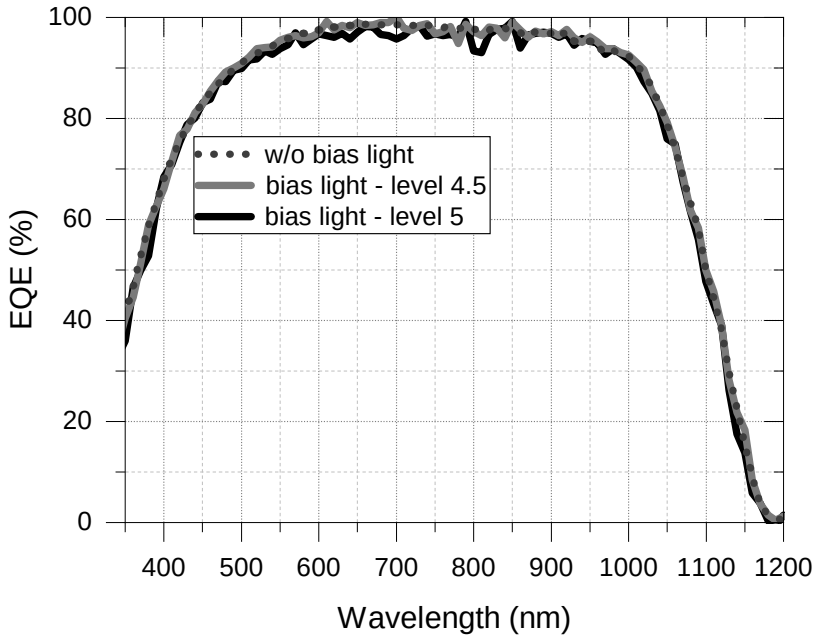


Figure 2.8

Figure 2.9: Influence of bias light on EQE spectral measurements of a non-irradiated Ga60 160 $\mu m$ cell with $1.5 \times 1.5$ $cm^2$ format. A picture of the bias light setup is shown in Figure 4.6.

### 2.3.8 Light Beam Induced Current

In our p-type solar cells, $L_n$ was mapped using a light-beam-induced-current (LBIC) equipment from *Semilab* in order to assess in-plane $L_n$ variations. $L_n$ is calculated from $J_{SC}$ and reflectance $R$ (unitless) mappings at 3 different wavelengths—976 $nm$, 946 $nm$, and 852 $nm$—whose absorption depths in c-Si are respectively—99 $\mu m$, 61 $\mu m$, and 18 $\mu m$—. From these $J_{SC}$ and $R$ measurements, $L_n$ is extracted from the internal quantum efficiency (IQE) defined as:

$$IQE(\lambda) = \frac{EQE(\lambda)}{(1 - R(\lambda))} = \frac{1}{1 - R(\lambda)} \frac{J_{SC}(\lambda)}{\Gamma_0(\lambda) q} \tag{2.5}$$

where $\Gamma_0$ is the incident photon flux ($photons.cm^{-2}.s^{-1}$), beforehand measured with a fluxmeter. Then, using Equation 2.6, it is possible to get $L_n$ by plotting $\frac{1}{IQE}$ as a function of $\frac{1}{\alpha}$ with:

$$\frac{1}{IQE(\lambda)} \approx 1 + \frac{1}{L_n(\lambda)} \frac{1}{\alpha(\lambda)} \tag{2.6}$$

However, strong hypotheses are made [176]:

- $L_n$ should be lower than the third of the sample thickness. Otherwise, the fitting to the plot will underestimate the extracted minority carrier diffusion length, then called $L_{eff}$.

- the penetration depth of the light should be lower than the sample thickness. Therefore, these $L_n$ mappings could only be used for cells thicker than 100 $\mu m$, considering the absorption depth of the wavelengths used.
- the thickness of the SCR and the emitter should be significantly lower than the penetration depth of the light, thus only long wavelengths are used to satisfy this condition.

It is also important to take into account the texturing of the cell as in this case, due to lower light absorption depths, the calculated $L_n$ overestimates the true $L_n$. The effect of the texturing can however be taken into account by multiplying by 0.74 the computed $L_n$.

## 2.4 Simulation softwares used

### 2.4.1 Effects of proton irradiation

In this study, the effects of proton irradiation on Si (with thickness values corresponding to those of experimental devices) were modeled using numerical simulations based on Monte Carlo methods. Low energy proton particles, for which the projected range occurs at a depth within the Si thickness, induce heterogeneous displacement damages in the material. This degradation can be simulated using SRIM/TRIM softwares that model the interactions between particles and matter (described in [94]). SRIM is a software tool used to simulate and calculate the interactions between ions and matter. It primarily helps in determining the stopping power (the energy an ion loses per unit distance), the projected range (depth of ion penetration), and the damage profile/spread of ions as they pass through different materials. TRIM is a component of the SRIM software package that focuses specifically on the transport of ions within a material at an atomic-scale, for instance ion trajectories, scattering angles, and the spatial distribution of ions. Two main features were used in Chapter 4:

- The projected ranges of $H^+$ ions as they travel through Si target material as a function of their energy. SRIM simulates the energy loss of particles as they cross the material, providing detailed information on the depth at which the particles stop within Si.
- The number of vacancies normalized for one $H^+$ ion (produced from atomic displacement) created along the proton track in Si. Three proton energies were considered for these simulations: 1, 3, and 10 MeV. The calculations were performed within a 160 $\mu m$ depth of Si, enabling the estimation of the vacancy density created by proton irradiation. The ion distribution and quick calculation of damage along the Si depth was used for this purpose.

The main output results obtained from these simulations, such as ion penetration depth, were integrated into a numerical model of the solar cells to get deeper insights into the behavior of the solar cells that were irradiated with these proton energies.

### 2.4.2 Solar cell modeling program

Solar cell modeling studies with PC1D were carried out to evaluate the change in $\Delta n$ following electron irradiation, this at different voltages, as discussed in Chapter 3. PC1D

was also used to investigate the evolution of the c-Si bulk properties after proton irradiation, as discussed in Chapter 4. For this purpose, PC1Dmod 6.1 version was used [177]. PC1D software solves quasi-one-dimensional fundamental semiconductor equations to simulate the behavior of charge carriers within a solar cell (Poisson's equation, continuity equations for electrons and holes, and transport equations). It incorporates advanced physical models, such as Fermi-Dirac statistics, bandgap narrowing, incomplete ionization of dopants, and recombination mechanisms (e.g., Shockley-Read-Hall, Auger, radiative), to accurately represent real-world device behavior. This software is however not designed for modeling modern passivated contacts such as a-Si(H)/c-Si interfaces in SHJ cells. Furthermore, only one defect energy level per layer can be modeled. However, as will be detailed in Chapter 3 and Chapter 4, PC1D was sufficient to effectively model the different experimental behaviors of the irradiated solar cells despite the above-mentioned limitations.

The PC1D solar cell model used in this manuscript is the following (illustrated in Figure 2.10(a)). The reflectance spectrum used is the one displayed in Figure 3.18. This spectrum was measured on precursor solar cells, and thus does not take into account the metal front grid reflection. The $J_{SC}$ values are thus overestimated compared to those obtained from our solar cells I-V measurements.

A front region specific to the n-type emitter, with a thickness of 0.1 $\mu m$ and an uniform doping concentration of $n_0 = 5 \times 10^{20}\ cm^{-3}$, was created since passivated contacts modeling was not possible. The SRH recombination parameters of this region were set to $\tau_{n0} = \tau_{p0} = 1000\ \mu s$ and $E_t - E_i = 0\ eV$. It is worth noting that, in this software, only a single defect can be modeled for each layer, for which only the parameters $\tau_{n0}$, $\tau_{p0}$, and $E_t - E_i$ can be varied.

The front and rear surface recombination parameters were set to $S_p = S_n = 1\ cm/s$ and $E_t - E_i = 0\ eV$. The thickness and doping concentration in the bulk varied depending on the specific case being studied; $p_0$ was set to $2.6 \times 10^{14}\ cm^{-3}$ in Ga60 case for instance. The SRH recombination parameters were set to $\tau_{n0} = \tau_{p0} = 1000\ \mu s$ and $E_t - E_i = 0\ eV$ for BOL case. These parameters were also adjusted based on the irradiation conditions of the cells being modeled.

A p-type rear diffusion (erfc profile with a $0.1 \mu m$ depth factor) was set to $p_0 = 1 \times 10^{19}\ cm^{-3}$.

As a result, the simulated AM0 I-V values for BOL Ga60 160 $\mu m$ cells were $J_{SC} = 49\ mA/cm^2$, $V_{OC} = 720\ mV$ and $FF = 81\%$. Although this model did not exactly represent the SHJ cells used in the study, it provided a good compromise, resulting in reasonable I-V performances and similar spectral responses (see Figure 2.10(b)).

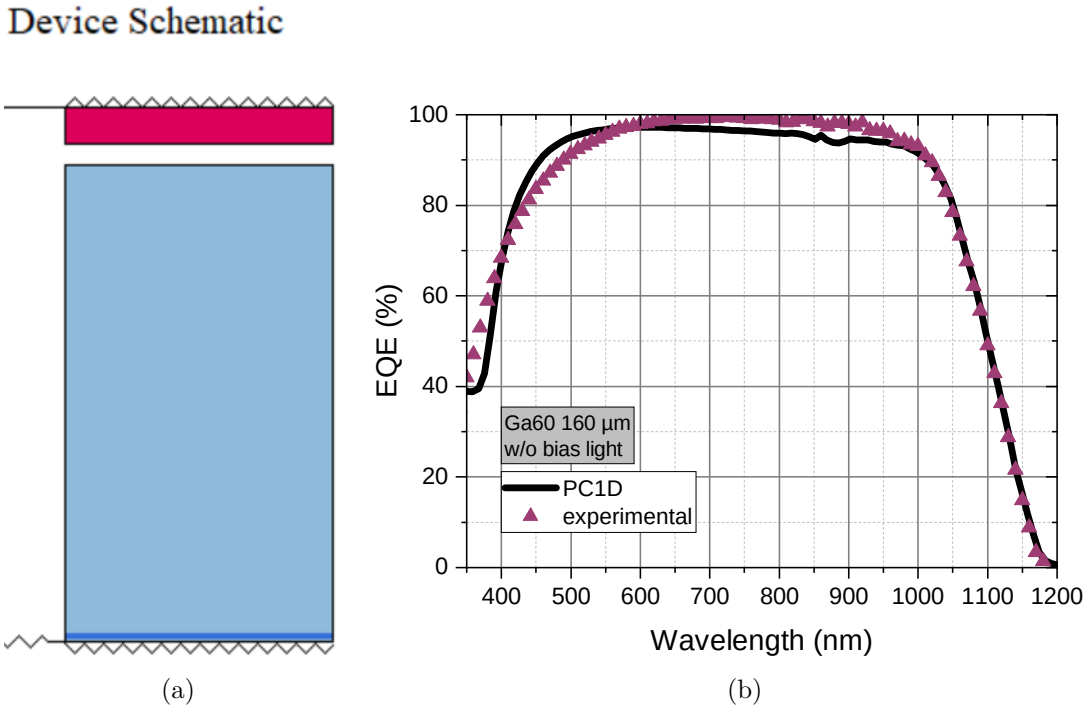


(a) (b)

Figure 2.10: (a) Illustration of the cell structure used in PC1D. Pink refers to n-type c-Si, blue to p-type c-Si, and light colors to low equilibrium majority carrier concentrations. (b) Comparison of EQE spectral variations of experimental BOL Ga60 160 $\mu m$ cell (triangles) and its modeling with PC1Dmod 6.1 (full line).

CHAPTER 3

# Electron irradiation of SHJ cells: effects of the material composition and wafer thickness

Mitigation strategies regarding the effects of electron irradiation on the performances of c-Si solar cells have been studied [90], [99], [25] from the early space developments, and were introduced in Chapter 1. p-Type c-Si was for instance selected for the bulk material of space solar cells for its superior radiation hardness compared to n-type c-Si. Additionally, a front-junction structure was preferred due to the low EOL $\tau$ values. Thinning the c-Si solar cells absorber was also seen as an important positive lever; even if at this time, the main advantage of the thinning was the higher power-to-weight ratio which led to overall cost reductions [134]. A B-doped c-Si wafer resistivity of 10 $\Omega.cm$ was historically chosen for space applications due to its resulting higher post-electron irradiation performances compared to those obtained with 2 $\Omega.cm$ resistivity wafers, as already discussed in Section 1.2.4.1 [90].

Most of the studies introduced in Chapter 1 were conducted a few decades ago. Thus, they were related to c-Si materials and cell technologies that are not representative of the current PV industry as introduced in Section 1.1.4 and Section 1.1.5. In particular, Ga replaced B for p-type doping and significantly lower $[O_i]$ are now obtained. This is particularly interesting as it is known that several electrically-active defects in electron-irradiated p-type c-Si are related to complexes involving $O_i$ and acceptor dopants (e.g., $B_i - O_i$ or $Ga - O_i$) [119], [25]. $O_i$ also leads to thermal donor (TD) defects, which can impact the resistivity, $\tau$ and efficiency as documented for terrestrial PV solar cells [178]. In parallel, strong PV performances at high resistivity are now possible at BOL [179], which would suggest an advantage in increasing the resistivity according to the study previously cited [90]. When comparing the use of B doping versus Ga doping regarding the c-Si solar cells resilience to irradiations, either similar performances for both or an advantage in favor of Ga doping were reported [130], [133], [27]. Also, the wafer thickness used in PV industry tends to decrease with similar BOL efficiency values, e.g. thanks to the implementation of adequate rear side reflectors.

Therefore, it is of paramount importance to assess and understand how the composition of modern c-Si wafers influence the properties of electron irradiated cells, especially by processing advanced passivated contact devices, such as SHJ cells. This is the aim of this chapter, which will also pay a particular attention to the effects of the substrate thickness.

In this context, amorphous Si (a-Si) / Ga-doped c-Si SHJ solar cells are promising, as they combine a high efficiency potential [180] and a compatibility with ultra-thin wafers [181]. Furthermore, with their existing process, front-junction structures are formed by using p-type wafers. Therefore, this study investigates the resilience of modern Ga-doped SHJ solar cells to 1 $MeV$ electron irradiation ($1.5 \times 10^{14} - 1.5 \times 10^{15}$ $cm^{-2}$ fluences), which corresponds historically to a standard test condition. In particular, the influences of the wafer resistivity, and of the cell thickness on the radiation hardness are at the center of this study. For this purpose, three types of Ga-doped wafers with different composition properties, along with different wafer thicknesses, are investigated. First, the evolution of the equilibrium hole concentration $p_0$ with increasing fluence is examined to monitor any potential carrier removal effect. Then, the EOL carrier recombination is analyzed as a function of wafer resistivity, composition properties, and the dopant type (Ga or B). After that, the photovoltaic properties after irradiation are evaluated as a function of $p_0$ and the cell thickness. Particular attention is paid to in-plane variations of the electron diffusion length $L_n$.

A large part of this chapter is based on the following publications: [182], [183].

## 3.1 Design of experiments

The design of experiments for this electron hardness study on SHJ solar cells is illustrated in Figure 3.1. Three groups of *sister* Ga-doped M2 ($156.75 \times 156.75$ $mm^2$) c-Si wafers (i.e., for a given group, wafers sampled from the same region of the parent ingot, with similar composition properties) were selected according to their resistivity: i) 0.9 $\Omega.cm$ representative of the industrial standard, ii) 15 $\Omega.cm$ close to the preferred resistivity values in literature for space applications, and iii) 60 $\Omega.cm$ to explore high resistivity EOL performances. They are respectively labeled Ga0.9, Ga15 and Ga60 in the following. The resistivity values of all the wafers are measured using the non-contact eddy current method. For chosen *sister* wafers of each group, these resistivity measurements were conducted before and after the intentional formation and annihilation of TD (OxyMap technique [170] detailed in Chapter 2). This method enables to obtain the composition properties (i.e. $[O_i]$, [TD], [Ga]). Unless specified, the composition properties and resistivity values displayed in the following refer to the average of the resistivity values measured along the diagonal of the wafer. Two types of samples—SHJ solar cells and SHJ cell precursors (non-metalized)—were produced from wafers of the same group in order to assess both the electronic and PV properties associated to each wafer type. The detail of the SHJ fabrication process is provided in Chapter 2. The widths of the SCR of the SHJ cells, determined by modeling with Afors-Het [184], were: $\approx 300$ $nm$ for Ga0.9, $\approx 1$ $\mu m$ for Ga15, and $\approx 2$ $\mu m$ for Ga60.

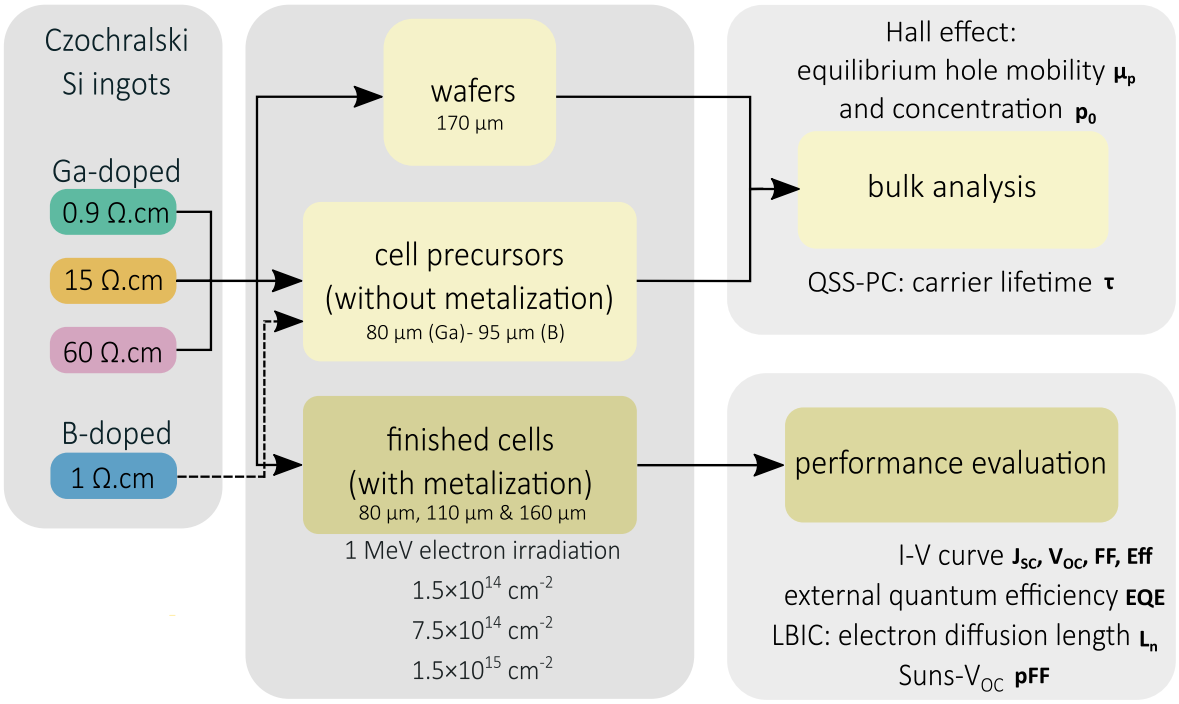


Figure 3.1: Design of experiments for the p-type silicon heterojunction solar cells electron radiation hardness study.

In order to better leverage the available irradiation time for this experiment, the SHJ solar cells were cut in smaller size than the initial M2 format. In the case of cell precursors, the final M2 samples were laser cut in $4.5 \times 4.5\ cm^2$ samples. In the case of metalized solar cells, the $3.0 \times 3.2\ cm^2$ format was chosen. For this purpose, nine small cells were first screen-printed using a specific mask and subsequently laser-cut from each M2 sample. This enabled to maximize the number of configurations to be included in the irradiation test while keeping a reasonable sample surface. Each sample was laser numbered to ensure a good traceability. A photoluminescence (PL) image of a printed M2 cell is shown in Figure 3.2. Dark areas, characterized by lower PL values, can be observed in this PL image and originate from defectivity. This defectivity was mainly due to handling and transportation steps (contact with belts, trays, traces left by handling clamps, etc) during the fabrication process.

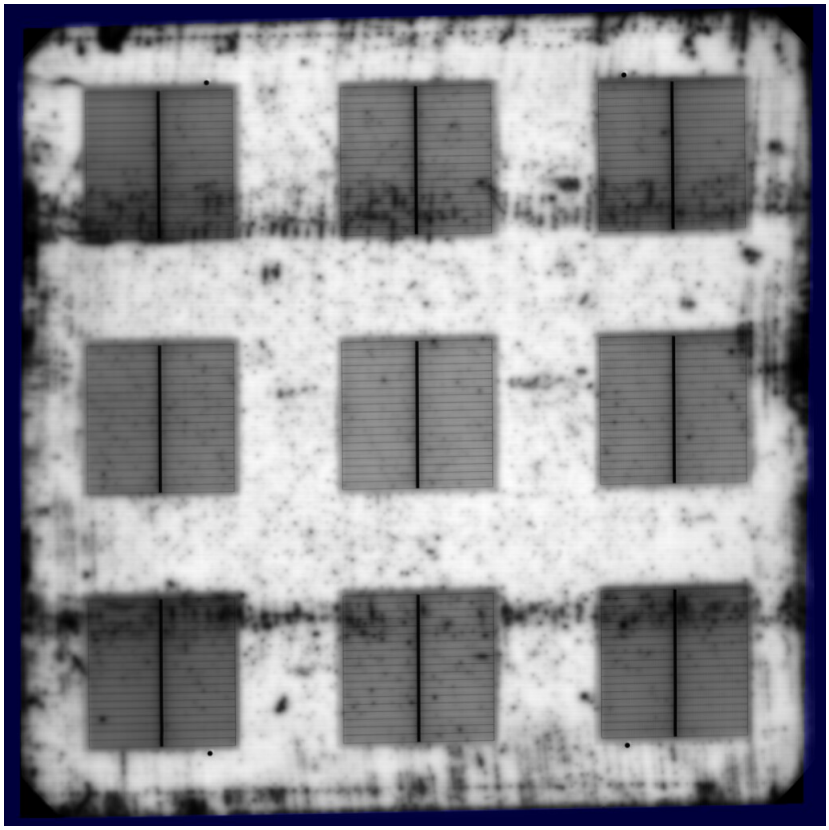

Figure 3.2: PL image of a Ga60 M2 printed solar cell gathering nine 80 $\mu m$-thick solar cells, which were cut afterwards in $3.0 \times 3.2$ $cm^2$ format.

The equilibrium hole mobility $\mu_p$, and $p_0$ were monitored on $1.5 \times 1.5$ $cm^2$ c-Si wafers through Hall effect measurements coupled with resistivity measurements (Van Der Pauw method). The $\tau$ was measured on cell precursors (non-metalized samples) via transient (for Ga15 & Ga60 at BOL) and quasi-steady state (QSS) (for Ga0.9 at BOL; Ga0.9, Ga15, & Ga60 at EOL) photoconductance measurements. The solar cells performances were monitored by I-V measurements, at BOL with a Neonsee solar simulator, and at EOL with a Wavelabs solar simulator. For this second case, the BOL condition refers to complementary measurements made on *sister* solar cells. The reason of this set-up change is detailed in Chapter 2. EQE measurements were performed without bias light and enabled to identify the main regions of degradation since short wavelengths are absorbed close to the front surface and long wavelengths are absorbed in the bulk or close to the rear surface. The pseudo-FF ($pFF$) was measured with the Suns-$V_{OC}$ technique. The $L_n$ was extracted on the irradiated $3.0 \times 3.2$ $cm^2$ cells via LBIC measurements combined with reflectance measurements at three different wavelengths: 852, 946 and 976 $nm$.

Additionally, 95 $\mu m$-thick symmetrically passivated 1 $\Omega.cm$ B-doped c-Si wafers (B1) were produced, also cut in $4.5 \times 4.5$ $cm^2$ format. Only QSS-PC $\tau$ measurements at BOL and EOL were performed on these samples.

Samples from the four resistivity groups corresponding to every condition of the experi-

mental plan were irradiated: wafers (170 $\mu m$), cell precursors (80 $\mu m$ and 95 $\mu m$) and solar cells (80 $\mu m$, 110 $\mu m$ and 160 $\mu m$). They were irradiated at three 1 $MeV$ electron fluences: $1.5 \times 10^{14}$ $cm^{-2}$, and $7.5 \times 10^{14}$ $cm^{-2}$, $1.5 \times 10^{15}$ $cm^{-2}$ (see Figure 3.1). Each condition is tested on two identical samples, with the exception of the cell precursors for Ga60 and B1 groups, for which 3 samples per condition were tested, and for the wafers, for which one sample per condition was tested.

It is generally accepted that 1 $MeV$ electrons induce homogeneous degradation in the bulk of the solar cells. However, this was challenged recently [143]. Indeed in [143], experimental EOL (1 $MeV$ electrons) EQE values for high wavelengths (800–1000 $nm$) could not be reproduced with a uniform generation profile. A better agreement was found by supposing that the defect density followed an exponential decay from the front to the rear side.

## 3.2 Initial properties

For Ga0.9, the resistivity values were in the range $[0.75; 0.95]$ $\Omega.cm$ regarding the values at the center of the wafers, and in the range $[0.79; 0.96]$ $\Omega.cm$ for the average of the resistivity values measured along the diagonal of the wafer (see Figure 3.3). Likewise, the resistivity ranges for Ga15 were $[11.5; 14.9]$ $\Omega.cm$ at center, and $[13.6; 16.3]$ $\Omega.cm$ in average, and for Ga60 $[44.5; 61.4]$ $\Omega.cm$ at center and $[55.2; 58.8]$ $\Omega.cm$ in average. For B1, only two *sister* wafers were measured as a good uniformity was expected. The resistivity values were $[1.01; 1.06]$ $\Omega.cm$ at center and $[1.03; 1.08]$ $\Omega.cm$ in average.

Then, the composition of the Ga-doped c-Si wafers used was analyzed in details. The $p_0$ values for each group were calculated from [TD] and [Ga] (see Equation 1.39: $p_0 = [Ga] - 2[TD]$). The Ga0.9 and Ga60 wafers have approximately the same amount of $[O_i]$ (only $\approx 5\%$ difference) and a small variation of [TD] yet very different [Ga], $2\times$ and almost $27\times$ higher respectively for Ga0.9 (see Figure 3.3). Conversely, the Ga15 and Ga60 wafers have close [Ga] yet large $[O_i]$ and [TD] differences, $1.4\times$ and almost $4\times$ higher respectively for Ga60. Thus, most of the resistivity variation between them is related to changes in [TD]. In addition, $p_0$ was measured on wafers from the same resistivity groups by Hall effect in order to directly monitor this parameter after irradiation. The observed differences in Figure 3.3 between calculated $p_0$ (from [Ga] and [TD]) and measured $p_0$ (from Hall effect) could essentially come from slight disparities of the wafers composition within the same group (as shown by the resistivity ranges previously displayed). The $p_0$ values obtained from Hall effect measurement were used for the rest of this study. This composition analysis will be used as hints on whether the $p_0$, [Ga] or $[O_i]$ play the main roles in the EOL performances.

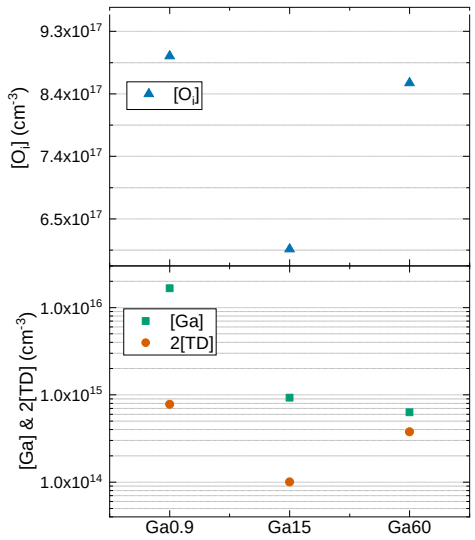


| | **Ga0.9** | **Ga15** | **Ga60** |
|---|---|---|---|
| $\rho$ **(Ω.cm) range** wafer center | [0.75; 0.95] | [11.5; 14.9] | [44.5; 61.4] |
| $\rho$ **(Ω.cm) range** wafer diagonal average | [0.79; 0.96] | [13.6; 16.3] | [55.2; 58.8] |
| **[$O_i$] ($cm^{-3}$)** | $8.9 \times 10^{17}$ | $6.1 \times 10^{17}$ | $8.5 \times 10^{17}$ |
| **[TD] ($cm^{-3}$)** | $3.9 \times 10^{14}$ | $5.0 \times 10^{13}$ | $1.9 \times 10^{14}$ |
| **[Ga] ($cm^{-3}$)** | $1.7 \times 10^{16}$ | $9.2 \times 10^{14}$ | $6.3 \times 10^{14}$ |
| **$p_0$ ($cm^{-3}$)** Calculated | $1.6 \times 10^{16}$ | $8.2 \times 10^{14}$ | $2.5 \times 10^{14}$ |
| **$p_0$ ($cm^{-3}$)** Hall effect | $2.3 \times 10^{16}$ | $1.2 \times 10^{15}$ | $2.6 \times 10^{14}$ |

Figure 3.3: Mean values of $[O_i]$, [TD], [Ga] and $p_0$ for the three groups of Ga-doped c-Si wafers studied. $[O_i]$, [TD], [Ga] were obtained from non-contact eddy current resistivity measurements (carried out before/after the intentional formation/annihilation of TDs). The $p_0$ *calculated* is calculated from [Ga] and [TD] using Equation 1.39. The $p_0$ *Hall effect* was obtained from Hall effect measurements made on *sister* wafers (corrected by a Hall factor $r_H = 0.75$) [166].

The impact of laser cut from M2 to $4.5 \times 4.5$ $cm^2$ format on BOL $\tau$ measurements (cell precursors) is shown in Figure 3.4 for 3 material groups—Ga0.9, Ga15, and Ga60—and 3 thicknesses—80 $\mu m$, 110 $\mu m$, and 160 $\mu m$—. The $\tau$ scattering for M2 format between the different samples from one group is striking. For instance, $\tau$ values ranged from 885 $\mu s$ to 4080 $\mu s$ for Ga60 160 $\mu m$ case. It is worth noting that the majority of these samples suffered from process defectivity issues, as aforementioned. In addition, these high $\tau$ are especially sensitive to the surface passivation quality. For the Ga15 110 $\mu m$ group, one M2 1904 $\mu s$ sample was cut into 9 sub precursors resulting in a $\tau$ range of [928; 1177] $\mu s$. This result shows that the sample underwent a clear $\tau$ decrease after laser cut, possibly via shunting effects and increased edge recombination [185]. Notably, this loss in $\tau$ is particularly significant for the cell precursors in the Ga15 and Ga60 groups. Despite this decrease, the $\tau$ values for the cell precursors that were subsequently irradiated showed significantly lower values and minimal scattering, thus ensuring reliable analysis after irradiation.

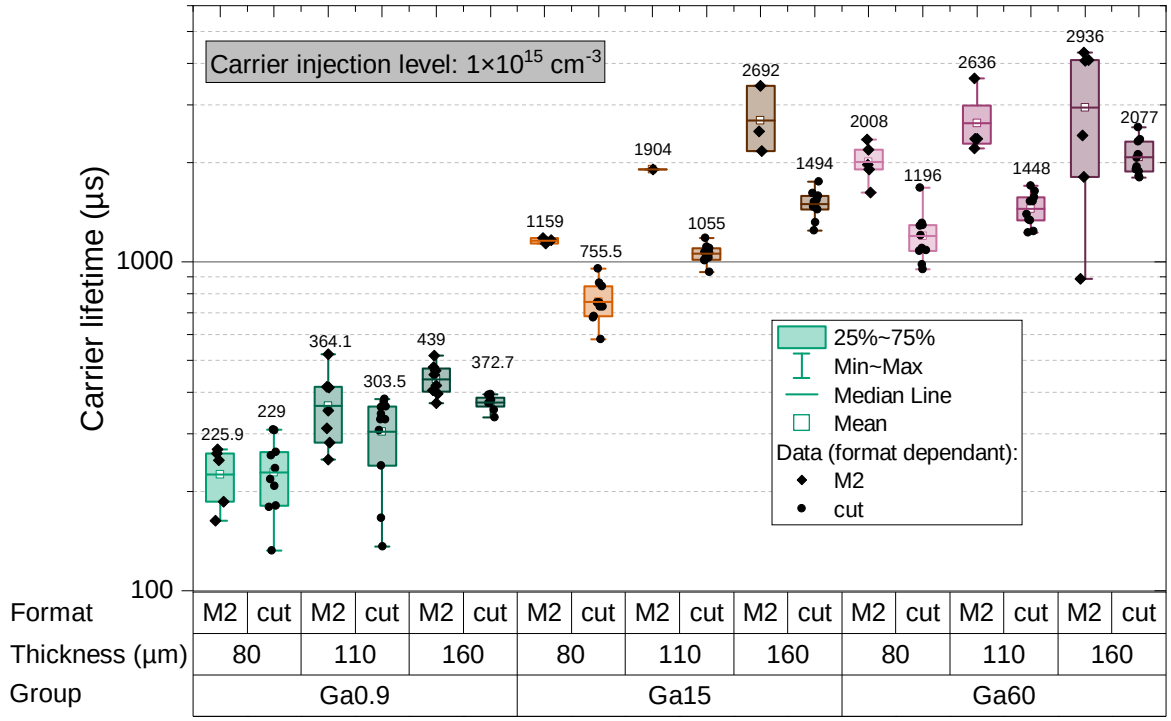


Figure 3.4: τ obtained from transient (Ga15 and Ga60) and QSS (Ga0.9) photoconductance measurements for the three precursor groups: Ga0.9 (green), Ga15 (orange to brown) and Ga60 (pink). The results are organized in three precursor thicknesses: 80 $\mu m$ (light color), 110 $\mu m$ (medium color) and 160 $\mu m$ (dark color). The impact of the laser cut is compared between M2 surface (diamond) and $4.5 \times 4.5$ $cm^2$ surface (circle). The mean value ($\mu s$) for each box is displayed above.

BOL τ values ranges measured at the carrier injection level $\Delta n = 1 \times 10^{15}$ $cm^{-3}$ for the 80 $\mu m$-thick selected samples to be irradiated were: [210; 310] $\mu s$ for Ga0.9, [680; 860] $\mu s$ for Ga15, [980; 1680] $\mu s$ for Ga60, and [124; 150] $\mu s$ for B1. With the dispersion obtained, a clear trend within the Ga-doped samples is observed: the highest τ values are associated with the highest resistivity values. For instance, the average τ of Ga60 is approximately 4.7× higher than that of Ga0.9, which correlates with its higher τ range. However, despite similar resistivity levels between Ga0.9 and B1, the average τ is ≈ 2× higher for Ga0.9 than for B1. This indicates that Ga-doped c-Si performs better than B-doped c-Si in terms of BOL τ. The B1 cell precursors exhibited significant degradations in τ even before irradiation, despite being stored in boxes. For instance, the initial τ value for the non-irradiated B1 sample was 125 $\mu s$, but it decreased to 27 $\mu s$ when measured one month later. Such a rapid degradation was not observed in the Ga-doped samples, highlighting the superior stability of Ga-doped c-Si, despite identical storage conditions. B-doped wafers might have been more sensitive to environmental exposure, possibly exhibiting early-stage light-induced degradation (e.g. during the different characterization measurements).

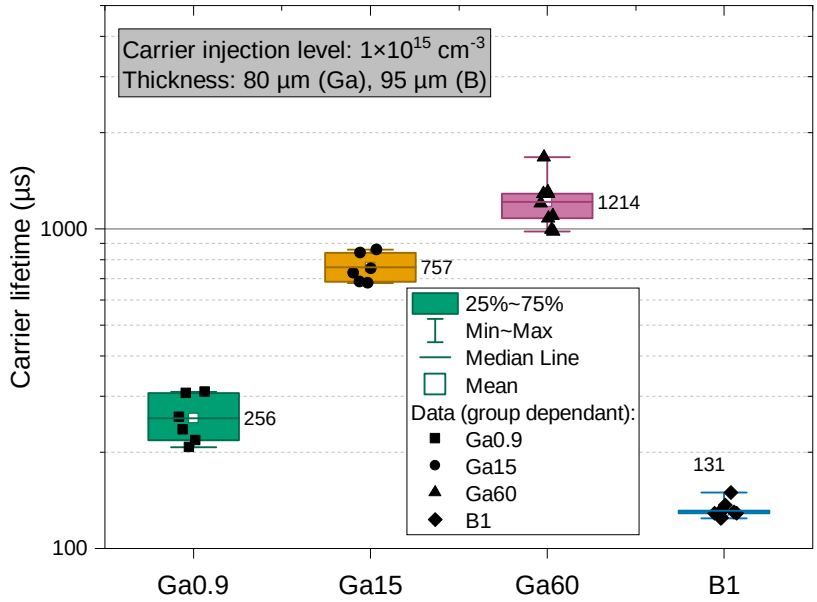


Figure 3.5: BOL $\tau$ of the $4.5 \times 4.5$ $cm^2$ passivated wafers later irradiated for the four groups: 80 $\mu m$ Ga0.9 (green, square), 80 $\mu m$ Ga15 (orange, circle), 80 $\mu m$ Ga60 (pink, triangle), and 95 $\mu m$ B1 (blue, diamond). The mean value ($\mu s$) for each box is displayed next to it.

Initially, the I-V performances of the solar cells were assessed with a Neonsee equipment that enables measurements with an AM1.5G spectrum. These BOL I-V measurements of the solar cells later irradiated plus a spare per condition are shown in Figure 3.6. The BOL efficiency values of the solar cells are comprised between 17.25% to 19.25% (AM1.5G) which are values relatively low compared to the potential of SHJ design. This can be explained by the surface defectivity mentioned above. One should also note though that metalization grids were not optimum in this format. Moreover, edge recombination effects are more impacting compared to large area cells due to increased edge recombination combined with a higher perimeter over surface ratio [186]. Looking at these results in more details, the $FF$ parameter is particularly low with average values $\approx$ 72.5%, when 80% values are usually reached, essentially due to edge recombination along with defectivity. It is worth noting that p-type SHJ cells $FF$ values are expected to be lower than the n-type ones [187]. The average values of $J_{SC}$ and $V_{OC}$ were $\approx 35.5$ $mA/cm^2$ and $\approx 725$ $mV$, respectively. No specific trends were observed neither between groups nor between thicknesses. Despite the aforementioned problems of edge recombination effects and defectiveness, the cells still exhibit good $V_{OC}$ BOL values. As this parameter is particularly sensitive to bulk recombination, these cells are well suited for studying the effects of irradiation on SHJ cells.

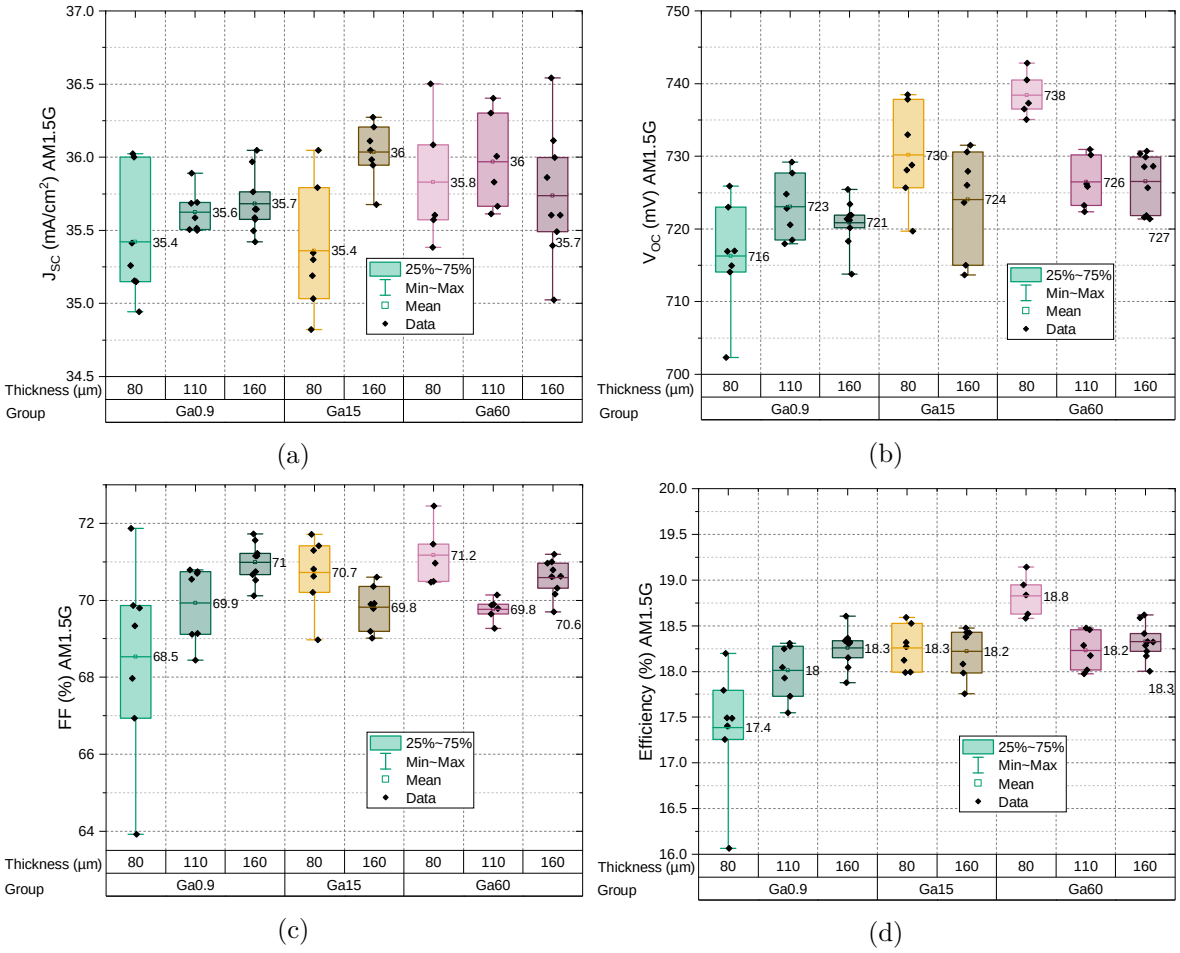


Figure 3.6: BOL I-V parameters of $3.0 \times 3.2\ cm^2$ solar cells measured under 1 Sun AM1.5G spectrum: $J_{SC}$ (a), $V_{OC}$ (b), $FF$ (c), and Efficiency (d). The results are shown for the three solar cell groups: Ga0.9 (green), Ga15 (orange) and Ga60 (pink). The results are divided in three cell precursor thicknesses: 80 $\mu m$ (light color), 110 $\mu m$ (medium color) and 160 $\mu m$ (dark color). The mean value for each box is displayed next to it.

The $J_{SC}$ trend of the cells was further analyzed by conducting EQE measurements. The EQE spectral variations obtained are shown in Figure 3.7. The spectral variations are similar, for a given thickness, between the three groups. Variations in the wafer thickness induce slight changes in the EQE values for the long wavelengths $> 900\ nm$, as can be seen between 80 $\mu m$ and 160 $\mu m$ thicknesses. Only one group is displayed for the 160 $\mu m$ thickness for better clarity. This can be due to non optimal optical reflectors that would not be efficient enough to maintain good photogeneration at long wavelengths.

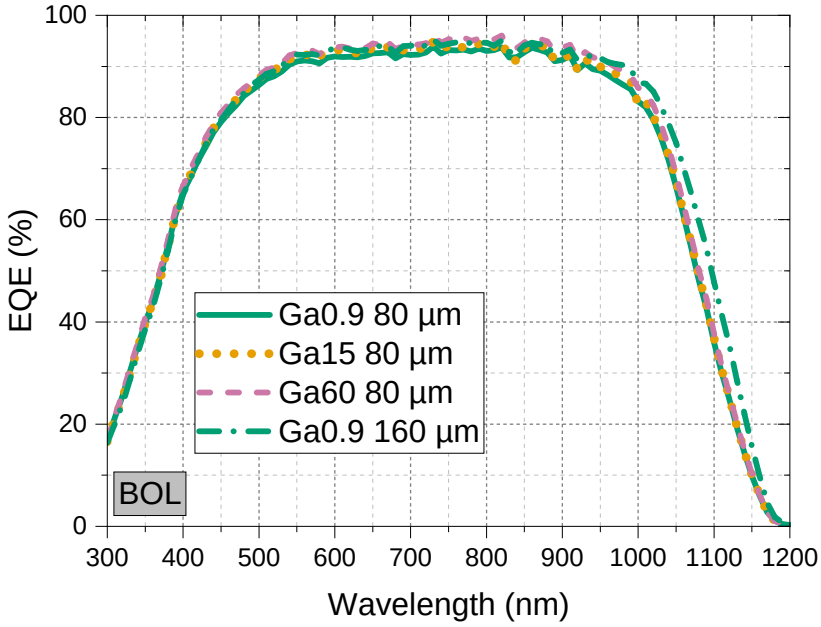


Figure 3.7: BOL EQE spectral variations of SHJ solar cells ($3.0 \times 3.2\ cm^2$) for the three 80 $\mu m$ solar cell groups: Ga0.9 (green line), Ga15 (orange dot line), and Ga60 (pink dash line). The EQE spectral variation of Ga0.9 solar cell is also shown for the 160 $\mu m$ thickness (green dash dot line).

## 3.3 Equilibrium hole concentration and mobility

The Hall effect measurements performed on BOL and EOL wafers result in no noticeable reduction of $p_0$ (see Figure 3.8(a)) for electron fluences $\leq 1.5 \times 10^{15}\ cm^{-2}$. This is true even for the highest resistivity material and the highest electron fluence tested in this study. Previous results reported lower carrier removal rate $R_c$ for Ga-doped c-Si ($0.04\ cm^{-1}$) compared to B-doped c-Si ($0.15\ cm^{-1}$) [133]. A ratio of 2 in favor of Ga-doped c-Si was later found for c-Si low gain avalanche detectors irradiated with neutrons [188]. This $R_c$ difference was attributed either to greater difficulty to displace/deactivate Ga from the lattice site than B [188]. It was also attributed to the donor-like electron level $E_c - 0.18\ eV$ acting as a compensating center in B-doped c-Si, which is related to $B_i - O_i$ complex, and would be at the origin of 60% of the difference in $p_0$ after irradiation with high fluence [133]. Using Equation 1.42 with $p_0 = 2.6 \times 10^{14}\ cm^{-3}$ and $1.5 \times 10^{15}\ cm^{-2}$ fluence, these $R_c$ values would have resulted in $p_0 = 2.0 \times 10^{14}\ cm^{-3}$ for $R_c = 0.04\ cm^{-1}$, and $p_0 = 3.5 \times 10^{13}\ cm^{-3}$ for $R_c = 0.15\ cm^{-1}$ [133]. With $p_0$ that remained higher than $p_0 = 2.0 \times 10^{14}\ cm^{-3}$ for the same fluence, our experimental value corroborate well with the previous good results obtained on Ga-doped c-Si.

Additionally, no clear trends (variations within measurement error margins) are observed for $\mu_p$ dependence with 1 $MeV$ electron fluence (see Figure 3.8(b)). The $p_0$ and $\mu_p$ values were thus not reduced, suggesting that the densities of electrically-active defects were significantly lower than the $p_0$ values.

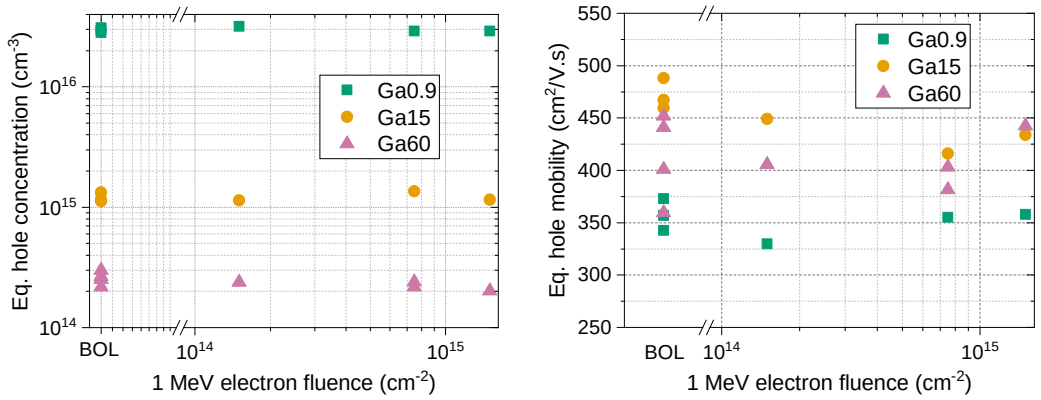


(a) (b)

Figure 3.8: Equilibrium hole concentration (a) and mobility (b) (extracted from Hall effect measurements and corrected by a Hall factor $r_H = 0.75$) [166] as a function of electron fluence for the three types of materials: Ga0.9 (green squares), Ga15 (orange circles), and Ga60 (pink triangles).

## 3.4 Recombination

### 3.4.1 Carrier lifetime

80 $\mu m$-thick solar cell precursors were used to probe $\tau$ variations in the three groups of samples. BOL $\tau$ values ranges measured at $\Delta n = 1 \times 10^{15}\ cm^{-3}$ were: $[210; 310]\ \mu s$ for Ga0.9, $[680; 860]\ \mu s$ for Ga15 and $[980; 1680]\ \mu s$ for Ga60. After irradiation, the $\tau$ are shown at $\Delta n = 1 \times 10^{14}\ cm^{-3}$, a value that was chosen in order to obtain $\tau$ values outside the measurement noise for all materials and fluences. At $\Delta n = 1 \times 10^{14}\ cm^{-3}$, the $\tau$ values of all samples are reduced below 10 $\mu s$ (see Figure 3.9). The best results are obtained for the highest resistivity values with $\tau$ 4.4× higher for Ga60 in comparison with Ga0.9 at the $1.5 \times 10^{14}\ cm^{-2}$ fluence. This $\tau$ gap between the highest and the lowest resistivity values keeps increasing with increasing fluence. Indeed, the $\tau$ of Ga60 wafers is 5.8× higher than the values found for the Ga0.9 wafers at the $1.5 \times 10^{15}\ cm^{-2}$ fluence.

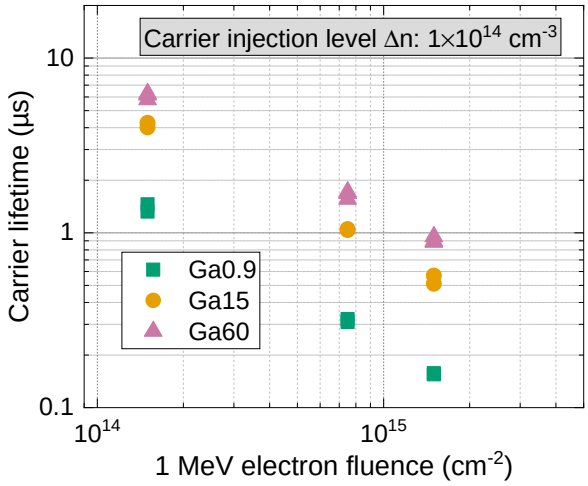


Figure 3.9: Carrier lifetime variations with increasing electron fluence on 80 $\mu m$ cell precursors for Ga0.9 (green squares), Ga15 (orange circles) and Ga60 (pink triangles).

The reduction of $\tau$ observed in Figure 3.9 shows that the two samples per condition did result in the same EOL $\tau$ despite the strong variations of BOL $\tau$ (see Section 3.2). In addition to the variations in $\tau$ values, the dynamics of $\tau = f(\Delta n)$ also differentiate between the different resistivity groups, as displayed in Figure 3.10. The cell precursors based on Ga60 show a decrease of $\tau$ with increasing $\Delta n$, the ones based on Ga15 result in quite flat dynamics with increasing $\Delta n$, while the ones based on Ga0.9 show an increase of $\tau$ with increasing $\Delta n$, especially at the lowest fluence. Therefore, the trends of $\tau = f(p_0)$ can change significantly as a function of $\Delta n$. For instance, Ga60 and Ga0.9 result in similar $\tau$ values at $\Delta n = 2 \times 10^{15}\ cm^{-3}$ for cell precursors exposed to $1.5 \times 10^{14}\ cm^{-2}$ 1 $MeV$ electron fluence. These recombination properties being a function of each group, they suggest $\tau$-limiting defects linked to the composition properties (including $p_0$).

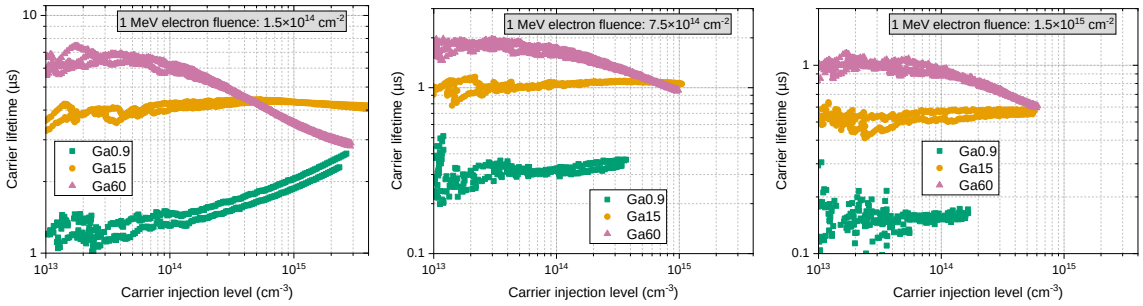


(a) (b) (c)

Figure 3.10: Carrier lifetime variations with carrier injection level on 80 $\mu m$ cell precursors for Ga0.9 (green squares), Ga15 (orange circles) and Ga60 (pink triangles) for three 1 $MeV$ electron fluences: $1.5 \times 10^{14}\ cm^{-2}$ (a), $7.5 \times 10^{14}\ cm^{-2}$ (b) and $1.5 \times 10^{15}\ cm^{-2}$ (c).

### 3.4.2 SRH modeling

Two main hypotheses could explain the different $\tau$ values and $\tau = f(\Delta n)$ dynamics obtained for the different material groups. The first one is related to an irradiation-induced defect

whose concentration would vary with the concentration of dopants/impurities (e.g., $Ga_i - O_i$ is reported in literature [122]). The second one is that the τ-limiting radiation-induced defects would introduce shallow energy levels in the c-Si band gap, with a recombination strength thus enhanced by high $p_0$. A SRH modeling with PV Lighthouse software [189] was used to investigate the nature of the τ-limiting defect in our electron irradiated samples, based on the SRH parameters of a previously identified defect (see Table 3.1). This defect was reported in the literature from T-IDLS analyses conducted on B-doped double-side passivated structures irradiated with $1 \times 10^{14}$ $cm^{-2}$ and $1 \times 10^{15}$ $cm^{-2}$ 1 $MeV$ electron fluences [127]. This technique offers the advantage to detect the defect energy level having the main impact on τ. Furthermore, its symmetry factor k—defined in Equation 1.23—can be determined. It is worth noting that a T-IDLS analysis results in two possibilities of energy levels (lower and upper halves of the band gap, see Table 3.1). When referring to past literature on irradiated c-Si, the lower half defect energy level ($\approx E_v + 0.22$ $eV$) could correspond to $V - V$, $Ga - O_i$ or $C_i - C_s$ complexes. The upper half defect energy level ($\approx E_c - 0.25$–$28$ $eV$) could correspond to $V - V$, $B_i - O_i$ or $V - O - B$ complexes [119], [126], [88] (see Table 1.2). The SRH $\tau_{n0}$ and $\tau_{p0}$ were adapted from each defect energy level $E_t$ and symmetry factor $k$ to fit the experimental Ga15 τ data irradiated at $1.5 \times 10^{15}$ $cm^{-2}$ electron fluence. Due to the low τ values obtained, the assumption that $\tau = \tau_{bulk}$ was made, thereby neglecting the impact of surface recombination as suggested previously in [127]. Surface recombination velocities (SRV) for the a-Si:H(p)/a-Si:H(i) stack were recently estimated on irradiated n-type SHJ solar cells, with a value of 576 $cm/s$ after $1 \times 10^{15}$ $cm^{-2}$ 1 $MeV$ electron fluence [100]. With Equation 1.27, this values gives $\tau_{surf} = 7$ $\mu s$. This is at least 6× higher than the measured τ for all resistivity groups at the $1.5 \times 10^{15}$ $cm^{-2}$ fluence, thus supporting the $\tau = \tau_{bulk}$ approximation.

| **Irradiation fluence** | **$1 \times 10^{14}$ cm$^{-2}$** | | **$1 \times 10^{15}$ cm$^{-2}$** | |
|---|---|---|---|---|
| | **Lower half** | **Upper half** | **Lower half** | **Upper half** |
| **Energy level (eV)** | $E_v + 0.22 \pm 0.01$ | $E_c - 0.25 \pm 0.01$ | $E_v + 0.22 \pm 0.01$ | $E_c - 0.28 \pm 0.01$ |
| **Symmetry factor k** | $2.2 \pm 0.3$ | $2.0 \pm 0.4$ | $7.3 \pm 0.2$ | $6.5 \pm 0.4$ |

Table 3.1: Values of reported main SRH recombination centers at $1 \times 10^{14}$ $cm^{-2}$ and $1 \times 10^{15}$ $cm^{-2}$ 1 $MeV$ electron fluences [127].

From this shallow defect, a strong dependence of τ on $p_0$ is observed, favoring the lowest $p_0$ values as expected (see Figure 3.11). For our measured data, interestingly, the modeling from the lower and upper half energy levels reproduces well the dynamic between Ga15 and Ga0.9. Thus, this shows that this defect could also be the τ-limiting defect in irradiated Ga-doped Cz-Si for this range of resistivity values. It suggests a complex not related to B as the recombination strength appears to be independent on the nature of the acceptor dopant, a V-V complex for instance.

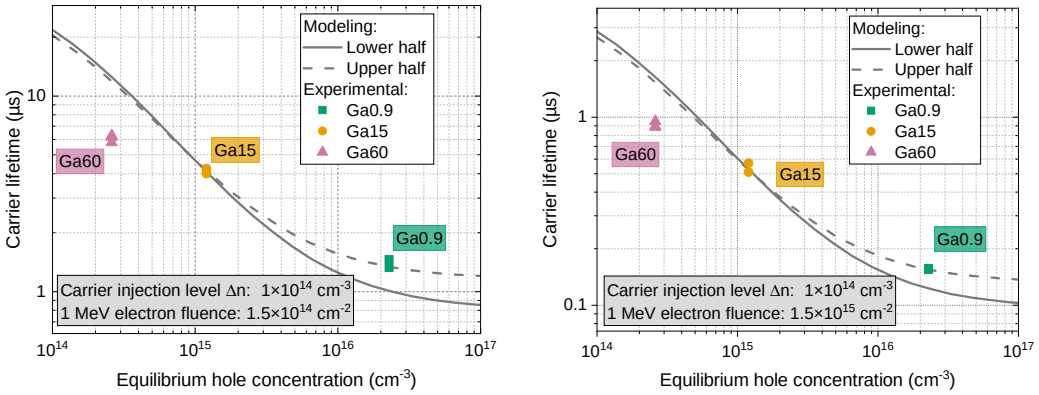


(a) (b)

Figure 3.11: Carrier lifetime variations of cell precursors at $\Delta n = 1 \times 10^{14}\ cm^{-3}$ with the equilibrium hole concentration ($p_0$) at $1.5 \times 10^{14}\ cm^{-2}$ (a) and $1.5 \times 10^{15}\ cm^{-2}$ (b) 1 $MeV$ electron fluences. Solid (band gap lower half) and dash lines (band gap upper half) correspond to SRH modeling with PV Lighthouse (see Table 3.1 for defects description) & symbols to experimental points from Ga0.9 (green squares), Ga15 (orange circles) and Ga60 (pink triangles).

A relatively good agreement between experimental data and SRH modeling of the $\tau_{bulk} = f(\Delta n)$ dynamics (see Figure 3.12) is observed for every resistivity at the two studied fluences. It confirms that the defect identified in [127] would also be the τ-limiting defect in Ga-doped c-Si wafers. The slight mismatch between the computed and experimental τ for the Ga60 sample observed on Figure 3.11 could be due to different causes. A first possibility is that there could be an additional recombination-active defect that would affect more the low $p_0$ irradiated materials since the previously discussed shallow defect is here less active. Also, the Ga60 material was significantly compensated with [TD] ($[Ga] \approx 2[TD]$) and featured strong spatial variations of its electronic properties (as presented hereafter). Both effects may induce errors in the QSS-PC measurements, which in particular resulted from an illuminated 40 $mm$ diameter area and require a precise knowledge of the carrier mobility, this last parameter featuring different values in compensated c-Si [166]. Finally, the experimental uncertainties of the T-IDLS study conducted by Khan *et al.* were not taken into account.

Interestingly, the τ dynamics of both Ga0.9 and Ga15 are reproduced by the same defect, this without changing the defect concentration, despite strong differences in $[O_i]$ and [TD] for both materials (see Figure 3.8(a)). This suggests that $O_i$ and TD are not involved in the defect that limits the τ, which further supports the V-V dominant defect hypothesis.

This study could have been completed with DLTS analysis to monitor the evolution of the defect concentrations combined with T-IDLS technique to monitor the recombination activity of the main defect with increasing fluence. This would have been particularly interesting with the range of $[O_i]$ used in this study. Here, [TD] seems to only have an impact on τ due to their impact on $p_0$.

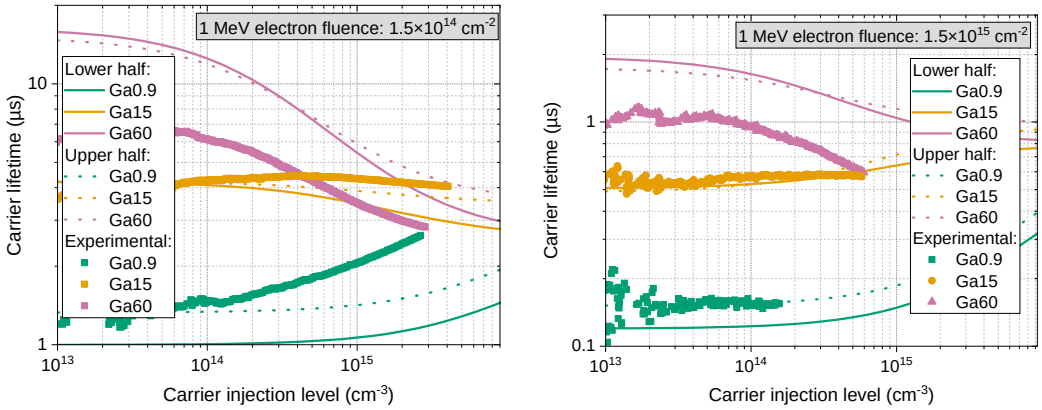


(a) (b)

Figure 3.12: Carrier lifetime variations of cell precursors with the carrier injection level at $1.5 \times 10^{14}$ $cm^{-2}$ (a) and $1.5 \times 10^{15}$ $cm^{-2}$ (b) 1 $MeV$ electron fluences. Solid (band gap lower half) and dot lines (band gap upper half) correspond to SRH modeling with PVLighthouse (see Table 3.1 for defects description) adapted to each resistivity group & symbols to experimental points from Ga0.9 (green squares), Ga15 (orange circles) and Ga60 (pink triangles).

### 3.4.3 Influence of dopant atom on carrier lifetime

As previously demonstrated, Ga-doped c-Si is less sensitive to carrier removal compared to B-doped c-Si. Therefore, the focus here is on examining the EOL $\tau$ parameter in B-doped c-Si vs Ga-doped c-Si. B-doped cell precursors were also irradiated with the same conditions. As mentioned in the experimental section, the surface structure of these B-doped precursors differs a little since they feature a stack of intrinsic/n-type a-Si:H on both surfaces of the wafer, as described in Chapter 2. If this symmetric structure can induce a slight change of the BOL $\tau$, the impact disappears for the low EOL $\tau$ values. These precursors have the same $4.5 \times 4.5$ $cm^2$ surface but are a bit thicker, with 95 $\mu m$ thickness. The $\tau$ results at $\Delta n = 1 \times 10^{14}$ $cm^{-3}$ are displayed in Figure 3.13 along with the $\tau$ obtained for Ga-doped irradiated precursors already displayed in Section 3.4.1. Despite the stronger $\tau$ obtained at BOL for Ga0.9 (256 $\mu s$) than for B1 (131 $\mu s$), the B1 precursors resulted in slightly higher EOL $\tau$. At $7.5 \times 10^{14}$ $cm^{-2}$ electron fluence, the Ga0.9 group results in $\tau = 0.3$ $\mu s$ when the B1 group results in $\tau = 0.4$ $\mu s$, i.e. values 25% higher for B1 than Ga0.9 group. This result is rather contradictory with previous studies on 1 $MeV$ electron irradiated solar cells that showed higher $K_L$ (homojunction cells) [133] and more recently higher efficiency for Ga-doped solar cells (SHJ cells) [27]. In this study, the resulting EOL $\tau$ difference appears to be more $p_0$ dependent ($p_0$ being slightly lower for B1) than a function of the dopant atom nature.

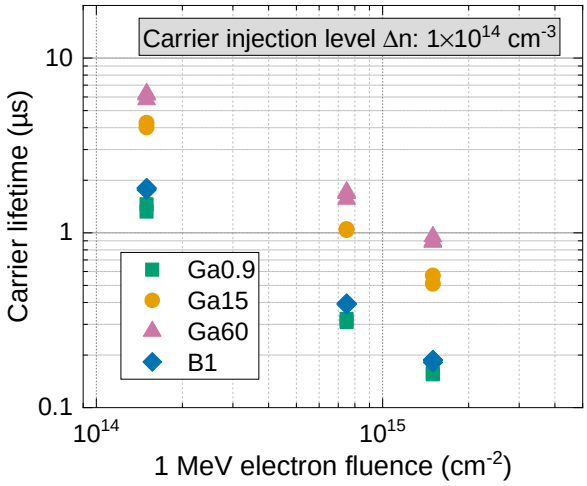


Figure 3.13: Carrier lifetime variations with increasing electron fluence on 80 $\mu m$ cell precursors for Ga0.9 (green squares), Ga15 (orange circles), Ga60 (pink triangles), and 95 $\mu m$ B1 surface-passivated samples (blue diamonds).

The $\tau = f(\Delta n)$ curves for B1 are displayed in Figure 3.14 after irradiation at two electron fluences—$1.5 \times 10^{14}$ $cm^{-2}$ (3.14(a)) and $1.5 \times 10^{15}$ $cm^{-2}$ (3.14(b))—along with Ga groups results and modeling work. In the case of B1 group, the $\tau$ also increases with increasing $\Delta n$ as it was the case for the Ga0.9 group for both fluences. However, this increase is sharper for B1 group than the modeled curve and Ga0.9 group. Therefore, Ga0.9 results in similar or slightly higher $\tau$ at low level of injection (LLI) conditions, i.e. conditions corresponding to $J_{SC}$ parameter.

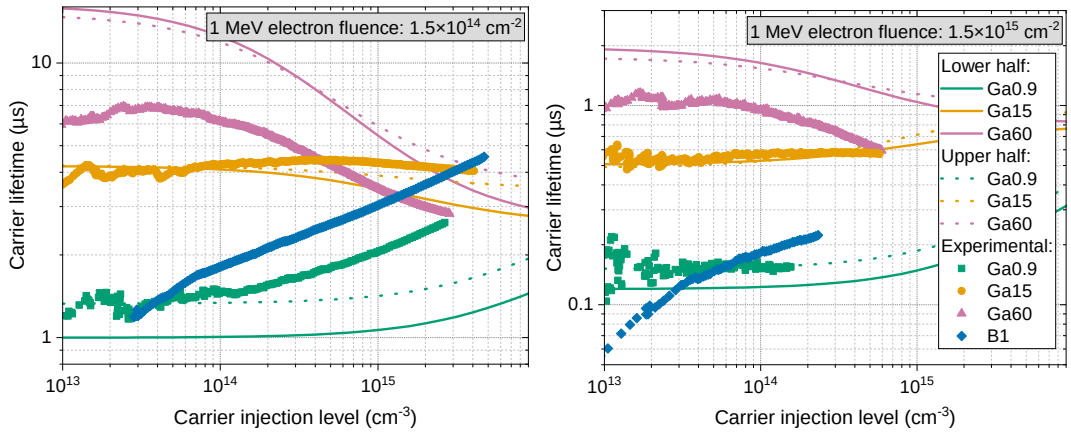


(a) (b)

Figure 3.14: Carrier lifetime variations $\Delta n$ of surface-passivated samples at $1.5 \times 10^{14}$ $cm^{-2}$ (a) and $1.5 \times 10^{15}$ $cm^{-2}$ (b) 1 $MeV$ electron fluences. Solid (lower half) and dash lines (upper half) correspond to SRH modeling with PV Lighthouse (see [127] for defects description) & symbols to experimental points from Ga0.9 (green squares), Ga15 (orange circles), Ga60 (pink triangles), and B1 (blue diamonds).

## 3.5 Performance of the Ga-doped solar cells

The variations of the I-V parameters of every solar cell irradiated in this study by 1 $MeV$ electron with fluences up to $1.5 \times 10^{15}$ $cm^{-2}$ are shown in Figure 3.15.

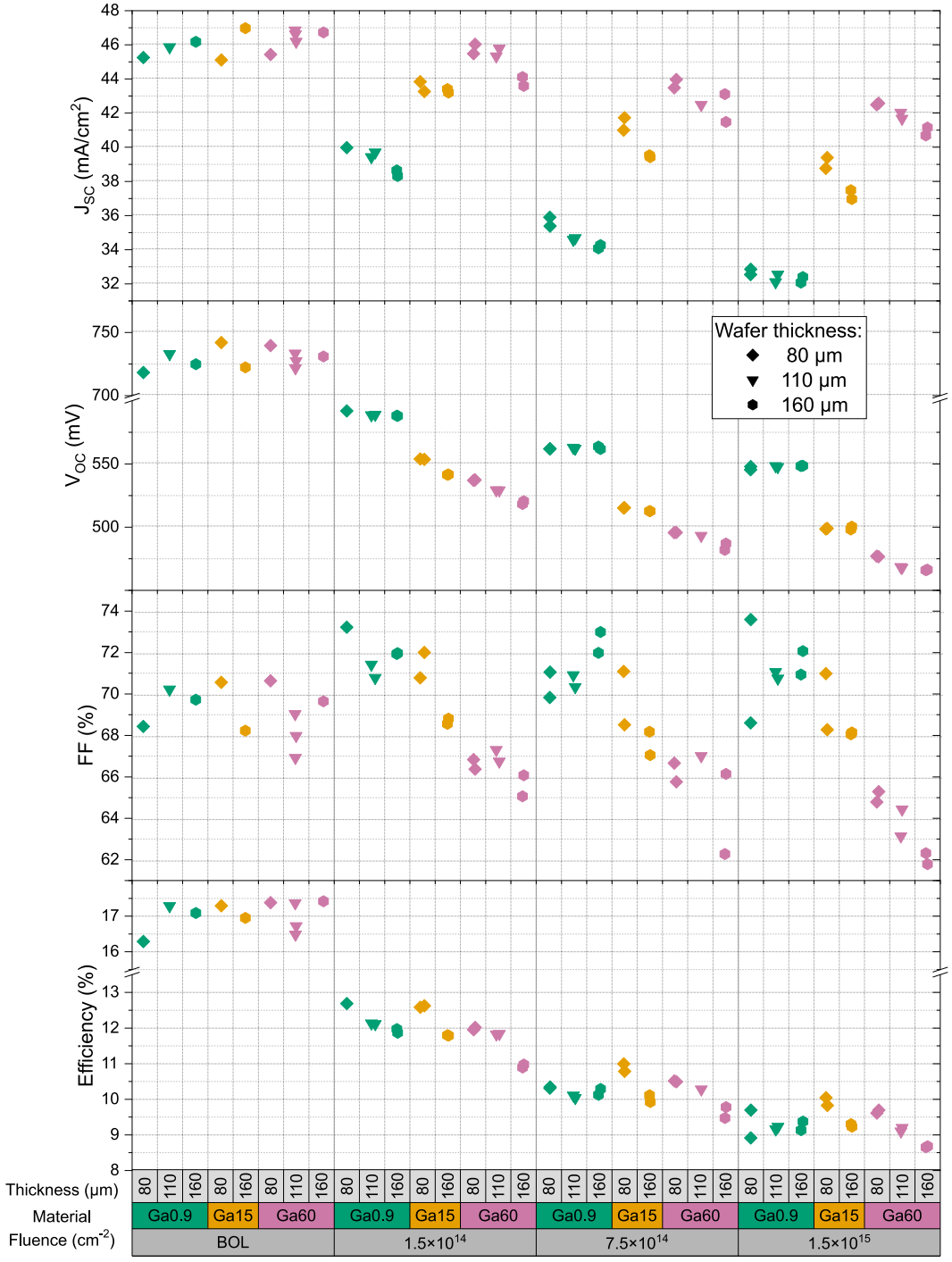


Figure 3.15: BOL and EOL AM0 I-V measurements of SHJ solar cells ($3.0 \times 3.2$ $cm^2$) for 3 different thicknesses: 80 $\mu m$ (diamonds), 110 $\mu m$ (down triangles) and 160 $\mu m$ (hexagons); and three wafer resistivity values: 0.9 $\Omega.cm$ (green), 15 $\Omega.cm$ (orange) and 60 $\Omega.cm$ (pink). From top to bottom: $J_{SC}$, $V_{OC}$, $FF$ & Efficiency.

Overall, all the cells feature strong degradation regardless of the resistivity or the thickness. Some of the most interesting trends will be detailed in the following.

### 3.5.1 $J_{SC}$ and electron diffusion length

The EQE spectral variations, directly related to $J_{SC}$ (see Equation 1.38), result in a significant decrease of the EQE values after irradiation (see Figure 3.16). Indeed, the collection efficiency dropped for wavelengths above $\approx 600\ nm$, as a result to low EOL $\tau_{bulk}$. However, the collection efficiency of the shorter wavelengths remains unchanged after irradiation, suggesting in particular that the front optical properties are not degraded.

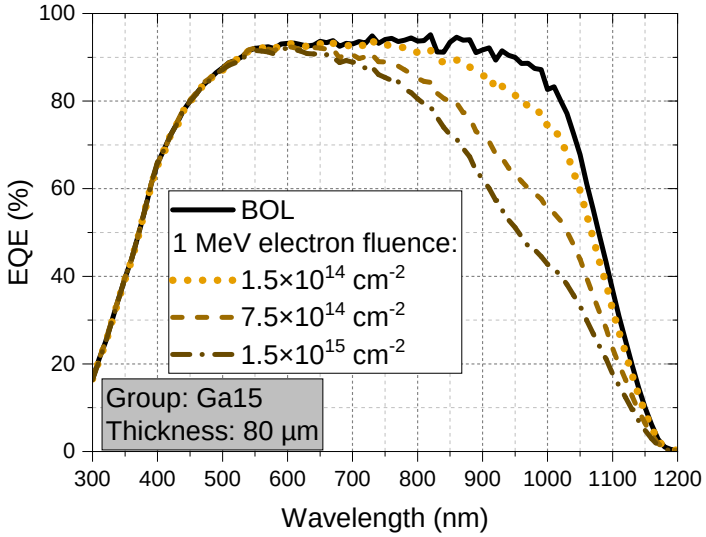


Figure 3.16: EQE measurements of Ga15 solar cells with 80 $\mu m$ thickness under BOL (solid line) and EOL conditions for 3 different 1 $MeV$ electron fluences: $1.5 \times 10^{14}\ cm^{-2}$ (dot line), $7.5 \times 10^{14}\ cm^{-2}$ (dash line) and $1.5 \times 10^{14}\ cm^{-2}$ (dot dash line).

When looking closer at EOL $J_{SC}$ performances, the highest resistivity values (i.e. lowest $p_0$) lead to the highest radiation hardness for this parameter (see Figure 3.17(a)), owing to the higher $\tau$ obtained (see Figure 3.9). Similarly to the $\tau$ results at low $\Delta n$ ($\leq 1 \times 10^{14}\ cm^{-3}$), the gap of $J_{SC}$ between Ga60 and the other two resistivity values is increasing with increasing fluence with a relative difference for Ga15 going from 1.2% at $1.5 \times 10^{14}\ cm^{-2}$ fluence to 9.0% at $1.5 \times 10^{15}\ cm^{-2}$ fluence. Figure 3.17(b) shows, for 160 $\mu m$-thick cells, the influence of the material group on the spectral variation of the EQE at an electron fluence of $1.5 \times 10^{15}\ cm^{-2}$. The EQE response decreases strongly with decreasing resistivity, in good correlation with the $J_{SC}$ results obtained by I-V measurements. The wavelength at which the collection efficiency drops is dependent on the resistivity: $\lambda > 550\ nm$ for Ga0.9, $\lambda > 600\ nm$ for Ga15, and $\lambda > 650\ nm$ for Ga60. This phenomenon is amplified for the lowest resistivity values because of the lower $\tau_{bulk}$ values in such wafers. Indeed, for such low $\tau_{bulk}$ values, the minority carriers photogenerated from the wavelengths absorbed deep in the bulk recombine before reaching the front junction.

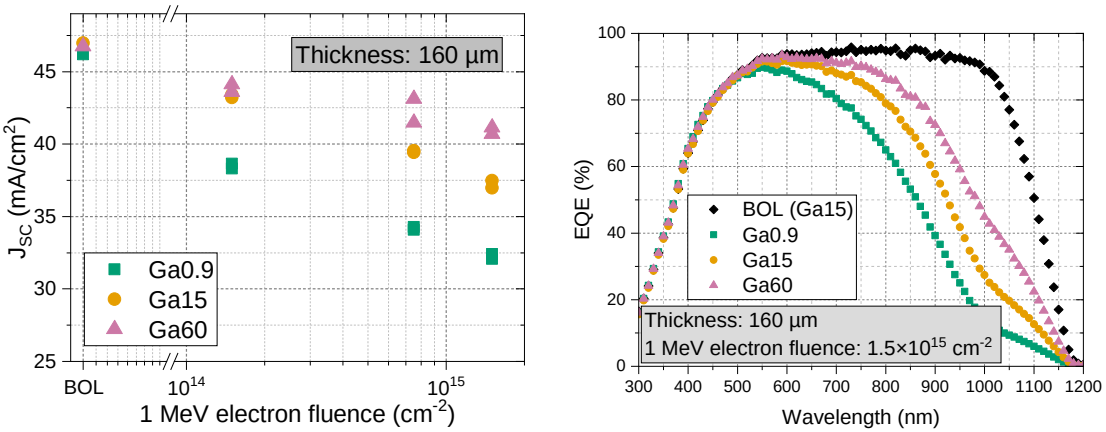


(a) (b)

Figure 3.17: (a) BOL and EOL $J_{SC}$ results of $3.0 \times 3.2\ cm^2$ 160 $\mu m$ SHJ solar cells under AM0 spectrum for Ga0.9 (green squares), Ga15 (orange circles), and Ga60 (pink triangles) materials. (b) EQE spectral variations of the same solar cells subjected to $1.5 \times 10^{15}\ cm^{-2}$ electron irradiation.

A loss in spectral response after irradiation due to increased reflectance was ruled out with spectrophotometer measurements as shown in Figure 3.18. Indeed, measurements of the spectral variation of the reflectance of both BOL and $1.5 \times 10^{15}$ 1 $MeV$ electron fluence irradiation conditions on Ga0.9 160 $\mu m$ solar cells resulted in the same reflectance values, even for long wavelengths.

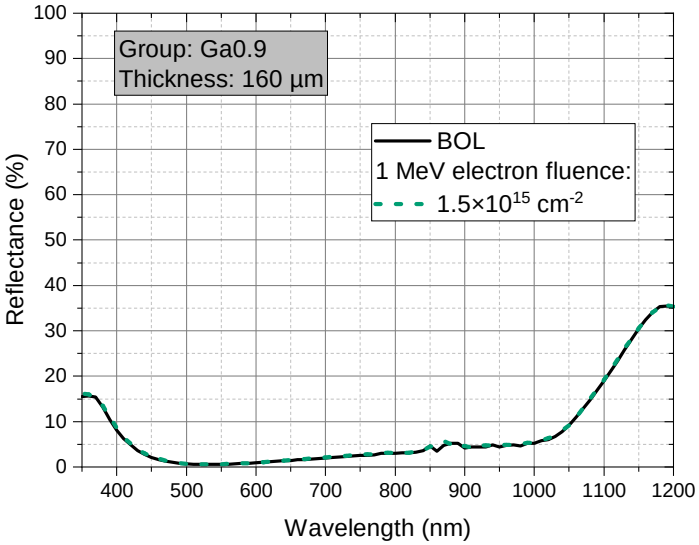


Figure 3.18: Comparison of spectral reflectance curve of Ga0.9 160 $\mu m$ cell precursors between BOL (black line) and $1.5 \times 10^{15}\ cm^{-2}$ 1 $MeV$ electron fluence (green dash line) conditions.

Figure 3.19 shows the influence of the wafer thickness on the EQE spectral variations for two 1 $MeV$ electron fluences—$1.5 \times 10^{14}\ cm^{-2}$, and $1.5 \times 10^{15}\ cm^{-2}$—for both Ga0.9 cells (Figures 3.19(a) and 3.19(b)) and Ga60 cells (Figures 3.19(c) and 3.19(d)). A discontinuity

is observed at ≈ 1000 $nm$, with higher values for the 80 $\mu m$ cells in comparison to 160 $\mu m$ cells in this region (see Figure 3.19). This wavelength corresponds to an absorption depth of about 150 $\mu m$ in c-Si (see Figure 1.3). This could be the result of the backside reflection of the photons by which the longer wavelengths are absorbed closer to the junction in the 80 $\mu m$ case, thus allowing to reach better EOL performances when thinning the solar cells.

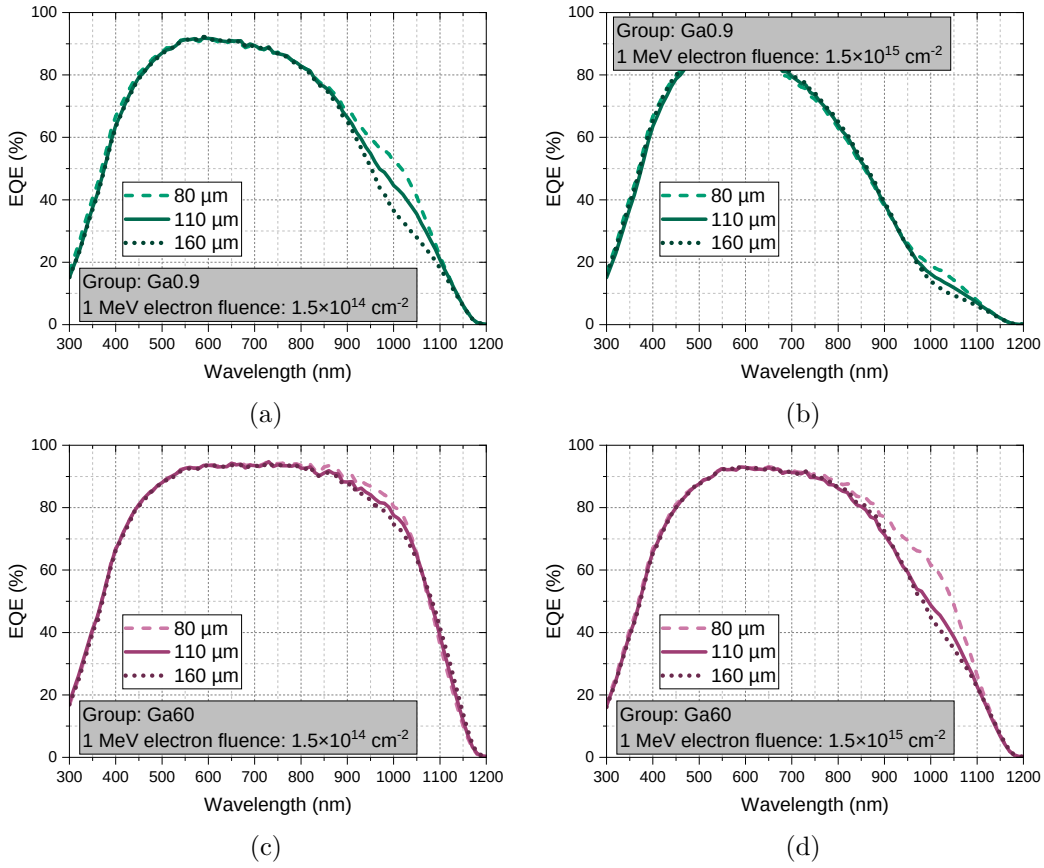


Figure 3.19: Comparison of the effect of the solar cells thicknesses—80 $\mu m$ (dash line), 110 $\mu m$ (solid line), and 160 $\mu m$ (dot line)—after 1 $MeV$ electron irradiation at $1.5 \times 10^{14}$ $cm^{-2}$ (a), (c) and $1.5 \times 10^{15}$ $cm^{-2}$ (b), (d) fluences.

The $J_{SC}$ strongly depends on $L_n$, especially when the $L_n$ values are lower than the thickness of the c-Si substrate. $L_n$ was defined earlier in Equation 1.29 and is a function of the electron diffusivity $D_n$ and $\tau$ (here $\tau_{bulk}$). The $L_n$ experimental results (see Figure 3.20(a)) were obtained from LBIC mapping measurements on 160 $\mu m$ solar cells; the values presented here refer to the average of the 3 $cm$ diameter circular mapping values of one solar cell for each condition. The in-plane standard deviation—indicated with error bars—are therefore computed from the mapping values within one same solar cell. As expected, the solar cells also undergo strong degradation of $L_n$ with values of 16 $\mu m$ for Ga0.9 and 86 $\mu m$ for Ga60 for the highest fluence ($1.5 \times 10^{15}$ $cm^{-2}$), therefore in good agreement with the $\tau$ data previously discussed.

With $L_n$ values 4× below the thickness of the thinner cells for Ga0.9 for the highest fluence tested, the effect of the backside reflection, expected to favor the lower thicknesses after

electron irradiation, becomes relatively small. When looking at the impact of the thickness on EOL $J_{SC}$ for Ga0.9, we find a relative increase of $\approx 4\%$ of the $J_{SC}$ for the 80 $\mu m$ solar cells in comparison to the 160 $\mu m$ solar cells at both $1.5 \times 10^{14}$ $cm^{-2}$ and $7.5 \times 10^{14}$ $cm^{-2}$ fluences when it is reduced to 1.4% at $1.5 \times 10^{15}$ $cm^{-2}$ fluence (see Figure 3.20(b)). It suggests that almost no advantage in $J_{SC}$ remains for the thinner cells (80 $\mu m$) in comparison with the thicker cells (160 $\mu m$) when exposed to the highest electron fluence tested here ($1.5 \times 10^{15}$ $cm^{-2}$). Therefore, the thinning of the solar cells under high fluences appears less relevant for Ga0.9, this without considering mass saving benefits. This is well illustrated in the spectral response of Ga0.9 solar cells irradiated at $1.5 \times 10^{14}$ $cm^{-2}$ (see Figure 3.19(a)) and $1.5 \times 10^{15}$ $cm^{-2}$ (see Figure 3.19(b)) 1 $MeV$ electron fluences, for which $L_n$ is equal to 69 $\mu m$ and 16 $\mu m$, respectively. The advantage towards thinner cells is more noteworthy in the lowest fluence tested. However, in the case of Ga60 solar cells, thinning the cells proves to be more beneficial after $1.5 \times 10^{15}$ $cm^{-2}$ fluence (see Figure 3.19(d)) than after $1.5 \times 10^{14}$ $cm^{-2}$ fluence (see Figure 3.19(c)), for which $L_n$ is equal to 86 $\mu m$ and 470 $\mu m$, respectively. Therefore, the advantage of thinning the cells between 160 $\mu m$ and 80 $\mu m$ seems particularly efficient when $L_n \approx 80$ $\mu m$, i.e. the thickness of the solar cell.

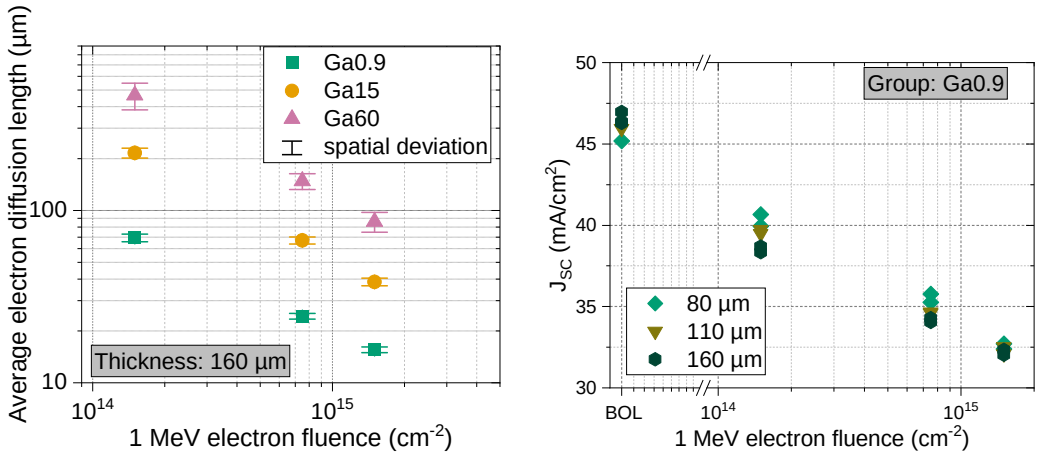


Figure 3.20: (Left) Electron diffusion length (averaged from LBIC mappings) variations with increasing electron fluence on $3.0 \times 3.2$ $cm^2$ 160 $\mu m$ SHJ solar cells for Ga0.9 (green squares), Ga15 (orange circles), and Ga60 (pink triangles) materials. The error bars refer to spatial standard deviation calculated for each cell. (Right) BOL and EOL $J_{SC}$ results of $3.0 \times 3.2$ $cm^2$ Ga0.9 SHJ solar cells under AM0 spectrum for 80 $\mu m$ (diamonds), 110 $\mu m$ (down triangles), and 160 $\mu m$ (hexagons) thicknesses.

### 3.5.2 In-plane electron diffusion length variations

Figure 3.21 shows the $L_n$ mappings of Ga0.9, Ga15, and Ga60 solar cells irradiated at a $1.5 \times 10^{15}$ $cm^{-2}$ 1 $MeV$ fluence. One can notice clear lines showing slightly higher $L_n$ values (highlighted by black frames) for Ga0.9 and Ga15 cells. This could be due to an irregular irradiation pattern due to the scanning electron beam mode, thereby resulting in a zone exposed to slightly lower fluences. For instance, the minimum measured $L_n$ value for Ga0.9

(14 $\mu m$) is increased locally by a maximum of 3 $\mu m$ due to the irregular irradiation pattern. This feature is detailed hereafter (see Figure 3.23). Nonetheless, these variations are negligible in comparison to the $L_n$ spatial variations for Ga60. Indeed, $L_n$ values vary from 60 $\mu m$ to about 125 $\mu m$. A strong spatial deviation of 13% is thus observed for the Ga60 solar cells with clear ring-like structures. Those structures could be associated to the presence of TDs (here formed during ingot cooling), as pointed out in [178].

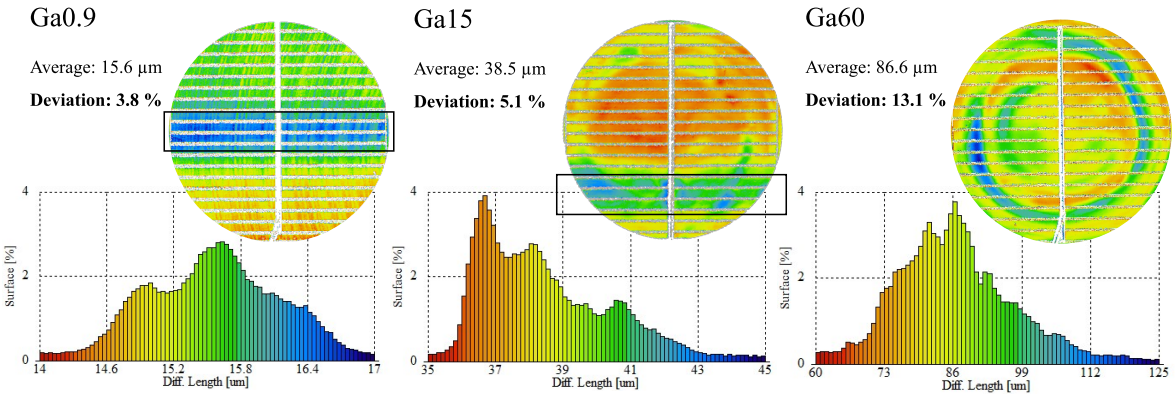


Figure 3.21: Electron diffusion length mappings (3 $cm$ diameter circular surface) on the center of $3.0 \times 3.2$ $cm^2$ 160 $\mu m$ SHJ solar cells irradiated at a $1.5 \times 10^{15}$ $cm^{-2}$ 1 $MeV$ fluence. The color scale differs on each map.

To understand the origin of the ring-like structure observed on the EOL Ga60 solar cells, we assumed again the hypothesis stating that one single shallow defect would be responsible of the EOL $\tau$ values, and thus EOL $L_n$ values. From $p_0$ determined on the diagonal axis of *sister* wafers (with the OxyMap technique aforementioned), the $L_n$ values were computed. The method was the same as previously described, through SRH recombination via the band gap lower half energy level identified in [127] (see Figure 3.22). Low $\Delta n$ ($1 \times 10^{10}$ $cm^{-3}$) were specified as LBIC measurements are conducted in short-circuit conditions. We observe a good correlation on the average $L_n$ between computed and experimental values (see Figure 3.22). The slight disagreement for Ga15 could be explained by the fact that there were disparities (see Section 3.2) between the wafers for this batch. The trend in $L_n$ spatial deviations shows the highest computed deviations with the highest resistivity as obtained with LBIC measurements. However, the computed spatial deviation values are at least twice lower than the experimental values. For Ga0.9 and Ga15, this could be due to the areas less irradiated, which were not taken into account in this modeling. For Ga60, this could be linked to the low number of points of the $p_0$ experimental measurement (10 $mm$ spacing between acquisition points); while the LBIC mapping had a resolution of 62.5 $\mu m$ and that the ring-like structures could be 3 $mm$ wide. In addition and as mentioned previously, the involvement of another defect for the Ga60 cells, which feature the highest $\tau$ values, cannot be ruled out. Overall, it thus appears that the $p_0$ plays an important role regarding both the degradation and the spatial distribution of $\tau$ and $L_n$ in the studied samples.

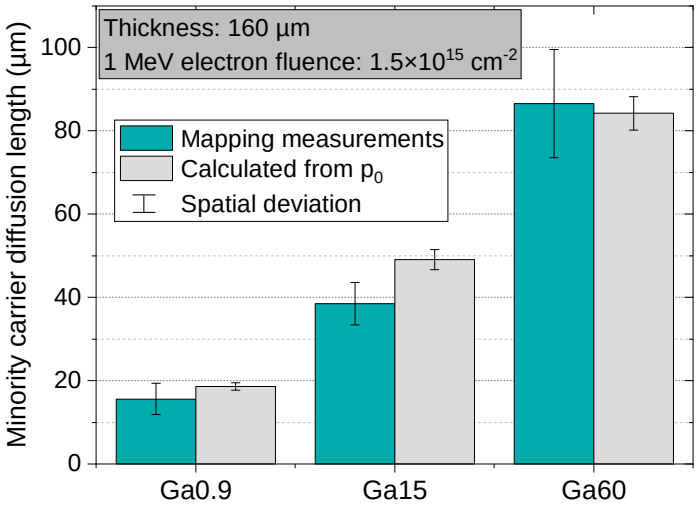


Figure 3.22: Comparison between experimental (from LBIC, in blue/green) and calculated (SRH modeling from $p_0$ determined from OxyMap technique, see Chapter 2, on M2 wafers, in grey) values of the electron diffusion length. The average values and spatial standard deviations were calculated from wafer diagonal scans.

**Scanning pattern of electron irradiation and its impact on $L_n$**

As mentioned previously, it was observed that the solar cells irradiated with electron beams presented non-uniform fluences especially at interfaces between beam scanning lines. As described in Chapter 2, the samples were scanned line by line using an electron beam of an approximately 2.5 $cm$ width and less radiation-induced degradation were observed between each scan line on the samples. These gaps appeared as brighter areas in PL imaging and were more precisely characterized by the $L_n$ mappings. These $L_n$ mappings show a 5 $mm$ to 9 $mm$ wide region, in-between two scanning lines, with longer $L_n$.

Evaluating the influence of these less damaged regions on electron-irradiated samples presented in this chapter (see Figure 3.21) was challenging due to the small sample size and strong heterogeneities in $L_n$. The $L_n$ heterogeneities were indeed strongly affected by the initial $p_0$ variations, which in turn were mainly driven by [TD] variations, particularly when combined with low τ, as previously discussed. However, an opportunity arose to test solar cells with 2 $\Omega.cm$ resistivity (Ga2) and half M2 dimensions. These cells exhibited low $[O_i]$ and [TD] levels, making them undetectable by the OxyMap technique. This enabled a more accurate assessment of $L_n$ heterogeneities that were primarily due to the scanning pattern of the electron beam, rather than variations in $p_0$. Further details on this cell structure can be found there and in Table 2.1. Their key characteristics include a 110 $\mu m$ thickness, and a SiN coating on top of a thin ITO.

The $L_n$ mapping of one of these solar cells that was irradiated at a $7.5 \times 10^{14}$ $cm^{-2}$ 1 $MeV$ electron fluence is shown in Figure 3.23. The scanning pattern is clearly visible, with wide green bands representing regions that received the full electron fluence, and narrower blue bands indicating the gaps where the fluence was reduced. It is worth noting that, for this sample, the scanning pattern coincides with the gap between the busbars (26 $mm$); however,

this is merely a coincidence.

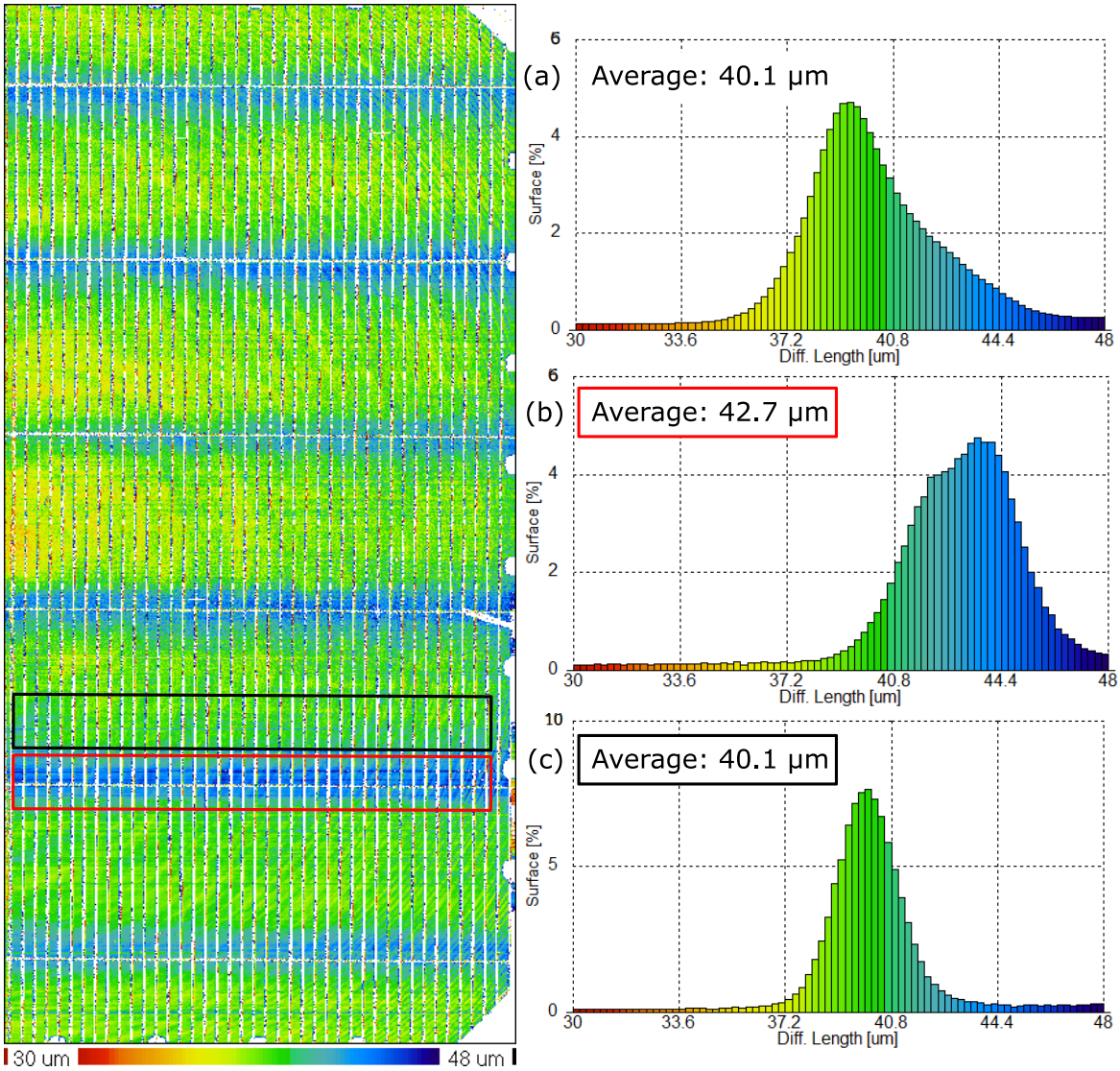


Figure 3.23: $L_n$ mappings of half M2 surface Ga2 110 $\mu m$ SHJ solar cells irradiated at a $7.5 \times 10^{14}$ $cm^{-2}$ electron fluence. Distribution of $L_n$ values is shown representing (a) the whole cell surface, (b) the red region representing a gap between scanning lines, and (c) the black region representing a scanning line.

The average $L_n$ values of the two regions identified with red and black frames, each 7.6 $mm$ wide were compared. The red region (b) corresponds to a gap slightly less electron irradiated, while the black region (c) corresponds to a fully irradiated scanning line. A relative difference on $L_n$ of 6.5% was found between the two regions, with the red region having a higher $L_n$ value (42.7 $\mu m$) compared to the black region (40.1 $\mu m$). Interestingly, the average $L_n$ value across the entire cell surface was the same as the average $L_n$ in the black region. This suggests that the higher $L_n$ values in the less irradiated gaps may be offset by the lower $L_n$ values at the center of the cell (orange color).

### 3.5.3 $V_{OC}$

The $V_{OC}$ decreased strongly after irradiation, in particular with values lower than 550 $mV$ after irradiation of Ga60 group solar cells with a $1.5 \times 10^{14}$ $cm^{-2}$ electron fluence. This degradation is essentially due to strong $\tau$ decreases, itself mainly due to $\tau_{bulk}$ degradation as aforementioned. Thus, only the degradation of the c-Si bulk properties will be considered in the following analysis. Regarding the influence of the resistivity on the electrical performances, the $J_{SC}$ is less deteriorated with electron degradation when increasing the resistivity (i.e. lowering $p_0$). However, an opposite trend is observed for the $V_{OC}$ (see Figures 3.15 and 3.24). The Ga0.9 group results in more than 10% relative difference higher EOL $V_{OC}$ in comparison to the Ga60 group.

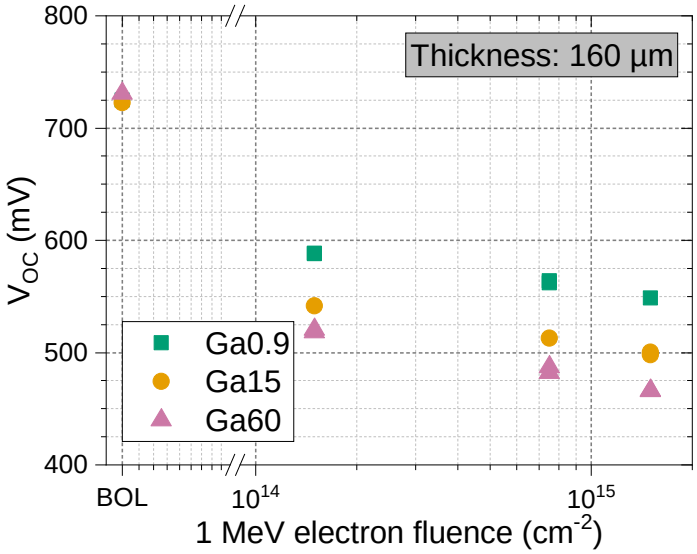


Figure 3.24: BOL and EOL $V_{OC}$ results of $3.0 \times 3.2$ $cm^2$ 160 $\mu m$ SHJ solar cells under AM0 spectrum for Ga0.9, Ga15, and Ga60 materials.

$V_{OC}$ can be approximated by Equation 1.35 ($V_{OC} = \frac{k_B T}{q} \ln\left(\frac{\Delta n(p_0+\Delta n)}{{n_i}^2} + 1\right)$), which depends on the $\Delta n$ and the $p_0$. A basic modeling of a p-type 160 $\mu m$-thick front-emitter homojunction solar cell introduced in Chapter 2 was conducted with the PC1D software. The simulations were made for both BOL and EOL (at a $1.5 \times 10^{15}$ $cm^{-2}$ 1 $MeV$ electron fluence) conditions, from which the bulk $\Delta n$ values corresponding to $V_{OC}$ conditions were extracted (red circles in Figure 3.25). The solar cell model is detailed in Chapter 2. The illumination is made by 1 Sun AM0 spectrum. For the BOL case, the SRH-recombination parametrization is: middle gap defect, and $\tau_{n0} = \tau_{p_0} = 1000$ $\mu s$. For the EOL case, the SRH-recombination parametrization of the bulk is varied, based on our own $\tau$ experimental values and the SRH signature of the lower energy level defect identified by Khan *et al.* [127]. The results show that with the low EOL $\tau$ values, the $\Delta n$ parameter also becomes low, decreasing from $> 4 \times 10^{15}$ $cm^{-3}$ at BOL to $< 8 \times 10^{13}$ $cm^{-3}$ at EOL, thereby reaching values significantly lower than $p_0$ values, e.g. $p_0 = 2.6 \times 10^{14}$ $cm^{-3}$ for Ga60. Thus, at one specific fluence, the $p_0$ parameter becomes the leading factor for the $V_{OC}$ between each resistivity

group at EOL: the higher the $p_0$, the higher the $V_{OC}$. This is in good agreement with the experimental results.

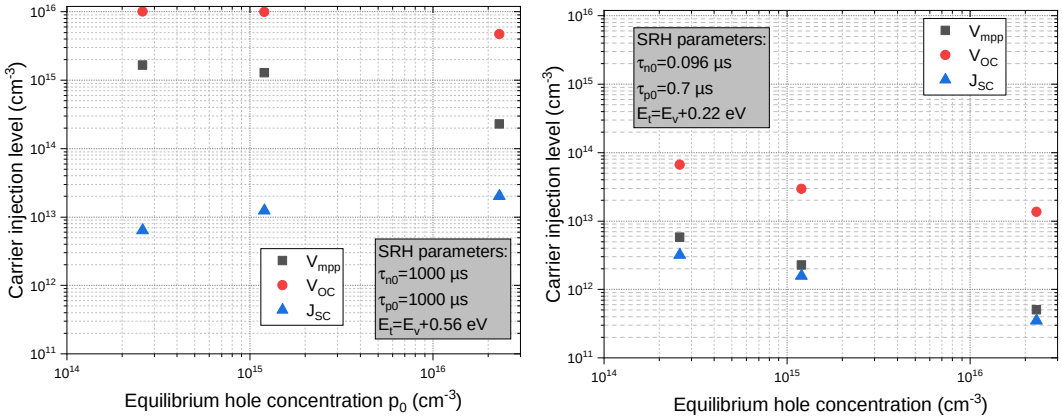


(a) (b)

Figure 3.25: PC1D modeling of a p-type 160 $\mu m$-thick front-emitter homojunction solar cell, as introduced in Chapter 2. The bulk $\Delta n$ values correspond to the maximum voltage power point $V_{mpp}$ (black square), the $V_{OC}$ (red circle), and the $J_{SC}$ (blue triangle) conditions. The modeling was done for both BOL (a) and at $1.5 \times 10^{15}$ $cm^{-2}$ fluence (b), the latter referring to the lower energy level defect identified by Khan *et al.* [127]. The $\Delta n$ was calculated for the $p_0$ of the three material groups: Ga60 ($p_0 = 2.6 \times 10^{14}$ $cm^{-3}$), Ga15 ($p_0 = 1.2 \times 10^{15}$ $cm^{-3}$), and Ga0.9 ($p_0 = 2.3 \times 10^{16}$ $cm^{-3}$).

### 3.5.4 Fill factor

The $FF$ results obtained for all electron-irradiated solar cells are shown in Figure 3.15. The $FF$ significant decreases only for the Ga60 solar cells. However, even for these Ga60 cells, the degradation remains limited in comparison with the other PV parameters, with the $FF$ decreasing by less than 10% in absolute value. The remaining factor (RF) for the $FF$ of Ga60 solar cells with a thickness of 160 $\mu m$, irradiated at a fluence of $1.5 \times 10^{15}$ $cm^{-2}$ electrons, is 0.9, while the RF for $V_{OC}$ under the same fluence is 0.6. Therefore, although the FF reduction is not negligible, it is not the dominant factor contributing to the EOL efficiency degradation. This stands in contrast with a study recently made on 2.6 $\Omega.cm$ p-type SHJ cells with a front emitter (10.2% BOL AM0 efficiency) irradiated with 15 $MeV$ and 16 $MeV$ protons, leading to homogeneous degradation in the bulk. In this study, the $FF$ was the primary contributor to efficiency losses [28]. The authors attributed this degradation to a decrease of $R_{sh}$, which could be related to the appearance and accumulation of point defects through the junction, in addition to an increase of $R_s$.

This part is thus aimed at understanding this $FF$ degradation only present for the highest resistivity solar cells. When looking at the pseudo-FF ($pFF$) measured with the Suns-$V_{OC}$ technique (Figure 3.26), one can observe that this parameter is not degraded even under the highest fluence tested, meaning that the EOL $FF$ is strongly affected by an increase of $R_s$, and not by a potential decrease of $R_{sh}$.

$R_s$ depends, among other factors, on the bulk resistivity. In order to provide insights into the $R_s$ decrease, the bulk resistivity under illumination at BOL and after exposure to an electron fluence of $1.5 \times 10^{15}$ $cm^{-2}$ was determined. The bulk $\Delta n$ values corresponding to the maximum power point condition (at $V_{mpp}$) were extracted (see black squares in Figure 3.25). From the $\Delta n$ and $p_0$ values, the c-Si bulk resistivity $\rho$ was computed from the inverse of the bulk conductivity $\sigma$ under illumination, defined by Equation 1.9 as $\sigma = q\,(\Delta n(\mu_n + \mu_p) + p_0\mu_p + n_0\mu_n)$, $mu_p$ and $\mu_n$ being set fixed. The computed results show that, from BOL to EOL, the c-Si bulk resistivity remains largely unchanged for the Ga0.9 cells. In contrast, for the Ga15 and Ga60 cells, the resistivity increases by factors of 5.1 and 24, respectively. Under illumination, the EOL $\sigma$ for each group—Ga0.9, Ga15, and Ga60—is primarily determined by $p_0$ due to low $\Delta n$, which favors the Ga0.9 cells. For the Ga0.9 cells, no significant change in $\sigma$ occurs since their BOL conductivity is already dominated by the high $p_0$. However, the BOL conductivity of the Ga60 cells was initially driven mostly by $\Delta n$, leading to a substantial change in conductivity between BOL and EOL conditions. As $R_s$ is thickness dependent, it also explains why the loss in $FF$ appears slightly stronger for the highest thicknesses at $1.5 \times 10^{15}$ $cm^{-2}$ fluence.

This confirms once again that $p_0$ has a strong influence on the EOL performances when low $\Delta n$ resulting from low $\tau$ are involved.

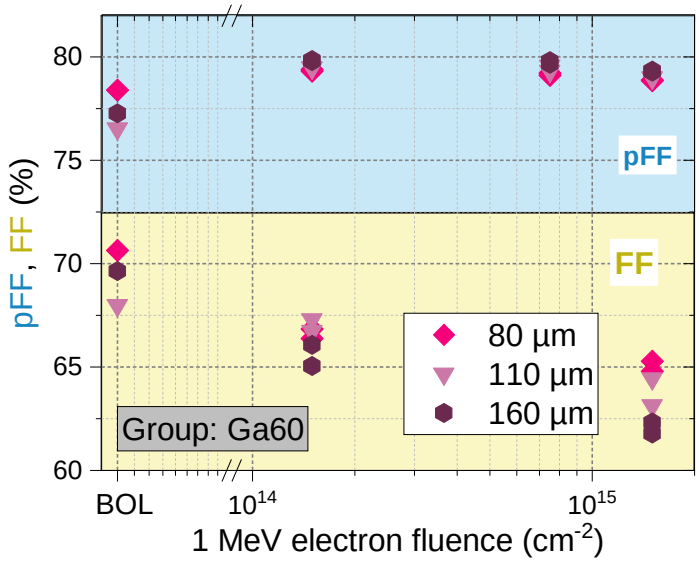


Figure 3.26: Comparison of $FF$ (lower part in yellow) and pFF (upper part in blue) for Ga60 solar cells between 80 $\mu m$ (diamonds), 110 $\mu m$ (down triangles), and 160 $\mu m$ (hexagons) thicknesses.

Ma *et al.* showed in a simulation study that the irradiation-induced increase in $R_s$ for lightly doped substrates depends on the solar cell architecture [143]. In particular, a more pronounced decline in the $FF$ was observed in PERC cells compared to p-TOPCon cells. This behavior was attributed to the fact that, in PERC structures, majority carriers must travel not only vertically but also laterally to reach the rear metal contact, leading to an increased sensitivity to resistive losses. However, this mechanism is specific to PERC architectures and is therefore not expected to be relevant for SHJ cells.

Therefore, the $FF$ was found to decrease significantly after irradiation only for low $p_0$ wafers. This $FF$ decrease should not be neglected and it is suggested that when using low $p_0$ wafers, cell structures that are compatible with high bulk resistivity values should be used.

### 3.5.5 Resulting efficiency

To summarize, on the one hand the $p_0$ has a direct impact on EOL $\tau$, with lower $p_0$ leading to less degraded $\tau$ and therefore less degraded $J_{SC}$. On the other hand, a lower $p_0$ leads to higher degradation of both $V_{OC}$ and $FF$ (low $p_0$ cannot compensate the strong $\Delta n$ decreases due to the $\tau$ degradation). The resulting PV conversion efficiencies, displayed in Figure 3.27 for 80 $\mu m$ (see Figure 3.27(a)) and 160 $\mu m$ (see Figure 3.27(b)) solar cells, illustrate the existence of a compromise between these two opposite trends. For the 80 $\mu m$ solar cells, the best efficiencies are obtained for both Ga0.9 and Ga15 cells at the lowest fluence ($1.5 \times 10^{14}$ $cm^{-2}$). However, the Ga15 cells feature the best performances for the two highest fluences, with an increasing efficiency difference at high fluences between the Ga15 and Ga0.9 cells. This increased difference could be explained by the stronger degradation of $L_n$ for Ga0.9 in comparison with Ga15, the effect of backside reflection becoming almost negligible for Ga0.9. Regarding the 160 $\mu m$ solar cells, the Ga0.9 condition results in slightly better efficiencies for every fluence tested. This translates the loss in $FF$ which is stronger for the 160 $\mu m$ solar cells for both Ga15 and Ga60 materials. Thus, the optimum resistivity values are a function of the thickness and fluence as reported previously in [134] and [90].

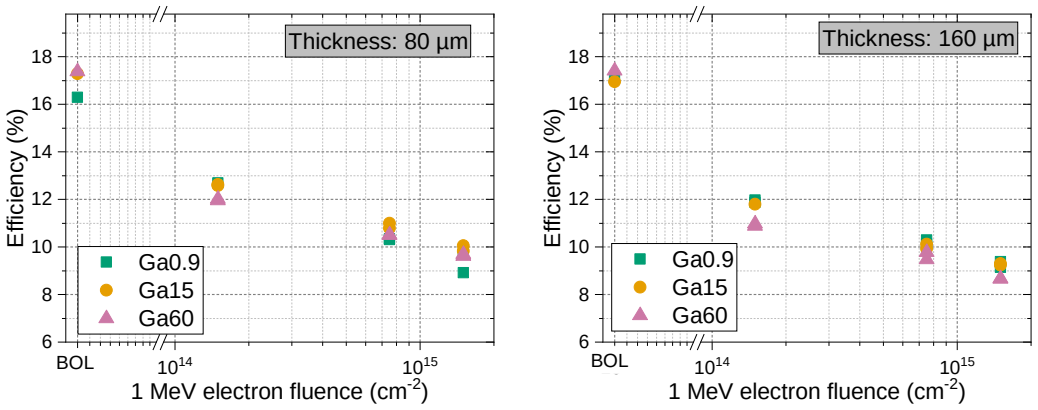


(a) (b)

Figure 3.27: BOL and EOL efficiency results of $3.0 \times 3.2$ $cm^2$ SHJ solar cells under AM0 spectrum for solar cells between Ga0.9 (green squares), Ga15 (orange circles), and Ga60 (pink triangles) materials. The solar cells thicknesses are 80 $\mu m$ (Left) and 160 $\mu m$ (Right).

Overall, for solar cells irradiated at the $1.5 \times 10^{15}$ $cm^{-2}$ fluence:

- the thickness reduction from 160 $\mu m$ to 80 $\mu m$ results in a 1% absolute increase of efficiency for Ga60.
- the best efficiency is obtained with a Ga15 80 $\mu m$ cell, with a 10.0% value. This is however less than the 12.5% efficiency obtained after $1 \times 10^{15}$ $cm^{-2}$ fluence (slightly

lower fluence) from Azurspace c-Si solar cells. [5]. This difference can come—among other factors—from the small size and high defectivity of the solar cells used in this study, not optimized metalization grids, and the low front transparency of the SHJ solar cells. It is worth noting that the solar cells produced by Azurspace, the main European manufacturer, required a high cost process, while the solar cells used in this study can be produced at large scale in a cost-effective manner.

- using Ga15 80 $\mu m$ solar cells instead of Ga0.9 160 $\mu m$ solar cells (industry standard until recently) leads to an absolute increase of [0.4–0.9]% efficiency. It is worth noting that this result corresponds to only 2 solar cells per condition and would need to be confirmed with higher quantities of irradiated solar cells.

## Conclusion

In this chapter, the resilience of modern Ga-doped SHJ solar cells to 1 $MeV$ electron irradiation was investigated, with a focus on the influence of the wafer composition and resistivity, and of the cell thickness.

The $\tau$ degradation dynamics with electron fluence were evaluated and their dependence on the material composition properties highlighted: the lower the $p_0$, the higher the EOL $\tau$ at low $\Delta n$. In addition, significant spatial variations of $L_n$ were revealed through surface mappings of the Ga60 samples most likely driven by the non-homogeneous spatial distribution of the O-related TDs (causing $p_0$ variations for this compensated material) induced by the Cz ingot manufacturing process. SRH recombination via defects previously identified in B-doped c-Si and possibly linked to divacancy complexes reproduced well those effects. The $\tau$-limiting defect density was neither dependent on the nature and concentration of the dopant nor dependent on $[O_i]$ or [TD]. The 4× higher $\tau$ at low $\Delta n$ for Ga60 wafers in comparison to the value found for Ga0.9 wafers resulted in a 12% relative difference in $J_{SC}$ in favor of Ga60. In addition, a study conducted on the influence of the dopant atom (either Ga or B) on EOL $\tau$ confirmed that the choice of dopant had few impact on EOL $\tau$. However, this study demonstrated stable $p_0$ and $\mu_p$ within the doping ranges and fluences investigated. This would confirm that Ga-doped c-Si would be less affected by carrier removal effect than B-doped c-Si. However, the benefit of a large $p_0$ for both the $V_{OC}$ and $FF$ parameters, when irradiation significantly affects $\tau$, was highlighted and subsequently explained. In particular, with low $p_0$ wafers, the irradiation-induced $FF$ degradation was essentially caused by a bulk resistivity increase.

Overall, lowering the wafer thickness benefited to the conversion efficiency, the gain being stronger for the cells with the lowest $p_0$. The mass savings yet remain a strong motivation for thin wafers whatever the material properties. For a given irradiation fluence, it is thus necessary to find the best compromise when choosing the resistivity of the samples without neglecting the impact of the wafer thickness. The best solar cell efficiency (10.0% at the $1.5 \times 10^{15}$ $cm^{-2}$ 1 $MeV$ electron fluence) was obtained for Ga15 80 $\mu m$ solar cells, and could be further increased by thinning even more the wafers. Considering the EOL efficiencies obtained and that the SHJ cells could be further optimized at BOL (e.g. with adapted metalization

grids), this study shows that the SHJ technology is relevant for space applications.

CHAPTER 4

# Proton irradiation of high resistivity SHJ cells

As introduced in Figure 1.13, each satellite mission will face specific irradiation conditions (i.e. various particles, fluences and energies). For ageing tests performed on Earth, the c-Si solar cells designed for space were commonly irradiated to 1 $MeV$ electron beams, partly because of historically easier access to this type of facility. Also, this type of mono-energetic electron beam produces homogeneous degradation throughout the c-Si substrate, which facilitates the use of the NIEL method introduced in Chapter 1. This feature is also valid for 10 $MeV$ protons, for which the projected range is about 709 $\mu m$. However, in space, c-Si solar cells are also exposed to low energy protons, with projected ranges lower than the cell thickness, during operation, for which non-uniform damages are generated in the depth of the substrate. This type of degradation involves more complex mechanisms. Therefore, this chapter aims to explore the behavior of modern SHJ solar cells under proton irradiation with energies of 1 $MeV$ and 3 $MeV$. For these two proton energies, equivalent fluences beyond those corresponding to standard missions were applied to trigger and investigate drastic failure modes.

To illustrate the heterogeneous degradation throughout the c-Si cell thickness, the projected ranges of these two proton energies were evaluated with SRIM and TRIM softwares [94]. This evaluation resulted in a depth of 16.3 $\mu m$ for 1 $MeV$ protons, and a depth of 92.1 $\mu m$ for 3 $MeV$ protons. The number of vacancies produced by 99,999 $H^+$ ions impinging the c-Si surface (by taking into account those produced per ions and per recoils) in 160 $\mu m$-thick c-Si was calculated with TRIM software. The resulting numbers of vacancies normalized per incident 1 $H^+$ ion are displayed in Figure 4.1. From these data, it is clear that the 10 $MeV$ protons create homogeneous degradation in the bulk whereas 1 $MeV$ and 3 $MeV$ protons induce high Bragg peaks with almost no vacancies created deeper than 20 $\mu m$, and 100 $\mu m$, respectively. It is worth noting that in the damaged bulk, higher amounts of vacancies are created for the lowest energies.

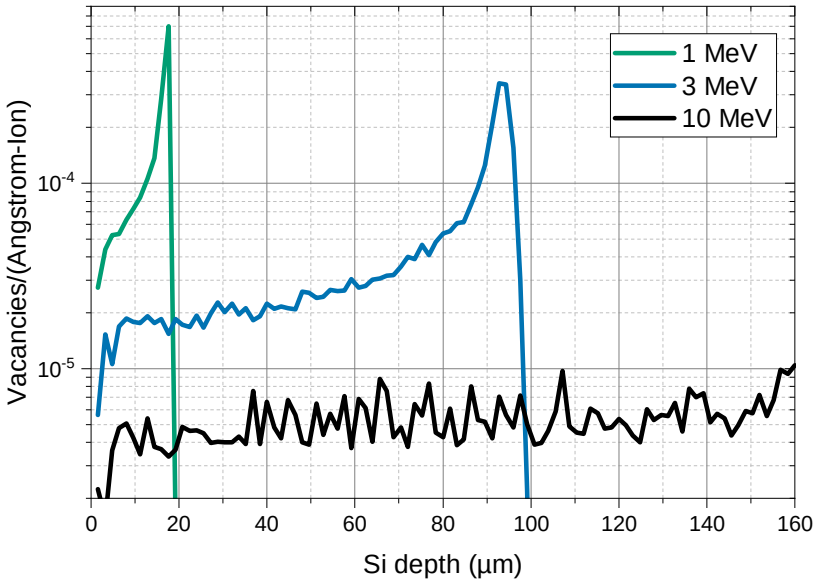


Figure 4.1: Vacancies produced per incident $H^+$ ion in a 160 $\mu m$-thick c-Si wafer for 1 $MeV$ energy, 3 $MeV$ energy and 10 $MeV$ energy.

Among the literature on the proton irradiation of c-Si solar cells, a few studies tackle the influence of the proton energy on the photovoltaic performances of the irradiated devices. Two of them highlighted maximum conversion efficiency degradations when the solar cells are irradiated by intermediate proton energies ($1.5 - 2.3\ MeV$). More precisely, the effect of proton irradiation on the performances of $2 - 10\ \Omega.cm$ p-type front emitter homojunction solar cells was studied by Tada *et al.* in 1982 [114]. Later on, in 2009, Ferrara reported investigations on 1 $\Omega.cm$ p-type front emitter (without intrinsic layer) SHJ solar cells under proton beam with different energies [190]. In the first study, the relative damage coefficients (RDC)—normalization of the degradation of a parameter for each proton energy to another at a specific fluence—are determined within a $[0.1; 100]\ MeV$ energy range (see Figure 1.20). 1.5 $MeV$ and 2.3 $MeV$ protons were found to induce the highest degradation on $J_{SC}$ and $V_{OC}$, respectively. In the second study, I-V curves for a $2 \times 10^{11}\ cm^{-2}$ fluence were measured for 4 proton energies: 0.8 $MeV$, 1 $MeV$, 1.7 $MeV$, and 4 $MeV$. 1.7 $MeV$ protons are found to produce the highest degradation on both $J_{SC}$ and $V_{OC}$ parameters.

When examining specifically 1 $MeV$ and 3 $MeV$ energies that are investigated in this chapter, two groups [114], [107] found more $J_{SC}$ degradation at 1 $MeV$ energy. Particularly, Yamaguchi *et al.* led a study on high-fluence proton ($1 \times 10^{11} - 2 \times 10^{14}\ cm^{-2}$) irradiation effects of $7 - 14\ \Omega.cm$ front-emitter B-doped c-Si homojunction 50 $\mu m$-thick solar cells. They found both a higher decrease rate of the equilibrium hole concentration $p_0$ via carrier removal effect and a higher decrease rate of the electron diffusion length $L_n$ with 1 $MeV$ protons, in comparison with 3 $MeV$ protons [107]. These effects are quantified through both the carrier removal rate $R_c$ and the $L_n$ damage coefficient $K_L$, defined in Section 1.2. For 3 $MeV$ proton irradiated solar cells, $R_c = 50 - 100\ cm^{-1}$ was obtained via capacitance-voltage (C-V) and $J_{SC}$ measurements. For 1 $MeV$ proton irradiated solar cells, $R_c = 500\ cm^{-1}$ was obtained via $J_{SC}$ measurements. $K_L$ was determined in both cases from $J_{SC}$ measurements, resulting in

$K_L = 5 \times 10^{-7}$ for 3 $MeV$ proton proton irradiated solar cells and $K_L = 1 \times 10^{-6}$ for 1 $MeV$ irradiated solar cells. It is worth noting that higher values correspond to higher damage rates. Additionally, they demonstrated that cell failure ($J_{SC} \approx 0\ mA/cm^2$) occurred at high fluences, at $\approx 1 \times 10^{13}\ cm^{-2}$ for 1 $MeV$ proton energy and $\approx 1 \times 10^{14}\ cm^{-2}$ for 3 $MeV$ proton energy. This effect was attributed to a conductivity type inversion in the bulk following a strong carrier removal effect.

The features of different p-type front emitter solar cells structures irradiated at a range of $5 \times 10^{10} - 5 \times 10^{12}\ cm^{-2}$ 1.7 $MeV$ proton fluences were also investigated in 2004-2009 by Neitzert *et al.* [191], [144] and Ferrara [190]. They compared homojunction cells with different variations of SHJ structures [191], including with or without intrinsic layers [144]. Overall, they found that the predominant degradation mechanism for all studied devices was attributed to $L_n$ decrease in the p-type substrate.

Owing to the use of higher-purity materials and recent developments in SHJ architectures, this work aims to clarify the degradation mechanisms and dynamics involved in proton-irradiated modern Ga-doped SHJ solar cells. 60 $\Omega.cm$ (Ga60) 160 $\mu m$-thick SHJ cells were chosen for this study. Indeed, no significant reduction of $p_0$ and high $\tau$ resilience were found for these high resistivity Ga60 solar cells irradiated to a $1.5 \times 10^{14} - 1.5 \times 10^{15}\ cm^{-2}$ 1 $MeV$ electron fluence range (see Chapter 3). This was particularly of interest as the behavior under proton irradiation of solar cells with this resistivity range was not well covered in literature.

These 60 $\Omega.cm$ SHJ cells were characterized under BOL and EOL conditions. As described later in this chapter, pronounced decreases in $J_{SC}$ were observed after certain proton irradiation; this motivated an investigation into the potential contribution of carrier removal effects, in combination with reductions in $\tau$, to these losses. To this end, a modeling analysis based on spectral response measurements was performed. This analysis accounts for the influence of bias light, the impact of carrier removal effects, and variations in in-plane bulk electronic properties. The study was further complemented by direct experimental evidence of carrier removal effects.

## 4.1 Experimental methods

In this study, the Ga60 solar cells used are from the same batch as the one used in Chapter 3. The composition properties of Ga60 wafers were evaluated in Chapter 3 and resulted in $[TD] = 1.9 \times 10^{14}\ cm^{-3}$, and $[Ga] = 6.3 \times 10^{14}\ cm^{-3}$. As $[Ga] \approx 2[TD]$, Ga60 has the specific characteristics of compensated materials, notably strong in-plane $p_0$ variations of $[2.3; 3.0] \times 10^{14}\ cm^{-3}$ within one same wafer (measurements from one side to another). These $p_0$ variations follow ring-like patterns specific to the Cz-growth process. Manufactured on M2 format wafers, the studied solar cells were first cut in $3.0 \times 3.2\ cm^2$ pieces, and they were cut anew to reach $1.5 \times 1.5\ cm^2$ format in order to fit the JANNuS proton irradiation facility. As high $V_{OC}$ solar cells such as SHJ are particularly sensitive to perimeter (i.e. edge) recombination, the AM0 BOL conversion efficiency values dropped down to under 15% AM0 for these small cut cells. $J_{SC}$, $V_{OC}$, and $FF$ parameters were all impacted compared to uncut

cells. The BOL measurements of the solar cells are shown in Figure 4.2. The average values (and associated standard deviation values) for each parameter are $J_{SC} = 43.3 \pm 0.2\ mA/cm^2$, $V_{OC} = 705 \pm 6\ mV$, $FF = 65.7 \pm 0.6\%$, and PV conversion efficiency= $14.7 \pm 0.2\%$. In this experimental study, a wafer thickness of 160 $\mu m$ was chosen for several reasons, but mostly to reduce the risk of breakage. Also, such a high thickness could facilitate the extraction of the $L_n$ values from LBIC measurements. As seen in Chapter 3, this 60 $\Omega.cm$ material presents strong in-plane heterogeneities of its electronic properties, it was therefore important to also monitor for this proton irradiation investigation.

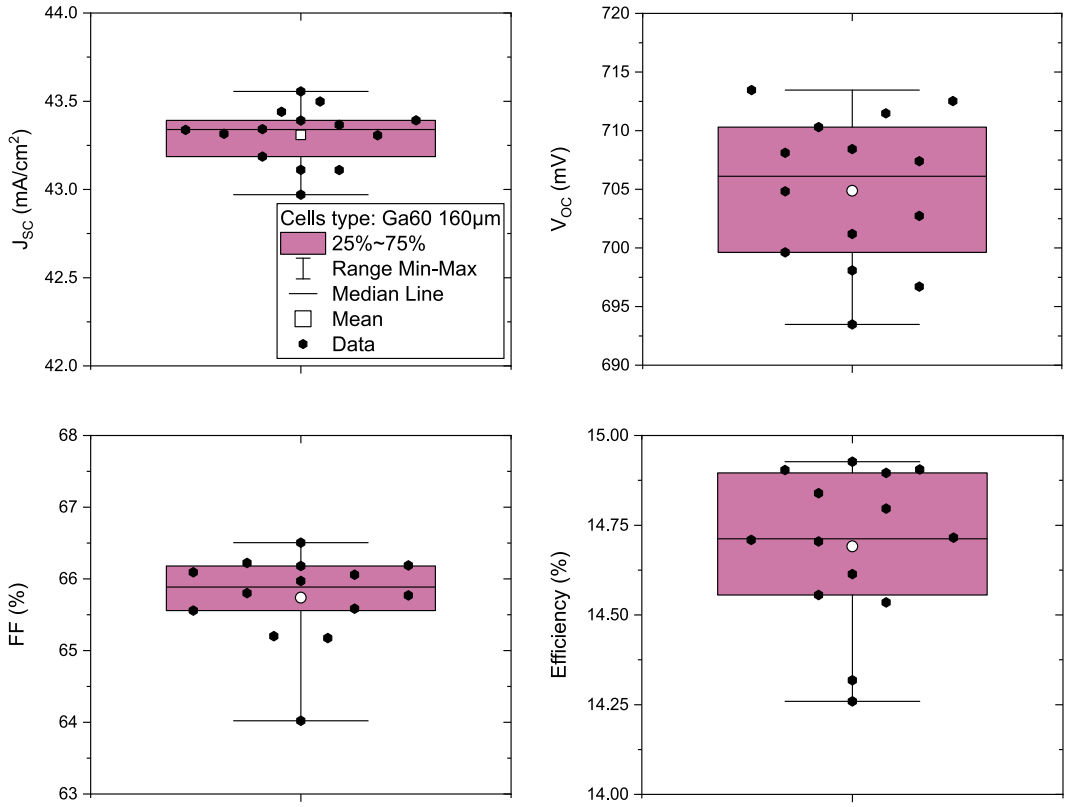


Figure 4.2: 1 Sun AM0 BOL I-V measurements of the Ga60 SHJ solar cells selected for proton irradiation.

The irradiation conditions were constrained by the chamber size and the fluence/energy range available in the JANNuS-Saclay platform. The proton energies chosen were 1 $MeV$ and 3 $MeV$, to offer comparable conditions with literature data, and the fluences chosen went from $1 \times 10^{12}\ cm^{-2}$ to $1 \times 10^{14}\ cm^{-2}$ (as shown in Table 4.1). The lowest fluence tested was at the lowest limit of the beam exposure time in this set-up (see Section 2). Two solar cells ($1.5 \times 1.5\ cm^2$) were irradiated per condition. According to Figure 1.13(a), these irradiation conditions correspond to extreme environments and can be attained mostly for high LEO orbits and long mission durations.

| Fluence tested ($cm^{-2}$) | $1 \times 10^{12}$ | $5 \times 10^{12}$ | $1 \times 10^{13}$ | $1 \times 10^{14}$ |
|---|---|---|---|---|
| 1 $MeV$ | × | × | × | |
| 3 $MeV$ | × | × | × | × |

Table 4.1: Proton irradiation conditions tested on JANNuS Japet accelerator beam (2 cells per condition).

The conducted characterizations were: I-V, Suns-$V_{OC}$, 4-point probe measurements, EQE and LBIC ($L_n$ mapping). Most of the denoted BOL measurements refer to measurements made on non-irradiated *sister* solar cells, except for I-V measurements under 1 Sun intensity, for which the same cells were used under BOL and EOL conditions. This is summarized in Table 4.2. All these measurements were carried out at room temperature (i.e. 25 °$C$).

| **Ga60 160 $\mu$m 1.5 × 1.5 cm$^2$ SHJ solar cells** | **BOL** | **EOL** |
|---|---|---|
| AM0 I-V 1 Sun | same cells as EOL | × |
| AM1.5G I-V 0.1 Sun | *sister* cells | × |
| Suns-$V_{OC}$ | *sister* cells | × |
| EQE | *sister* cells | × |
| LBIC | *sister* cells | × |
| 4-point probe sheet resistance | *sister* wafers | × |

Table 4.2: List of measurements carried out at BOL and EOL, at room temperature.

**Modeling**

The PC1D modeling approach was based on the approximation of a homojunction solar cell, with the assumption that the post-irradiation performance decreases are essentially due to changes in the bulk electronic properties (see Chapter 3). The model for BOL equivalent PC1D cell structure is detailed in Chapter 2. Considering the projected ranges associated to 1 $MeV$ and 3 $MeV$ proton energies, only the first 16 $\mu m$ and 92 $\mu m$ of the bulk, respectively, will be considered damaged in the analysis, as shown in Figure 4.3. Thus, for the modeling of the 1 $MeV$ irradiated cells, only the equilibrium carrier concentration $p_0$ (or $n_0$) in addition to the SRH parameters (defined in Section 1.1.2.1) $\tau_{p0}$, $\tau_{p0}$, and $E_t - E_i$ of the first 16 $\mu m$ of the bulk are varied. The parameters of the 144 $\mu m$-thick region below the damaged area remain the same as parameterized in Chapter 2. The same approach is applied for the 3 $MeV$ irradiated cells, this time with a 92 $\mu m$-thick damaged zone and a 68 $\mu m$-thick undamaged zone. It is worth noting that this remains a strong approximation. As illustrated in Figure 4.1, a more accurate approach would consist in defining three regions, including two damaged regions, one of which would be specific to the Bragg peak. Additionally, vacancies are still created a few $\mu m$ beyond the Bragg peak. This model nevertheless provides a good approximation for understanding and reproducing the experimental results.

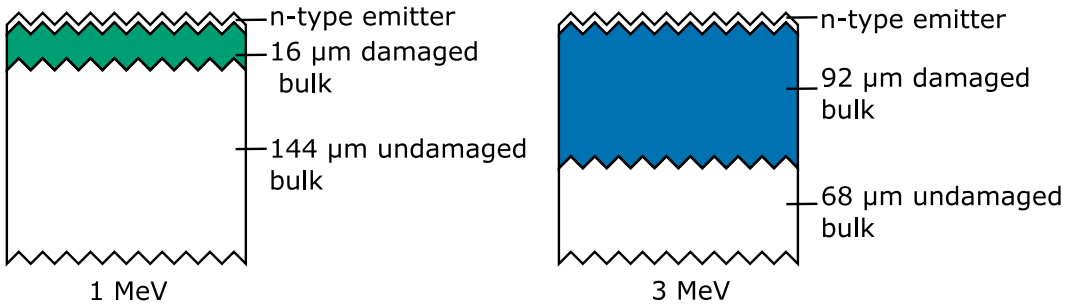


Figure 4.3: Structures of the solar cells used in PC1D modeling to understand the spectral responses after irradiation with 1 $MeV$ protons (left) and 3 $MeV$ protons (right).

## 4.2 1 Sun I-V results

This part focuses on the evolution of the PV performance with increasing proton fluence for each proton energy (1 $MeV$ and 3 $MeV$). To this end, I-V measurements under 1-Sun AM0 spectrum were performed.

Overall, the efficiency of the solar cells drops drastically already at $1 \times 10^{12}$ $cm^{-2}$ fluence with values of 4.8% for 1 $MeV$ protons and 2.1% for 3 $MeV$ protons (see Figure 4.4). This difference between the two energy conditions is also observed for higher fluences. Proton irradiation at 3 $MeV$ leads to efficiency values that are approximately a factor of two lower than those measured for 1 $MeV$ proton irradiation, this for the whole range of studied fluences. At a $1 \times 10^{13}$ $cm^{-2}$ fluence, the solar cell efficiencies drop to 1.7% and 0.68% for proton energies of 1 $MeV$ and 3 $MeV$, respectively.

The $V_{OC}$ strongly decreases between BOL and EOL with values below 500 $mV$ after $1 \times 10^{12}$ $cm^{-2}$ fluence: 448 $mV$ for 3 $MeV$ proton energy and 403 $mV$ for 1 $MeV$ proton energy. Interestingly, the $V_{OC}$ trend versus the fluence differs between the two proton energies. In the 1 $MeV$ case, the $V_{OC}$ decreases monotonically with increasing fluence, with a value of 347 $mV$ at $1 \times 10^{13}$ $cm^{-2}$ fluence. Whereas for the 3 $MeV$ case, the $V_{OC}$ slightly increases from $1 \times 10^{12}$ $cm^{-2}$ to $1 \times 10^{13}$ $cm^{-2}$ fluence, reaching 483 $mV$, before decreasing again down to 410 $mV$ at $1 \times 10^{14}$ $cm^{-2}$ fluence. The $V_{OC}$ parameter can decrease for several possible reasons, including decreases in the carrier lifetime $\tau$ and the $p_0$. However, in the 3 $MeV$ case, the $V_{OC}$ slightly increases with increasing fluence. This suggests that major—and unusual—changes occurred in the electronic properties (e.g. $p_0$ variations across the thickness).

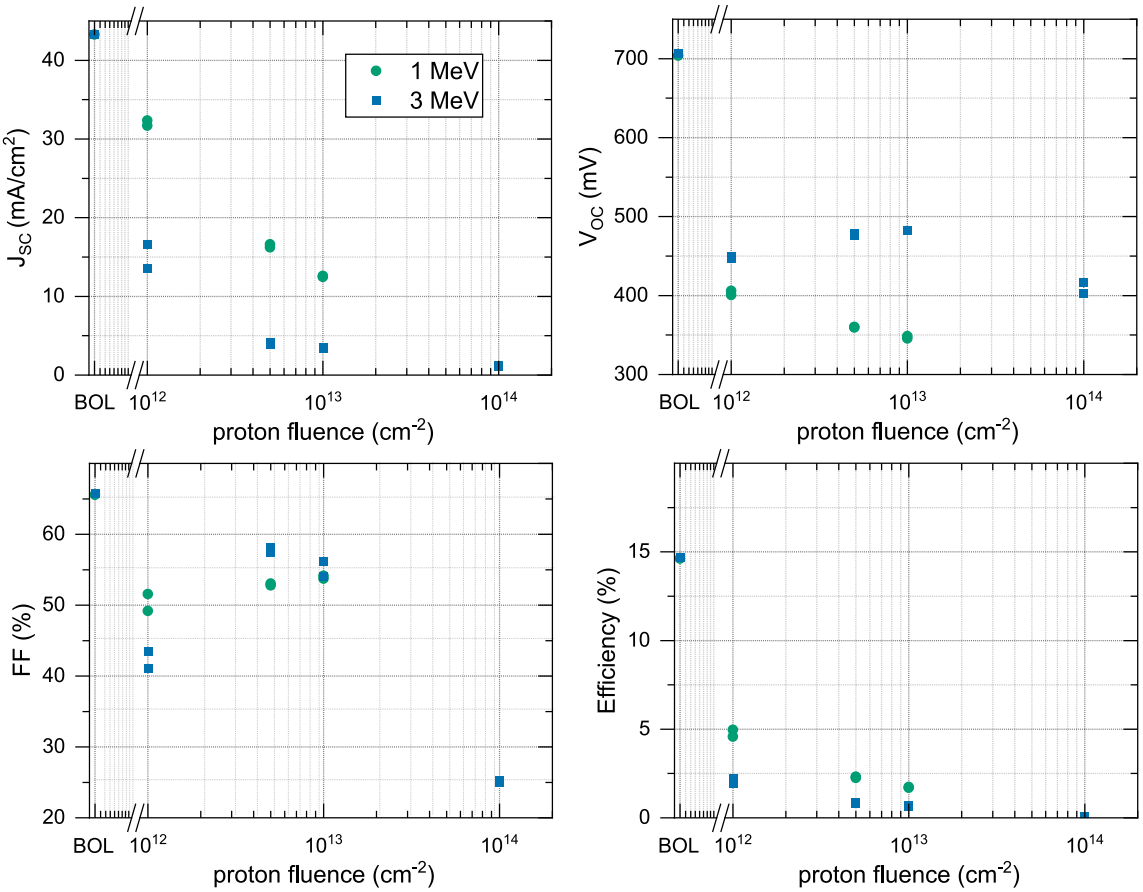


Figure 4.4: 1 Sun AM0 EOL I-V measurements for SHJ solar cells following a proton beam exposure with 1 $MeV$ (green circles) and 3 $MeV$ (blue squares) energies.

The results of the EOL $FF$ are also complex to interpret. Upon the results obtained with electron irradiation (see Section 3.5.4), the $FF$ was expected to decrease due to the strong influence of low $\tau$ on the series resistance $R_s$ in the case of low $p_0$ solar cells, as described in Chapter 3. It is indeed the case under proton irradiation with $FF$ values of 50.4% for 1 $MeV$ energy and 42.2% for 3 $MeV$ energy at a $1 \times 10^{12}$ $cm^{-2}$ fluence. Unexpectedly, both proton energies result in higher $FF$ at $5 \times 10^{12}$ $cm^{-2}$ and $1 \times 10^{13}$ $cm^{-2}$ fluences. Finally, the $FF$ dramatically decreases to 25% at a $1 \times 10^{14}$ $cm^{-2}$ 3 $MeV$ fluence. The $pFF$ measurements presented later in this section will provide further insights into this $FF$ trend.

The strong monotonic degradation of the efficiency are essentially driven by the monotonic losses in $J_{SC}$, with values already below 20 $mA/cm^2$ under 3 $MeV$ protons at $1 \times 10^{12}$ $cm^{-2}$ fluence, the lowest fluence tested. Indeed, the remaining factor (RF), defined as the ratio between EOL and BOL values, for $V_{OC}$ in the 3 $MeV$ case ranges from 0.57 to 0.70 for every fluence tested, while the RF for $J_{SC}$ is below 0.39. For the 1 $MeV$ case and for fluences $\geq 5 \times 10^{12}$ $cm^{-2}$, the $J_{SC}$ RF is $< 0.39$, thus below the $V_{OC}$ RF that ranges from 0.49 to 0.52. As expected, protons create more damage than electrons for similar energy and fluence due to their higher mass and cross section.

It is worth noting that the $J_{SC}$ suffers from twice more degradation for 3 $MeV$ protons

than for 1 $MeV$ protons at each tested fluence and is therefore at the origin of the trend between the two energies observed for the efficiency. This is in opposition with the previous literature results aforementioned [114], [107]. Notice however that one of these studies was conducted on B-doped c-Si ($7 - 17\ \Omega.cm$ resistivity) solar cells with 50 $\mu m$ thickness, which is lower than the 92 $\mu m$ projected range for the 3 $MeV$ energy protons. Therefore, these cells suffered from homogeneous degradation in the bulk after 3 $MeV$ proton irradiation [107].

The solar cells irradiated at the highest fluence with 3 $MeV$ protons (i.e. $1 \times 10^{14}\ cm^{-2}$) result in a $J_{SC}$ of $\approx 1\ mA/cm^2$, thus leading to a quasi-failure of the device. It was previously seen that a strong decrease of $\tau$ led to a decrease of $J_{SC}$ (see Chapter 3). However, the decrease is here so dramatic that it suggests a conductivity type inversion in the c-Si substrate in addition to low $\tau$, as previously observed in [108], due to a potentially high $R_c$.

The $pFF$ values obtained from Suns-$V_{OC}$ measurements (see Figure 4.5) give in particular information about the role of the $R_s$ on $FF$ losses, the higher the $R_s$, the lower the $\frac{FF}{pFF}$ ratio. The $R_s$ parameter can, among others, be influenced by the resistive losses through the emitter and the bulk of the solar cell, thus to $\tau$ ($\tau$ influencing $\Delta n$, and therefore the bulk photoconductance) and $p_0$ variations. Already at 0.8 in BOL state, the $\frac{FF}{pFF}$ ratio has a non-monotonic variation (in the $[0.8; 0.4]$ range) for both energies and for the fluences tested here. At $1 \times 10^{12}\ cm^{-2}$ and $1 \times 10^{14}\ cm^{-2}$ 3 $MeV$ proton fluences, the ratio $\frac{FF}{pFF}$ falls bellow 0.6, indicating that the $FF$ is strongly limited by $R_s$ losses. These especially high losses are probably explained by in-depth in-homogeneous electronic properties of the irradiated solar cells. For instance, it could be due to low $p_0$ regions and electrostatic barriers affecting the carrier transport. It should also be noted that contrary to the electron irradiation study, the $pFF$ decreased slightly with increasing fluence in this study. It thus highlights a possible decrease of $R_{sh}$ with fluence increase.

It was seen in Chapter 3 that a 60 $\Omega.cm$ SHJ cell with high SRH recombination featured low $FF$, attributed to high bulk resistance. Here, this effect could be amplified by lower $\tau$ values, significant local $p_0$ reductions, and even electrostatic transport barriers due to changes in the cell architecture, resulting in $FF$ as low as 40%.

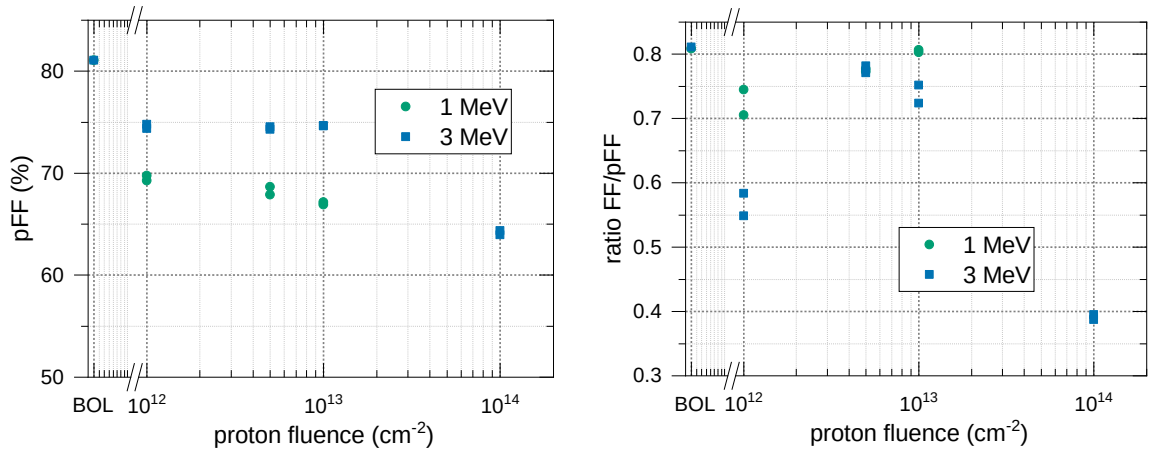


(a) (b)

Figure 4.5: (a) pFF of the solar cells irradiated with protons obtained by Suns-$V_{OC}$ measurements. (b) Ratio between the $pFF$ and $FF$ obtained by AM0 I-V measurements.

## 4.3 Spectral response analyses

As the $J_{SC}$ is the main PV parameter governing the efficiency losses due to proton irradiation, analyses of the spectral responses of the irradiated cells were conducted. These analyses aimed to provide further insights into this degradation, as well as on the differences between both 1 $MeV$ and 3 $MeV$ proton irradiations. First, the influence of the bias light during the spectral response acquisition of the irradiated solar cells is analyzed. Then, the role of the carrier removal effect on the EQE spectral dynamics is studied through modeling. Finally, the in-plane variations of the spectral response are examined.

### 4.3.1 Influence of bias light

Spectral response measurements on the electron-irradiated cells presented in Chapter 3 were conducted without bias light. It was also verified that the bias light did not affect these measurements (data not shown here).

However, the use of bias light proved necessary for thoroughly assessing the properties of solar cells irradiated with protons (setup shown in Figure 4.6). The intensity of the white bias light used is rated from 1 (lowest intensity of the setup) to 6 (highest intensity of the setup). A white bias light at level 6 was required to ensure that the $J_{SC}$ values extracted from the EQE matched the $J_{SC}$ data obtained from I–V measurements under 1 Sun illumination. The impact of bias light during EQE measurements on calculated $J_{SC}$ is shown in Figure 4.7.

It is worth noting that in one of the studies of the literature with SHJ solar cells irradiated to similar proton energies and fluences, the EQE measurements could be performed without bias light [190]. The strongest difference with our study is the 1 $\Omega.cm$ bulk resistivity of the solar cells that were used in [190] in comparison with the 60 $\Omega.cm$ bulk resistivity of the solar cells presented here. This difference highlights the peculiar behavior of the 60 $\Omega.cm$ solar cells investigated here. Interestingly, in our study, the effect of the bias light for 1 $MeV$ and

3 $MeV$ proton energies is different. Particularly, the $J_{SC}$ is increased with the use of bias light for the 1 $MeV$ case, while the $J_{SC}$ is decreased with the use of bias light for the 3 $MeV$ case. This is detailed hereafter.

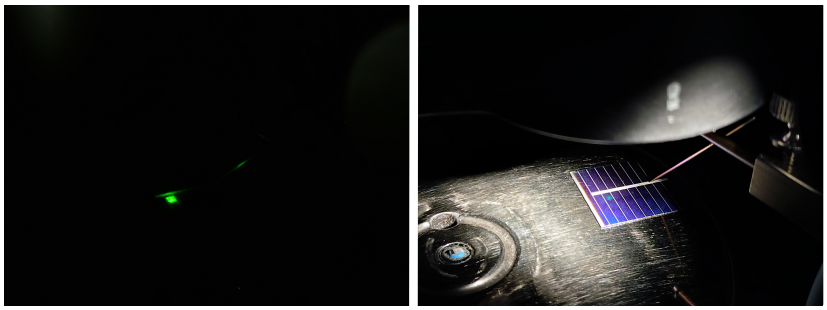

Figure 4.6: EQE setup without (left) and with (right) white bias light (level 6). The size of the monochromatic spot is $1.1 \times 1.2$ $mm^2$.

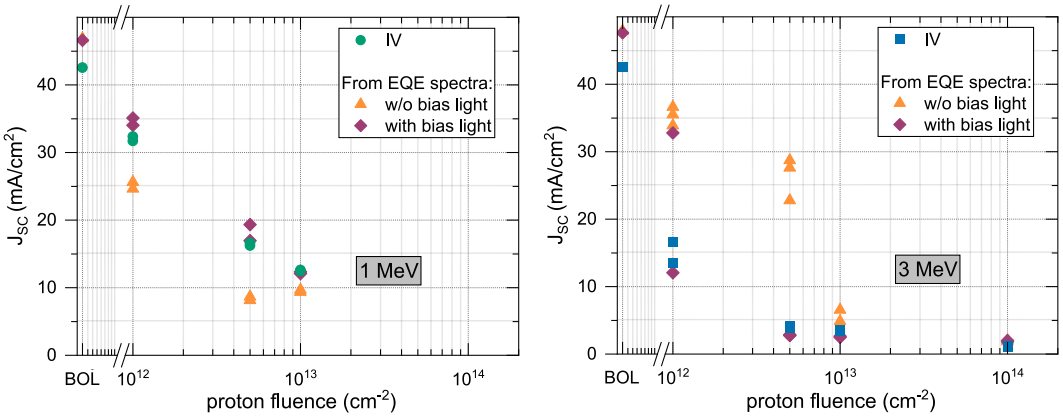


Figure 4.7: Comparison of 1 Sun AM0 $J_{SC}$ values obtained with I-V measurements (green dots for 1 $MeV$ case—left—, blue squares for 3 $MeV$ case—right—) and extracted from EQE measurements conducted without bias light (triangles) and with (level 6) white bias light (diamonds).

### 1 MeV protons

Without the use of bias light, the EOL EQE spectral responses present unusual shapes with discontinuities and result in lower $J_{SC}$ than $J_{SC}$ obtained with I-V measurements. For instance, at a $5 \times 10^{12}$ $cm^{-2}$ 1 $MeV$ proton fluence, $J_{SC} = 8.4$ $mA/cm^2$ was calculated from EQE measurements, while the I-V measurements resulted in $J_{SC} = 16$ $mA/cm^2$ for the same solar cell. Thus, the $J_{SC}$ resulting from the two measurements differ by almost a factor 2. By adding bias light, the $J_{SC}$ extracted from EQE increased to 18.1 $mA/cm^2$, thus approaching the I-V results. The impact of the bias light on the spectral response is illustrated in Figure 4.8 for two 1 $MeV$ proton fluences, $5 \times 10^{12}$ $cm^{-2}$ and $1 \times 10^{13}$ $cm^{-2}$. For each fluence, a discontinuity peak near 1000 $nm$ can be observed and corresponds to one of the Xe peaks of the EQE lamp (see Figure 2.7).

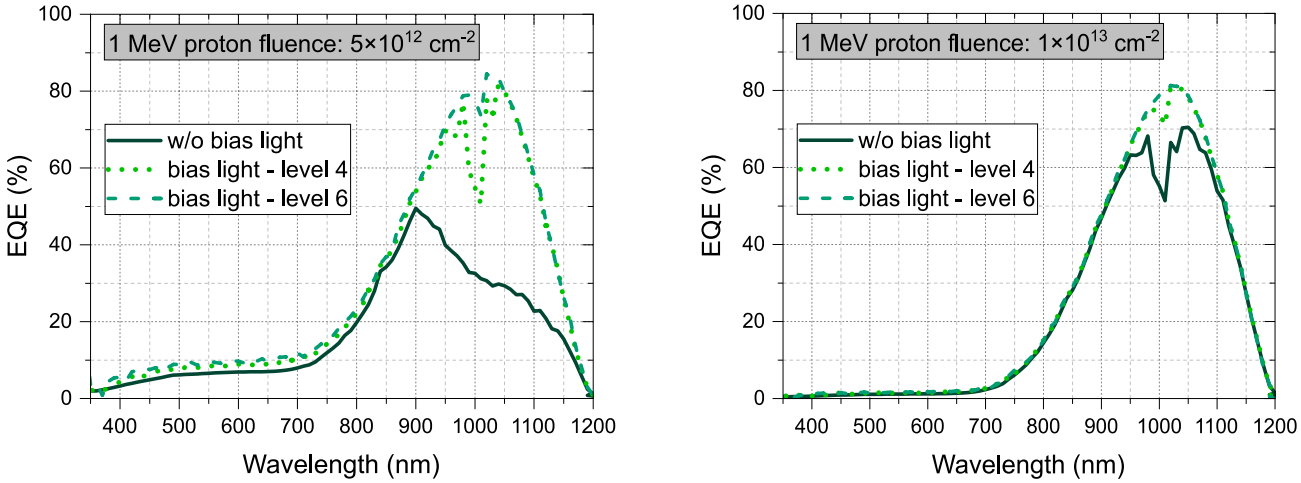


Figure 4.8: EQE spectral responses obtained on solar cells irradiated by 1 $MeV$ protons at 2 fluences: $5 \times 10^{12}$ $cm^{-2}$ (left) and $1 \times 10^{13}$ $cm^{-2}$ (right). For each case, the impact of 3 different levels of bias light are tested: no bias light (solid line), level 4 (dot line) and level 6 (dash line).

It is worth noting that these EQE variations are reversible as we found the initial low values again by doing a measurement without bias light right after. Thus, B-O LID or LeTID defects (introduced in Chapter 1) could be ruled out of the hypotheses.

**3 MeV protons**

On the contrary, in the 3 $MeV$ proton case, the EQE response results, without bias light, in a relatively higher $J_{SC}$ than the $J_{SC}$ obtained with I-V measurements. For instance, at a $5 \times 10^{12}$ $cm^{-2}$ fluence, $J_{SC} = 26$ $mA/cm^2$ was calculated from EQE measurements without bias light, whereas the I-V measurements resulted in $J_{SC} = 4.1$ $mA/cm^2$. The difference between both $J_{SC}$ values is significant (factor 6). Once again, the $J_{SC}$ extracted from EQE with bias light is closer to the I-V results with a value of 2.8 $mA/cm^2$ at the same $5 \times 10^{12}$ $cm^{-2}$ fluence. The strong influence of the bias light is illustrated in Figure 4.9 (upper right) with the EQE spectral variations obtained for several bias light levels. For the lowest fluences, the bias light level used can completely change the spectral dynamic of the EQE (with either short or long wavelengths mainly collected). This effect will be thoroughly investigated in Section 4.3.2. In the same way as the 1 $MeV$ case, this bias light dependence was found to be completely reversible.

Similarly to the 1 $MeV$ case, the discontinuity peaks correspond to those of the Xe EQE lamp, near 500 $nm$, 830 $nm$, 900 $nm$ (e.g. at $5 \times 10^{12}$ $cm^{-2}$ fluence) and 1000 $nm$ (at $1 \times 10^{14}$ $cm^{-2}$ fluence).

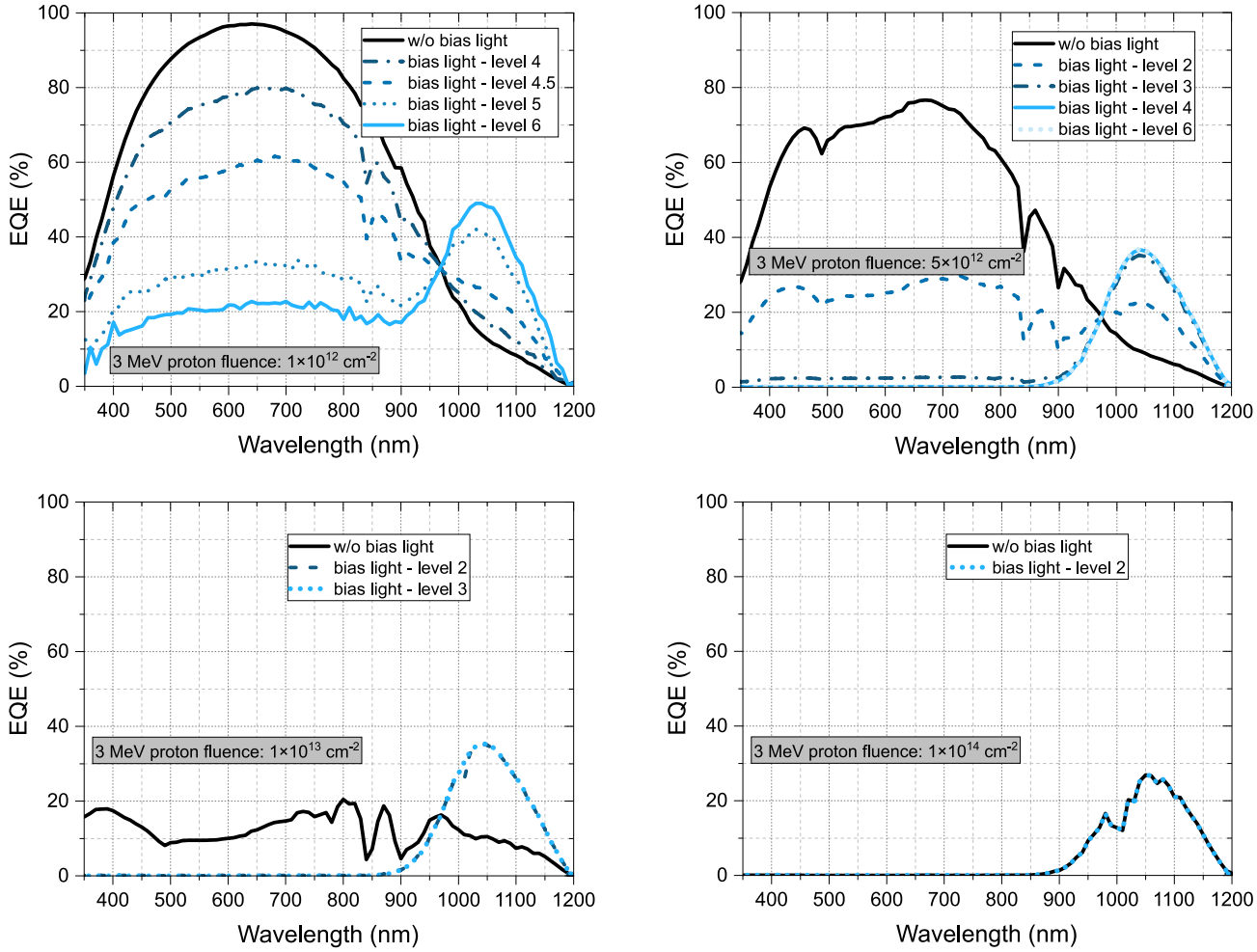


Figure 4.9: EQE spectral responses obtained on solar cells irradiated by 3 $MeV$ protons at 4 fluences: $1 \times 10^{12}$ $cm^{-2}$ (upper left), $5 \times 10^{12}$ $cm^{-2}$ (upper right), $1 \times 10^{13}$ $cm^{-2}$ (lower left), and $1 \times 10^{14}$ $cm^{-2}$ (lower right). For each case, the impact of different levels of bias light is studied.

For each fluence and under high levels of bias light, only the long wavelengths significantly contribute to the $J_{SC}$ with a maximum EQE at $\lambda = 1050$ $nm$. Furthermore, these maximum EQE values are relatively low, from 50% at $1 \times 10^{12}$ $cm^{-2}$ fluence, down to $< 25\%$ at $1 \times 10^{14}$ $cm^{-2}$ fluence. This EQE spectral dynamic behavior will then be referred to as the rear-emitter behavior. Indeed, such dynamics are regularly observed in rear junction cells with low $\tau$ values. At fluences $\geq 5 \times 10^{12}$ $cm^{-2}$, once this rear-emitter behavior is observed at one bias light level, an increase of bias light intensity systematically resulted in the same EQE values. It is worth noting that this rear-emitter behavior is reached for lower bias light intensity values with increasing fluence. It is possible that at $1 \times 10^{12}$ $cm^{-2}$ fluence, this threshold would be reached for higher bias light intensities, not accessible with our setup.

#### I-V measurements at low light intensity

The influence of light intensity on $J_{SC}$ between 1 $MeV$ and 3 $MeV$ proton energies was further investigated with I-V measurements under 0.1 Sun illumination, as shown in Figure 4.10. At each fluence, under 1 Sun illumination, a difference of at least a factor of 2 in $J_{SC}$ is observed between the two proton energies. Under 0.1 Sun illumination, the $J_{SC}$ values between the two proton energies overlay at $1 \times 10^{12}$ $cm^{-2}$ fluence. However, for higher fluences, there is a factor 2 between the $J_{SC}$ values for the two proton energies, as it was observed under 1 Sun illumination. By comparing these $J_{SC}$ values with the $J_{SC}$ computed from the EQE data (not detailed here), it was estimated that the 0.1 Sun illumination would correspond to an intermediate bias light level, between 2 and 4.5.

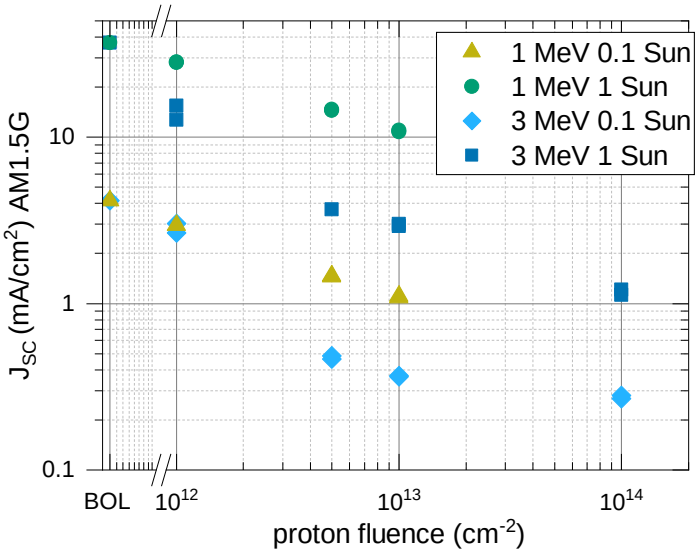


Figure 4.10: $J_{SC}$ obtained for $AM1.5G$ spectrum for two intensities: 0.1 Sun (light colors) and 1 Sun (dark colors) for solar cells irradiated with 1 $MeV$ (green) and 3 $MeV$ (blue) protons.

### 4.3.2 PC1D modeling of the proton irradiated cells

From $5 \times 10^{12}$ $cm^{-2}$ fluence, under high bias light level, the spectral responses of solar cells irradiated under both 1 $MeV$ and 3 $MeV$ proton energies were typical of the behavior of a degraded bulk combined with a rear emitter [27]. Therefore, this part aims to model the irradiated cells in order to reproduce and understand these EQE spectral variations. The modeling is conducted with PC1D, specifically by varying, in the damaged region and as illustrated in Figure 4.3, the equilibrium majority carrier concentration, the conductivity type, and the SRH recombination parameters. Indeed, all three parameters are expected to be affected by proton irradiation, based on the previous sections.

#### 1 MeV protons

According to the spectral response with highest bias light displayed in Figure 4.8 (left) at $5 \times 10^{12}$ $cm^{-2}$ 1 $MeV$ proton fluence, the short wavelengths are not collected ($< 20\%$ until $\lambda = 750$ $nm$) while the long wavelengths still result in good EQE values ($\approx 85\%$ at $\lambda = 1025$ $nm$). This is typical of the behavior of a solar cell combining a degraded bulk (i.e. low $\tau$) with a rear junction. This suggests that the junction has possibly changed side due to a conductivity type change within the base of the solar cell.

The equilibrium majority carrier concentration, the conductivity type, and the SRH recombination parameters were varied in the 16 $\mu m$ damaged region. In this study, the light intensity is set to 1 Sun, the recombination-dominating defect is assumed to be a mid-gap defect ($E_t - E_i = 0$ $eV$) in all simulations. $\tau_{n0}$ & $\tau_{p0}$ are varied to reproduce different bulk degradation levels, but are chosen to be equal for the sake of simplicity. Therefore, the two parameters varied in the following abacus (i.e., computed EQE spectral variations) are $\tau_{n0} = \tau_{p0}$, and the equilibrium majority carrier concentration by considering p-type or n-type conductivity type. With this, three abacus are obtained with different $p_0$ (or $n_0$ for n-type) for $\tau_{n0} = \tau_{p0} = 0.1$ $\mu s$ (see Figure 4.11), $\tau_{n0} = \tau_{p0} = 0.01$ $\mu s$ (see Figure 4.12), and $\tau_{n0} = \tau_{p0} = 0.003$ $\mu s$ (see Figure 4.13). For better clarity, $p_0$ (without type inversion) and $n_0$ (with type inversion) are separated in left and right figures, respectively.

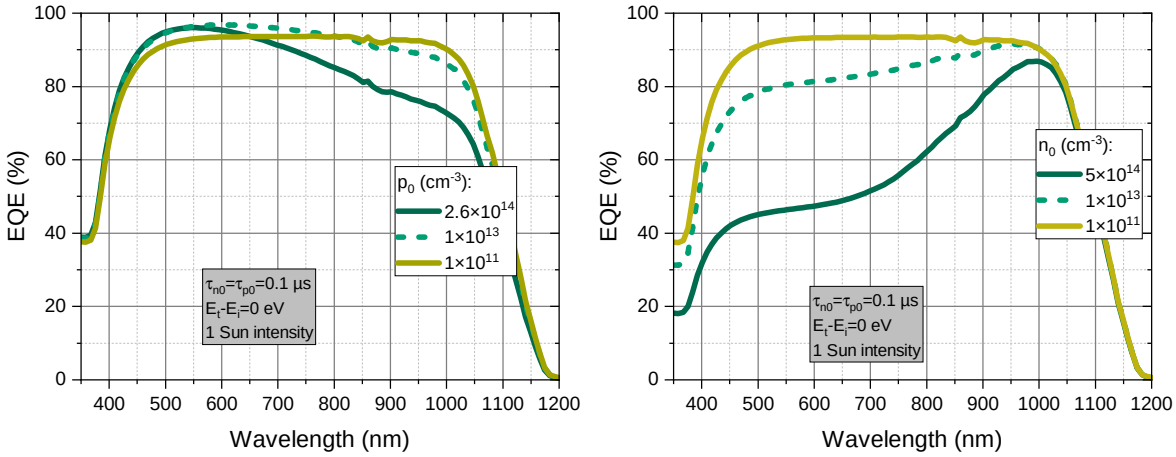


(a) (b)

Figure 4.11: 1 $MeV$ protons. PC1D computed EQE spectral variations for various equilibrium majority carrier concentrations for holes as majority carriers (a) and electrons as majority carriers (b) in the 16 $\mu m$ damaged c-Si region. The fixed parameters are: 1 Sun intensity, $E_t - E_i = 0$ $eV$, $\tau_{n0} = \tau_{p0} = 0.1$ $\mu s$.

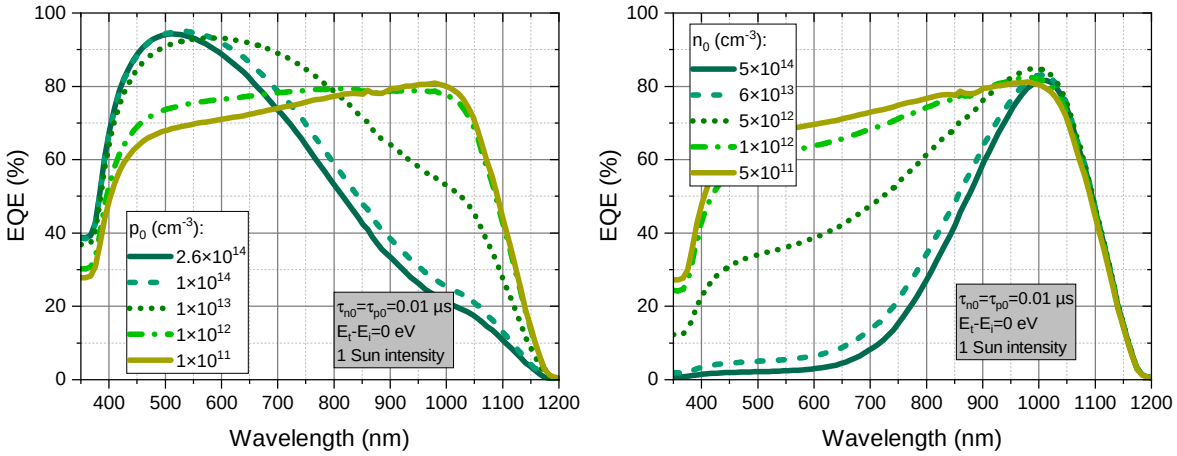


(a) (b)

Figure 4.12: 1 $MeV$ protons. PC1D computed EQE spectral variations for various equilibrium majority carrier concentrations for holes as majority carriers (a) and electrons as majority carriers (b) in the 16 $\mu m$ damaged c-Si region. The fixed parameters are: 1 Sun intensity, $E_t - E_i = 0\ eV$, $\tau_{n0} = \tau_{p0} = 0.01\ \mu s$.

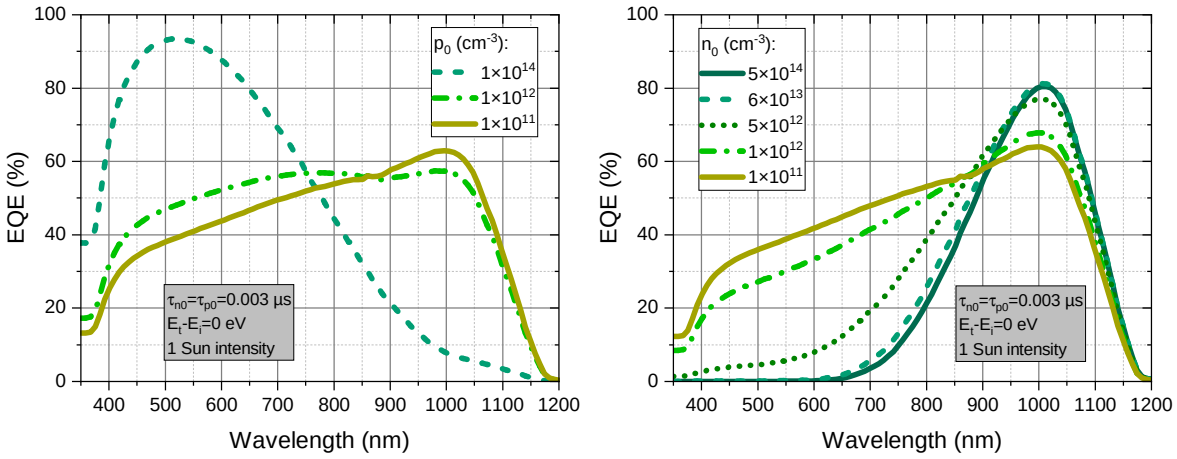


(a) (b)

Figure 4.13: 1 $MeV$ protons. PC1D computed EQE spectral variations for various equilibrium majority carrier concentrations for holes as majority carriers (a) and electrons as majority carriers (b) in the 16 $\mu m$ damaged c-Si region. The fixed parameters are: 1 Sun intensity, $E_t - E_i = 0\ eV$, $\tau_{n0} = \tau_{p0} = 0.003\ \mu s$.

In the case of a modeled p-type damaged region, the short wavelengths are well collected (EQE>70%) for the first two SRH recombination rate parameters ($\tau_{n0} = \tau_{p0} = 0.1\ \mu s$, see Figure 4.11(a) and $\tau_{n0} = \tau_{p0} = 0.01\ \mu s$, see Figure 4.12(a)). For the highest SRH recombination rate tested ($\tau_{n0} = \tau_{p0} = 0.003\ \mu s$, see Figure 4.13(a)), low $p_0$ values result in higher collection for the long wavelengths than for the short wavelengths, but the collection of the short wavelengths is still way higher (40% at $\lambda = 550\ nm$) than the experimental values (below 10% at $\lambda = 550\ nm$).

However, in the case of a modeled n-doped damaged region, it is worth noting that the increase of SRH recombination rates strongly affects the collection of short wavelengths but has little effect on the collection of the long ones.

Interestingly, the experimental EQE spectral variations at $5 \times 10^{12}\ cm^{-2}$ and $1 \times 10^{13}\ cm^{-2}$ $1\ MeV$ proton fluences (see Figure 4.8, with high bias light) could be reproduced by the PC1D computations in Figures 4.12(b) and 4.13(b), i.e. for a type inversion in the damaged layer, combined with high SRH recombination.

Therefore, this modeling work suggests a type inversion in the damaged region at fluences $\geq 5 \times 10^{12}\ cm^{-2}$.

Overall, the modeling parameters in the damaged region required to reproduce our EQE measurements under bias light with cells irradiated at $1\ MeV$ proton fluences $\geq 5 \times 10^{12}\ cm^{-2}$ are:

- high SRH recombination: typically $\tau_{p0} = \tau_{n0} < 0.1\ \mu s$,
- conductivity type inversion, with $n_0 > 1 \times 10^{12}\ cm^{-3}$.

The comparison of the experimental $5 \times 10^{12}\ cm^{-2}$ $1\ MeV$ proton fluence EQE curves with those computed with PC1D is shown in Figure 4.14. The modeled cell structure is illustrated in Figure 4.14(a). The following parameters were chosen in the damaged c-Si region: $n_0 = 2 \times 10^{13}\ cm^{-3}$, $E_t - E_i = 0\ eV$ and $\tau_{p0} = \tau_{n0} = 0.008\ \mu s$ .

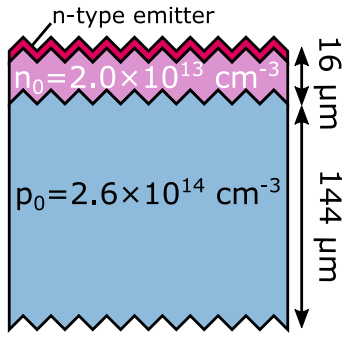


(a)

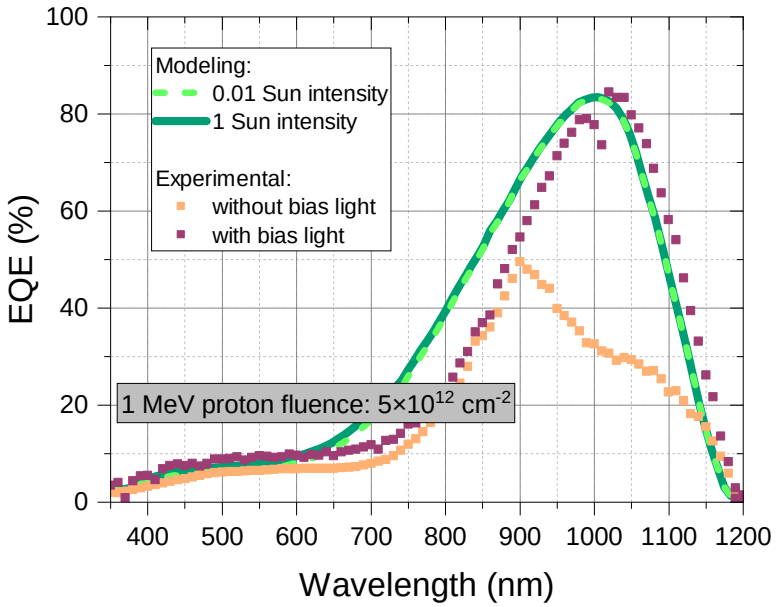


(b)

Figure 4.14: (a) Structure used in PC1D with corresponding equilibrium majority carrier concentrations. (b) Comparison of data obtained from measurements (symbols) and modeling (solid and dash lines) for a solar cell exposed to a $5 \times 10^{12}\ cm^{-2}$ $1\ MeV$ proton fluence with and w/0 bias light. The chosen parameters of the damaged region for the modeling are: $n_0 = 2 \times 10^{13}\ cm^{-3}$, $E_t - E_i = 0\ eV$ and $\tau_{p0} = \tau_{n0} = 0.008\ \mu s$.

Overall, the experimental EQE spectral variations obtained with bias light could be well reproduced with these parameters. However, the effect of the illumination level on the spectral response could not be reproduced by PC1D modeling. It is worth noting that the modeling of the bias light intensity was only made by varying the illumination intensity of the primary light, i.e. the monochromatic light, from 0.01 Sun to 1 Sun. This method was chosen as no consistent results were obtained by adding a white bias light in addition to the monochromatic light necessary for the EQE calculations. This PC1D limitation was previously mentioned in literature [192].

**3 MeV protons**

For the 3 $MeV$ proton case, it is worth focusing on the EQE spectral dynamic without bias light of the solar cell irradiated at a $5 \times 10^{12}$ $cm^{-2}$ fluence (Figure 4.9 upper right). This cell features a relatively good collection of the short wavelengths with $EQE \approx 70\%$ at 600 $nm$ but not for long wavelengths with a decrease starting at 650 $nm$ to reach EQE values below 20% for $\lambda > 950$ $nm$. Such an EQE dynamic is typical of a front junction cell combined with a degraded $\tau_{bulk}$. After the addition of bias light, the EQE was close to zero for $\lambda < 900$ $nm$ and the maximum value obtained for $\lambda = 1040$ $nm$ was below 40%. Therefore, the behavior of the solar cell completely changed with the use of bias light, acting as a front junction device under low illumination and like a rear junction device under strong illumination.

Once more, abacus were made via PC1D modeling (see Figures 4.15 and 4.16) by varying the equilibrium majority carrier concentration, the conductivity type and the SRH recombination parameters. For each case, the left Figure (a) models the 0.01 Sun intensity case ($\approx$ no bias light), while the right Figure (b) models the 1 Sun intensity case ($\approx$ with high level of bias light).

This simulation study focused on the influence of the equilibrium carrier concentration and of the conductivity type. The question was whether the 92 $\mu m$-thick damaged layer (as illustrated in Figure 4.3) was still p-type after irradiation or if it underwent a type inversion, and therefore would become n-type. The SRH recombination parameters are fixed to $\tau_{n0} = \tau_{p0} = 0.01$ $\mu s$ and $E_t - E_i = -0.2$ $eV$. The chosen $E_t - E_i = -0.2$ $eV$ defect energy level seemed a reasonable choice as it was reported as recombination center and majority carrier trap center [126]. In Figure 4.15, $n_0$ is varied from $1 \times 10^{11}$ $cm^{-3}$ to $2 \times 10^{13}$ $cm^{-3}$. In Figure 4.16, $p_0$ is varied from $5 \times 10^{10}$ $cm^{-3}$ ($\approx$ intrinsic) to $2 \times 10^{13}$ $cm^{-3}$. For the $n_0$ case (i.e., n-type damaged region), similar EQE spectral dynamics (typical of a rear junction cell with a degraded $\tau$) are obtained for both high and low illumination levels. This feature is in disagreement with the experimental results. On the contrary, in the $p_0$ case (i.e., p-type damaged region), the effect previously measured is retrieved (see Figure 4.9). The long wavelengths significantly contribute under 1 Sun intensity, while the short wavelengths significantly contribute under 0.01 Sun intensity. However, this is only the case for intermediate equilibrium carrier concentrations, i.e. $p_0 \in [3 \times 10^{11}$ $cm^{-2} - 5 \times 10^{12}$ $cm^{-2}]$ for the $p_0$ values investigated. For $p_0 = 5 \times 10^{10}$ $cm^{-2}$ ($\approx$ intrinsic), the behavior is similar of the behavior

occurring for a n-doped region. For $p_0 = 2 \times 10^{13}\ cm^{-2}$, there is no change of EQE dynamic between the illumination conditions.

Interestingly, this time both the EQE spectral dynamics and the bias light dependence observed experimentally could be reproduced by modeling a p-type damaged region, as can be seen in Figure 4.16. Therefore, this PC1D modeling study seems to conclude that no conductivity type inversion is occurring, at least until $5 \times 10^{13}\ cm^{-2}$ fluence, for these 3 $MeV$ irradiation tests.

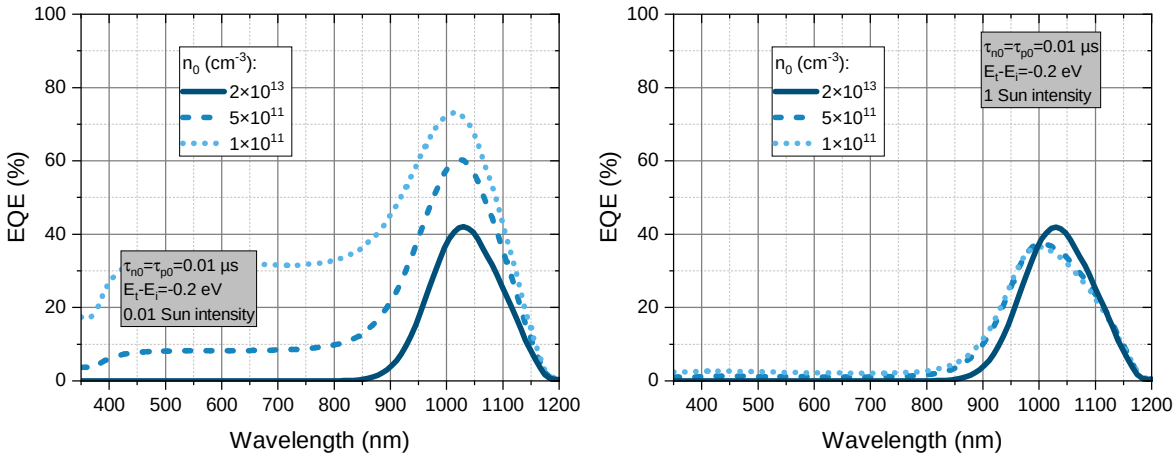


(a) (b)

Figure 4.15: PC1D computed EQE spectral variations for various equilibrium carrier concentrations for electron as majority carriers in the 92 $\mu m$-thick damaged region. They are represented for 2 light intensities: 0.01 Sun (a) and 1 Sun (b). In the damaged region, the fixed parameters are: $E_t - E_i = -0.2\ eV$, $\tau_{n0} = \tau_{p0} = 0.01\ \mu s$.

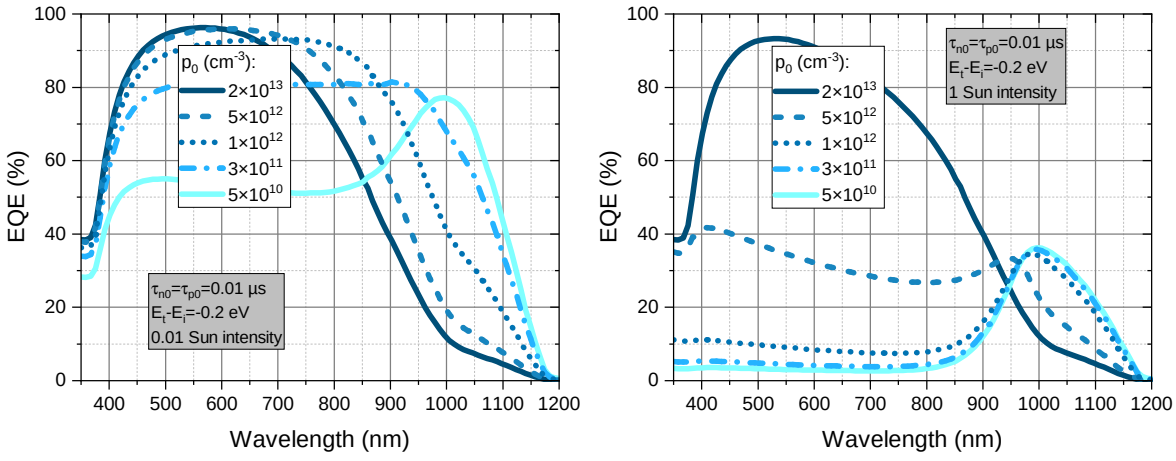


(a) (b)

Figure 4.16: PC1D computed EQE spectral variations for various equilibrium carrier concentrations for holes as majority carriers in the 92 $\mu m$-thick damaged region. They are represented for 2 light intensities: 0.01 Sun (a) and 1 Sun (b). In the damaged region, the fixed parameters are: $E_t - E_i = -0.2\ eV$, $\tau_{n0} = \tau_{p0} = 0.01\ \mu s$.

Overall, the modeling parameters, in the damaged region, required to reproduce our measurements of the cells irradiated with $1 \times 10^{12} - 5 \times 10^{12}$ $cm^{-2}$ 3 $MeV$ proton fluences displayed in Figure 4.9 were:

- high SRH recombination: typically $\tau_{p0} = \tau_{n0} < 1$ $\mu s$,
- near intrinsic doping with $p_0 < 2 \times 10^{13}$ $cm^{-3}$.

For instance, to reproduce the EQE at $5 \times 10^{12}$ $cm^{-2}$ 3 $MeV$ fluence, the chosen parameters in the damaged bulk were: $p_0 = 3 \times 10^{11}$ $cm^{-3}$, $E_t - E_i = -0.2$ $eV$ and $\tau_{p0} = \tau_{n0} = 0.008$ $\mu s$ (see Figure 4.17).

As one can see, if the global trend—especially at short wavelengths—is well reproduced by this model, the model fails to reproduce the EQE degradation observed for long wavelengths under low bias light intensity. This could be due to additional defect energy levels, non-explored SRH parameters (e.g. symmetry factor $k$), and/or limitations in the model/software with respect to more complex mechanisms at play and in particular the highly defective zone corresponding to the Bragg peak region. This modeling study could be refined with a software (e.g. Afors-Het [184]) able to simulate heterojunction structures, specific defect parameters, and the coexistence of several SRH defects, which is not possible with PC1D software.

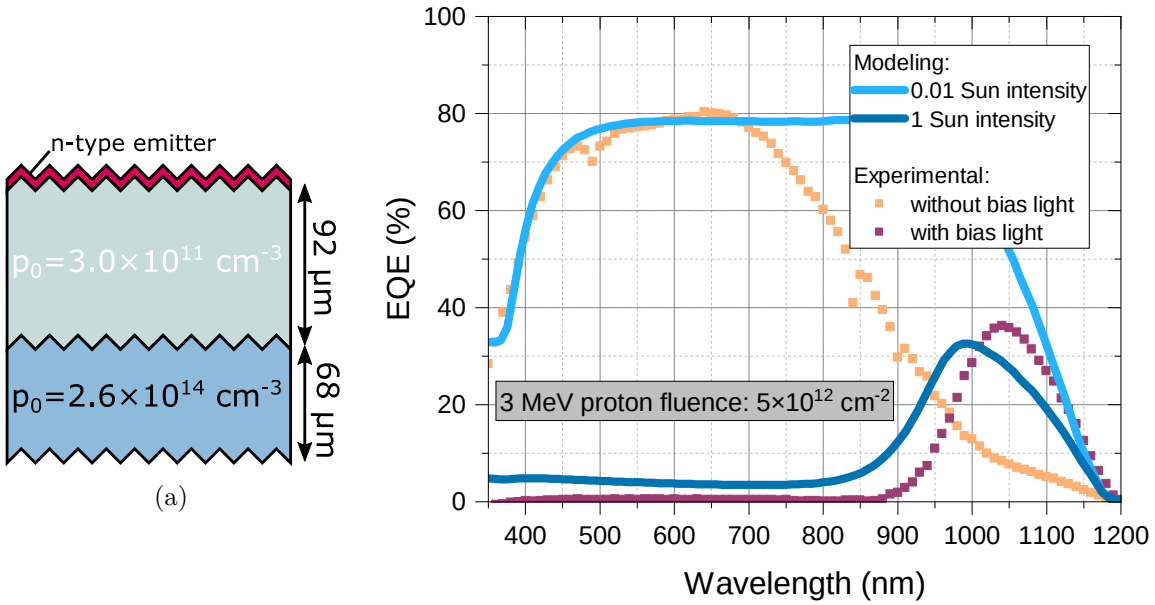


Figure 4.17: (a) Structure used in PC1D with corresponding $p_0$ values. (b) Comparison of EQE data obtained from measurements (symbols) and modeling (solid lines) for a solar cell exposed to $5 \times 10^{12}$ $cm^{-2}$ 3 $MeV$ proton fluence with and w/0 bias light. The chosen parameters of the damaged region for the modeling are: $p_0 = 3 \times 10^{11}$ $cm^{-3}$, $E_t - E_i = -0.2$ $eV$ and $\tau_{p0} = \tau_{n0} = 0.008$ $\mu s$.

To get further insights into the significant changes of the spectral dynamic with the illumination level, the carrier densities in function of the cell depth were extracted for the modeling parameters used in Figure 4.17. The wavelength chosen for the light source is

500 $nm$, as for this wavelength, there is a strong difference in EQE values, with $\approx 80\%$ for 0.01 Sun intensity and $\approx 0\%$ for 1 Sun intensity. In the damaged bulk (from the emitter to 92 $\mu m$ below the front side), the carrier density gradients observed under both conditions are unexpectedly inverted compared to what is typically observed in non-irradiated cells. Specifically, under 1 Sun illumination, the density gradients for both electrons and holes are oriented in the same direction, which is in contrast to the usual behavior where the gradients are opposite, and could lead to issues with charge extraction. The second thing to be noticed is the depth at which the holes become the majority carriers. This corresponds to 13 $\mu m$ at 0.01 Sun intensity. This depth is lower for 1 Sun intensity—5 $\mu m$—, but the concentrations of holes and electrons remain similar until $\approx 40$ $\mu m$ in this second case. Thus, irradiation seems to result in a shift from shallow to deep junction under 1 Sun condition. The influence of the illumination is really strong here as the injection level ($\approx 2 \times 10^{12}$ $cm^{-3}$ at 20 $\mu m$ for 1 Sun) is higher than the doping level ($p_0 = 3 \times 10^{11}$ $cm^{-3}$).

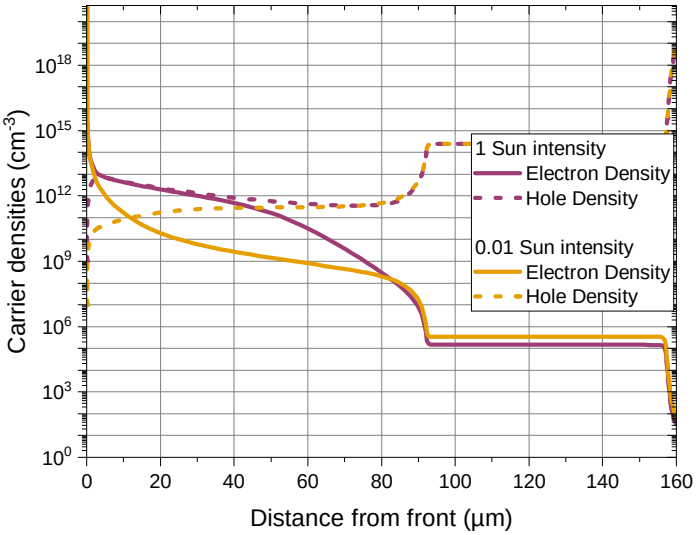


Figure 4.18: PC1D simulation of the electron (solid lines) and hole (dash lines) densities for 1 Sun (purple) and 0.01 Sun (orange) light intensities in function of the distance below the front surface. The chosen parameters for the modeling are: $p_0 = 3 \times 10^{11}$ $cm^{-3}$, $E_t - E_i = -0.2$ $eV$ and $\tau_{p0} = \tau_{n0} = 0.008$ $\mu s$. The light source is monochromatic with $\lambda = 500$ $nm$.

### 4.3.3 In-plane parameters variations

$L_n$ mappings were conducted for some of the irradiated samples at $1 \times 10^{12}$ $cm^{-2}$ fluence for 1 $MeV$ and 3 $MeV$ proton energies, and $5 \times 10^{12}$ $cm^{-2}$ 1 $MeV$ proton fluence (see Figures 4.19, 4.21, 4.22, 4.25 and 4.27). It is worth noting that the $L_n$ extraction procedure is strongly affected by the non-homogeneous electronic properties of the irradiated samples through the substrate thickness. Nevertheless, the $L_n$ mappings provide an interesting mean to investigate the distribution of the PV properties across the surface area of the samples. Please also note that the measurements were made complicated by the small size of the samples ($1.5 \times 1.5$ $cm^2$). Indeed, the vacuum zone normally used to maintain the sample

could not be used as its location was too far from the measurement probe. Kapton adhesive was then used at the corners of the sample.

For all studied conditions, the $L_n$ mappings featured strong in-plane disparities. Some mappings even displayed white color areas (see Figures 4.19, 4.22 and 4.25), where $L_n$ could not be extracted due to significant non-uniform damage across the cell depth, potentially associated with a region where the conductivity type could be inverted. We previously underlined large $L_n$ in-plane distributions in Chapter 3 on electron irradiated Ga60 solar cells. This was attributed to initial $p_0$ in-plane heterogeneities ($[2.3; 3.0] \times 10^{14}\ cm^{-3}$) associated to the presence of TDs [178], combined with $\tau$ values dominated by a shallow energy level ($p_0$-dependent recombination strength). In this study, $p_0$ reductions (and conductivity type inversions) also contribute to the highlighted heterogeneities, as seen hereafter.

**1 MeV protons**

A $L_n$ mapping of a solar cell irradiated at a $1 \times 10^{12}\ cm^{-2}$ $1\ MeV$ proton fluence is shown in Figure 4.19. This mapping highlights strong $L_n$ variations (e.g., from 40 $\mu m$ to $250 - 300\ \mu m$) and areas where $L_n$ could not be extracted (indicating a change in the EQE spectral dynamic). In addition, the $L_n$ distribution follows ring-like patterns. To get further insights into these variations, EQE measurements with or without bias light were performed at the 2 positions indicated in the mapping and are shown in Figure 4.20(a). Position 1 and Position 2 correspond to two different $L_n$ areas, with low value (red) for Position 1 and partly unextractable value (white) for Position 2. The spectral responses obtained for Positions 1 & 2 result in similar EQE spectral variations without bias light. However, completely different local spectral variations are obtained with bias light. Under bias light, charges are mainly collected for $\lambda < 700\ nm$ for Position 1 and charges mainly collected for $\lambda > 700\ nm$ for Position 2. These EQE shapes obtained with higher bias light intensity could be well reproduced by using the model presented in Section 4.3.2. Especially, a good fitting is obtained with the following SRH parameters: $E_t - E_i = 0\ eV$, $\tau_{n0} = \tau_{p0} = 0.01\ \mu s$. For Position 1, the $p_0$ of the 16 $\mu m$-thick damaged layer is slightly lowered from $p_0 = 2.6 \times 10^{14}\ cm^{-3}$ to $p_0 = 1 \times 10^{14}\ cm^{-3}$. For Positions 2, the dynamic is best reproduced by implementing a type inversion in the damaged layer to $n_0 = 1 \times 10^{12}\ cm^{-3}$ combined with the same SRH parameters. These PC1D-computed EQE spectral variations are found in Figure 4.12. These computations allowed to reproduce the two different EQE spectral dynamics obtained with bias light in the same cells with the same SRH recombination parameters, but with different types of conductivity and densities of majority carriers, as shown in Figure 4.20(b).

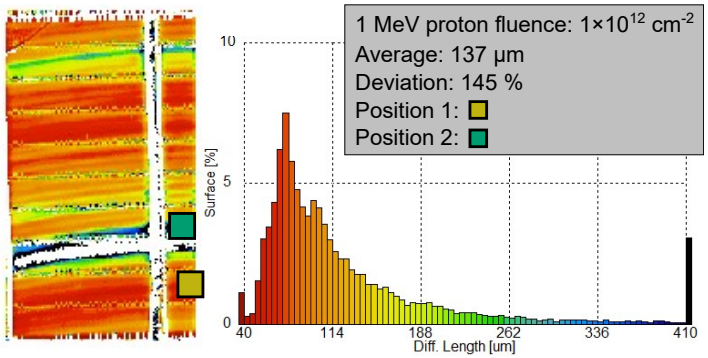


Figure 4.19: $L_n$ mapping of a solar cell irradiated at a $1 \times 10^{12}$ $cm^{-2}$ 1 $MeV$ proton fluence. The colored squares refer to the different locations of the EQE beam light of Figure 4.20(a).

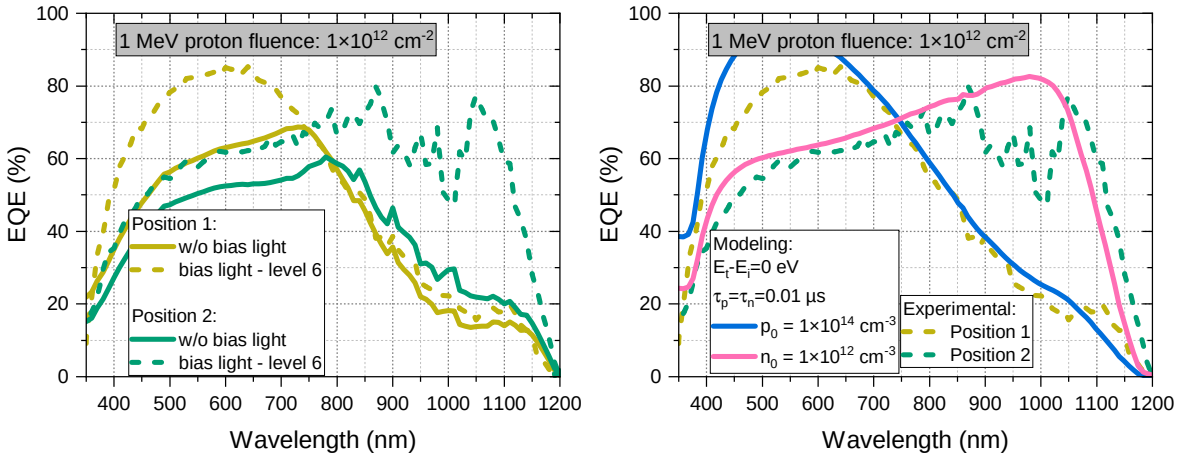


(a) (b)

Figure 4.20: (a) Experimental EQE spectral variations obtained at different locations on the same solar cell irradiated at a $1 \times 10^{12}$ $cm^{-2}$ 1 $MeV$ fluence. The positions are identified in Figure 4.19. (b) Reproduction of (a) curves obtained with bias light with PC1D simulations at 1 Sun. The different modeling parameters are modified only in the 16 $\mu m$ damaged region.

The $L_n$ mapping of the other solar cell irradiated at a $1 \times 10^{12}$ $cm^{-2}$ 1 $MeV$ proton fluence is shown in Figure 4.21. This second mapping confirms the strong in-plane $L_n$ variations and the ring-like pattern of $L_n$ distribution. However, no white color areas are visible for this mapping. Nonetheless, all the solar cells irradiated at $1 \times 10^{12}$ $cm^{-2}$ 1 $MeV$ proton fluence resulted in similar $J_{SC}$, as shown in Figure 4.4. This suggests that the local in-plane type inversions do not contribute significantly to the overall solar cell performance for this irradiation condition.

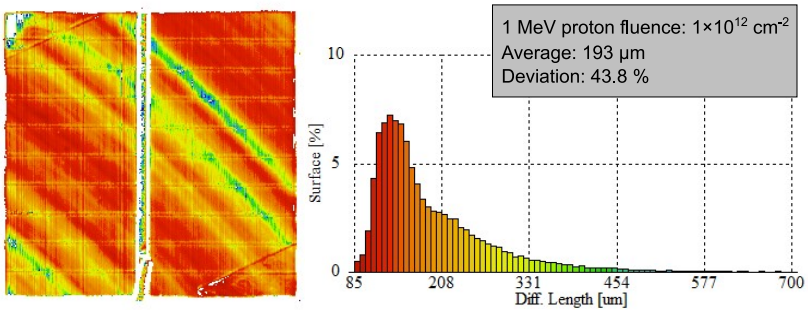


Figure 4.21: $L_n$ mapping of a solar cell irradiated at a $1 \times 10^{12}$ $cm^{-2}$ 1 $MeV$ proton fluence.

At higher 1 $MeV$ proton fluence ($5 \times 10^{12}$ $cm^{-2}$), the $L_n$ mapping still showed the same kind of variations as those shown in Figure 4.19 with areas with and without measurable values (see Figure 4.22). Additional EQE measurements were performed at the two positions indicated in the LBIC mapping, corresponding to unextractable $L_n$ values (white) for Position 1 and low $L_n$ values (red) for Position 2 (see Figure 4.23). This time, similar EQE spectral variations were obtained for both positions, and this with and without bias light. They were typical of type inversions within the damaged regions. As modeled in Figure 4.13, once the type inversion is achieved, the variations in $n_0$ result in small EQE variations.

However, we were not able to perform LBIC mapping measurements for other irradiation conditions, probably due to poor contacting.

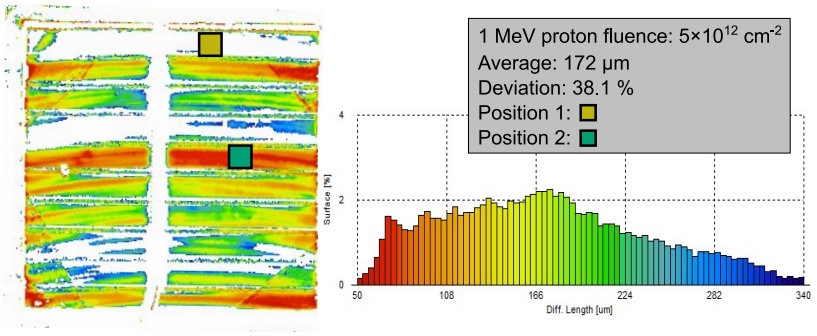


Figure 4.22: $L_n$ mapping of a solar cell irradiated at a $5 \times 10^{12}$ $cm^{-2}$ 1 $MeV$ proton fluence. The colored squares refer to the different locations of the EQE beam light of Figure 4.23.

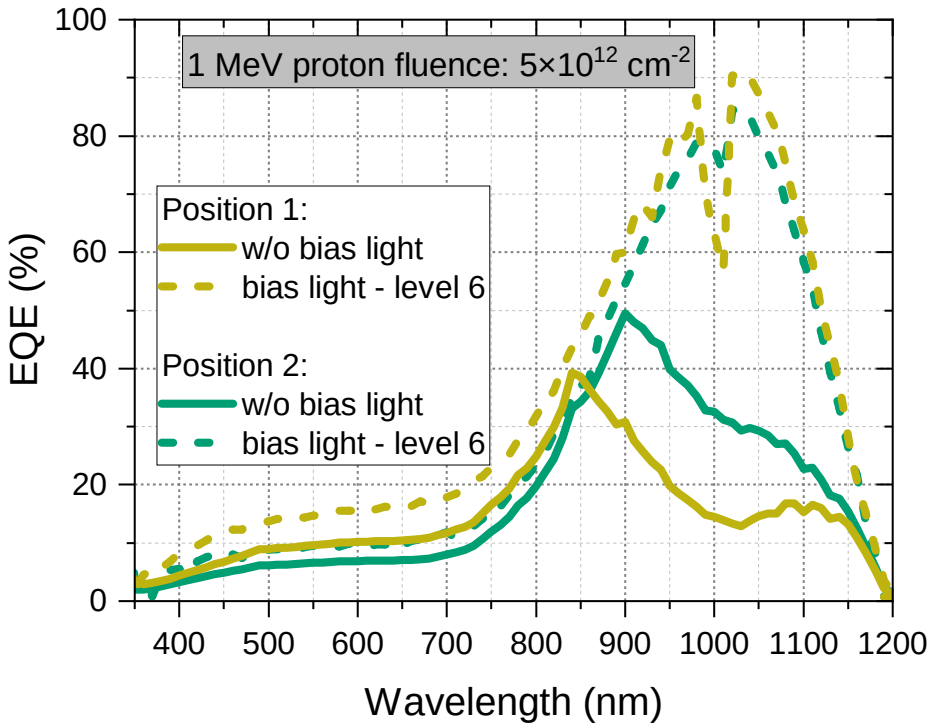


Figure 4.23

Figure 4.24: Experimental EQE spectral variations obtained at several locations of one solar cell irradiated at a $5 \times 10^{12}$ $cm^{-2}$ 1 $MeV$ proton fluence. The positions are identified in Figure 4.19.

**3 MeV protons**

Similarly, the solar cells irradiated by 3 $MeV$ protons feature strong in-plane variations of their electronic properties. This can be seen in Figure 4.25 at $1 \times 10^{12}$ $cm^{-2}$ fluence. Again, the $L_n$ in-plane distribution follows ring-like patterns. Two positions are identified, Position 1 corresponds to unextractable $L_n$ values (white), while Position 2 corresponds to low $L_n$ values (red). Additional EQE spectral measurements were made at these two positions (see Figure 4.26(a)). The results at Position 1 were already displayed in Figure 4.9 (upper left) and referred to the behavior introduced in Section 4.3.2, where the cell behaves as a front emitter device without bias light, and behaves as a rear emitter device under bias light. This means (according to the modeling study previously presented) that in the damaged region near-intrinsic doping is reached, i.e. $p_0 \approx 5 \times 10^{12}$ $cm^{-3}$. The EQE spectral variations obtained at Position 2 are similar to the ones at Position 1 without bias light. However, the bias light has almost no effect at this position, meaning that the $p_0$ is less reduced, probably $\geq 2 \times 10^{13}$ $cm^{-3}$. The possible simulation parameters and their resulting EQE are shown in Figure 4.26(b). Unfortunately, LBIC measurements could not be made on other fluences of 3 $MeV$ irradiated cells, probably due to poor contacting.

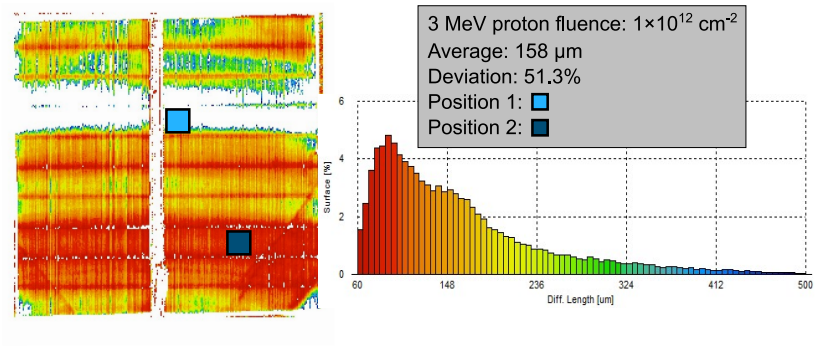


Figure 4.25: $L_n$ mapping of a solar cell irradiated at a $1 \times 10^{12}$ $cm^{-2}$ 3 $MeV$ fluence. The colored squares refer to the different locations of the EQE beam light of Figure 4.26(a).

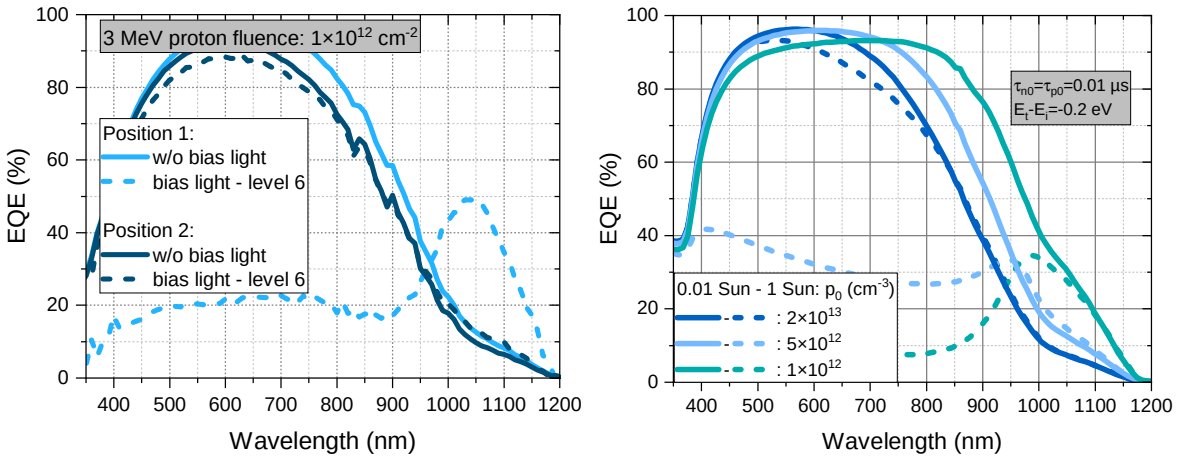


(a) (b)

Figure 4.26: (a) Experimental EQE spectral variations obtained with and without bias light at several locations of one solar cell irradiated at a $1 \times 10^{12}$ $cm^{-2}$ 3 $MeV$ proton fluence. The different locations are identified in Figure 4.25. (b) Reproduction of (a) curves measured with PC1D simulations at 1 Sun and 0.01 Sun. The different modeling parameters are modified only in the 92 $\mu m$ damaged region.

The BOL in-plane $p_0$ variations result in stronger EOL in-plane $p_0$ variations, in addition to strong $p_0$ decreases. Knowing the BOL in-plane $p_0$ variations on 3 *sister* Ga60 wafers ($[2.3; 3.0] \times 10^{14}$ $cm^{-3}$), it is possible to calculate the respective EOL $p_0$ at a specific fluence by using $R_c$, as already defined in Equation 1.42. A $R_c$ value of $50 - 100$ $cm^{-1}$ was previously reported for 3 $MeV$ irradiated B-doped solar cells [107]. Therefore, assuming the BOL $p_0$ variations aforementioned, $1 \times 10^{12}$ $cm^{-2}$ fluence, and $R_c = 100$ $cm^{-1}$, Equation 1.42 gives a $p_0$ variation in the range $[1.3; 2.0] \times 10^{14}$ $cm^{-3}$. This is far from the estimated EOL $p_0$ variations obtained with PC1D modeling combined with EQE measurements ($[\approx 5 \times 10^{12} - \geq 2 \times 10^{13}]$ $cm^{-3}$). An estimated $R_c$ value of 225 $cm^{-1}$ would result in a $p_0$ variation in the range $[5.0 \times 10^{12}; 7.5 \times 10^{13}]$ $cm^{-3}$ after $1 \times 10^{12}$ $cm^{-2}$ fluence. This is closer to the values obtained from the previous analysis. All these estimated EOL $p_0$ values are summarized in Table 4.3. This estimated $R_c$ value of 225 $cm^{-1}$ is more than twice higher than the value reported

on literature with B-doped solar cells. This is noteworthy as Ga-doped c-Si was previously reported to result in 4× lower $R_c$ values than B-doped c-Si [133] for solar cells irradiated with 1 $MeV$ electrons. Additionally, the low $R_c$ attributed to Ga-doping was confirmed with Ga60 material in the electron irradiation study conducted in Chapter 3. Nonetheless, in [107] study, the solar cells irradiated were 50 $\mu m$-thick, while the solar cells irradiated in this study are 160 $\mu m$-thick. Thus, the 50 $\mu m$-thick solar cells were not subjected to the 3 $MeV$ proton Bragg peak occurring at 92 $\mu m$ Si depth, and leading to the highest amount of irradiation-induced defects. Therefore, it can be assumed that the damaged bulk of the 160 $\mu m$-thick solar cells experienced more severe damage at the same energy, making the comparison with the study by Yamaguchi *et al.* [107] not straightforward.

| **3 MeV proton fluence** | **Method used** | **$p_0$(min) cm$^{-3}$** | **$p_0$(max) cm$^{-3}$** |
|---|---|---|---|
| BOL | OxyMap, see Chapter 2 | $2.3 \times 10^{14}$ | $3.0 \times 10^{14}$ |
| $1 \times 10^{12}$ $cm^{-2}$ | Equation 1.42 with $R_c = 100$ $cm^{-1}$ ([107]) | $1.3 \times 10^{14}$ | $2.0 \times 10^{14}$ |
| $1 \times 10^{12}$ $cm^{-2}$ | PC1D modeling and EQE measurements | $\approx 5 \times 10^{12}$ | $\geq 2 \times 10^{13}$ |
| $1 \times 10^{12}$ $cm^{-2}$ | Equation 1.42 with $R_c = 225$ $cm^{-1}$ (estimated) | $5.0 \times 10^{12}$ | $7.5 \times 10^{13}$ |

Table 4.3: Influence of initial in-plane $p_0$ variations (from min and max) on EOL ($1 \times 10^{12}$ $cm^{-2}$ fluence) $p_0$, calculated from Equation 1.42 with $R_c = 100$ $cm^{-1}$ ([107]) and $R_c = 225$ $cm^{-1}$ (estimated). Min and max $p_0$ obtained from combination of PC1D modeling and EQE measurements on one same cell irradiated at a $1 \times 10^{12}$ $cm^{-2}$ 3 $MeV$ proton fluence.

These high equilibrium carrier concentration variations obtained after 3 $MeV$ irradiation are yet not as high as for the 1 $MeV$ case where the type inversion is already reached in some in-place areas for the same fluence. This suggests a higher $R_c$—in the damaged bulk—for lower energy protons, in good agreement with TRIM simulations (see Figure 4.1) and with [107], for which the $R_c$ was higher in the 1 $MeV$ case than in the 3 $MeV$ case.

The $L_n$ mapping of the other solar cell irradiated at a $1 \times 10^{12}$ $cm^{-2}$ 3 $MeV$ proton fluence is shown in Figure 4.27. Similarly to the second solar cell of the 1 $MeV$ case for this fluence, no white areas are obtained and additional EQE spectral measurements performed in the green/blue areas (corresponding to the highest $L_n$ values) do not result in the spectral variations typical of high carrier concentration reductions. However, in the 3 $MeV$ case, the two solar cells irradiated at the $1 \times 10^{12}$ $cm^{-2}$ 3 $MeV$ proton fluence exhibit slightly different $J_{SC}$, as shown in Figure 4.4. The cell with unextractable $L_n$ values results in a $J_{SC}$ value of 3 $mA.cm^{-2}$, lower than the other cell. These unextractable $L_n$ values correspond to reduced EQE spectral variations for irradiation with 3 $MeV$ protons compared to 1 $MeV$ protons. This could explain the greater impact of these white regions on the total $J_{SC}$ for 3 $MeV$ protons.

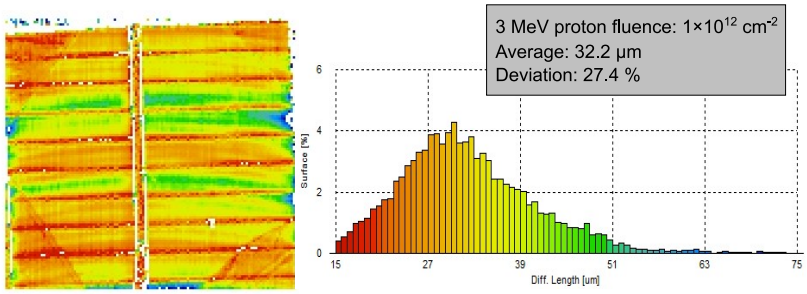


Figure 4.27: $L_n$ mapping of a solar cell irradiated at a $1 \times 10^{12}$ $cm^{-2}$ 3 $MeV$ proton fluence.

## 4.4 Bulk resistivity variations with increasing proton fluence

This part aims at evidencing experimentally potential majority carrier concentration reductions and changes in the conductivity type in proton irradiated c-Si, as discussed in the previous sections.

The non-homogeneous in-depth degradation disqualified several measurement techniques, including the Hall effect, which was used for electron irradiated wafers. The choice went first on electrochemical capacitance-voltage (ECV) measurements, which allow in-depth measurements of the equilibrium majority carrier concentration. However, the contact resistivity was too high in all the samples (mainly due to low doping), making the ECV measurements impossible. Therefore, it was decided to investigate if 4-point probe measurements could provide interesting insights into these $p_0$ reduction effects.

In order to carry out the measurements, and as only solar cells were irradiated in this study, all the surface layers of the chosen solar cells were chemically etched by HCL and KOH solutions so that only the c-Si wafers were left. Given the destructive nature of this approach, only 3 irradiation conditions were tested with one wafer each: $1 \times 10^{13}$ $cm^{-2}$ fluence for 1 $MeV$ protons as it was the harshest condition tested. For 3 $MeV$ protons, two fluences were tested: $5 \times 10^{12}$ $cm^{-2}$ and $1 \times 10^{14}$ $cm^{-2}$, as we expected to only have the type inversion, for the highest fluence for this proton energy. The sheet resistance $R_{sheet}$ was measured after irradiation by 4-point probe measurements on these 3 samples.

$R_{sheet}$ was measured on the front side and on the rear side of each cell. The damaged bulk is supposed to suffer from carrier removal effect, when the undamaged bulk not. Two layers featuring different resistivity values (or in some cases different types of conductivity) are thus supposedly formed (see Figure 4.3). Therefore, if significant carrier removal effects occurred, different $R_{sheet}$ values are expected for front-side and back-side measurements. In case of type inversion in the damaged bulk, a pn junction is thereby created. Thus, assuming type inversions, the front-side $R_{sheet}$ data shown in Figure 4.28 refers to the $R_{sheet}$ value of the damaged region only, when the rear-side measurement refers to the one of the undamaged region only. As shown in this figure, for all samples, significant differences between the front and rear $R_{sheet}$ values are obtained. $R_{sheet}$ is higher for front-side compared to rear-side

measurements, 6.6× higher at the $5 \times 10^{12}$ $cm^{-2}$ 3 $MeV$ proton fluence, 8.4× higher at the $1 \times 10^{13}$ $cm^{-2}$ 1 $MeV$ proton fluence, and 2.1× higher at the $1 \times 10^{14}$ $cm^{-2}$ 3 $MeV$ proton fluence.

Therefore, the $R_{sheet}$ measurements confirm that at least two zones with distinct $R_{sheet}$ values are found in these irradiated samples.

A noticeable evolution of the front-side $R_{sheet}$ with fluence is observed for the 3 $MeV$ case. Particularly, after a sharp increase (18.3× higher) between BOL condition and the $5 \times 10^{12}$ $cm^{-2}$ fluence, the $R_{sheet}$ decreases at the $1 \times 10^{14}$ $cm^{-2}$ fluence, to a value only 5.9× higher than at BOL. This could be explained by a conductivity type inversion, occurring either before $5 \times 10^{12}$ $cm^{-2}$ fluence or before $1 \times 10^{14}$ $cm^{-2}$ fluence. The second case would be consistent with the spectral response-based modeling study carried out. For the 1 $MeV$ case, only a difference of equilibrium majority carrier concentration between the undamaged and damaged regions can here be concluded.

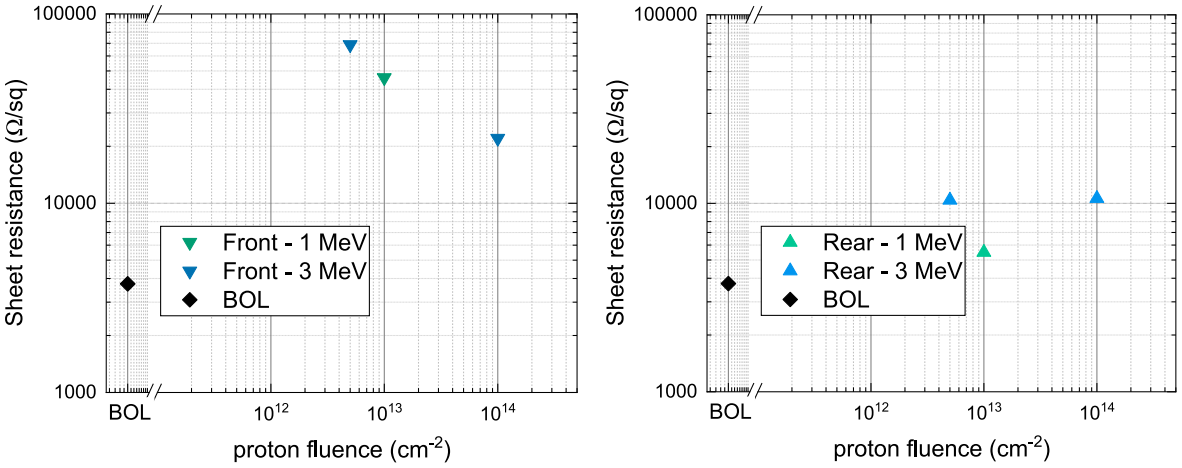


Figure 4.28: Sheet resistance values obtained by 4-point probe measurements on chemically etched samples. The measurements were made on the front-side (left) and rear-side (right) of the samples.

Supposing that for both proton energies, the degradation is homogeneous till the Bragg peak, and that type inversion is reached in the damaged bulk, the $R_{sheet}$ depends on the resistivity $\rho$ of the layer, but also of the thickness $d$ of the layer, with the following relation:

$$R_{sheet} = \frac{\rho}{d} \tag{4.1}$$

Uncertainties can come from the fact that a third zone could be created for the Bragg peak, for instance with a type inversion only occurring in the Bragg peak region. Uncertainties could also come from the thickness of the damaged region chosen, as the real degradation extends slightly beyond the Bragg peak.

Therefore, assuming the same layer thicknesses as those used in the modeling study (see Figure 4.3) and considering a type inversion in the damaged bulk, the resulting values of $\rho$ for the undamaged region (and their associated doping levels) are:

- for 3 $MeV$ protons: 71 $\Omega.cm$ ($p_0 = 1.9 \times 10^{14}$ $cm^{-3}$) at the $5 \times 10^{12}$ $cm^{-2}$ fluence and, after a type inversion, 72 $\Omega.cm$ ($p_0 = 1.9 \times 10^{14}$ $cm^{-3}$) at the $1 \times 10^{14}$ $cm^{-2}$ fluence,
- for 1 $MeV$ protons: 79 $\Omega.cm$ ($p_0 = 1.7 \times 10^{14}$ $cm^{-3}$) at the $1 \times 10^{13}$ $cm^{-2}$ fluence.

Thus, the trend obtained for rear measurements after irradiation are consistent with BOL values. It should be noted that in this specific study, the $p_0$ and $n_0$ values were extracted from resistivity values with PC1D, by assuming in particular a non compensated material (i.e., standard carrier mobility model).

Taking the same hypotheses into account, the expected $\rho$ for the damaged region (and their associated doping levels) are:

- for 3 $MeV$ protons: 630 $\Omega.cm$ ($n_0 = 7.0 \times 10^{12}$ $cm^{-3}$) at $5 \times 10^{12}$ $cm^{-2}$ fluence and 200 $\Omega.cm$ ($n_0 = 2.2 \times 10^{13}$ $cm^{-3}$) at $1 \times 10^{14}$ $cm^{-2}$ fluence,
- for 1 $MeV$ protons: 74 $\Omega.cm$ ($n_0 = 6.0 \times 10^{13}$ $cm^{-3}$) at $1 \times 10^{13}$ $cm^{-2}$ fluence.

For the $1 \times 10^{13}$ $cm^{-2}$ 1 $MeV$ fluence, the obtained $n_0 = 6 \times 10^{13}$ $cm^{-3}$ was chosen as parameter in the modeling study (see Figures 4.13 and 4.12). The computed EQE spectral variations (1 Sun intensity) resulted in $\approx 0\%$ value for $\lambda < 700$ $nm$ and a maximum of 80% for $\lambda = 1000$ $nm$. This is in good correlation with the experimental EQE values (see Figure 4.24).

For the $1 \times 10^{14}$ $cm^{-2}$ 3 $MeV$ fluence, the obtained $n_0 = 2 \times 10^{13}$ $cm^{-3}$ was chosen as parameter in the modeling study (see Figure 4.15). The computed EQE values resulted in $\approx 0\%$ value for $\lambda < 850$ $nm$ and a maximum of $\approx 40\%$ for $\lambda = 1040$ $nm$, this at 1 Sun and 0.01 Sun intensities. This is also in good correlation with the experimental values, with the exception of the maximum EQE value, which is below with a $\approx 30\%$ value (see Figure 4.9). This may be mitigated by choosing a higher SRH recombination rate.

Overall, there is a good correlation between the $p_0$ obtained from these measurements and the modeling study.

In this section, a type inversion is considered in the damaged bulk for the $5 \times 10^{12}$ $cm^{-2}$ 3 $MeV$ proton fluence case. This seems to be not consistent with the spectral response-based modeling study, from which a type inversion would have been obtained starting from the $5 \times 10^{13}$ $cm^{-2}$ fluence. However, the two results are not incompatible. Indeed, it is worth noting that the $n_0 = 7.0 \times 10^{12}$ $cm^{-3}$ value obtained is close to intrinsic doping level. Additionally, these Ga60 samples feature high in-plane variations, as previously mentioned. No $L_n$ mappings could be obtained for this fluence, and none of the solar cells irradiated at this fluence was EQE mapped entirely. Therefore, EQE measurements at other positions could have resulted in different EQE spectral dynamics. It is then possible that the type inversion would have occurred only in specific in-plane locations of the cell.

It is also possible that no type inversion was indeed reached, in compliance with the modeling study. However, further analysis would be required to evaluate the impact that a lower $p_0$ in only a part of the bulk thickness would have on the $R_{sheet}$ values.

Therefore, further measurements and additional characterization techniques would be interesting to strenghten this investigation. The EQE measurements could be completed with

further in-plane positions. Electron beam-induced current (EBIC) could have been used to detect the in-depth location of the junction. Spreading resistance measurements would have allowed to actually get all the carrier concentration variations in the depth, enabling more accurate modeling work with different layers and with different levels of damage.

## Conclusion

In this study, the effects of irradiation with 1 $MeV$ and 3 $MeV$ proton energies on high resistivity (60 $\Omega.cm$) Ga-doped c-Si SHJ solar cells were investigated, resulting in heterogeneous degradation across the bulk thickness. Overall, the PV performances of the solar cells were significantly degraded for the tested fluences, with particularly severe degradation observed in $J_{SC}$. The 3 $MeV$ proton irradiation induced twice the degradation in $J_{SC}$ compared to the 1 $MeV$ proton irradiation, which was unexpected given the previous studies conducted in 1982 [114] and 1996 [107]. To get further insights, this $J_{SC}$ degradation was thoroughly analyzed using EQE measurements.

The importance of using a bias light for EQE measurements was emphasized. Particularly, bias light was required to match the $J_{SC}$ values obtained from both I-V and EQE measurements. Interestingly, these two energies exhibited different behaviors under illumination. For 1 $MeV$ proton energy, the spectral response improved with increasing light intensity, while for 3 $MeV$ proton energy, the spectral response degraded with increasing light intensity. This was further confirmed by I-V measurements at varying light intensities.

Most of the EQE spectral variations after proton irradiation were successively explained and reproduced by PC1D modeling. The modeled solar cell consisted in a proton penetration depth-thick damaged bulk zone and an undamaged bulk zone below. The damaged bulk zone model suggested a strong $\tau$ degradation (via SRH bulk recombination) and particularly pronounced carrier removal effects, resulting in conductivity type inversions for specific irradiation conditions. This spectral response-based modeling study was supported by $R_{sheet}$ measurements, which highlighted strong resistivity changes in the damaged regions of the irradiated samples. The extracted $p_0$ and $n_0$ values were in good agreement between both studies (i.e., EQE-based modeling and 4-point probe characterizations). The carrier removal effect for 3 $MeV$ proton irradiated solar cells was estimated to result in $R_c = 225\ cm^{-1}$. In comparison, no $p_0$ reduction was previously found for 1 $MeV$ electron-irradiated solar cells to a $1.5 \times 10^{15}\ cm^{-2}$ fluence (see Chapter 3). This supports the expectation of a stronger $R_c$ for 1 $MeV$ proton irradiation ($\approx 500\ cm^{-1}$ [107]) compared to 1 $MeV$ electron irradiation ($\approx 0.1\ cm^{-1}$ [122]).

The solar cells irradiated with 3 $MeV$ protons underwent less carrier removal effect in the damaged bulk than those irradiated with 1 $MeV$ protons, as expected from TRIM simulations. However, for the 3 $MeV$ case, even a small reduction of the carrier concentration had a significant effect on the solar cell performance, unlike the 1 $MeV$ case. Our results indeed showed that a $p_0$ close to the intrinsic level, combined with a low $\tau$ over a large portion (92 $\mu m$) of the cell thickness (160 $\mu m$), could result in rear-emitter behavior with low EQE values. Therefore, it is possible that the $J_{SC}$ would have been similar for solar cells exposed

to the 2 proton energies (similarly to literature) at lower doses, at which the carrier removal effect had not yet begun. The specific proton energy-dependent behavior highlighted would thus be a result of both the high fluences used and the initial low $p_0$.

Additionally, significant in-plane variations of the electronic properties (i.e., equilibrium carrier concentrations, conductivity type, $\tau$) were observed after proton irradiation through $L_n$ mappings and local EQE spectral measurements. This peculiar effect was linked to both the initial high resistivity of the samples and the significant initial $p_0$ in-plane variations of this compensated material, originating from oxygen-related thermal donors distribution. These $p_0$ in-plane variations were accentuated by the carrier removal effect induced by proton irradiation. For some irradiation conditions, conductivity-type inversions were observed only for specific in-plane regions.

# Conclusion & Perspectives

In the context of the rapid growth of the space sector—particularly with the rise of satellite constellations—c-Si solar cells are becoming an attractive alternative to multi-junction cells, which are more expensive and have limited production capacities. Among the different c-Si technologies, silicon heterojunction (SHJ) solar cells stand out due to their high beginning-of-life (BOL) efficiency, compatibility with thin wafers, and industrial maturity. This thesis focuses on understanding the degradation mechanisms induced by particle irradiation specific to the space environment in Ga-doped SHJ cells, with the goal of identifying key levers to optimize their end-of-life (EOL) performance.

High concentrations of particles—electrons and protons— are found abundantly in Earth's Van Allen belts, and represent the primary source of performance degradation of c-Si solar cells in space. These particles can induce atomic displacements within the silicon crystal lattice, leading to the formation of numerous defects. These defects mainly reduce the carrier lifetime $\tau$ (reduction quantified by using the minority carrier diffusion length damage coefficient $K_L$) and decrease the majority carrier concentration, $p_0$ in p-type material (reduction quantified by using $R_c$, the majority carrier removal rate). In extreme cases, this reduction in majority carrier concentration can even lead to a conductivity type inversion. To mitigate the impact of these effects on the EOL performances of c-Si solar cells, optimizing both the cell architecture and the material properties is essential. It is widely accepted, for instance, that using a front-side emitter in combination with a p-type, potentially very thin, substrate can help to limit the performance degradation. However, the optimal values for other parameters related to radiation resilience, such as substrate resistivity, or oxygen concentration, remain unclear. Notably, most existing researches on this topic are over 20 years old. Therefore, it is particularly relevant to evaluate the radiation resilience of state-of-the-art solar cell technologies—now developed for terrestrial applications—which have seen significant advances in both materials and designs in the past two decades.

This work therefore evaluated the radiation resilience of SHJ solar cells through two main axes. The first study focused on the influence of resistivity, Ga concentration (with Ga having recently become the standard dopant for p-type c-Si), oxygen and oxygen-related defects contents on the resilience of both c-Si materials and SHJ cells to electron irradiation. Within the second study, the performance limits of c-Si solar cells were investigated under harsh simulated space conditions using particularly high fluences of low-energy protons, which create a non-uniform distribution of defects throughout the cell depth.

The measurements techniques used in this PhD, and introduced in Chapter 2, ranged from bulk analyses (e.g., Hall effect, four-point probe, QSS-PC, and OxyMap) to device performance evaluations (e.g., I-V, EQE, LBIC mappings and Suns-$V_{OC}$). PC1D modeling

further enhanced the understanding of several behaviors and trends observed experimentally.

In **Chapter 3**, the resilience of modern Ga-doped SHJ solar cells to 1 $MeV$ electron irradiation (at fluences ranging from $1.5 \times 10^{14}$ to $1.5 \times 10^{15}$ $cm^{-2}$) was studied, with a focus on the influence of wafer composition, resistivity, and cell thickness. To this end, SHJ solar cells of three different thicknesses (80 $\mu m$, 110 $\mu m$, and 160 $\mu m$) were fabricated using Ga-doped c-Si wafers with three different resistivity levels: 0.9 $\Omega.cm$ (Ga0.9), 15 $\Omega.cm$ (Ga15), and 60 $\Omega.cm$ (Ga60). The Ga15 and Ga60 groups share similar Ga concentrations but differ significantly in the concentration of thermal donors (TDs), with the Ga60 group exhibiting approximately four times more TDs. These TDs, oxygen-related and specific to Czochralski (Cz) ingot manufacturing process, feature an in-plane distribution with circular patterns. TDs act as double donors and therefore directly influence the initial equilibrium hole concentration $p_0$, affecting various aspects of the cells' response to both electron and proton irradiations.

This study demonstrated stable $p_0$ and $\mu_p$ within the doping ranges and 1 $MeV$ electron fluences investigated. This confirmed that Ga-doped c-Si was less affected by carrier removal effects than reported in literature for B-doped c-Si. The $\tau$ degradation dynamics with electron fluence were quantified and their dependence on $p_0$ values highlighted: the lower the $p_0$, the higher the EOL $\tau$ at low $\Delta n$. In addition, significant spatial variations of $L_n$ were revealed through in-plane $L_n$ mappings of the Ga60 samples. The $L_n$ variations were most likely driven by the $p_0$ variations for this compensated material (already present in BOL), which originated from the non-homogeneous spatial distribution of the TDs. SRH recombination via defects previously identified in B-doped c-Si possibly linked to divacancy complexes reproduced well those effects. In addition, a study conducted on the influence of dopant atoms (either Ga or B) on EOL $\tau$ seemed to show that the nature of the dopant has a limited impact on the EOL $\tau$. This study suggested that the $\tau$-limiting defect density was neither dependent on the nature and concentration of the dopant nor dependent on $[O_i]$ or [TD]. Overall, the $\tau$ parameter appeared to be determined by $p_0$ after irradiation. Particularly, the [TD] seemed to only have an influence on $\tau$ due to their impact on $p_0$.

This study could have been completed with DLTS analyses to assess the evolution of the defect concentrations combined with T-IDLS procedures to monitor the recombination activity of the $\tau$-limiting defect with increasing fluence. This would have been particularly interesting with the range of $[O_i]$ used in this study.

The 4× higher $\tau$ at low $\Delta n$ for Ga60 wafers in comparison to the value found for Ga0.9 wafers resulted in 9% relative change in $J_{SC}$ in favor of Ga60 at $1.5 \times 10^{15}$ $cm^{-2}$ fluence. However, the advantage of high $p_0$ when the irradiation significantly affected $\tau$ for both the $V_{OC}$ and $FF$ parameters was highlighted. With low $p_0$ wafers, the radiation-induced $FF$ degradation was essentially caused by bulk resistivity increases. Overall, lowering the wafer thickness benefited to the conversion efficiency, the gain being stronger for the cells with the lowest $p_0$. The mass savings are also a strong motivation for thin wafers. For a given irradiation fluence, it is thus necessary to find the best compromise when choosing the $p_0$ of the samples, without neglecting the influence of the wafer thickness. The best EOL solar cell efficiency was obtained for Ga15 80 $\mu m$ solar cells. Overall, for solar cells irradiated at the

$1.5 \times 10^{15}$ $cm^{-2}$ fluence:

- the wafer reduction from 160 $\mu m$ to 80 $\mu m$ resulted in a 1% absolute increase of efficiency for Ga60.
- the best efficiency among the tested samples was for a Ga15 80 $\mu m$ cell with a 10.0% value.
- using Ga15 80 $\mu m$ solar cells instead of Ga0.9 160 $\mu m$ (industry standard at the beginning of this PhD) led to an absolute increase of [0.4–0.9]% efficiency.

As seen in this chapter, a lever in the increase of performances relies on the optimization of the $FF$ parameter. Indeed, no reduction of $FF$ at EOL was found for Ga0.9 solar cells. This means that the higher the BOL $FF$, the higher the EOL $FF$ when using high $p_0$ wafers. When using low $p_0$ wafers, the cell structure should be carefully chosen to cope with high bulk resistivity without suffering from high performance degradation. An enhanced BOL $J_{SC}$ due to improved optical properties can also enhance the EOL $J_{SC}$, while it is not the case for the $V_{OC}$ parameter. This aspect was further investigated (the main results are presented in the appendix) within this PhD through a study that focused on the improvement of $J_{SC}$ parameter by adapting the thickness of the thin layers on the front side of the SHJ cells. This study conducted to significant $J_{SC}$ improvement and the developed architecture was protected by a patent application.

In **Chapter 4**, the effects of 1 $MeV$ and 3 $MeV$ proton energies on 160 $\mu m$-thick Ga-doped SHJ solar cells with high bulk resistivity (60 $\Omega.cm$, referred to as Ga60) were investigated. These low-energy protons caused non-uniform degradation through the c-Si bulk, affecting only the first 16 $\mu m$ of the cell in the case of 1 $MeV$ irradiation, and the first 92 $\mu m$ in the case of 3 $MeV$ irradiation. A peak in damage, known as the Bragg peak, occurs at the end of these damaged regions, where protons stop in the c-Si. It is worth noting that, in this study, the cell sample dimensions were further reduced ($1.5 \times 1.5$ $cm^2$) to meet the constraints imposed by the use of the proton beam.

Overall, the performance of the solar cells was significantly degraded for the tested fluences (ranging from $1 \times 10^{12}$ $cm^{-2}$ to $1 \times 10^{14}$ $cm^{-2}$), with particularly severe degradation observed in $J_{SC}$. For a same fluence, the EOL $J_{SC}$ values were at least twice higher for the solar cells irradiated with 1 $MeV$ protons than with 3 $MeV$ protons. These $J_{SC}$ degradations were thoroughly analyzed using EQE measurements.

The importance of using a bias light for EQE measurements was emphasized. Particularly, it was required to match the $J_{SC}$ values obtained from both I-V and EQE measurements. Interestingly, these two proton energies resulted in irradiated solar cells with different behaviors under illumination. For 1 $MeV$ proton irradiation, the spectral response improved with increasing light intensity, while for 3 $MeV$ proton irradiation, the spectral response degraded with increasing light intensity. This was further confirmed by I-V measurements at various light intensities.

Most of the EQE spectral variations after proton irradiation were successively explained and reproduced by PC1D modeling. The modeled solar cell consisted in a proton penetration

depth-thick damaged bulk zone and an undamaged bulk zone beneath. The damaged bulk zone model suggested both strong $\tau$ degradations (via SRH bulk recombination) and particularly pronounced carrier removal effects, resulting in conductivity type inversions for some irradiation conditions. This spectral response-based modeling study was supported by $R_{sheet}$ measurements, which highlighted strong resistivity changes in the damaged regions of the irradiated samples. The extracted $p_0$ and $n_0$ values were in good agreement between both studies (i.e., EQE-based modeling and 4-point probe characterizations). The carrier removal effect for 3 $MeV$ proton irradiated solar cells was estimated to result in $R_c = 225\ cm^{-1}$.

The solar cells irradiated to 3 $MeV$ proton underwent less carrier removal effect in the damaged bulk than those irradiated with 1 $MeV$ protons, as expected from TRIM simulations. However, for the 3 $MeV$ case, even a small reduction of carrier concentration had a significant effect on the solar cell performance, unlike the 1 $MeV$ case. Our results indeed showed that a $p_0$ close to the intrinsic level, combined with a low $\tau$ over a large portion (92 $\mu m$) of the cell thickness (160 $\mu m$), could result in rear-emitter behavior with low EQE values. Therefore, the $J_{SC}$ for solar cells exposed to either 1 $MeV$ protons or 3 $MeV$ protons could possibly be similar (as observed in the literature) at lower fluences, before the carrier removal effect becomes significant. The specific proton energy-related behavior we highlighted was thus a result of both the high fluences used and the initial low $p_0$.

Additionally, significant in-plane variations of the electronic properties were observed after proton irradiation through $L_n$ mappings and local EQE spectral measurements. This particular effect is linked to both the initial high resistivity of the samples and the significant initial $p_0$ in-plane variations of this compensated material originating from oxygen-related thermal donors distribution. These $p_0$ in-plane variations were accentuated by the carrier removal effect induced by proton irradiation. For some irradiation conditions, conductivity-type inversions were observed only for specific in-plane regions.

Overall, this modeling study successfully explained and reproduced most of the observed experimental features. However, the analysis could have been refined using a software capable of modeling heterojunction structures, and including a detailed description of defects and multiple defects (e.g., Afors-Het). Considering the in-plane inhomogeneities of these samples, software such as SILVACO would have been able to model their associated behaviors effectively.

Further measurements would be interesting to complete this investigation. The EQE measurements could be completed with further in-plane locations, and measurements on the cell rear-side as well. Electron beam-induced current (EBIC) could have been used to detect the in-depth location of the junction. Spreading resistance measurements would have allowed to actually get all the carrier concentration variations in the depth, enabling a more accurate modeling.

These results could also be completed with a lower fluence with similar solar cells. It would also be interesting to irradiate in the same conditions solar cells of lower resistivity (e.g. 0.9 $\Omega.cm$), in order to assess the influence of the initial $p_0$.

Overall, the damage underwent by the solar cells exposed to these proton irradiation conditions was strong. This degradation was mainly caused by high reductions of majority

carrier concentration, and the impact was particularly noticeable due to the high initial resistivity. Two key points should be considered. Firstly, such high fluences should only be reached in case of long missions in particularly proton rich orbits such as upper LEO and MEO. Secondly, the solar cells are expected to be encapsulated when assembled into solar arrays, the Bragg peaks for these energies would then be located within the front shielding materials (e.g. coverglass). Therefore, it would be interesting to conduct similar studies by using cells mounted in PVA (i.e., modules).

# Appendix. Optical properties adaptation for improved EOL performances

As seen in Chapter 3, the irradiation of SHJ solar cells with 1 $MeV$ electrons at fluences ranging from $1.5 \times 10^{14}$ $cm^{-2}$ to $1.5 \times 10^{15}$ $cm^{-2}$ primarily affects the bulk $\tau$. As a result, the EOL spectral responses exhibited a reduction in EQE values only for the long wavelengths, thereby reducing the $J_{SC}$. However, the EQE values for the short wavelengths remained unchanged between BOL and EOL conditions.

A significant reduction of the $V_{OC}$ was also observed after 1 $MeV$ electron irradiation, as detailed in Chapter 3. For Ga15 (15 $\Omega.cm$ Ga-doped c-Si) solar cells, the $V_{OC}$ decreased from $\approx 730$ $mV$ to $\approx 550$ $mV$ and $\approx 500$ $mV$ after irradiation at fluences of $1.5 \times 10^{14}$ $cm^{-2}$ and $1.5 \times 10^{15}$ $cm^{-2}$, respectively. It is noteworthy that with $\tau_{bulk}$ as low as $\approx 4$ $\mu s$ after irradiation at a $1.5 \times 10^{14}$ $cm^{-2}$ 1 $MeV$ electron fluence, a higher surface recombination velocity (SRV) has minimal impact on the recombination-induced $V_{OC}$ losses.

The TCO and a-Si:H layers used in SHJ solar cells are known for their high absorbance, leading to sub-optimal $J_{SC}$ values. Therefore, the question arises whether thinner front TCO and a:Si:H layers could benefit to the EOL efficiency of the solar cells. Previous studies showed that the TCO layer thickness could be reduced from 100 $nm$ to 15 $nm$ with a $SiN_x$:H capping layer without significant efficiency losses [71]. Reducing the a:Si:H layers thickness would inevitably decrease the front passivation, it was thus crucial to evaluate the impact of thinner a-Si:H layers on EOL performances.

### Design of experiments

For this purpose, the 90 $\mu m$-thick Ga15 SHJ solar cells (half M2 dimensions) described in Table A.1 were produced at CEA/INES pilot line. The variations included replacing the front 100 $nm$ TCO layer with 15 $nm$ of TCO capped with 100 $nm$ of $SiN_x$:H. The thicknesses of the different front a-Si:H layers were also varied. It is worth noting that the expected total thicknesses (indicated by the number following the letter "a" in the group names) were not measured post-deposition. The thicknesses of each layer were adjusted by tuning the deposition process duration. These cells were irradiated at $1.5 \times 10^{14} - 1.5 \times 10^{15}$ $cm^2$ 1 $MeV$ electron fluences.

| Group | a8- ITO 100 nm | a8- full (i), full (n) | a5- 0 (i), full (n) | a4- half (i), half (n) | a2.5- 0 (i), half (n) |
|---|---|---|---|---|---|
| **Front** | | | | | |
| $SiN_x$:H (nm) | 0 | 100 | | | |
| TCO (nm) | 100 | 15 | | | |
| a-Si:H (n) (nm) | 5 | | | 2.5 | |
| a-Si:H (i) (nm) | 3 | | 0 | 1.5 | 0 |
| **Bulk** | | | | | |
| Dopant | Ga | | | | |
| Resistivity ($\Omega.cm$) | 15 | | | | |
| Thickness ($\mu m$) | 90 | | | | |
| **Rear** | | | | | |
| a-Si:H (i) (nm) | 3 | | | | |
| a-Si:H (p) (nm) | 5 | | | | |
| TCO (nm) | 40 | | | | |
| SiN (nm) | 0 | | | | |

Table A.1: Summary of the cell architecture features of the irradiated samples.

## Results

The average BOL $J_{SC}$ and $V_{OC}$ values obtained with AM0 I-V measurements are summarized in Table A.2. A slight increase of 0.5 $mA/cm^2$ in $J_{SC}$ is observed when switching from a front 100 $nm$ ITO (a8- ITO 100 nm) to the stack consisting of thin ITO and $SiN_x$:H layers (a8- full (i), full (n)). Conversely, the $V_{OC}$ is reduced by 11 $mV$ in the case of the thin ITO and $SiN_x$:H stack. It is noteworthy that this difference was not anticipated based on previous results obtained on the same pilot line [71], and could be due to an anomaly in this particular batch of samples. Overall, the solar cells in this study exhibited low $FF$ with significant variations that were not fully understood. For this reason, $FF$ and efficiency data are not presented here.

Regarding the variations of BOL $J_{SC}$ and $V_{OC}$ as a function of the a-Si:H layer thicknesses, a 3% gain is obtained in $J_{SC}$ by reducing the a-Si:H stack thickness from 8 $nm$ to 2.5 $nm$. Under the same conditions, the $V_{OC}$ decreased by 20%, with values dropping to 612 $mV$ for the 2.5 $nm$ a-Si:H stack thickness, due to a significant surface passivation reduction.

| average BOL AM0 I-V | $J_{SC}$ (mA/cm$^{-2}$) | $V_{OC}$ (mV) |
|---|---|---|
| **a8- ITO 100 nm** | 45.4 | 736 |
| **a8- full (i), full (n)** | 45.9 | 725 |
| **a5- 0 (i), full (n)** | 46.3 | 699 |
| **a4- half (i), half (n)** | 47.0 | 648 |
| **a2.5- 0 (i), half (n)** | 47.3 | 612 |

Table A.2: $J_{SC}$ and $V_{OC}$ values obtained with AM0 I-V measurements on BOL Ga15 SHJ cells. The different groups are described in Table A.1

The $J_{SC}$ and $V_{OC}$ values obtained before and after irradiation with AM0 I-V measurements for 1 $MeV$ electron irradiated cells are shown in Figure A.1. For every fluence tested, the $V_{OC}$ of all the cell groups converged to the same value, values similar to those reported in Chapter 3 for the Ga15 group cells. The gain in $J_{SC}$ when reducing the a-Si:H stack from 8 $nm$ to 2.5 $nm$ remains at 3% at $1.5 \times 10^{14}$ $cm^{-2}$ fluence. This gain yet gradually decreases with increasing fluence: 2% at a fluence of $7.5 \times 10^{14}$ $cm^{-2}$, and 1.5% at a fluence of $1.5 \times 10^{15}$ $cm^{-2}$.

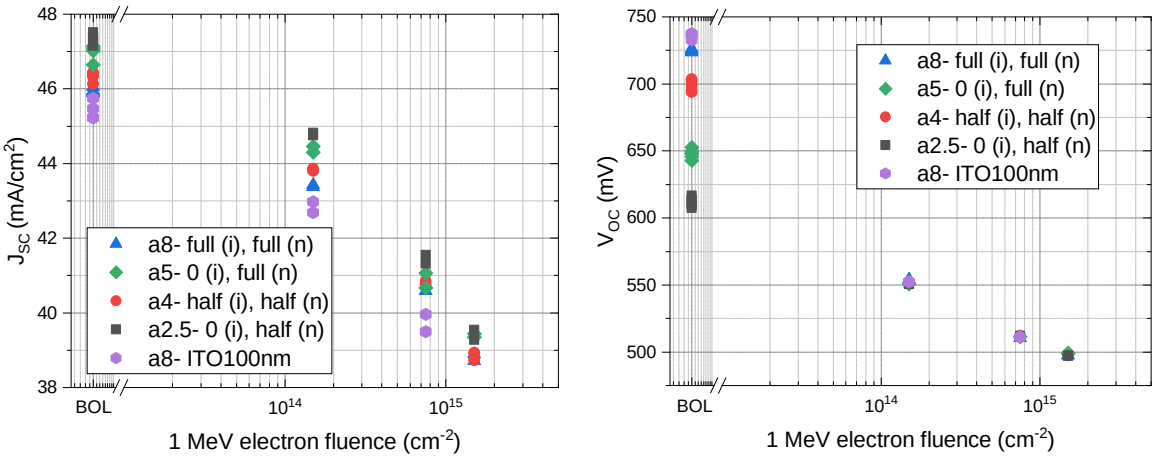


(a) (b)

Figure A.1: (a) $J_{SC}$ and (b) $V_{OC}$ values obtained with AM0 I-V measurements on Ga15 SHJ cells irradiated with 1 $MeV$ electrons. The different groups are described in Table A.1

The spectral variations in EQE for the different groups of Ga15 SHJ cells irradiated at a $7.5 \times 10^{14}$ $cm^{-2}$ 1 $MeV$ electron fluence are shown in Figure A.2. It appears that both a2.5-0 (i), half (n) and a5- 0 (i), full (n) groups exhibited higher EQE values for short wavelengths compared to the standard condition. This highlights the benefit of improving the front surface transparency by reducing the thickness of the a-Si:H (i) layer rather than the thickness of the a-Si:H (n) layer.

The EQE equipment here in this study is from *Aescusoft*. This equipment is capable of measuring large-area solar cells ($> 100$ $cm^2$), with the cell fully illuminated, making it relevant for this study. It is worth noting that the EQE values presented in Figure A.2 appear to be

overestimated, likely due to a non-optimized calibration. However, since all measurements were carried out during the same session with the same calibration set-up, relative comparisons remain valid.

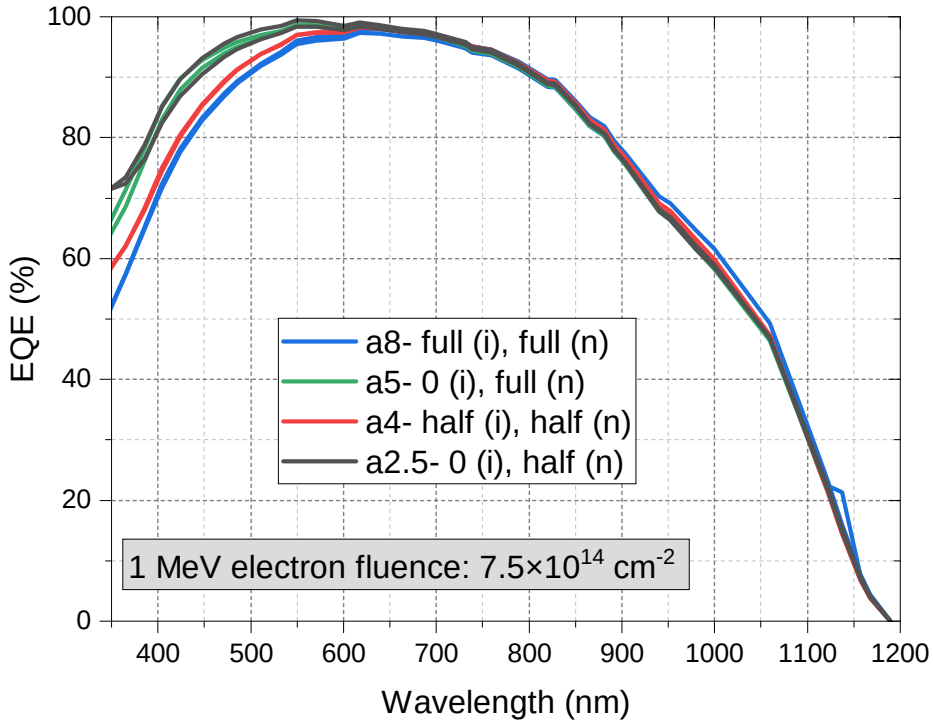


Figure A.2: EQE spectral variations of Ga15 SHJ cells irradiated at a 7.5 $\times 10^{14}$ $cm^{-2}$ 1 $MeV$ electron fluence. The different groups are described in Table A.1.

## Conclusion

A gain of up to 3 % of $J_{SC}$ can be achieved at EOL by reducing the thickness of the front a-Si:H layers, without leading to a reduction of $V_{OC}$ (at EOL). With a suppressed a-Si:H (i) layer, reducing or not the a-Si:H (n) layer resulted in similar $J_{SC}$ gains at EOL. Suppressing only the a-Si:H (i) layer without reducing the thickness of the a-Si:H (n) layer results however in better BOL $V_{OC}$ values compared to cells with a 2.5 nm a-Si:H stack, and could thus be a good compromise.

Optical simulations were conducted in parallel and confirmed that the $J_{SC}$ benefits would remain after the encapsulation of the solar cells.

# Bibliography


[1] D. M. Chapin, C. S. Fuller, and G. L. Pearson. "A New Silicon p-n Junction Photocell for Converting Solar Radiation into Electrical Power". *Journal of Applied Physics* 25.5 (May 1954), pp. 676–677. ISSN: 0021-8979. DOI: 10.1063/1.1721711.

[2] R. L. Easton and M. J. Votaw. "Vanguard I IGY Satellite (1958 Beta)". *Review of Scientific Instruments* 30.2 (Feb. 1959), pp. 70–75. ISSN: 0034-6748, 1089-7623. DOI: 10.1063/1.1716492.

[3] Z. I. Alferov, V. M. Andreev, M. B. Kagan, I. I. Protasov, and V. G. Trofim. "Solar-energy converters based on p-n AlxGal-x As-GaAs heterojunctions". *Sov. Phys. - Semicond. (Engl. Transl.); (United States)* 4:12 (June 1971).

[4] D. H. Walker. *Results of the solar cell experiments on the NTS-2 satellite after 223 days in orbit*. Tech. rep. Sept. 1978.

[5] – *SPACE Solar Cells - AZUR SPACE Solar Power GmbH*. URL: https://www.azurspace.com/index.php/en/products/products-space/space-solar-cells (visited on 02/17/2025).

[6] *Best Research-Cell Efficiency Chart*. July 2025. URL: https://www.nrel.gov/pv/cell-efficiency (visited on 08/08/2025).

[7] W. Shockley and H. Queisser. "Detailed balance limit of efficiency of p–n junction solar cells". 2 (2011), pp. 35–54.

[8] S. Rühle. "Tabulated values of the Shockley–Queisser limit for single junction solar cells". *Solar Energy* 130 (June 2016), pp. 139–147. ISSN: 0038-092X. DOI: 10.1016/j.solener.2016.02.015.

[9] *27.81 %! LONGi Refreshes the World Record for the Efficiency of Monocrystalline Silicon Cells Again*. Apr. 2025. URL: https://www.longi.com/en/news/isfh-hibc-conversion-efficiency/ (visited on 08/08/2025).

[10] M. A. Green *et al.* "Solar Cell Efficiency Tables (Version 66)". *Progress in Photovoltaics: Research and Applications* 33.7 (2025), pp. 795–810. DOI: 10.1002/pip.3919.

[11] S. W. Glunz, S. Rein, J. Y. Lee, and W. Warta. "Minority carrier lifetime degradation in boron-doped Czochralski silicon". *Journal of Applied Physics* 90.5 (Sept. 2001), pp. 2397–2404. ISSN: 0021-8979, 1089-7550. DOI: 10.1063/1.1389076.

[12] A. Ansari Dezfoli. "Optimizing cooling strategies in the Czochralski process for large-diameter silicon ingots". *Journal of Crystal Growth* 649 (Jan. 2025), p. 127920. ISSN: 0022-0248. DOI: 10.1016/j.jcrysgro.2024.127920.

[13] S. W. Glunz, S. Rein, J. Knobloch, W. Wettling, and T. Abe. "Comparison of boron- and gallium-doped p-type Czochralski silicon for photovoltaic application". *Progress in Photovoltaics: Research and Applications* 7.6 (Nov. 1999), pp. 463–469. ISSN: 1062-7995, 1099-159X. DOI: 10.1002/(SICI)1099-159X(199911/12)7:6<463::AID-PIP293>3.0.CO;2-H.

[14] S. W. Glunz *et al.* "n-type silicon - enabling efficiencies > 20% in industrial production". *2010 35th IEEE Photovoltaic Specialists Conference*. June 2010, pp. 50–56. DOI: 10.1109/PVSC.2010.5614203.

[15] S. Tepner and A. Lorenz. "Printing technologies for silicon solar cell metallization: A comprehensive review". *Progress in Photovoltaics: Research and Applications* 31.6 (2023), pp. 557–590. ISSN: 1099-159X. DOI: 10.1002/pip.3674.

[16] M. Fischer. *International Technology Roadmap for Photovoltaics (ITRPV) 16th edition*. 2025. URL: https://www.vdma.eu/en-GB/international-technology-roadmap-photovoltaic.

[17] S. D. Wolf, A. Descoeudres, Z. C. Holman, and C. Ballif. "High-efficiency Silicon Heterojunction Solar Cells: A Review". *Green* 2.1 (Mar. 2012), pp. 7–24. ISSN: 1869-8778. DOI: 10.1515/green-2011-0018.

[18] R. V. K. Chavali, S. De Wolf, and M. A. Alam. "Device physics underlying silicon heterojunction and passivating-contact solar cells: A topical review". *Progress in Photovoltaics: Research and Applications* 26.4 (2018), pp. 241–260. ISSN: 1099-159X. DOI: 10.1002/pip.2959.

[19] Z. Sun, X. Chen, Y. He, J. Li, J. Wang, H. Yan, and Y. Zhang. "Toward efficiency limits of crystalline silicon solar cells: recent progress in high-efficiency silicon heterojunction solar cells". *Advanced Energy Materials* 12.23 (2022), p. 2200015. DOI: 10.1002/aenm.202200015.

[20] A. Razzaq, T. G. Allen, W. Liu, Z. Liu, and S. D. Wolf. "Silicon heterojunction solar cells: Techno-economic assessment and opportunities". *Joule* 6.3 (Mar. 2022), pp. 514–542. ISSN: 2542-4785, 2542-4351. DOI: 10.1016/j.joule.2022.02.009.

[21] R. Verduci, V. Romano, G. Brunetti, N. Yaghoobi Nia, A. Di Carlo, G. D'Angelo, and C. Ciminelli. "Solar Energy in Space Applications: Review and Technology Perspectives". *Advanced Energy Materials* 12.29 (Aug. 2022), p. 2200125. ISSN: 1614-6832, 1614-6840. DOI: 10.1002/aenm.202200125.

[22] A. Jasenek and U. Rau. "Defect generation in Cu(In,Ga)Se2 heterojunction solar cells by high-energy electron and proton irradiation". *Journal of Applied Physics* 90.2 (July 2001), pp. 650–658. ISSN: 0021-8979. DOI: 10.1063/1.1379348.

[23] H. Afshari, B. K. Durant, C. R. Brown, K. Hossain, D. Poplavskyy, B. Rout, and I. R. Sellers. "The role of metastability and concentration on the performance of CIGS solar cells under Low-Intensity-Low-Temperature conditions". *Solar Energy Materials and Solar Cells* 212 (2020), p. 110571. ISSN: 0927-0248. DOI: 10.1016/j.solmat.2020.110571.

[24] H. Wei and J. Huang. "Halide lead perovskites for ionizing radiation detection". *Nature Communications* 10.1 (Mar. 2019), p. 1066. ISSN: 2041-1723. DOI: 10.1038/s41467-019-08981-w.

[25] M. Yamaguchi, K.-H. Lee, K. Araki, N. Kojima, Y. Okuno, and M. Imaizumi. "Analysis for nonradiative recombination loss and radiation degradation of Si space solar cells". *Progress in Photovoltaics: Research and Applications* 29.1 (Jan. 2021), pp. 98–108. ISSN: 1062-7995, 1099-159X. DOI: 10.1002/pip.3346.

[26] Y. Gurimskaya *et al.* "Effective Annealing of Proton and Electron Radiation Damage in Ultra-Thin Silicon Solar Cells". *2023 13th European Space Power Conference (ESPC)*. Oct. 2023, pp. 1–5. DOI: 10.1109/ESPC59009.2023.10298179.

[27] V. S. Kalinovskii *et al.* "Studies of Degradation Silicon Heterojunction Solar Cells by 1 MeV Electrons Irradiation". *Applied Solar Energy* 59.5 (Oct. 2023), pp. 604–611. ISSN: 1934-9424. DOI: 10.3103/S0003701X23600984.

[28] S. Duarte-Cano *et al.* "Proton irradiation effects on silicon heterojunction solar cells with MoOx selective contacts". *Materials Science in Semiconductor Processing* 190 (May 2025), p. 109312. ISSN: 1369-8001. DOI: 10.1016/j.mssp.2025.109312.

[29] R. Cariou, A. Danel, N. Enjalbert, F. Jay, and S. Dubois. "Investigation of p-Type Silicon Heterojunction Radiation Hardness". *IEEE Journal of Photovoltaics* 14.1 (Jan. 2024), pp. 41–45. ISSN: 2156-3381, 2156-3403. DOI: 10.1109/JPHOTOV.2023.3333197.

[30] A. Reinders, P. Verlinden, W. v. Sark, and A. Freundlich, eds. *Photovoltaic solar energy: from fundamentals to applications*. Chichester, West Sussex, United Kingdom ; Hoboken, NJ: John Wiley & Sons Ltd, 2017. ISBN: 978-1-118-92746-5. DOI: 10.1002/9781118927496.

[31] P. Würfel. "Basic Structure of Solar Cells". *Physics of Solar Cells*. John Wiley & Sons, Ltd, 2005, pp. 109–136. ISBN: 978-3-527-61854-5. DOI: 10.1002/9783527618545.ch6.

[32] S. Rein. *Lifetime Spectroscopy: A Method of Defect Characterization in Silicon for Photovoltaic Applications*. Ed. by R. Hull, R. Osgood, J. Parisi, and H. Warlimont. Vol. 85. Springer Series in Material Science. Berlin, Heidelberg: Springer, 2005. ISBN: 978-3-540-25303-7. DOI: 10.1007/3-540-27922-9.

[33] H. Schlangenotto, H. Maeder, and W. Gerlach. "Temperature dependence of the radiative recombination coefficient in silicon". *physica status solidi (a)* 21.1 (1974), pp. 357–367. DOI: 10.1002/pssa.2210210140.

[34] P. AUGER. "Sur les rayons beta secondaires produits dans un gaz par des rayons X." *CR Acad. Sci. (F)* 177 (1923), p. 169.

[35] L. Meitner. "Über den Zusammenhang zwischen beta- und gamma-Strahlen". *Zeitschrift für Physik* 9.1 (Dec. 1922), pp. 145–152. ISSN: 0044-3328. DOI: 10.1007/BF01326963.

[36] D. Matsakis, A. Coster, B. Laster, and R. Sime. "A renaming proposal: "The Auger–Meitner effect"". *Physics Today* 72.9 (Sept. 2019), pp. 10–11. ISSN: 0031-9228. DOI: 10.1063/PT.3.4281.

[37] J. Dziewior and W. Schmid. "Auger coefficients for highly doped and highly excited silicon". *Applied Physics Letters* 31.5 (1977), pp. 346–348. DOI: 10.1063/1.89694.

[38] A. Richter, S. W. Glunz, F. Werner, J. Schmidt, and A. Cuevas. "Improved quantitative description of Auger recombination in crystalline silicon". *Physical Review B* 86.16 (Oct. 2012), p. 165202. DOI: 10.1103/PhysRevB.86.165202.

[39] T. Niewelt *et al.* "Reassessment of the intrinsic bulk recombination in crystalline silicon". *Solar Energy Materials and Solar Cells* 235 (2022), p. 111467. ISSN: 0927-0248. DOI: 10.1016/j.solmat.2021.111467.

[40] L. E. Black and D. H. Macdonald. "On the quantification of Auger recombination in crystalline silicon". *Solar Energy Materials and Solar Cells* 234 (2022), p. 111428. ISSN: 0927-0248. DOI: 10.1016/j.solmat.2021.111428.

[41] W. Shockley and W. T. Read. "Statistics of the Recombinations of Holes and Electrons". *Physical Review* 87.5 (Sept. 1952), pp. 835–842. ISSN: 0031-899X. DOI: 10.1103/PhysRev.87.835.

[42] R. A. Sinton and A. Cuevas. "Contactless determination of current–voltage characteristics and minority-carrier lifetimes in semiconductors from quasi-steady-state photoconductance data". *Applied Physics Letters* 69.17 (Oct. 1996), pp. 2510–2512. ISSN: 0003-6951. DOI: 10.1063/1.117723.

[43] C. Honsberg and S. Bowden. *Photovoltaics Education Website*. 2019. URL: www.pveducation.org.

[44] *Solar Spectra*. URL: https://www.nrel.gov/grid/solar-resource/spectra (visited on 11/03/2023).

[45] C. Ballif, F.-J. Haug, M. Boccard, P. J. Verlinden, and G. Hahn. "Status and perspectives of crystalline silicon photovoltaics in research and industry". *Nature Reviews Materials* 7.8 (Mar. 2022), pp. 597–616. ISSN: 2058-8437. DOI: 10.1038/s41578-022-00423-2.

[46] M. Hirsch, U. Rau, and J. H. Werner. "Analysis of internal quantum efficiency and a new graphical evaluation scheme". *Solid-State Electronics* 38.5 (1995), pp. 1009–1015. ISSN: 0038-1101. DOI: 10.1016/0038-1101(95)98669-T.

[47] W. Zulehner. "Czochralski growth of silicon". *Journal of Crystal Growth* 65.1 (Dec. 1983), pp. 189–213. ISSN: 0022-0248. DOI: 10.1016/0022-0248(83)90051-9.

[48] B. Fickett and G. Mihalik. "Multiple batch recharging for industrial CZ silicon growth". *Journal of Crystal Growth* 225.2 (2001), pp. 580–585. ISSN: 0022-0248. DOI: 10.1016/S0022-0248(01)00956-3.

[49] J. Kamphues, A. Herguth, J. Miech, X. Bai, Y. Wang, G. Hahn, and F. Geml. "The impact of gettering on LeTID in industrial Czochralski grown gallium-doped p-type silicon ingots with melt recharging". *Solar Energy Materials and Solar Cells* 282 (2025), p. 113423. ISSN: 0927-0248. DOI: 10.1016/j.solmat.2025.113423.

[50] E. Letty. “Identification and neutralization of lifetime-limiting defects in Czochralski silicon for high efficiency photovoltaic applications”. PhD thesis. Université de Lyon, Oct. 2017.

[51] B. Zhou, W. Chen, Z. Li, R. Yue, G. Liu, and X. Huang. “Reduction of oxygen concentration by heater design during Czochralski Si growth”. *Journal of Crystal Growth* 483 (Feb. 2018), pp. 164–168. ISSN: 0022-0248. DOI: 10.1016/j.jcrysgro.2017.11.008.

[52] X. Yu, J. Chen, X. Ma, and D. Yang. “Impurity engineering of Czochralski silicon”. *Materials Science and Engineering: R: Reports* 74.1 (Jan. 2013), pp. 1–33. ISSN: 0927-796X. DOI: 10.1016/j.mser.2013.01.002.

[53] V. Meemongkolkiat, K. Nakayashiki, A. Rohatgi, G. Crabtree, J. Nickerson, and T. L. Jester. “Resistivity and lifetime variation along commercially grown Ga- and B-Doped Czochralski Si ingots and its effect on light-induced degradation and performance of solar cells”. *Progress in Photovoltaics: Research and Applications* 14.2 (2006), pp. 125–134. ISSN: 1099-159X. DOI: 10.1002/pip.659.

[54] J. Haunschild, J. Broisch, I. Reis, and S. Rein. “Cz-Si wafers in solar cell production: Efficiency-limiting defects and material quality control”. *Photovoltaics international* 15 (2012), pp. 40–46.

[55] W. Kaiser, H. L. Frisch, and H. Reiss. “Mechanism of the Formation of Donor States in Heat-Treated Silicon”. *Physical Review* 112.5 (Dec. 1958), pp. 1546–1554. DOI: 10.1103/PhysRev.112.1546.

[56] J. Svensson, B. G. Svensson, and J. L. Lindström. “Thermal donor formation in electron-irradiated Czochralski silicon”. *Applied Physics Letters* 49.21 (Nov. 1986), pp. 1435–1437. ISSN: 0003-6951. DOI: 10.1063/1.97346.

[57] P. Wagner and J. Hage. “Thermal double donors in silicon”. *Applied Physics A* 49.2 (Aug. 1989), pp. 123–138. ISSN: 1432-0630. DOI: 10.1007/BF00616290.

[58] J. Huang *et al.* “Effect of oxygen-related defects on the performance of seed-end wafers in Ga-doped recharged Czochralski silicon: Thermal donors”. *Journal of Crystal Growth* 630 (Mar. 2024), p. 127602. ISSN: 0022-0248. DOI: 10.1016/j.jcrysgro.2024.127602.

[59] J. Veirman, S. Dubois, N. Enjalbert, J. P. Garandet, D. R. Heslinga, and M. Lemiti. “Hall mobility reduction in single-crystalline silicon gradually compensated by thermal donors activation”. *Solid-State Electronics* 54.6 (June 2010), pp. 671–674. ISSN: 0038-1101. DOI: 10.1016/j.sse.2010.02.002.

[60] Z. Wang, X. Zhu, S. Yuan, X. Yu, and D. Yang. “Comprehensive characterization of efficiency limiting defects in the swirl-shaped region of Czochralski silicon”. *Solar Energy Materials and Solar Cells* 236 (Mar. 2022), p. 111533. ISSN: 0927-0248. DOI: 10.1016/j.solmat.2021.111533.

[61] H. Angelskår, R. Søndenå, M. S. Wiig, and E. S. Marstein. "Characterization of Oxidation-Induced Stacking Fault Rings in Cz Silicon: Photoluminescence Imaging and Visual Inspection After Wright etch". *Energy Procedia*. Proceedings of the 2nd International Conference on Crystalline Silicon Photovoltaics SiliconPV 2012 27 (Jan. 2012), pp. 160–166. ISSN: 1876-6102. DOI: 10.1016/j.egypro.2012.07.045.

[62] M. Tomassini, J. Veirman, R. Varache, E. Letty, S. Dubois, Y. Hu, and Ø. Nielsen. "Recombination activity associated with thermal donor generation in monocrystalline silicon and effect on the conversion efficiency of heterojunction solar cells". *Journal of Applied Physics* 119.8 (Feb. 2016), p. 084508. ISSN: 0021-8979. DOI: 10.1063/1.4942212.

[63] J. Lindroos, M. Yli-Koski, A. Haarahiltunen, M. C. Schubert, and H. Savin. "Light-induced degradation in copper-contaminated gallium-doped silicon". *physica status solidi (RRL) – Rapid Research Letters* 7.4 (2013), pp. 262–264. ISSN: 1862-6270. DOI: 10.1002/pssr.201307011.

[64] D. Chen *et al.* "Hydrogen-induced degradation: Explaining the mechanism behind light- and elevated temperature-induced degradation in n- and p-type silicon". *Solar Energy Materials and Solar Cells* 207 (2020), p. 110353. ISSN: 0927-0248. DOI: 10.1016/j.solmat.2019.110353.

[65] C. Chen, H. Wang, J. Wang, J. Lv, and H. Yang. "Performance degradation of commercial Ga-doped passivated emitter and rear cell solar modules in the field". *Progress in Photovoltaics: Research and Applications* 30.3 (2022), pp. 300–309. ISSN: 1099-159X. DOI: 10.1002/pip.3512.

[66] N. E. Grant, J. R. Scowcroft, A. I. Pointon, M. Al-Amin, P. P. Altermatt, and J. D. Murphy. "Lifetime instabilities in gallium doped monocrystalline PERC silicon solar cells". *Solar Energy Materials and Solar Cells* 206 (Mar. 2020), p. 110299. ISSN: 0927-0248. DOI: 10.1016/j.solmat.2019.110299.

[67] R. Post, T. Niewelt, W. Kwapil, and M. Schubert. "Carrier Lifetime Limitation of Industrial Ga-Doped Cz-Grown Silicon After Different Solar Cell Process Flows". *IEEE Journal of Photovoltaics* 12.1 (Jan. 2022), pp. 238–243. ISSN: 2156-3381, 2156-3403. DOI: 10.1109/JPHOTOV.2021.3116017.

[68] T. G. Allen, J. Bullock, X. Yang, A. Javey, and S. De Wolf. "Passivating contacts for crystalline silicon solar cells". *Nature Energy* 4.11 (Nov. 2019), pp. 914–928. ISSN: 2058-7546. DOI: 10.1038/s41560-019-0463-6.

[69] S. Dubois, B. Paviet-Salomon, J. Chen, W. Favre, R. Cabal, A. Bettinelli, and R. Kopecek. *n-Type Crystalline Silicon Photovoltaics: Technology, applications and economics*. IET Digital Library, Dec. 2022. ISBN: 978-1-83953-177-4. DOI: 10.1049/PBPO175E.

[70] G. Simandl, S. Paradis, and L. Simandl. "Future of photovoltaic materials with emphasis on resource availability, economic geology, criticality, and market size/growth". *CIM Journal* 14.3 (2023), pp. 133–157. DOI: 10.1080/19236026.2023.2168419.

[71] T. Gageot *et al.* "Feasibility test of drastic indium cut down in SHJ solar cells and modules using ultra-thin ITO layers". *Solar Energy Materials and Solar Cells* 261 (Oct. 2023), p. 112512. ISSN: 0927-0248. DOI: 10.1016/j.solmat.2023.112512.

[72] J. Haschke *et al.* "The impact of silicon solar cell architecture and cell interconnection on energy yield in hot & sunny climates". *Energy & Environmental Science* 10.5 (2017), pp. 1196–1206. DOI: 10.1039/C7EE00286F.

[73] D. Qiu *et al.* "Front contact optimization for rear-junction SHJ solar cells with ultra-thin n-type nanocrystalline silicon oxide". *Solar Energy Materials and Solar Cells* 209 (2020), p. 110471. ISSN: 0927-0248. DOI: 10.1016/j.solmat.2020.110471.

[74] ESA. *Types of orbits*. Mar. 2020. URL: https://www.esa.int/Enabling_Support/Space_Transportation/Types_of_orbits (visited on 05/08/2025).

[75] NASA. *Properties of Earth's Upper Atmosphere*. July 2010. URL: https://www.nasa.gov/image-article/properties-of-earths-upper-atmosphere/ (visited on 05/08/2025).

[76] M. M. Finckenor and K. de Groh. "A researcher's guide to: space environmental effects". *Researcher's Guide Series. National Aeronautics and Space Administration International Space Station* 15 (2017).

[77] Y. Lu, Q. Shao, H. Yue, and F. Yang. "A review of the space environment effects on spacecraft in different orbits". *IEEE access* 7 (2019), pp. 93473–93488. DOI: 10.1109/ACCESS.2019.2927811.

[78] *ARES | Orbital Debris Program Office | Debris Modeling*. URL: https://www.orbitaldebris.jsc.nasa.gov/modeling/ (visited on 07/14/2025).

[79] *NASA - Space debris*. URL: https://www.nasa.gov/headquarters/library/find/bibliographies/space-debris/ (visited on 07/14/2025).

[80] L. Giudici, C. Colombo, A. Horstmann, L. Francesca, and S. Lemmens. "Density-based evolutionary model of the space debris environment in low-Earth orbit". *Acta Astronautica* 219 (June 2024), pp. 115–127. ISSN: 0094-5765. DOI: 10.1016/j.actaastro.2024.03.008.

[81] Y. Akahoshi *et al.* "Influence of space debris impact on solar array under power generation". *International Journal of Impact Engineering* 35.12 (2008), pp. 1678–1682. ISSN: 0734-743X. DOI: 10.1016/j.ijimpeng.2008.07.048.

[82] E. Stofel and D. Joslin. "Low-Energy Proton Damage to Silicon Solar Cells". *IEEE Transactions on Nuclear Science* 17 (Jan. 1970), pp. 250–255. ISSN: 0018-9499. DOI: 10.1109/TNS.1970.4325801.

[83] J. A. Van Allen. "Radiation Belts around the Earth". *Scientific American* 200.3 (1959), pp. 39–47. ISSN: 0036-8733.

[84] C. Carreau. *ESA Science & Technology - Earth's plasmasphere and the Van Allen belts*. Sept. 2023. URL: https://sci.esa.int/web/cluster/-/52831-earth-plasmasphere-and-the-van-allen-belts (visited on 05/08/2025).

[85] T. P. OBrien, M. D. Looper, and J. B. Blake. "Quantification of relativistic electron microburst losses during the GEM storms". *Geophysical Research Letters* 31.4 (2004). DOI: 10.1029/2003GL018621.

[86] W. Schimmerling and S. B. Curtis. *Workshop on the radiation environment of the satellite power system*. Tech. rep. California Univ., Berkeley (USA). Lawrence Berkeley Lab., 1978.

[87] A. R. Kirmani *et al.* "Countdown to perovskite space launch: Guidelines to performing relevant radiation-hardness experiments". *Joule* 6.5 (May 2022), pp. 1015–1031. ISSN: 2542-4785, 2542-4351. DOI: 10.1016/j.joule.2022.03.004.

[88] C. Claeys and E. Simoen. "Displacement Damage in Group IV Semiconductor Materials". *Radiation Effects in Advanced Semiconductor Materials and Devices*. Ed. by C. Claeys and E. Simoen. Berlin, Heidelberg: Springer, 2002, pp. 53–108. ISBN: 978-3-662-04974-7. DOI: 10.1007/978-3-662-04974-7_3.

[89] J. Srour, C. Marshall, and P. Marshall. "Review of displacement damage effects in silicon devices". *IEEE Transactions on Nuclear Science* 50.3 (June 2003), pp. 653–670. ISSN: 1558-1578. DOI: 10.1109/TNS.2003.813197.

[90] D. J. Curtin and R. L. Statler. "Review of Radiation Damage to Silicon Solar Cells". *IEEE Transactions on Aerospace and Electronic Systems* AES-11.4 (July 1975), pp. 499–513. ISSN: 0018-9251. DOI: 10.1109/TAES.1975.308112.

[91] C. J. Dale and P. W. Marshall. "Displacement damage in Si imagers for space applications". *Charge-Coupled Devices and Solid State Optical Sensors II* 1447 (1991), pp. 70–86. DOI: doi.org/10.1117/12.45316.

[92] J. Linnros, P. Norlin, and A. Hallén. "Depth resolved carrier lifetime measurements of proton irradiated thyristors". *International Electron Devices Meeting 1991 [Technical Digest]*. IEEE. 1991, pp. 157–160. DOI: 10.1109/IEDM.1991.235477.

[93] S. Wood, N. J. Doyle, J. A. Spitznagel, W. J. Choyke, R. M. More, J. N. McGruer, and R. B. Irwin. "Simulation of Radiation Damage in Solids". *IEEE Transactions on Nuclear Science* 28.6 (Dec. 1981), pp. 4107–4112. ISSN: 1558-1578. DOI: 10.1109/TNS.1981.4335684.

[94] J. F. Ziegler, M. Ziegler, and J. Biersack. "SRIM – The stopping and range of ions in matter". *Nuclear Instruments and Methods in Physics Research Section B: Beam Interactions with Materials and Atoms* 268.11 (2010), pp. 1818–1823. ISSN: 0168-583X. DOI: 10.1016/j.nimb.2010.02.091.

[95] J. Srour and J. McGarrity. "Radiation effects on microelectronics in space". *Proceedings of the IEEE* 76.11 (Nov. 1988), pp. 1443–1469. ISSN: 1558-2256. DOI: 10.1109/5.90114.

[96] A. Fedoseyev and S. Herasimenka. "Space radiation effects in silicon solar cells: Physics based models, software, simulation and radiation effect mitigation". *AIP Conference Proceedings* 2164.1 (Oct. 2019), p. 120002. ISSN: 0094-243X. DOI: 10.1063/1.5130862.

[97] H. Amekura, N. Kishimoto, and T. Saito. "Photoconductivity evolution due to carrier trapping by defects in 17 MeV-proton irradiated silicon". *Journal of applied physics* 77.10 (1995), pp. 4984–4992. DOI: doi.org/10.1063/1.359307.

[98] W. Rosenzweig, F. Smits, and W. Brown. "Energy dependence of proton irradiation damage in silicon". *Journal of Applied Physics* 35.9 (1964), pp. 2707–2711. DOI: 10.1063/1.1713827.

[99] P. A. Iles. "Evolution of space solar cells". *Solar Energy Materials and Solar Cells*. Solar cells in space 68.1 (Apr. 2001), pp. 1–13. ISSN: 0927-0248. DOI: 10.1016/S0927-0248(00)00341-X.

[100] S. Utamuradova, E. Terukov, O. Ataboev, I. Panaiotti, R. Kabulov, and A. Troshin. "Influence of 1 MeV electron irradiation on the output parameters of silicon heterojunction solar cells". *Nuclear Instruments and Methods in Physics Research Section B: Beam Interactions with Materials and Atoms* 560 (2025), p. 165630. ISSN: 0168-583X. DOI: 10.1016/j.nimb.2025.165630.

[101] M. Yamaguchi and C. Amano. "Numerical analysis for radiation-resistant GaAs heteroface solar cell structures". *Journal of Applied Physics* 57.2 (Jan. 1985), pp. 537–544. ISSN: 0021-8979, 1089-7550. DOI: 10.1063/1.334788.

[102] T. Markvart. "Radiation damage in solar cells". *Journal of Materials Science: Materials in Electronics* 1.1 (May 1990), pp. 1–12. ISSN: 0957-4522, 1573-482X. DOI: 10.1007/BF00716008.

[103] J. J. Loferski and P. Rappaport. "Radiation Damage in Ge and Si Detected by Carrier Lifetime Changes: Damage Thresholds". *Physical Review* 111.2 (July 1958), pp. 432–439. ISSN: 0031-899X. DOI: 10.1103/PhysRev.111.432.

[104] R. Pease, E. Enlow, G. Dinger, and P. Marshall. "Comparison of proton and neutron carrier removal rates". *IEEE Transactions on Nuclear Science* 34.6 (2007), pp. 1140–1146. DOI: 10.1109/TNS.1987.4337443.

[105] N. Keskitalo and A. Hallén. "Resistivity profile measurements of proton-irradiated n-type silicon". *Solid-State Electronics* 37.1 (Jan. 1994), pp. 55–60. ISSN: 0038-1101. DOI: 10.1016/0038-1101(94)90104-X.

[106] M. Yamaguchi, S. J. Taylor, S. Matsuda, and O. Kawasaki. "Mechanism for the anomalous degradation of Si solar cells induced by high fluence 1 MeV electron irradiation". *Applied Physics Letters* 68.22 (May 1996), pp. 3141–3143. ISSN: 0003-6951, 1077-3118. DOI: 10.1063/1.115804.

[107] M. Yamaguchi, S. J. Taylor, M.-J. Yang, S. Matsuda, O. Kawasaki, and T. Hisamatsu. "High-energy and high-fluence proton irradiation effects in silicon solar cells". *Journal of Applied Physics* 80.9 (Nov. 1996), pp. 4916–4920. ISSN: 0021-8979, 1089-7550. DOI: 10.1063/1.363534.

[108] S. J. Taylor, M. Yamaguchi, M.-J. Yang, M. Imaizumi, S. Matsuda, O. Kawasaki, and T. Hisamatsu. "Type conversion in irradiated silicon diodes". *Applied Physics Letters* 70.16 (Apr. 1997), pp. 2165–2167. ISSN: 0003-6951, 1077-3118. DOI: 10.1063/1.118946.

[109] L. Bosisio, S. Dittongo, E. Quai, and I. Rachevskaia. "Observation of substrate-type inversion in high-resistivity silicon structures irradiated with high-energy electrons". *IEEE Transactions on Nuclear Science* 50.1 (Feb. 2003), pp. 219–225. ISSN: 1558-1578. DOI: 10.1109/TNS.2002.807861.

[110] D. Pitzl *et al.* "Type inversion in silicon detectors". *Nuclear Instruments and Methods in Physics Research Section A: Accelerators, Spectrometers, Detectors and Associated Equipment* 311.1 (Jan. 1992), pp. 98–104. ISSN: 0168-9002. DOI: 10.1016/0168-9002(92)90854-W.

[111] S. R. Messenger, G. P. Summers, E. A. Burke, R. J. Walters, and M. A. Xapsos. "Modeling solar cell degradation in space: A comparison of the NRL displacement damage dose and the JPL equivalent fluence approaches†". *Progress in Photovoltaics: Research and Applications* 9.2 (2001), pp. 103–121. ISSN: 1099-159X. DOI: 10.1002/pip.357.

[112] C. Baur. "Consistent approach of predicting the degradation of solar cells due to particle irradiation". *2023 13th European Space Power Conference (ESPC)*. Oct. 2023, pp. 1–6. DOI: 10.1109/ESPC59009.2023.10298190.

[113] S. Messenger, E. Burke, T. Morton, G. Summers, R. Walters, and J. Warner. "Modelling low energy proton radiation effects on solar cells". *Proceedings of 3rd World Conference on Photovoltaic Energy Conversion, 2003*. Vol. 1. May 2003, 716–719 Vol.1.

[114] H. Y. Tada, J. R. Carter, B. E. Anspaugh, and R. G. Downing. *Solar cell radiation handbook*. Nov. 1982. URL: https://ntrs.nasa.gov/citations/19830006416 (visited on 02/29/2024).

[115] G. D. Watkins. "Vacancies and interstitials and their interactions with other defects in silicon". *Proc. 3rd Symp. Defects Silicon (Electrochem. Soc.)* 1999, pp. 38–52.

[116] J. W. Corbett and G. D. Watkins. "Silicon Divacancy and its Direct Production by Electron Irradiation". *Physical Review Letters* 7.8 (Oct. 1961), pp. 314–316. ISSN: 0031-9007. DOI: 10.1103/PhysRevLett.7.314.

[117] B. L. Gregory. "Minority Carrier Recombination in Neutron Irradiated Silicon". *IEEE Transactions on Nuclear Science* 16.6 (Dec. 1969), pp. 53–62. ISSN: 1558-1578. DOI: 10.1109/TNS.1969.4325505.

[118] E. Simoen, C. Claeys, E. Gaubas, and H. Ohyama. "Impact of the divacancy (?) on the generation-recombination properties of 10 MeV proton irradiated Float-Zone silicon diodes". *Nuclear Instruments and Methods in Physics Research Section A: Accelerators, Spectrometers, Detectors and Associated Equipment* 439.2-3 (2000), pp. 310–318. DOI: 10.1016/S0168-9002(99)00915-8.

[119] P. M. Mooney, L. J. Cheng, M. Süli, J. D. Gerson, and J. W. Corbett. "Defect energy levels in boron-doped silicon irradiated with 1-MeV electrons". *Physical Review B* 15.8 (Apr. 1977), pp. 3836–3843. ISSN: 0556-2805. DOI: 10.1103/PhysRevB.15.3836.

[120] A. Hallén, N. Keskitalo, F. Masszi, and V. Nágl. “Lifetime in proton irradiated silicon”. *Journal of Applied Physics* 79.8 (Apr. 1996), pp. 3906–3914. ISSN: 0021-8979. DOI: 10.1063/1.361816.

[121] B. Baliga and A. Evwaraye. “Correlation of Lifetime with Recombination Centers in Electron-Irradiated P-Type Silicon”. *Journal of the Electrochemical Society* 130.9 (1983), p. 1916. DOI: 10.1149/1.2120123.

[122] M. Yamaguchi *et al.* “Effects of gallium impurity on radiation-resistance of Si single crystal space solar cells”. *3rd World Conference onPhotovoltaic Energy Conversion*. Ed. by IEEE. Vol. 1. 2003, pp. 701–704.

[123] Y.-H. Lee and J. W. Corbett. “EPR studies of defects in electron-irradiated silicon: A triplet state of vacancy-oxygen complexes”. *Physical Review B* 13.6 (1976), p. 2653. DOI: 10.1103/PhysRevB.13.2653.

[124] C. A. Londos. “Room-temperature irradiation of p-type Silicon”. *physica status solidi (a)* 92.2 (1985), pp. 609–614. ISSN: 1521-396X. DOI: 10.1002/pssa.2210920235.

[125] G. Watkins and J. Corbett. “Defects in irradiated silicon. I. Electron spin resonance of the Si-A center”. *Physical Review* 121.4 (1961), p. 1001. DOI: 10.1103/PhysRev.121.1001.

[126] M. Yamaguchi, A. Khan, S. J. Taylor, K. Ando, T. Yamaguchi, S. Matsuda, and T. Aburaya. “Deep level analysis of radiation-induced defects in Si crystals and solar cells”. *Journal of Applied Physics* 86.1 (July 1999), pp. 217–223. ISSN: 0021-8979, 1089-7550. DOI: 10.1063/1.370698.

[127] M. U. Khan *et al.* “Degradation and regeneration of radiation-induced defects in silicon: A study of vacancy-hydrogen interactions”. *Solar Energy Materials and Solar Cells* 200 (Sept. 2019), p. 109990. ISSN: 09270248. DOI: 10.1016/j.solmat.2019.109990.

[128] J. Mandelkorn, L. Schwartz, J. Broder, H. Kautz, and R. Ulman. “Effects of impurities on radiation damage of silicon solar cells”. *Journal of Applied Physics* 35.7 (1964), pp. 2258–2260. DOI: 10.1063/1.1702830.

[129] M. Yamaguchi, A. Khan, S. Taylor, M. Imaizumi, T. Hisamatsu, and S. Matsuda. “A detailed model to improve the radiation-resistance of Si space solar cells”. *IEEE Transactions on Electron Devices* 46.10 (Oct. 1999), pp. 2133–2138. ISSN: 00189383. DOI: 10.1109/16.792008.

[130] H. Matsuura *et al.* “Si Substrate Suitable for Radiation-Resistant Space Solar Cells”. *Japanese Journal of Applied Physics* 45.4R (Apr. 2006), p. 2648. ISSN: 1347-4065. DOI: 10.1143/JJAP.45.2648.

[131] R. L. Crabb. “Photon Induced Degradation of Electron and Proton Irradiated Silicon Solar Cells”. *IEEE Transactions on Nuclear Science* 20.6 (1973), pp. 243–249. DOI: 10.1109/TNS.1973.4327402.

[132] A. Khan, M. Yamaguchi, M. Kaneiwa, T. Saga, T. Abe, O. Annzawa, and S. Matsuda. "Influence of the dopant species on radiation-induced defects in Si single crystals". *Journal of Applied Physics* 87.12 (June 2000), pp. 8389–8392. ISSN: 0021-8979, 1089-7550. DOI: 10.1063/1.373552.

[133] A. Khan *et al.* "Strategies for improving radiation tolerance of Si space solar cells". *Solar Energy Materials and Solar Cells* 75.1-2 (Jan. 2003), pp. 271–276. ISSN: 09270248. DOI: 10.1016/S0927-0248(02)00169-1.

[134] W. Berks and W. Luft. "Photovoltaic solar arrays for communication satellites". *Proceedings of the IEEE* 59.2 (Feb. 1971), pp. 263–271. ISSN: 1558-2256. DOI: 10.1109/PROC.1971.8131.

[135] V. D. Mihailetchi, C. Peter, L. Koduvelikulathu, R. Roescu, R. Kopecek, S. Pop, and M. Okandan. "Suitable Silicon Solar Cell Technologies for Use in Space Applications". Sept. 2021, p. 4.

[136] A. Suzuki. "High-efficiency silicon space solar cells". *Solar energy materials and solar cells* 50.1-4 (1998), pp. 289–303. DOI: 10.1016/S0927-0248(97)00160-8.

[137] H. Washio *et al.* "Development of high efficiency thin silicon space solar cells". *Conference Record of the Twenty Third IEEE Photovoltaic Specialists Conference - 1993 (Cat. No.93CH3283-9)*. Louisville, KY, USA: IEEE, 1993, pp. 1347–1351. ISBN: 978-0-7803-1220-3. DOI: 10.1109/PVSC.1993.346922.

[138] H. Sai, Y. Sato, T. Oku, and T. Matsui. "Very thin crystalline silicon cells: A way to improve the photovoltaic performance at elevated temperatures". *Progress in Photovoltaics: Research and Applications* 29.10 (2021), pp. 1093–1104. DOI: 10.1002/pip.3443.

[139] M. Taguchi *et al.* "24.7% Record Efficiency HIT Solar Cell on Thin Silicon Wafer". *IEEE Journal of Photovoltaics* 4.1 (2014), pp. 96–99. DOI: 10.1109/JPHOTOV.2013.2282737.

[140] M. A. Cappelletti, G. A. Casas, A. P. Cédola, and E. L. Peltzer y Blancá. "Theoretical study of the maximum power point of n-type and p-type crystalline silicon space solar cells". *Semiconductor Science and Technology* 28.4 (Apr. 2013), p. 045010. ISSN: 0268-1242, 1361-6641. DOI: 10.1088/0268-1242/28/4/045010.

[141] A. Wang. "High efficiency PERC and PERL silicon solar cells". PhD thesis. Sidney: UNSW, 1992.

[142] E. Snow, A. Grove, and D. Fitzgerald. "Effects of ionizing radiation on oxidized silicon surfaces and planar devices". *Proceedings of the IEEE* 55.7 (2005), pp. 1168–1185. DOI: 10.1109/PROC.1967.5776.

[143] F.-J. Ma *et al.* "Comparative analysis of radiation-induced effects on the performance of p-type PERC and TOPCon solar cells for space applications". *Solar Energy Materials and Solar Cells* 274 (Aug. 2024), p. 113002. ISSN: 0927-0248. DOI: 10.1016/j.solmat.2024.113002.

[144] H.-C. Neitzert, M. Ferrara, T. Mueller, M. Scherff, and W. Fahrner. "Bulk and Interface Degradation of Amorphous Silicon / Crystalline Silicon Heterojunction Solar Cells Under Proton Irradiation". *2006 IEEE 4th World Conference on Photovoltaic Energy Conference*. Waikoloa, HI: IEEE, May 2006, pp. 1822–1825. ISBN: 978-1-4244-0016-4. DOI: 10.1109/WCPEC.2006.279847.

[145] M. Scherff *et al.* "Proton Damage in Amorphous Silicon/Crystalline Silicon Heterojunction Solar Cells". *Journal of The Electrochemical Society* 153.12 (2006), G1117. ISSN: 00134651. DOI: 10.1149/1.2360771.

[146] H. Presting, J. Konle, D. Behammer, A. Gruhle, P. Uebele, and G. Strobl. "Fabrication of Si trench solar cells with improved radiation hardness for space applications". *Conference Record of the Twenty-Eighth IEEE Photovoltaic Specialists Conference - 2000 (Cat. No.00CH37036)*. Anchorage, AK, USA: IEEE, 2000, pp. 1293–1296. ISBN: 978-0-7803-5772-3. DOI: 10.1109/PVSC.2000.916127.

[147] P. Espinet-Gonzalez *et al.* "Radiation Tolerant Nanowire Array Solar Cells". *ACS Nano* 13.11 (Nov. 2019), pp. 12860–12869. ISSN: 1936-0851, 1936-086X. DOI: 10.1021/acsnano.9b05213.

[148] A. Suzuki. "High-efficiency silicon space solar cells". *Solar Energy Materials and Solar Cells* 50.1 (1998), pp. 289–303. ISSN: 0927-0248. DOI: 10.1016/S0927-0248(97)00160-8.

[149] Y. Tonomura *et al.* "Development of both-side junction silicon space solar cells". *Solar Energy Materials and Solar Cells* 66.1-4 (Feb. 2001), pp. 551–558. ISSN: 09270248. DOI: 10.1016/S0927-0248(00)00237-3.

[150] A. Khan, M. Yamaguchi, S. J. Taylor, T. Hisamatsu, and S. Matsuda. "Effects of Annealing on Type Converted Si and Space Solar Cells Irradiated with Heavy Fluence 1 MeV Electrons". *Japanese Journal of Applied Physics* 38.5R (May 1999), p. 2679. ISSN: 0021-4922, 1347-4065. DOI: 10.1143/JJAP.38.2679.

[151] G. J. Brucker. "Electrical Studies of Electron-Irradiated Lithium-Containing n-Type Silicon". *Physical Review* 183.3 (July 1969), pp. 712–724. DOI: 10.1103/PhysRev.183.712.

[152] J. J. Wysocki. "Role of Lithium in Damage and Recovery of Irradiated Silicon Solar Cells". *IEEE Transactions on Nuclear Science* 14.6 (Dec. 1967), pp. 103–109. ISSN: 0018-9499, 1558-1578. DOI: 10.1109/TNS.1967.4324781.

[153] I. Weinberg, C. Goradia, J. Stupica, and C. Swartz. "Cell performance and defect behavior in proton-irradiated lithium-counterdoped n+p silicon solar cells". *Journal of Applied Physics* 60.6 (Sept. 1986), pp. 2179–2181. DOI: 10.1063/1.337172.

[154] M. Okandan. "In-situ rapid annealing and operation of solar cells for extreme environment applications". US20220262973A1. Aug. 2022.

[155] G. Li *et al.* "Rapid Healing: How hydrogenation supercharges recovery of electron-irradiation defects in Ga-doped PERC solar cells". *Solar Energy Materials and Solar Cells* 290 (2025), p. 113729. ISSN: 0927-0248. DOI: doi.org/10.1016/j.solmat.2025.113729.

[156] H. Seidel, L. Csepregi, A. Heuberger, and H. Baumgärtel. "Anisotropic Etching of Crystalline Silicon in Alkaline Solutions: I . Orientation Dependence and Behavior of Passivation Layers". *Journal of The Electrochemical Society* 137.11 (Nov. 1990), p. 3612. DOI: 10.1149/1.2086277.

[157] M. Crose, J. Sang-Il Kwon, M. Nayhouse, D. Ni, and P. D. Christofides. "Multiscale modeling and operation of PECVD of thin film solar cells". *Chemical Engineering Science* 136 (2015), pp. 50–61. ISSN: 0009-2509. DOI: 10.1016/j.ces.2015.02.027.

[158] A. Baptista, F. Silva, J. Porteiro, J. Míguez, and G. Pinto. "Sputtering Physical Vapour Deposition (PVD) Coatings: A Critical Review on Process Improvement and Market Trend Demands". *Coatings* 8.11 (2018). ISSN: 2079-6412. DOI: 10.3390/coatings8110402.

[159] *Space engineering - Photovoltaic assemblies and components*. Standard. Noordwijk, The Netherlands: European cooperation for space standardization (ECSS), Apr. 2023.

[160] J. Lefevre, O. Cavani, and B. Boizot. "The Sirius facility: a powerful tool for studying irradiation effects in materials". *13th international topical meeting of nuclear applications of accelerators*. 2017.

[161] F. Hinterberger. "Electrostatic accelerators". *CAS - CERN Accelerator School: small accelerators* (2006), pp. 95–112. DOI: 10.5170/CERN-2006-012.95.

[162] S. Pellegrino *et al.* "The JANNUS Saclay facility: A new platform for materials irradiation, implantation and ion beam analysis". *Nuclear Instruments and Methods in Physics Research Section B: Beam Interactions with Materials and Atoms* 273 (2012), pp. 213–217. ISSN: 0168-583X. DOI: 10.1016/j.nimb.2011.07.078.

[163] *JANNuS-Saclay - JANNuS*. URL: https://jannus.in2p3.fr/jannus-saclay/ (visited on 08/05/2025).

[164] L. Van der Pauw. "A method of measuring specific resistivity and Hall effect of discs of arbitrary shape". *Philips Res. Rep* 13.1 (1958), pp. 1–9.

[165] F. Szmulowicz. "Calculation of the mobility and the Hall factor for doped p-type silicon". *Physical Review B* 34.6 (1986), p. 4031. DOI: 10.1103/PhysRevB.34.4031.

[166] J. Veirman, S. Dubois, N. Enjalbert, J. Garandet, D. Heslinga, and M. Lemiti. "Hall mobility reduction in single-crystalline silicon gradually compensated by thermal donors activation". *Solid-State Electronics* 54.6 (2010), pp. 671–674. ISSN: 0038-1101. DOI: 10.1016/j.sse.2010.02.002.

[167] A. Fauveau. "Etude des mécanismes de conduction électrique à basse température pour la mesure des teneurs en dopants dans le silicium photovoltaïque". PhD thesis. Université Grenoble Alpes, Oct. 2017.

[168] F. M. Smits. "Measurement of Sheet Resistivities with the Four-Point Probe". *Bell System Technical Journal* 37.3 (1958), pp. 711–718. DOI: 10.1002/j.1538-7305.1958.tb03883.x.

[169] J. Veirman, B. Martel, N. Enjalbert, S. Dubois, C. Picoulet, and P. Bonnard. *Oxygen-defect characterization for improving R&D relevance and Cz-Si solar cell efficiency*. pv-tech. Oct. 2016. URL: https://www.pv-tech.org/technical-papers/oxygendefect-characterization-for-improving-rd-relevance-and-czsi-solar-cell-efficiency/ (visited on 09/11/2025).

[170] J. Veirman, S. Dubois, N. Enjalbert, and M. Lemiti. "A Fast and Easily Implemented Method for Interstitial Oxygen Concentration Mapping Through the Activation of Thermal Donors in Silicon." *Energy Procedia* 8 (Jan. 2011), pp. 41–46. ISSN: 1876-6102. DOI: 10.1016/j.egypro.2011.06.099.

[171] R. Sinton, A. Cuevas, and M. Stuckings. "Quasi-steady-state photoconductance, a new method for solar cell material and device characterization". *Conference Record of the Twenty Fifth IEEE Photovoltaic Specialists Conference - 1996*. 1996, pp. 457–460. DOI: 10.1109/PVSC.1996.564042.

[172] H. Nagel, C. Berge, and A. G. Aberle. "Generalized analysis of quasi-steady-state and quasi-transient measurements of carrier lifetimes in semiconductors". *Journal of Applied Physics* 86.11 (1999), pp. 6218–6221. DOI: 10.1063/1.371633.

[173] R. A. Sinton, A. Cuevas, *et al.* "A quasi-steady-state open-circuit voltage method for solar cell characterization". *16th European Photovoltaic Solar Energy Conference*. Vol. 25. Taylor and Francis. 2000, pp. 1152–1155.

[174] Newport. *Oriel Legacy APEX2 Illumination Systems User's Manual*. 2015. URL: https://www.newport.com/f/apex2-integrated-arc-lamp-system (visited on 09/09/2025).

[175] Newport. *IQE-LIGHT-BIAS*. 2015. URL: https://www.newport.com/p/IQE-LIGHT-BIAS (visited on 09/09/2025).

[176] S. Keller, M. Spiegel, P. Fath, G. Willeke, and E. Bucher. "A critical evaluation of the effective diffusion length determination in crystalline silicon solar cells from an extended spectral analysis". *IEEE Transactions on Electron Devices* 45.7 (July 1998), pp. 1569–1574. ISSN: 1557-9646. DOI: 10.1109/16.701490.

[177] H. Haug, J. Greulich, A. Kimmerle, and E. S. Marstein. "PC1Dmod 6.1 – state-of-the-art models in a well-known interface for improved simulation of Si solar cells". *Solar Energy Materials and Solar Cells* 142 (2015), pp. 47–53. ISSN: 0927-0248. DOI: 10.1016/j.solmat.2015.05.047.

[178] J. Veirman, S. Dubois, N. Enjalbert, J. P. Garandet, D. R. Heslinga, and M. Lemiti. "Hall mobility drops in disordered boron-doped Czochralski silicon compensated by thermal donors activation". *physica status solidi c* 8.3 (2011), pp. 729–732. ISSN: 1610-1642. DOI: 10.1002/pssc.201000223.

[179] A. Augusto, A. Srinivasa, and S. G. Bowden. "Influence of the Bulk Resistivity on Silicon Heterojunction Solar Cells and Module Reliability". *Solar RRL* 6.5 (2022), p. 2100519. ISSN: 2367-198X. DOI: 10.1002/solr.202100519.

[180] M. A. Green *et al.* "Solar cell efficiency tables (Version 64)". *Progress in Photovoltaics: Research and Applications* 32.7 (2024), pp. 425–441. ISSN: 1099-159X. DOI: 10.1002/pip.3831.

[181] W. Liu *et al.* "Flexible solar cells based on foldable silicon wafers with blunted edges". *Nature* 617.7962 (May 2023), pp. 717–723. ISSN: 0028-0836, 1476-4687. DOI: 10.1038/s41586-023-05921-z.

[182] O. Guillot, J. Veirman, R. Cariou, N. Enjalbert, A. Danel, C. Aicardi, and S. Dubois. "Comprehensive Study of Performance of Silicon Heterojunction Solar Cells Under Electron Irradiation". *2023 13th European Space Power Conference (ESPC)*. Oct. 2023, pp. 1–4. DOI: 10.1109/ESPC59009.2023.10413251.

[183] O. Guillot, R. Cariou, J. Veirman, N. Enjalbert, A. Danel, C. Aicardi, and S. Dubois. "Influence of Material Composition and Wafer Thickness on the Performances of Electron Irradiated Gallium-Doped Silicon Heterojunction Solar Cells". *Solar RRL* 9.1 (2025), p. 2400669. DOI: 10.1002/solr.202400669.

[184] A. Froitzheim, R. Stangl, L. Elstner, M. Kriegel, and W. Fuhs. "AFORS-HET: a computer-program for the simulation of heterojunction solar cells to be distributed for public use". *3rd World Conference onPhotovoltaic Energy Conversion, 2003. Proceedings of.* Vol. 1. 2003, 279–282 Vol.1.

[185] D. Bäurle, A. Herguth, and G. Hahn. "Approaches to Mitigate Edge Recombination Effects in Silicon Lifetime Samples With Emitter". *IEEE Journal of Photovoltaics* 15.4 (2025), pp. 518–522. DOI: 10.1109/JPHOTOV.2025.3568471.

[186] V. Giglia, R. Varache, J. Veirman, and E. Fourmond. "Influence of cell edges on the performance of silicon heterojunction solar cells". *Solar Energy Materials and Solar Cells* 238 (2022), p. 111605. ISSN: 0927-0248. DOI: 10.1016/j.solmat.2022.111605.

[187] A. Danel, N. Chaugier, J. Veirman, R. Varache, M. Albaric, and E. Pihan. "Closing the gap between n- and p-type silicon heterojunction solar cells: 24.47% efficiency on lightly doped Ga wafers". *Progress in Photovoltaics: Research and Applications* (Oct. 2022), pip.3635. ISSN: 1062-7995, 1099-159X. DOI: 10.1002/pip.3635.

[188] G. Kramberger *et al.* "Radiation hardness of gallium doped low gain avalanche detectors". *Nuclear Instruments and Methods in Physics Research Section A: Accelerators, Spectrometers, Detectors and Associated Equipment* 898 (Aug. 2018), pp. 53–59. ISSN: 01689002. DOI: 10.1016/j.nima.2018.04.060.

[189] PV Lighthouse. *Recombination calculator Version 1.3.0*. 2023. URL: https://www.pvlighthouse.com.au/calculators (visited on 06/09/2025).

[190] M. Ferrara. "Electroluminescence of a-Si/c-Si heterojunction solar cells after high energy irradiation". PhD thesis. Fernuniversitaet (Gesamthochschule) Hagen (Germany), Nov. 2009.

[191] H.-C. Neitzert *et al.* "Stability of silicon based homojunction and heterojunction solar cells under space conditions". *Materials Science and Engineering: B*. EMRS 2006, Symposium V; Advanced Silicon for the 21st Century 134.2 (Oct. 2006), pp. 263–268. ISSN: 0921-5107. DOI: 10.1016/j.mseb.2006.06.044.

[192] M. Schädel, J. Isenberg, J. Suthues, C. Ballif, and G. Gobsch. "Improving quantum efficiency measurement in large area solar cells by using appropriate bias illumination". *21st European Photovoltaic Solar Energy Conference*. 2006, pp. 336–339.

# Résumé détaillé

## Introduction

Les cellules solaires en silicium cristallin (c-Si), après avoir été largement étudiées et utilisées au cours du dernier siècle pour les applications spatiales, connaissent aujourd'hui un regain d'intérêt dans ce domaine. La demande de sources d'énergie pour les satellites est en effet en pleine croissance avec l'arrivée de nombreux acteurs privés lançant de grandes constellations de satellites de télécommunications [1]. Si les cellules III-V multijonctions (MJSC) dominent encore le marché des cellules solaires spatiales en raison de leurs meilleures efficacités et résistances aux radiations, l'utilisation de cellules solaires c-Si s'avère indispensable pour répondre aux nouvelles exigences de volumes de production élevés et de coûts maîtrisés de ce secteur d'activité. Leur capacité de production, principal obstacle à l'utilisation des cellules MJSC, est en effet très élevée grâce à des processus de fabrication à l'usage des applications terrestres bien établis, avec plus de $\approx 600\ GW$ de panneaux solaires installés durant l'année 2024 [2]. De plus, le prix de vente par watt des modules photovoltaïques c-Si (0,08 $/W) est plusieurs centaines de fois inférieur à celui des MJSC. Il convient toutefois de noter que ce faible coût est légèrement contrebalancé par une efficacité après irradiation aux particules chargées (dénotée "EOL" par la suite) des cellules solaires c-Si environ deux fois inférieure à celle des MJSC, et donc entre autres par le coût du poids embarqué supplémentaire nécessaire pour augmenter la surface des cellules solaires.

Ces particules (electrons et protons), largement présentes dans les ceintures de Van Allen autour de la Terre, constituent la source première de dégradation des performances des cellules solaires c-Si. Elles peuvent effectivement induire des déplacements atomiques dans le réseau cristallin du silicium, ce qui génère une densité élevée de défauts. Ces défauts vont principalement réduire la durée vie des porteurs de charge $\tau$ (dégradation quantifiée avec $K_L$, le coefficient de dommage de la longueur de diffusion des porteurs minoritaires) et réduire la concentration en porteurs de charge majoritaires $p_0$ pour un matériau de type p (variation quantifiée avec $R_c$, le taux de réduction des porteurs de charge majoritaires). Cette réduction de porteurs de charges majoritaire peut même mener à une inversion du type de conductivité dans certaines conditions. Ainsi, pour réduire l'impact de ces effets sur les performances EOL des cellules solaires c-Si, l'optimisation de l'architecture des cellules ainsi que des propriétés des matériaux des wafers s'avère indispensable. Il est notamment largement admis qu'un émetteur face avant combiné à l'utilisation d'un substrat de type p, et possiblement très fin, permet de limiter ces dégradations [3]. L'optimum d'autres paramètres ayant un lien avec la résilience des cellules solaires c-Si est moins clair. C'est notamment le cas de la valeur de la résistivité du substrat c-Si, ou encore de la concentration en oxygène. Soulignons que la plupart des

recherches existantes sur ce sujet datent de plus de 20 ans. Il semble par conséquent important d'analyser la résilience aux radiations des technologies de cellules de pointe qui sont entre temps arrivées sur le marché pour les applications terrestres, avec des avancées significatives tant en matière de matériaux que d'architectures.

Parmi les différentes structures de cellules c-Si actuelles, les cellules solaires silicium à hétérojonctions (SHJ) sont particulièrement prometteuses pour les missions spatiales. Ces cellules peuvent être fabriquées en atteignant une haute efficacité avant irradiation de particules (dénotée "BOL" par la suite) et le procédé industriel standard de fabrication permet d'obtenir une structure à émetteur en face avant lorsque des substrats de type p sont utilisés. Les procédés de fabrications de SHJ sont également compatibles avec des wafers minces. Ces caractéristiques rendent cette technologie très intéressante pour améliorer les performances EOL. L'essor des études publiées depuis le début de ces travaux concernant la résilience des cellules solaires SHJ face à l'environnement spatial mettent en lumière l'intérêt croissant des acteurs du domaine spatial pour ce type de cellules [4], [5], [6], [7].

Ainsi, les études suivantes évaluent la résilience aux radiations des cellules solaires SHJ selon deux axes. Le premier axe se concentre sur l'impact de la résistivité, de la concentration en Ga (récemment devenu le dopant standard du c-Si de type p), des teneurs en oxygène et des défauts liés à l'oxygène, sur la résilience du matériau et des cellules SHJ à l'irradiation par électrons. Ensuite, les limites de l'utilisation des cellules solaires en c-Si sont explorées en simulant un environnement spatial sévère à l'aide de fluences élevées de protons à faible énergie, qui induisent la création de défauts hétérogènes à travers la profondeur de la cellule. Ces travaux permettent d'acquérir de nouvelles connaissances sur les mécanismes de dégradation des cellules SHJ modernes, tout en proposant des voies d'amélioration.

## Irradiation par électrons de cellules SHJ : effets de la composition du matériau et de l'épaisseur du wafer

Dans ce chapitre, la résilience des cellules solaires SHJ modernes dopées au Ga face à l'irradiation par électrons d'énergie 1 $MeV$ a été étudiée (pour des fluences de $1,5 \times 10^{14} - 1,5 \times 10^{15}$ $cm^{-2}$), en se concentrant sur l'influence de la composition du wafer, de sa résistivité, et de l'épaisseur de la cellule. Pour cela des cellules solaires SHJ de trois épaisseurs différentes (80 $\mu m$, 110 $\mu m$ et 160 $\mu m$) ont été fabriquées pour 3 gammes de résistivités différentes de c-Si dopé au Ga : $0,9$ $\Omega.cm$ (Ga0.9), 15 $\Omega.cm$ (Ga15) et 60 $\Omega.cm$ (Ga60). Les groupes Ga15 et Ga60 ont la particularité d'avoir des concentrations similaires en Ga, mais des concentrations 4 fois supérieures en donneurs thermiques (DT) pour le groupe Ga60. Ces défauts, dont la répartition dans le plan est circulaire (distribution inhomogène), sont liés à l'oxygène et spécifiques au tirage de lingots Czochralski (Cz). Ces DTs auront des impacts sur plusieurs aspects des résultats obtenus après irradiations electrons et protons. Ils agissent notamment comme double donneurs et influent donc directement sur la $p_0$.

Cette étude montre que la $p_0$ et la mobilité des trous à l'équilibre $\mu_p$ restent stables dans les plages de dopage et de fluences d'électrons étudiées. Cela confirme que le c-Si dopé au Ga

est moins affecté par l'effet de suppression des porteurs que le c-Si dopé au B, car pour un $R_c = 0,15\ cm^{-1}$ (correspondant à du c-Si dopé bore (B) [8]), une réduction de $p_0$ significative aurait dû être mesurée pour la condition Ga60.

La dynamique de dégradation de $\tau$ en fonction de la fluence d'électrons a été évaluée et sa dépendance aux propriétés de composition du matériau a été mise en évidence : plus la $p_0$ est faible, plus la $\tau$ (EOL) est élevée pour un faible niveau d'injection des porteurs. Les recombinaisons Shockley-Read-Hall (SRH) via des défauts précédemment identifiés dans des wafers c-Si dopés au B passivés et irradiés par des électrons 1 $MeV$ [9], probablement liés à des dilacunes, ont permis de bien reproduire ces effets (voir Figure 5.3(a)). De plus, une étude menée sur l'influence de l'atome dopant (qu'il soit Ga ou B) sur la $\tau$ EOL semble montrer que le choix du dopant a peu d'impact sur la $\tau$ en fin de vie (voir Figure 5.3(b)).

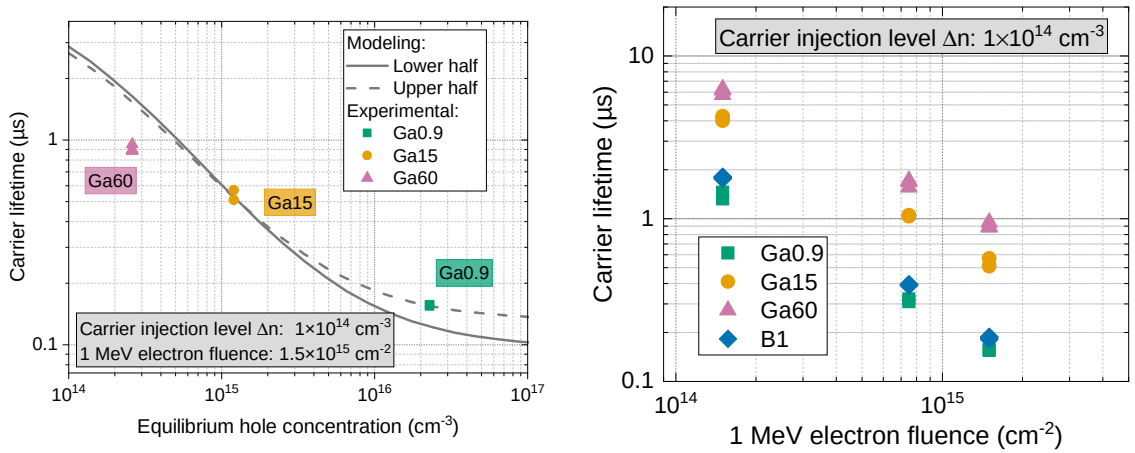


(a) (b)

Figure 5.3 : (a) Variations de la durée de vie des porteurs de charge en fonction de $p_0$ pour une fluence de $1,5 \times 10^{15}\ cm^{-2}$ d'électrons 1 $MeV$ sur des précurseurs de cellules SHJ dopées Ga et d'épaisseur 80 $\mu m$. Les courbes pleines (moitié basse de la bande interdite, $E_v + 0.22\ eV$) et pointillées (moitié haute de la bande interdite, $E_c - 0.25\ eV$) correspondent à la modélisation SRH effectuée avec PV Lighthouse (voir [9] pour la description des défauts). Les symboles correspondent aux points expérimentaux. (b) Variations de la durée de vie des porteurs de charge en fonction de la fluence d'électrons 1 $MeV$ pour des wafers à surfaces passivées. Les données expérimentales correspondent aux conditions 80 $\mu m$ Ga0.9 (carrés verts), 80 $\mu m$ Ga15 (cercles oranges), 80 $\mu m$ Ga60 (triangles roses) et 95 $\mu m$ B1, c-Si dopé B avec une résistivité de 1 $\Omega.cm$ (losanges bleus).

Des variations spatiales significatives de la longueur de diffusion des électrons $L_n$ ont été mises en évidence à travers des cartographies de surface des échantillons Ga60 (voir Figure 5.4). Ces variations sont probablement induites par la distribution non homogène des DTs mentionnée précédemment, en lien avec le procédé de fabrication du lingot c-Si. Les motifs circulaires liés aux variations de $L_n$ ne sont en effet pas (Ga0.9) ou peu (Ga15) visibles pour les wafers c-Si avec avec $[Ga] >> 2[DT]$ (considérés comme des matériaux non compensés, et donc avec moins d'influence des DTs). A nouveau, l'analyse de ces données a permis de montrer que les valeurs de $L_n$ sont particulièrement sensibles aux variations de $p_0$. Ce serait donc unique-

ment par la modification des valeurs de $p_0$ que les DTs auraient un impact sur les valeurs de $L_n$.

Les résultats EOL de la variation de $\tau$ avec $\Delta n$, ainsi que les cartographies $L_n$ montrent une forte influence de la répartition initiale circulaire de $p_0$ (due aux DTs). Cela suggère donc que le défaut limitant la $\tau$ n'est ni dépendant de la nature du dopant, ni de la concentration en oxygène $[O_i]$ ou des DTs, mais plus globalement du paramètre $p_0$.

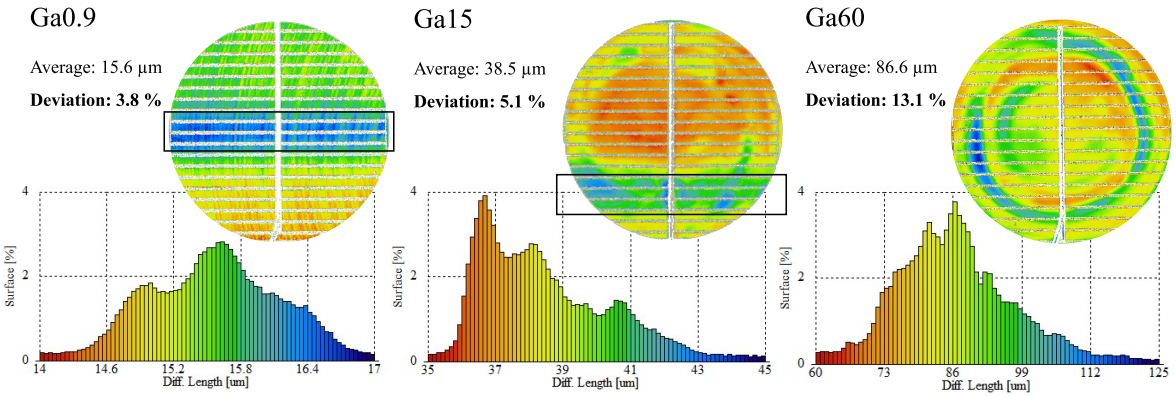


Figure 5.4 : Cartographies $L_n$ (surface circulaire de 3 $cm$ de diamètre) au centre des cellules solaires SHJ $3,0 \times 3,2$ $cm^2$ 160 $\mu m$ irradiées à une fluence de $1,5 \times 10^{15}$ $cm^{-2}$ d'électrons 1 $MeV$. Les échelles de couleurs diffèrent pour chaque cartographie.

Avec des $\tau$ quatre fois plus élevées à faible $\Delta n$ pour les wafers Ga60 par rapport aux valeurs mesurées pour les wafers Ga0.9, la densité de courant de court-circuit $J_{SC}$ EOL est ainsi plus élevée pour les cellules Ga60 par rapport aux cellules Ga0.9. En effet, l'irradiation d'électrons a entraîné un écart relatif de 9 % du $J_{SC}$ en faveur du groupe Ga60 (plus faible $p_0$) comparé au groupe Ga0.9 pour une fluence de $1.5 \times 10^{15}$ $cm^{-2}$ (voir Figure 5.5). Cependant, nous avons également mis en évidence et expliqué l'avantage d'une grande $p_0$ cette fois ci pour les paramètres de tension de circuit ouvert $V_{OC}$ et de facteur de forme $FF$, lorsque l'irradiation impacte la $\tau$ de manière significative (voir Figure 5.5). Pour les wafers à faible $p_0$, la dégradation du $FF$ induite par l'irradiation est principalement due à l'augmentation de la résistivité volumique sous éclairement après irradiation, alors que cette résistivité reste inchangée pour le groupe Ga0.9.

L'amincissement des wafers permet globalement un gain en efficacité EOL. Cependant, ce gain est plus marqué pour les cellules avec la plus faible $p_0$, notamment pour les plus fortes fluences. Les économies en matière de masse embarquée restent en outre une forte motivation pour l'utilisation de wafers fins, quelles que soient les propriétés du matériau.

La meilleure efficacité des cellules solaires pour des cellules irradiées, à une fluence de $1,5 \times 10^{15}$ $cm^{-2}$, a été obtenue pour des cellules avec des wafers de resistivité intermédiaire, Ga15, et de plus faible épaisseur, 80 $\mu m$. L'efficacité pourrait être encore améliorée, notamment en amincissant davantage les wafers. Finalement, ces résultats soulignent bien l'importance du compromis sur la $p_0$ des wafers afin de garantir la résilience des cellules SHJ aux environnements spatiaux sévères. Cette étude fournit des lignes directrices utiles pour la définition des spécifications des wafers en c-Si conduisant à des cellules solaires plus adaptées

à l'environnement spatial.

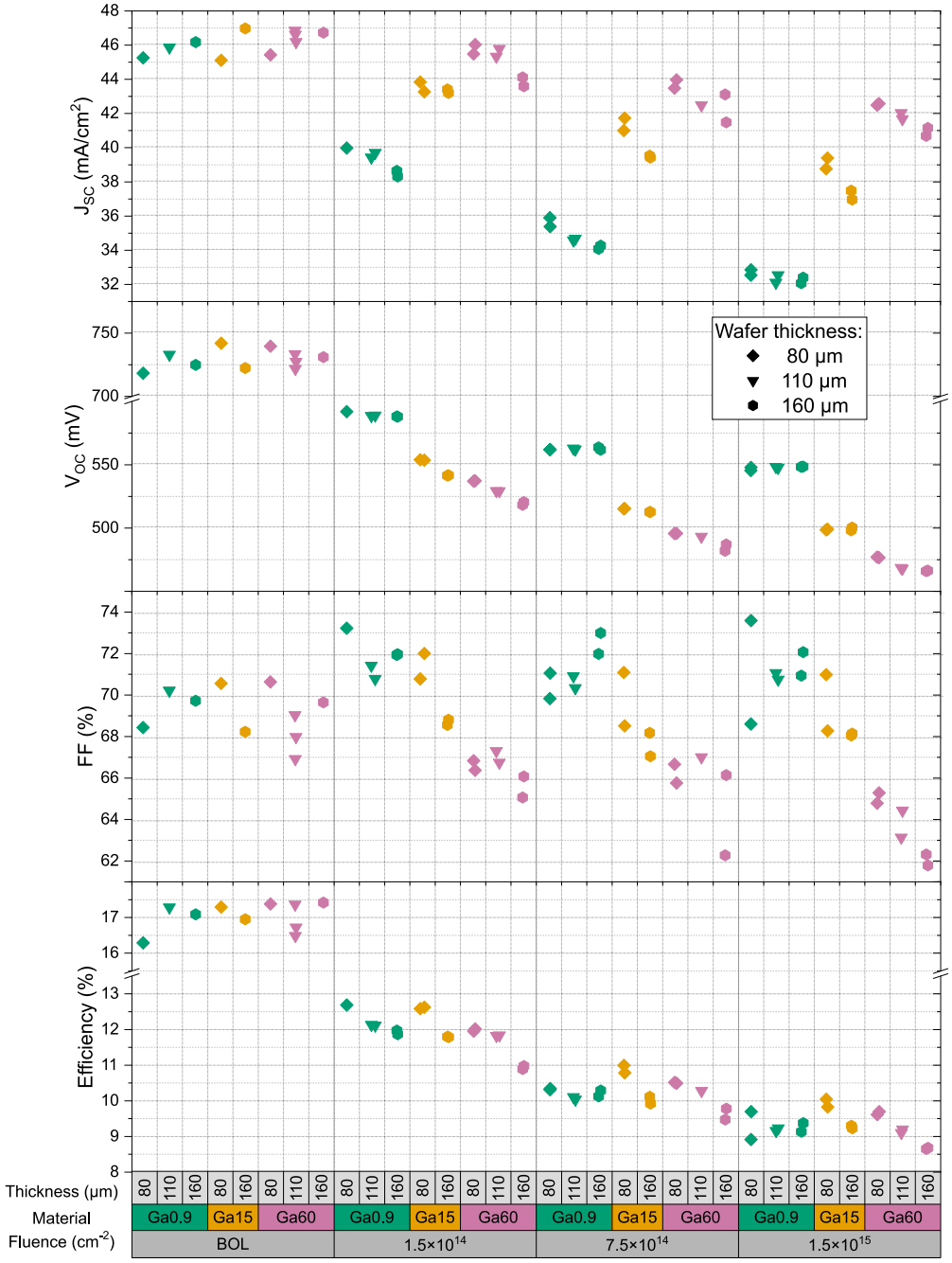


Figure 5.5 : Mesures I-V sous spectre AM0 à BOL et EOL de cellules solaires SHJ ($3,0 \times 3,2\ cm^2$) pour 3 épaisseurs différentes : 80 $\mu m$ (losanges), 110 $\mu m$ (triangles) et 160 $\mu m$ (hexagones) ; ainsi que trois valeurs de résistivité de wafers différentes : $0,9\ \Omega.cm$ (vert), 15 $\Omega.cm$ (orange) et 60 $\Omega.cm$ (rose). De haut en bas : $J_{SC}$, $V_{OC}$, $FF$ & Efficacité.

## Irradiation par protons de cellules SHJ de haute résistivité

Dans cette étude, nous avons examiné les effets de protons d'énergies 1 $MeV$ et 3 $MeV$ sur des cellules solaires SHJ 160 $\mu m$ dopées au Ga avec une résistivité élevée (60 $\Omega.cm$, Ga60). Ces basses énergies de protons entraînent des dégradations hétérogènes au travers de l'épaisseur du substrat de c-Si, avec seulement les 16 premiers microns de la cellules dégradés dans le cas 1 $MeV$, et les 92 premiers microns de la cellule dégradés dans le cas 3 $MeV$. Un pic de dégradation, appelé pic de Bragg, est présent à la fin de cette région endommagée, soit respectivement à 16 $\mu m$ et 92 $\mu m$ pour des énergies de 1 $MeV$ et 3 $MeV$. Il est à noter que les dimensions des cellules dans cette étude sont encore plus réduites ($1,5 \times 1,5\ cm^2$) pour répondre aux contraintes de l'utilisation du faisceau protons.

Globalement, les performances des cellules solaires ont été fortement dégradées pour les fluences testées ($1 \times 10^{12} - 1 \times 10^{14}\ cm^{-2}$), avec des dégradations particulièrement sévères de $J_{SC}$ (voir Figure 5.6). Les irradiations par protons 3 $MeV$ ont induit des dégradations de $J_{SC}$ deux fois plus importantes que celles produites par l'irradiation par protons 1 $MeV$. Cela était inattendu au regard d'études précédemment réalisées en 1982 [10] et 1996 [11] montrant des $J_{SC}$ légèrement plus élevées pour des cellules irradiées par des protons d'énergie 3 $MeV$. Il faut toutefois noter que ces études ont été menées sur du c-Si de plus faible résistivité $\leq 15\ \Omega.cm$. Aussi, la deuxième étude [11] a utilisé des cellules de 50 $\mu m$ d'épaisseur, ce qui joue un rôle important sur les résultats étant donné que le maximum de dégradation provoqué par les protons 3 $MeV$ (pic de Bragg) n'a donc pas lieu dans l'épaisseur de la cellule.

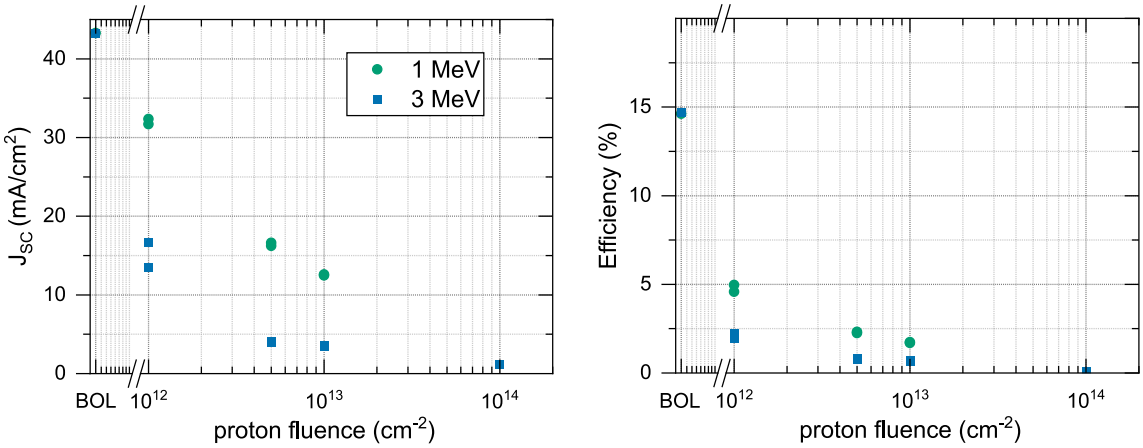


Figure 5.6 : Mesures de $J_{SC}$ (gauche) et d'efficacité (droite) sous spectre AM0 de cellules SHJ Ga60 irradiées par des protons d'énergie 1 $MeV$ (cercles verts) et 3 $MeV$ (carrés bleus).

Afin de mieux comprendre ces dynamiques, les dégradations de $J_{SC}$ ont été étudiées à l'aide d'analyses de réponses spectrales EQE. Nous avons d'abord souligné l'influence forte d'un éclairement additionnel pour les mesures EQE. L'ajout d'un éclairement supplémentaire est en effet nécessaire pour faire correspondre les valeurs de $J_{SC}$ obtenues à partir de mesures I-V et d'EQE. Il est intéressant de noter que les deux énergies induisent des comportements différents

sous illumination. Pour l'irradiation par protons de 1 $MeV$, la réponse spectrale s'est améliorée avec l'augmentation de l'intensité lumineuse, tandis que pour l'irradiation par protons de 3 $MeV$, la réponse spectrale s'est dégradée avec l'augmentation de l'intensité lumineuse, avec une meilleure collection pour des longueurs d'onde différentes (voir Figure 5.7(b) pour le cas 3 $MeV$). Ce résultat a été confirmé par des courbes I-V mesurées à différentes intensités lumineuses.

Une étude de modélisation et de simulation par PC1D a permis de reproduire les réponses spectrales EQE. Pour le cas 3 $MeV$, la modélisation s'est faite en considérant deux régions, une première d'épaisseur 92 $\mu m$ et considérée comme dégradée, et une seconde, d'épaisseur 68 $\mu m$ et considérée comme non dégradée (car au-delà du pic de Bragg) avec comme paramètres fixes $p_0 = 2,6 \times 10^{14}\ cm^{-3}$ (mesuré à BOL) et pour les recombinaisons SRH $E_t - E_i = 0\ eV$ et $\tau_{p0} = \tau_{n0} = 1000\ \mu s$. Ces paramètres ont donc été variés dans la première région pour reproduire les mesures EQE. Dans le cas d'une cellule irradiée par une fluence de $5 \times 10^{12}\ cm^{-2}$ de protons 3 $MeV$ illustrée en Figure 5.7(a), les paramètres suivants ont permis de reproduire avec succès les données expérimentales : $p_0 = 3 \times 10^{11}\ cm^{-3}$, $E_t - E_i = -0,2\ eV$ and $\tau_{p0} = \tau_{n0} = 0,008\ \mu s$. On voit donc un fort effet de réduction des porteurs de charge pour les cellules solaires irradiées par protons de 3 $MeV$, en plus de la réduction de $\tau$, avec un facteur 10 sur la $p_0$ entre les conditions BOL et EOL. De là a été estimée une valeur de $R_c = 225\ cm^{-1}$. En comparaison, aucune réduction de $p_0$ n'avait été observée dans les cellules solaires irradiées par des électrons de 1 $MeV$ avec une fluence de $1,5 \times 10^{15}\ cm^{-2}$.

La même méthode a été appliquée pour les cellules irradiées par des protons d'énergie 1 $MeV$, cette fois ci avec une région endommagée d'épaisseur 16 $\mu m$ pour la modélisation. Pour des fluences similaires, la réduction de $p_0$ a été encore plus forte, conduisant même à l'inversion du type de conductivité dans cette zone. Cette étude par modélisation a été appuyée par des mesures 4-pointes, donnant la résistance carrée $R_{sheet}$, et pour lesquelles une différence de valeur significative a été obtenue entre les mesures faites en face avant et en face arrière. Les valeurs extraites de $p_0$ et $n_0$ issues des deux études (c'est à dire mesures 4-pointes et modélisation PC1D) sont en bon accord.

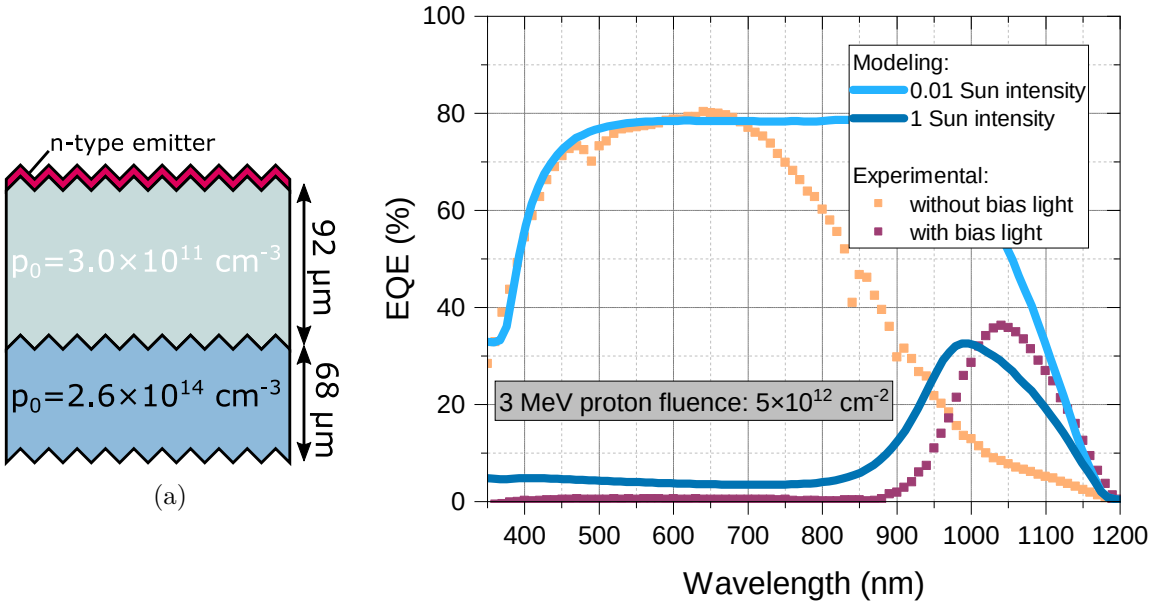


Figure 5.7 : (a) Structure de cellule utilisée dans les simulations PC1D afin de prendre en compte les dégradations par protons 3 $MeV$. Seuls les paramètres de la région dégradée (92 $\mu m$) sont modifiés par rapport à la condition BOL. (b) Comparaison des variations spectrales EQE obtenues à partir des mesures (symboles) et de la modélisation (courbes pleines) pour une cellule SHJ Ga60 irradiée à une fluence de $5 \times 10^{12}$ $cm^{-2}$ de protons 3 $MeV$ avec et sans utilisation d'éclairement additionnel. Les paramètres choisis pour la région dégradée de la simulation sont : $p_0 = 3 \times 10^{11}$ $cm^{-3}$, $E_t - E_i = -0,2$ $eV$ and $\tau_{p0} = \tau_{n0} = 0,008$ $\mu s$.

Les cellules solaires irradiées par des protons d'énergie 3 $MeV$ ont donc subi moins d'effet de réduction des porteurs de charge dans la zone endommagée que celles irradiées par des protons d'énergie 1 $MeV$. Cela était attendu au vu des simulations TRIM réalisées. En effet, pour une même fluence, la dégradation est donc moins condensée pour des protons 3 $MeV$ car la dégradation se fait sur une épaisseur plus grande. Cependant, dans le cas des protons de 3 $MeV$, même une faible réduction de la concentration des porteurs a eu un fort impact sur le comportement des cellules solaires, contrairement au cas des protons 1 $MeV$. On le voit bien sur les courbes avec un éclairement additionnel de la Figure 5.7(b), où seules les grandes longueurs d'onde sont collectées et avec un EQE toujours inférieur à 40 %. Comme l'impact de l'éclairement additionnel a été reproduit par simulation, ce comportement peut être attribué à des faibles $p_0$ combinées à de fortes recombinaisons SRH. Il est donc possible que le $J_{SC}$ ait été similaire pour les cellules solaires exposées aux deux énergies de protons (comme le suggère la littérature) pour des fluences plus faibles, pour lesquelles l'effet de suppression des porteurs n'est pas encore significatif. Ce comportement est donc spécifique à la combinaison de fortes fluences choisies et à la faible valeur initiale de $p_0$.

De plus, des variations importantes dans les propriétés électroniques dans le plan (c'est-à-dire les concentrations d'équilibre des porteurs, le type de conductivité et la $\tau$) ont été mises en évidence après irradiation par protons à travers des cartographies de $L_n$ et des

mesures spectrales locales d'EQE (voir Figure 5.8). Cet effet particulier est lié à la fois à la résistivité initialement élevée des wafers et aux variations dans le plan significatives de $p_0$ dans ce matériau compensé, résultant de la distribution des DTs. Ces variations dans le plan de $p_0$ sont accentuées par l'effet de suppression des porteurs induit par l'irradiation par protons. Par exemple, une inversion du type de conductivité a été mesurée uniquement dans une partie des zones dans le plan pour les cellules solaires irradiées à une fluence de $1 \times 10^{12}\ cm^{-2}$ de protons 1 $MeV$.

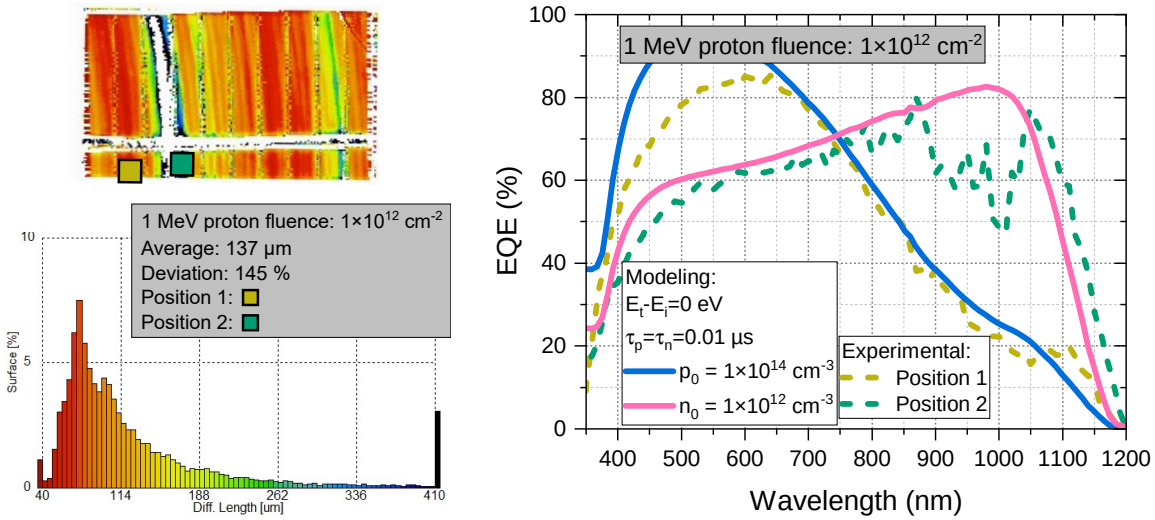


(a) (b)

Figure 5.8 : (a) Cartographie $L_n$ d'une cellule solaire Ga60 irradiée à une fluence de $1 \times 10^{12}\ cm^{-2}$ de protons 1 $MeV$. (b) Variations spectrales EQE obtenues à deux positions différentes de la même cellule (identifiées sur la cartographie $L_n$ (a)). Ces deux courbes ont été reproduites par des simulations PC1D dans lesquelles les dégradations protons 1 $MeV$ sont modélisées par une région endommagée de 16 $\mu m$. Les paramètres utilisés pour cette région sont : $E_t - E_i = 0\ eV$, $\tau_{n0} = \tau_{p0} = 0,01\ \mu s$ et $p_0 = 1 \times 10^{14}\ cm^{-3}$ (courbe bleue) ou $n_0 = 1 \times 10^{12}\ cm^{-3}$ (courbe rose).

## Conclusion

Dans un contexte de croissance rapide du secteur spatial, notamment avec l'essor des constellations de satellites, les cellules solaires c-Si redeviennent une solution attractive face aux cellules multijonctions, plus coûteuses et aux capacités de production faibles. Parmi elles, les cellules SHJ se distinguent par leur haute efficacité BOL, leur compatibilité avec des wafers minces, et leur maturité industrielle. Cette thèse s'est intéressée à la compréhension des mécanismes de dégradation induits par l'irradiation par particules spécifiques à l'environnement spatial pour des cellules SHJ dopées Ga, et ce afin d'identifier les leviers d'optimisation de leur performance EOL.

L'étude de l'irradiation par électrons d'énergie 1 $MeV$ a permis de quantifier la dégradation de $\tau$ en fonction de la composition du matériau. Il a été observé que les wafers à plus faible $p_0$ ont une meilleure résilience concernant la $\tau$, mais sont plus sujets aux variations des propriétés

électroniques dans le plan. Le choix du dopant (Ga ou B) semble avoir peu d'influence sur la dégradation de $\tau$, à fluence équivalente. En matière d'efficacité photovoltaïque, des résistivités intermédiaires semblent plus avantageuses. En effet, une faible $p_0$ conduira à de meilleures $J_{SC}$, mais également à une dégradation accrue des paramètres de $V_{OC}$ et de $FF$.

L'irradiation par protons de basse énergie (1 et 3 $MeV$) a ensuite permis d'explorer les limites de la résilience aux radiations des cellules SHJ à forte résistivité, notamment sur la $J_{SC}$. Contrairement aux électrons, les protons créent des défauts de manière non homogène sur l'épaisseur de la cellule, induisant une dégradation marquée du $J_{SC}$, augmentée par la réduction de $p_0$, allant jusqu'à des inversions locales de type de conductivité pour certaines conditions. Les mesures d'EQE et de $R_{sheet}$, combinées à des modélisations PC1D, ont en effet confirmé de forts effets de suppression de porteurs de charge majoritaires dans la région dégradée par les protons. Cette étude montre donc une autre limite à l'utilisation de wafers à faible $p_0$ pour des cellules solaires susceptibles de rencontrer un environnement spatial à niveau de radiation particulièrement élevé.

Ces études pourront être complétées notamment par de l'analyse plus fine des défauts après irradiation, ainsi que par la quantification de la dégradation pour des cellules de plus faible résistivité sous irradiations protoniques de faible énergie. Un travail a également été mené afin d'améliorer la transparence en face avant des cellules SHJ, qui a permis d'améliorer les performances EOL et conduit à un dépôt de brevet.

## Références


[1] R. Verduci, V. Romano, G. Brunetti, N. Yaghoobi Nia, A. Di Carlo, G. D'Angelo et C. Ciminelli. "Solar Energy in Space Applications : Review and Technology Perspectives". *Advanced Energy Materials* 12.29 (août 2022), p. 2200125. issn : 1614-6832, 1614-6840. doi : 10.1002/aenm.202200125.

[2] M. Fischer. *International Technology Roadmap for Photovoltaics (ITRPV) 16th edition*. 2025. url : https://www.vdma.eu/en-GB/international-technology-roadmap-photovoltaic.

[3] D. J. Curtin et R. L. Statler. "Review of Radiation Damage to Silicon Solar Cells". *IEEE Transactions on Aerospace and Electronic Systems* AES-11.4 (juill. 1975), p. 499-513. issn : 0018-9251. doi : 10.1109/TAES.1975.308112.

[4] Y. Gurimskaya et al. "Effective Annealing of Proton and Electron Radiation Damage in Ultra-Thin Silicon Solar Cells". *2023 13th European Space Power Conference (ESPC)*. Oct. 2023, p. 1-5. doi : 10.1109/ESPC59009.2023.10298179.

[5] V. S. Kalinovskii et al. "Studies of Degradation Silicon Heterojunction Solar Cells by 1 MeV Electrons Irradiation". *Applied Solar Energy* 59.5 (oct. 2023), p. 604-611. issn : 1934-9424. doi : 10.3103/S0003701X23600984.

[6] S. Duarte-Cano et al. "Proton irradiation effects on silicon heterojunction solar cells with MoOx selective contacts". *Materials Science in Semiconductor Processing* 190 (mai 2025), p. 109312. issn : 1369-8001. doi : 10.1016/j.mssp.2025.109312.

[7] R. Cariou, A. Danel, N. Enjalbert, F. Jay et S. Dubois. “Investigation of p-Type Silicon Heterojunction Radiation Hardness”. *IEEE Journal of Photovoltaics* 14.1 (jan. 2024), p. 41-45. issn : 2156-3381, 2156-3403. doi : 10.1109/JPHOTOV.2023.3333197.

[8] A. Khan et al. “Strategies for improving radiation tolerance of Si space solar cells”. *Solar Energy Materials and Solar Cells* 75.1-2 (jan. 2003), p. 271-276. issn : 09270248. doi : 10.1016/S0927-0248(02)00169-1.

[9] M. U. Khan et al. “Degradation and regeneration of radiation-induced defects in silicon : A study of vacancy-hydrogen interactions”. *Solar Energy Materials and Solar Cells* 200 (sept. 2019), p. 109990. issn : 09270248. doi : 10.1016/j.solmat.2019.109990.

[10] H. Y. Tada, J. R. Carter, B. E. Anspaugh et R. G. Downing. *Solar cell radiation handbook*. Nov. 1982. url : https://ntrs.nasa.gov/citations/19830006416 (visité le 29/02/2024).

[11] M. Yamaguchi, S. J. Taylor, M.-J. Yang, S. Matsuda, O. Kawasaki et T. Hisamatsu. “High-energy and high-fluence proton irradiation effects in silicon solar cells”. *Journal of Applied Physics* 80.9 (nov. 1996), p. 4916-4920. issn : 0021-8979, 1089-7550. doi : 10.1063/1.363534.

# List of publications

## Publications in peer-reviewed journals

- **O. Guillot**, R. Cariou, J. Veirman, N. Enjalbert, A. Danel, C. Aicardi, and S. Dubois, "Influence of Material Composition and Wafer Thickness on the Performances of Electron Irradiated Gallium-Doped Silicon Heterojunction Solar Cells". In: *Solar RRL* 9.1 (2025), p. 2400669. doi: 10.1002/solr.202400669.

## Conference proceedings

- **O. Guillot**, J. Veirman, R. Cariou, N. Enjalbert, A. Danel, C. Aicardi, and S. Dubois, "Comprehensive Study of Performance of Silicon Heterojunction Solar Cells Under Electron Irradiation". In: *2023 13th European Space Power Conference (ESPC)* (2023), pp. 1-4. doi: 10.1109/ESPC59009.2023.10413251.
- R. Cariou, N. Enjalbert, P. Voarino, **O. Guillot**, C. Jamin, A. Danel, "Silicon Passivated Contacts Photovoltaic Arrays: A Promising Technology for Space". In: *2023 13th European Space Power Conference (ESPC)* (2023), pp. 1-4. doi: 10.1109/ESPC59009.2023.10298133.

## Conference and workshops contributions

- **O. Guillot**, R. Cariou, N. Enjalbert, A. Danel, P. Voarino, C. Aicardi, M. Fongral, J. Mekki, and S. Dubois "Effect of proton irradiation energy on high resistivity silicon heterojunction solar cells". Oral presentation at the *2025 IEEE 53rd Photovoltaic Specialists Conference (PVSC)* (2025), Montreal, Canada.
- **O. Guillot**, R. Cariou, N. Enjalbert, A. Danel, P. Voarino, C. Aicardi, and S. Dubois, "Effect of proton irradiation on modern high resistivity Ga-doped Si heterojunction solar cells". Visual presentation at the *16th edition of International Symposium on Materials in the Space Environment (ISMSE) Conference* (2024), Saint-Raphaël, France.
- **O. Guillot**, R. Cariou, N. Enjalbert, A. Danel, J. Veirman, C. Aicardi, and S. Dubois, "Carrier recombination in Ga-doped silicon with space representative electron irradiations: influence of the material composition". Oral presentation at the *41st European Photovoltaic Solar Energy Conference and Exhibition (EU-PVSEC)* (2024), Vienna, Austria.

- **O. Guillot**, R. Cariou, N. Enjalbert, A. Danel, J. Veirman, C. Aicardi, and S. Dubois, "Si Heterojunction solar cells radiation hardness". Oral and visual presentations at the *Special PV Workshop* (2024), Paris, France.
- **O. Guillot**, R. Cariou, N. Enjalbert, A. Danel, J. Veirman, C. Aicardi, and S. Dubois, "Influence of silicon material compositional properties on the electronic quality of electron irradiated Ga-doped wafers for space solar cells". Visual presentation at the *14th SiliconPV conference*, (2024), Chambéry, France.
- **O. Guillot**, J. Veirman, R. Cariou, N. Enjalbert, A. Danel, C. Aicardi, and S. Dubois, "Comprehensive Study of Performance of Silicon Heterojunction Solar Cells Under Electron Irradiation". Oral presentation at the *2023 13th European Space Power Conference (ESPC)* (2023), Elche, Spain.

## Patent pending

- **O. Guillot**, R. Cariou, S. Dubois, A. Danel, J. Mekki, C. Aicardi, and J. Veirman, "Cellule solaire photovoltaïque" (Optimisation of $J_{SC}$ for space environment) (2024), Deposit number: FR2413685.